Magnetic antiskyrmions in Heusler shape memory alloys

By

Subir Sen

Enrolment No: PHYS11201604009

National Institute of Science Education and Research, Bhubaneswar

A thesis submitted to the

Board of Studies in Physical Sciences

In partial fulfillment of requirements

for the Degree of

DOCTOR OF PHILOSOPHY

of

HOMI BHABHA NATIONAL INSTITUTE

January, 2022

Homi Bhabha National Institute[1]

Recommendations of the Viva Voce Committee

As members of the Viva Voce Committee, we certify that we have read the dissertation prepared by **Mr. Subir Sen** entitled "**Magnetic antiskyrmions in Heusler shape memory alloys**" and recommend that it may be accepted as fulfilling the thesis requirement for the award of Degree of Doctor of Philosophy.

Chairman - Prof. Bedangadas Mohanty	Boondhanty 27/06/2022
Guide / Convener - Dr. Ajaya K. Nayak	27.06.2022
Co-guide -	
Examiner - Prof. K. G. Suresh	June 21, 2022
Member 1- Dr. Niharika Mohapatra	Mohapatra 27.06.2022
Member 2- Dr. Subhankar Bedanta	SBedanta 27/06/2022
Member 3- Dr. V. Ravi Chandra	Vuddmiri. R. Chandra 27-06-2022

Final approval and acceptance of this thesis is contingent upon the candidate's submission of the final copies of the thesis to HBNI.

I/We hereby certify that I/we have read this thesis prepared under my/our direction and recommend that it may be accepted as fulfilling the thesis requirement.

Date: 27.06.2022

Place: NISER, SPS, Jatni

Signature
Co-guide (if any)

27.06.2022
Signature
Guide

[1] This page is to be included only for final submission after successful completion of viva voce.

STATEMENT BY AUTHOR

This dissertation has been submitted in partial fulfillment of requirements for an advanced degree at Homi Bhabha National Institute (HBNI) and is deposited in the Library to be made available to borrowers under rules of the HBNI.

Brief quotations from this dissertation are allowable without special permission, provided that accurate acknowledgement of source is made. Requests for permission for extended quotation from or reproduction of this manuscript in whole or in part may be granted by the Competent Authority of HBNI when in his or her judgment the proposed use of the material is in the interests of scholarship. In all other instances, however, permission must be obtained from the author.

Subir Sen

Subir Sen

DECLARATION

I, hereby declare that the investigation presented in the thesis has been carried out by me. The work is original and has not been submitted earlier as a whole or in part for a degree / diploma at this or any other Institution / University.

Subir Sen

List of Publications arising from the thesis

Journal

- **Published**

1. "Observation of the topological Hall effect and signature of room-temperature antiskyrmions in Mn-Ni-Ga D2d Heusler magnets", **Subir Sen**, C. Singh, P. K. Mukharjee, R. Nath, and A. K. Nayak, *Phys. Rev. B* ***99****, 134404 (2019).*
2. "ac susceptibility study of magnetic relaxation phenomena in the antiskyrmion-hosting tetragonal Mn-Pt(Pd)-Sn system. ", P. V. P. Madduri*, **Subir Sen***, B. Giri, D. Chakrabartty, S. K. Manna, S. S. P. Parkin, and A. K. Nayak, *Phys. Rev. B* ***102****, 174402 (2020).* *Equal contribution
3. "Manipulation of antiskyrmion phase in $Mn_{2+x}Ni_{1-x}Ga$ tetragonal Heusler system ", **Subir Sen**, Somesh K., R. Nath, and A. K. Nayak, *Phys. Rev. Appl.* ***17****, 044040 (2022).*

- **Manuscript under preparation**

1. "Magnetic relaxation study in antiskyrmion phase of $Mn_{2+x}Ni_{1-x}Ga$ shape memory alloys", **Subir Sen**, and A. K. Nayak.

Conferences

1. Poster presentation at "International Conference on Magnetic Materials and Applications (ICMAGMA)-2018", National Institute of Science Education and Research (NISER), Bhubaneswar, India.
2. Poster presentation at "Modern Trends in Molecular Magnetism (MTMM)-2019", Indian Institute of Science Education and Research (IISER), Bhopal, India.

3. Attend the "Bringing The Nanoworld Together (BTNT)-2019" conference, National Institute of Science Education and Research (NISER), Bhubaneswar, India..

Others

1. "Anomalous magnetoresistance and magneto-thermal properties of the half-Heuslers, RPdSi (R = Y, Gd–Er)", A. Mukhopadhyay, K. Singh, **Subir Sen**, K Mukherjee, A K Nayak and N. Mohapatra, *J. Phys.: Condens. Matter* ***33,*** *435804 (12pp) (2021).*

Subir Sen

DEDICATIONS

Dedicated to

.....

My

Parents

.....

ACKNOWLEDGEMENTS

First of all, I would like to take the opportunity to express my obligation to my supervisor, Dr. Ajaya Kumar Nayak, for his constant support and encouragement throughout my Ph.D. tenure. I am highly grateful to him for giving me the opportunity for independent research. I am deeply thankful to him for his valuable discussions, guidance to improve my knowledge. I am also grateful to him for providing critical suggestions to improve this thesis manuscript.

I want to thank Prof. Bedangadas Mohanty, chairman of the doctoral committee, for his continuous encouragement and suggestions to improve our practical knowledge. I would also like to thank the rest of my doctoral committee members, Prof. Shubhankar Bedanta and Dr. V. Ravi Chandra, for the continuous assessment of my work. I would further thank Dr. Niharika Mohapatra from IIT Bhubaneswar for her kind evaluation of my work as an external doctoral committee member.

I am immensely grateful to our collaborator Prof. Ramesh Nath from IISER Trivandrum, Kerala, India, for allowing me to use the high-temperature X-ray diffractometer and physical properties measurement system (PPMS) available at IISER Trivandrum. I would also like to thank him for his valuable suggestions regarding the work. I also wish to acknowledge Prashanta K. Mukharjee, Somesh K. for their help in the experiment performed at IISER Trivandrum. My work would not have been completed without their continuous help in performing experiments.

I am extremely grateful to my labmates Charanpreet, Dola, Pradeep, Subhendu da, Bimalesh, Jamal, Pavan bhaiya, Prachi di, Sudhansu bhaiya, Sujit, Gyandeep, Mahadev, Kshyanaprava, Manas, Jeetendra bhaiya for their continuous care and always being patient with me while sharing good and bad moments.

I wish to thank my NISER friends: Dukhishyam, Jagannath, Sudip, Tanim, Reshmi, for their friendship and support throughout my tenure. I thank Dola and Charanpreet, the quintessential loyal friends always caring and listening to me. I

am so fortunate to have such good friends who made me feel NISER as my home away from home.

The financial assistance provided by NISER during my Ph.D. tenure is gratefully acknowledged.

Finally, my most valued thanks to my family members: my parents (baba and maa), borda, mejda, boromama, boromami, chordibhai, and bordibhai for their affection and love. I am very grateful to my parents for their blessing, moral support, and unconditional love and sacrifice, which strengthen me to embrace and complete my Ph.D. in time.

Contents

SUMMARY

Magnetic skyrmions are topologically-protected swirling kinds of noncoplanar spin textures that attract a lots of attention due to their potential application as data bits in the future racetrack memory based magnetic storage devices [1]. Skyrmions in the form of lattice were first discovered in a noncentrosymmetric B20 material-MnSi near the magnetic ordering temperature [2]. Subsequently, the existence of skyrmions was directly revealed in other B20 materials and also in different categories of noncentrosymmetric materials [3, 4, 5, 6, 7, 8, 9, 10, 11, 12, 13]. In these materials, the competition of Heisenberg exchange and Dzyaloshinkii-Moriya (DM) interaction plays a crucial role in the stabilization process of skyrmions. In these bulk materials, mostly Bloch skyrmions [3, 4, 5, 6, 7, 8] and a very few cases of Neel skyrmions [9, 10, 11, 12] were observed depending upon the crystal symmetry of the materials. Besides these two types of spin textures, a new kind of topological magnetic object with topological charge opposite to that of skyrmion, named antiskyrmion, has also been found recently in an acentric inverse tetragonal Heusler system Mn-Pt-Pd-Sn having a D_{2d} class of crystal symmetry [14, 15, 16]. In the case of antiskyrmion, the inhomogeneous type of DM interaction dictated by the D_{2d} crystal symmetry stabilizes the anisotropic type of in-plane spin configuration. Even though both skyrmions and antiskyrmions owing to their topological stability, exhibit several advantages over the domain wall-based racetrack memory [17, 18], a major shortcoming is the deviation from their straight-line motion along the current direction, called as skyrmion Hall effect [19, 20]. In this direction, the antiskyrmion Hall effect can be tuned to zero when current is applied along some particular direction due to the distinct type of spin configurations of antiskyrmion [21]. In contrast, the skyrmion Hall effect remains the same for all current directions in the case of Bloch and Neel skyrmions [21]. Hence the antiskyrmions possess a first-

hand advantage over the skyrmions for the their future application in spintronics. Therefore, the finding of antiskyrmions in new magnetic materials is a crucial step for the future application based on antiskyrmions. In this context, it was already theoretically proposed that the D_{2d} and S_4 class of symmetry supports the required inhomogeneous DM interaction for the realization of antiskyrmions [22]. The recent experimental discovery of antiskyrmion in the D_{2d} symmetric Mn-Pt-Pd-Sn materials also corroborates the theoretically predication.

The Mn-rich Mn-Ni-Ga based shape memory alloys possess all the prerequisites to host antiskyrmions. Generally, these alloys undergo structural transition from a high symmetric cubic phase to a low symmetric tetragonal phase. When the tetragonal structure is noncentrosymmetric, it falls under the D_{2d} class of symmetry. Then the antiskyrmions can be realized in the noncentrosymmetric tetragonal phase of these alloys. In the present thesis, the realization of antiskyrmions in the D_{2d} symmetric Mn-rich Mn-Ni-Ga alloys are mainly discussed.

For this purpose, Mn-rich Mn-Ni-Ga alloys are prepared using the arc melting furnace. All the samples are characterized through x-ray diffractometer (XRD), field-emission scanning electron microscopy (FESEM), and energy-dispersive x-ray spectroscopy (EDS) techniques. The dc magnetization measurement is performed using the superconducting quantum interference device (SQUID)-vibrating sample magnetometer (VSM) and VSM attached to the physical properties measurement system (PPMS). The ac susceptibility measurements are carried out using the AC Measurement System (ACMS) option in the PPMS. The AC transport (ACT) option of the PPMS is used to map out the magnetotransport properties of the samples. The Object Oriented MicroMagnetic Framework (OOMMF) simulation is utilized to perform the micromagnetic simulation to understand the experimental results.

The first part of the thesis is dedicated to the realization of antiskyrmions in the D_{2d} symmetric Mn_2NiGa compound. The dominant tetragonal crystal phase having

space group I-4m2 and small amount cubic crystal phase with space group F-43m is found from the XRD pattern recorded at the room temperature for Mn_2NiGa. The temperature-dependent XRD patterns and the finding of thermal hysteresis between the field-cooling (FC) and field-heating (FH) $M(T)$ curve around the room temperature confirms the presence of structural transition from the high-temperature cubic to low temperature tetragonal phase in Mn_2NiGa. The field-dependent magnetization, $M(H)$, measurement performed at $T = 2$ K for Mn_2NiGa gives a saturation magnetization of 1.41 $\mu_B/f.u.$. The $M(H)$ loop also shows a dip kind of anomaly at a particular magnetic field range. The dip kind of anomaly is found in the tetragonal dominated temperature range, i.e. up to 300 K. In contrast, no such anomaly is detected in the $M(H)$ loop recorded in the cubic phase of the sample. Inspired by the anomaly in the $M(H)$ measurement, the topological Hall effect measurement, which is frequently used to skyrmions [13, 23, 24, 25, 26, 27], is performed at different temperatures. The extracted topological Hall resistivity shows only a nonzero value in the temperature span where the tetragonal phase is dominantly present. In contrast, zero topological Hall resistivity is found for the cubic dominated temperature range. The finite value of extracted topological Hall resistivity in the D_{2d} symmetric material strongly indicates the presence of antiskyrmion phase up to room temperature. To further establish the presence of the antiskyrmion phase, ac susceptibility measurement, which is often employed to characterize the skyrmion phase [28, 29, 30, 31, 32, 33], is performed at various temperatures. The existence of a sharp kink-like features in the field-dependent ac susceptibility data strongly support the presence of antiskyrmion phase up to room temperature in Mn_2NiGa. The antiskyrmion size estimated from the topological Hall measurements is found around 20 nm. The smaller antiskyrmions size along with relatively low magnetization of Mn_2NiGa in comparison to that of Mn-Pt-Pd-Sn system play important role towards the realization of antiskyrmion based data storage devices.

A part of the thesis is concerned about the modification of the antiskyrmion phase present in the Mn_2NiGa alloy. Despite several advantages of antiskyrmion hosting Mn_2NiGa material over the antiskyrmion host Mn-Pt-Pd-Sn system, the stability of the antiskyrmion phase against temperature is one of the major obstacles for the future spintronics application. For any future high-density data storage device, the reduction of antiskyrmion size is an essential step. Even though the magnetic moment in Mn_2NiGa is lower than other existing antiskyrmion hosting materials, further lowering of magnetic moments may help to reduce the antiskyrmion Hall angle irrespective of current direction and for a better stability of the antiskyrmion phase against the in-plane magnetic fields. For this purpose, a series of $Mn_{2+x}Ni_{1-x}Ga$ (x = 0.1-0.28) samples are prepared using the arc-melting furnace. All the samples are characterized properly through XRD, FESEM, and EDS measurements. It is found from the room temperature XRD patterns that all the samples crystallize in the pure tetragonal phase in contrast to the mix-structural phase in Mn_2NiGa. The temperature-dependent magnetization measurements also support the absence of structural transition up to the magnetic order temperature of about 650 K. A monotonic decrease in the magnetic moment from 1.41 $\mu_B/f.u.$ $x = 0.00$ to 0.43 $\mu_B/f.u.$ for $x = 0.28$ is found in the dc magnetic hysteresis measurement. Interestingly, the field-dependent magnetization measurements in $x \leq 0.20$ reveal a similar anomaly as seen for the parent Mn_2NiGa compound. No anomalies are observed for $x = 0.25$, and 0.28 samples. Apart from the low field anomaly, a new type transition accompanied with hysteresis behavior appears in the $M(H)$ for x = 0.13, and 0.16. It is found that the topological Hall resistivity increases initially with composition before reaching the maximum value around 232 nΩ-cm and then again decreases for $x \geq 0.16$. Finally, a zero value of topological Hall resistivity is found for $x = 0.25$ and 0.28. Since the magnitude of topological Hall effect directly determines the size of the skyrmions/antiskyrmions, a tunable antiskyrmion size is

expected for the present samples. It is demonstrated that the anisotropy of the system controls the size of the antiskyrmion, resulting in the variation of topological Hall resistivity. Therefore, the largest value of topological Hall resistivity indicates a reduction of antiskyrmion size for $x = 0.13$ and 0.16. The field-driven ac susceptibility measurements show a small transition for $x \leq 0.1$, while more than one transitions are found for $x = 0.13$ and 0.16. No such kind anomalies are detected for $x = 0.25$ and 0.28. Hence, the observation of anomalies in the magnetic data and finite topological Hall resistivity strongly suggest the presence of antiskyrmion phase for $x \leq 0.20$. On the other hand, the absence of any peak and hump kind anomalies in the ac susceptibility measurements and almost zero value of topological Hall resistivity indicate the disappearance of the antiskyrmion phase for $x = 0.25$ and 0.28 samples. The presence of multiple transitions in ac susceptibility data and a double peak-like behavior in the topological Hall resistivity curve strongly indicate the presence of various topological phases with different topological charges for $0.10 < x < 0.20$. This is also supported by the micromagnetic simulation studies. The present findings of reduction in the size of antiskyrmions, smaller magnetization, and the presence of multiple topological phases are extremely important for realizing the antiskyrmions-based storage devices.

The final part of the thesis focuses on the magnetic relaxation study in the antiskyrmion phase of the inverse tetragonal Heusler compounds using ac susceptibility measurements. The frequency-dependent ac susceptibility data are analyzed in light of the Cole-Cole model to study the relaxation dynamics of the known antiskyrmion hosting Mn-Pt-Pd-Sn material. It is demonstrated that the Debye-type relaxation process with negligible distribution of relaxation time governs the magnetic relaxation in these materials. A slight deviation from this behavior is observed around the coexistence region consisting of helical and antiskyrmion phases (or antiskyrmion and field polarized state). The observation of unusual behavior in

the relaxation time and distinct maxima at the magnetic phase boundaries signify the presence of a slow relaxation process at the phase crossover region compared to the pure magnetic phase. Similar relaxation dynamics studies on the possible antiskyrmion hosting system Mn-Ni-Ga are carried out. The coexistence of the helical and antiskyrmion phase and the mixed-phase consisting of antiskyrmion and the field polarized state are evident from slow relaxation behavior around the phase boundaries. It is also observed that the relaxation process for the Mn-Ni-Ga alloys is faster than that of Mn-Pt-Pd-Sn alloys. This might be due to the smaller antiskyrmions size in the Mn-Ni-Ga system in copmarison to that of Mn-Pt-Pd-Sn system.

List of Figures

Chapter 1

Introduction

In 1965, Gordon Moore presented a golden statement based on his observation that the number of micro-components (transistors) in a chip or integrated circuit will be doubled in almost every two years. Therefore, the increase in the number of transistors in microelectronics devices in the last few years makes it difficult for device-makers to incorporate heating problems, electrical leakage, power consumption, and several other problems in the electronics devices. Hence, the reduction in size and lowering the power consumption in any electronic device are the most challenging aspects for researchers for the last 60 years. The problems mentioned above, along with the volatile nature and slowness of the memory devices, inspired the idea of spin logic which gave birth to the spintronics, i.e., spin degree of freedom of electrons is taken into account to control the current flow depending upon the spin interactions.

The era of spintronics starts with the discovery of Giant Magnetoresistance (GMR) [34, 35] and Tunneling Magnetoresistance (TMR) [36]. Both phenomena mentioned above rely on the change in the electronic properties due to the relative orientation of two magnetic layers separated by a non-magnetic metal/insulating layer. In general, depending upon the thickness of the non-magnetic layer, the two magnetic layers exhibit ferromagnetic (FM) or antiferromagnetic (AFM) coupling. This type of coupling depends on the Ruderman–Kittel–Kasuya–Yosida (RKKY)

interaction. Although the field of spintronics is expanding at a rapid speed, no significant development has been reported on the spin-based data storage devices. At present, the two primary sources of data storage are the solid-state-based random access memory (RAM) and the magnetic hard disk drive (HDD). Despite the rapid development of both types of data storage techniques, each has some drawbacks compared to the other. One of the major shortcomings of the RAM is its high cost to store a single data bit in comparison to the magnetic HDD. On the other hand, in the case of magnetic HDD, its response time is too large compared to the RAM because of the heavy mass of the rotating disks. Therefore, building a storage device as cheap as HDD and performance comparable to the solid-state RAM is highly desirable. In the last few years, Parkin *et al.* [37] have carried out a significant amount of work in this direction based on a novel high density, high performance, solid-state storage memory device - Racetrack Memory [37]. Racetrack memory, which is proposed to consist of magnetic nanowires consisting of several magnetic domains aligned vertically or horizontally on a silicon chip, is supposed to be three-dimensional (3D) in nature instead of the conventional two dimensional (2D) memory systems. Here, each magnetic domain wall is used to store information in the form of a bit. Therefore, a series of data bits can be stored along each magnetic nanowires of the racetrack. Such arrangement of the racetrack device would help to increase the data storage capacity enormously. In principle, reading and writing occur through the back and forth motion of domain walls along the racetrack of magnetic nanowires by application of nanosecond current pulses. It is to be noted here that the spin-transfer torque phenomenon is accountable for the domain walls motion in racetrack devices. However, it is found that the motion of the domain walls can only be achieved with a very high current density of the order 3×10^8 A/cm^2 [38, 39, 40]. Even though the domain wall-based racetrack memory possesses huge advantages in terms of storage capacity and speed, it has several demerits, e.g. (1) high current density to move the domain walls, (2) incapability to avoid pinning centers (magnetic impurities) where the domain wall can be annihilated. In this context, some of the recently discovered topological spin textures

attract much attention due to several advantages that they exhibit over the conventional domain walls. Recent experimental discovery of magnetic skyrmions [2, 3, 4, 8, 9, 29, 41], an example of the topological spin textures, fuels the research on topological aspects of different types of spin states. It has been shown that magnetic skyrmion, a vortex-like object with circular chiral spin configuration, starts to move with a critical current of 10^5 order less in magnitude in comparison to the domain walls owing to its topological protection [17, 18]. Another important aspect of skyrmions is that their ability to avoid the pinning centers without changing their topological character.

It has been proposed that the magnetic skyrmions can act as data bits '1' and '0' in the racetrack memory device [1]. Although it has been theoretically shown that the skyrmions as data bits may solve many problems of the racetrack memory, a lot of issues remain unsolved experimentally for their implementation in devices. In this prospect, the foremost challenges for the room temperature high-density data storage devices are the reduction of skyrmion size (<10 nm) and their stability in an extensive temperature range that includes room temperature. One of the major drawbacks is that skyrmions exhibit the skyrmion Hall effect (SkHE), the current-driven motion of the skyrmions toward the edge of the sample [19, 20]. It has been experimentally observed that the skyrmions under the application of electric current do not move along the straight-line path in the nano-tracks, rather they prefer to move towards the edge of the nano-tracks due to the skyrmion Hall effect [19, 20]. As a result, the information stored in the form of data bits can be lost as a consequence of the annihilation of skyrmions at the edge of the racetrack. In this framework, it is important to search for alternative topological objects that could possibly rectify all the problems mentioned above. Hence, the search for new skyrmion hosting materials with different topological charges is extremely important for any future applications pertaining skyrmions.

1.1 Motivation and outline of the thesis

As stated above, the skyrmion Hall effect is an unwanted quantity for the device application. It is expected that all the topological magnetic objects with non-zero topological number would exhibit the skyrmion Hall effect. However, depending on the nature of the spin configuration it may be possible that the motion of these topological objects can be controlled by directional current injection. In this regard, it has been recently shown that the angle of deflection of antiskyrmions, a new type of topological object with opposite topological charge to that of skyrmions, firmly depends on the direction of currents [21]. It can be noted here that the presence of inhomogeneous in-plane spin configurations of antiskyrmions in comparison to that of the skyrmions plays a major role in the anisotropic current driven motion of the former. Interestingly, it has also been reported that the antiskyrmion Hall effect can be nullified for a particular direction of current flow [21]. Because of this distinct characteristic of the antiskyrmions, they possess a first-hand advantage over the skyrmions for any future applications. Hence it is important to explore new materials that can exhibit antiskyrmion phase at room temperature.

It has been theoretically shown that the class of materials with crystal symmetry D_{2d} and S_4 can exhibit antiskyrmion phase [22]. In this context, the experimental demonstration of the antiskyrmion lattices has been carried out in the D_{2d} symmetry based Mn-Pt-Pd-Sn inverse tetragonal Heusler materials [14, 15, 16]. It is important to mention here that for any future application of antiskyrmions, their size should be very small in order to achieve the high density data storage. In addition, they must exist over a large temperature range including the room temperature. Furthermore, antiskyrmions in low magnetic moment materials are preferable to minimize the problem of skyrmion Hall effect as well as the stray field effect. Although the antiskyrmion lattice has been recently detected in the Mn-Pt-Pd-Sn samples at room temperature, the high magnetic moment of the order of 5 μ_B/f.u. of this system along with large size of the antiskyrmions are the primary limitations for the future high density storage application [14, 15, 16]. It has also been observed

recently that the antiskyrmions phase in Mn-Pt-Pd-Sn samples can be modified into skyrmion phase via trivial bubble under the application of small amount of in-plane magnetic fields [15, 16]. Due to this topological phase transformation, the antiskyrmions in the high magnetic moments based system may not be desirable in the context of skyrmion Hall effect. Hence, it is important to search for the low magnetic moment based new antiskyrmion hosting materials that can exhibit very small antiskyrmions.

Another important parameter that needs to be looked upon for any practical application in spintronics is the minimization of the energy loss as a result of the magnetic damping. It is well known that the damping of magnetization is related to the relaxation rate to attain the equilibrium state. In other words, the faster relaxation process indicates comparably higher magnetic damping and vice-versa. Therefore, the low damping based materials are preferable in some particular spintronics applications. In contrast, higher magnetic damping is sometime more advantageous in some applications, for instance, the requirement of lower critical current density for higher magnetic damped samples in the current-driven magnetization switching process of magnetic RAM. Therefore, the study of relaxation dynamics of skyrmion phase is an important aspect for the application perspective. No such relaxation dynamics study has been carried out yet on the antiskyrmion hosting materials. Therefore, it is required to throw some lights in this direction.

In the present thesis, an elaborate study on the antiskyrmion phase of Mn-Ni-Ga based Heusler shape memory alloys is presented by means of magnetic and magneto-transport measurements. In this context, various aspects of antiskyrmion phase are discussed by analyzing the data obtained from different experiments. The present thesis consists of six chapters. **Chapter-1** fully concentrates on the introductory part that includes the motivation behind the present work, theoretical background and literature survey associated with the present work. The experimental techniques used in these studies are described in details in **Chapter-2**. The realization of antiskyrmion phase in the Heusler shape memory alloy, Mn_2NiGa, is presented in **Chapter-3**. In this chapter, the antiskyrmion phase in these alloys are char-

acterized through static magnetization, magneto-transport, and ac susceptibility measurements. **Chapter-4** is focused on the modification of antiskyrmion phase in $Mn_{2+x}Ni_{1-x}Ga$ shape memory alloys. **Chapter-5** is assigned to the relaxation dynamics studies of the known antiskyrmion hosting Mn-Pt-Pd-Sn materials and the antiskyrmion hosting Mn-Ni-Ga system. The summary, conclusion and future aspects of the thesis are discussed in **Chapter-6**.

1.2 An overview about the fundamental Interactions in Magnetism

1.2.1 Exchange Interaction

The fundamental interaction that first comes into the picture to describe the formation of hydrogen molecule from two individual hydrogen atoms is known as the exchange interaction, which is nothing but an electrostatic interaction. The corresponding exchange force between the spins of two neighboring electron of the two individual hydrogen atoms acts as a glue to hold them together against the strong coulomb repulsion in order to minimize the energy. When the two spins are antiparallel, then the total energy of the system is minimum, and hence the corresponding force between the two atoms is attractive. Therefore, it can be easily concluded that the exchange force is an outcome of the Pauli exclusion principle when it is applied to two atoms as a whole. Besides this bonding theory of molecules, the fundamental origin of the molecular field in the Weiss theory, missing until 1928, could be successfully formulated when the quantum-mechanical approach was taken to deal with the problem by Heisenberg [42]. He could successfully demonstrate that the magnetic properties of magnetic materials can be explained in terms of exchange interaction, which determines the long range ordering in magnetic material. The exchange interaction between two neighboring spins, $\vec{S_i}$ and $\vec{S_j}$ located at i-th and

j-th sites can be expressed in terms of the exchange Hamiltonian,

$$H_{exchange} = -2J\vec{S_i}.\vec{S_j} \tag{1.1}$$

where, J is the exchange constant.

The above equation is derived for the two electron system. In early days of quantum mechanics, it was found that the above equation is also valid for all neighboring atom in many body system. Therefore, the Heisenberg Hamiltonian for many body system can be written as

$$H_{exchange} = -\sum_{ij} J_{ij}\vec{S_i}.\vec{S_j} \tag{1.2}$$

where, J_{ij} is the exchange constant between the i-th and j-th spins. The factor 2 is included in the summation for double counting of each pair of spins. The spin arrangement in two different neighboring sites depends on the sign of the exchange constant. If the J_{ij} is positive, the spins favor parallel arrangement to minimize the exchange energy, whereas the negative value of J_{ij} forces the antiparallel spin arrangement. Therefore, the positive value of J_{ij} is an important criteria for ferromagnetism and negative value of J_{ij} is generally found in antiferromagnetic materials. The magnetic ordering temperature can be determined from the magnitude of exchange constant.

1.2.2 Dzysloshnkii-Moriya Interaction

Dzysloshnkii-Moriya (DM) interaction is an asymmetric exchange interaction, which sometime dictates the magnetic properties of a system. In general, the Hamiltonian corresponding to DM interaction between two neighboring spins $\vec{S_i}$ and $\vec{S_j}$ can be expressed as $H_{DM} = -\vec{D_{ij}}.(\vec{S_i} \times \vec{S_j})$ where, $\vec{D_{ij}}$ is the DM vector. From the expression of DM Hamiltonian, it can be seen that the corresponding DM energy will be minimum if the DM vector $\vec{D_{ij}}$ lies normal to the plane that contains both the neighboring spins $\vec{S_i}$ and $\vec{S_j}$, and the alignment of these two spins must be perpendicular

to each other. This type of interaction was first-time introduced by Dzysloshnkii in 1958 to explain the 'weak-ferromagnetism' behavior of an antiferromagnetic α-Fe_2O_3 system [43]. Because of the preference of the perpendicular arrangement between two neighboring spins by this class of interaction, the magnetic spins exhibit a canting at certain angle as result of the competition between the DM interaction and the isotropic exchange interaction. This results in a small net ferromagnetic moment in this antiferromagnetic α-Fe_2O_3. The dependency on the spin-orbit coupling strength of the DM interaction was investigated by Moriya in 1960 [44]. He also proposed a few rule about the direction of the DM vectors acting on two magnetic moments based on the crystal symmetry. These rules are known as Moriya rules described as follows. Let's consider two atoms with spin magnetic moments positioned at 'A' and 'B'. 'AB' is the line that joins these two atoms, and 'C' is the bisect point of the line 'AB'. According to this rule, (1) $\vec{D} = 0$, provided 'C' must be the center of inversion of the system, (2) $\vec{D} \perp \vec{AB}$ or $\vec{D} \parallel$ the mirror plane, when a mirror plane passes perpendicular to the 'AB' line passing through 'C', (3) $\vec{D} \parallel \vec{AB}$ in case 'A' and 'B' magnetic atoms both lies in the mirror plane, (4) if a two-fold rotation axis is passing through 'C' is perpendicular to the 'AB' line, then $\vec{D} \perp$ to the two-fold rotational axis, (5) when a n-fold (n$\geq$2) rotational axis passes along the AB line, then $\vec{D} \parallel \vec{AB}$.

It is important to highlight here that the strength of the DM interaction strongly depends on the relativistic spin-orbit coupling in the system, whereas, the direction of the DM vector is firmly dictated by the crystal symmetry as described by Moriya [44]. Therefore, the strength of this interaction in materials with heavy element is generally much higher than that with lighter element in the periodic table, as the magnitude of the spin orbit coupling strength varies nearly with fourth power of the atomic number (Z), Z^4. Nonetheless, DM interaction strength actually depends on the electronic band structure of the system.

1.2.3 Magnetocrystalline Anisotropy

In general, all the magnetic materials prefer to get magnetized in a certain fixed direction under the external magnetic field. This directional preference of the magnetization in a certain fixed direction is known as magnetic anisotropy. For that specific fixed direction, a small magnetic field is needed to magnetize the system, known as easy-axis of magnetization. In contrast, a large magnetic field is required to magnetize the system for some specific crystallographic directions, called as hard-axis of magnetization. For instance, in case of face centered cubic crystal, nickel (Ni), it requires a small magnetic field to saturate the system along the $< 111 >$ direction, which is the easy-axis for the nickel cubic crystal. Whereas, relatively high magnetic field is needed to saturate the magnetization along $< \ 100 \ >$, the hard-axis of magnetization for nickel.

Even though several types of magnetic anisotropy (shape anisotropy, surface and interface anisotropy) appear in magnetic material, the magneto-crystalline anisotropy is the intrinsic property of all the crystalline systems. The origin of the magneto-crystalline anisotropy is related to the spin-orbit interaction. When a magnetic field is applied to the system, the spin of the electrons tries to follow the direction of magnetic field. As a consequence of spin-orbit coupling, the orbit of that electron also tries to reorient. The strong orbit-lattice coupling prevent the rotation of the spin axis. Therefore, it requires more energy to overcome the strength of the orbit-lattice, so that the spin axis will rotate accordingly. Therefore, the energy needed to rotate the spins from the easy-axis of the magnetization can be called as the magnetic anisotropy energy for the system. In cubic crystal, the magnetic anisotropy energy is defined as

$$E_{anisotropy}^{cubic} = K_1[\alpha_x^2\alpha_y^2 + \alpha_y^2\alpha_z^2 + \alpha_z^2\alpha_x^2] + K_2\alpha_x^2\alpha_y^2\alpha_z^2 + ... \tag{1.3}$$

where, α_x, α_y, α_z are the cosine angles of magnetization with respect to the crystallographic axes a, b, c, respectively, and K_1, K_2,.. are the constants for any particular

material at fixed temperature.

In case of hexagonal and tetragonal crystal systems, there are only one easy-axis direction of magnetization. Because of this, these crystal structures are called as uniaxial crystals. The easy axis direction for these crystal system is either a or c axis. Let us consider, c axis is the only easy direction of magnetization, then every directions lying in the basal plane are the hard axis of magnetization for this case. If θ is the angle between the c-axis and the direction of magnetization, then the magneto-crystalline anisotropy energy for these uniaxial crystal can be written as

$$E_{anisotropy}^{uniaxial} = K_1 \sin^2\theta + K_2 \sin^4\theta \tag{1.4}$$

It can be seen from the above expression that the energy will be minimum when $\theta = 0$, indicating that the c-axis is the easy direction of magnetization. It is to be noted here that the magnitude of the constants K_1, K_2 determines the strength of the anisotropy.

1.2.4 Dipole-Dipole Interaction

In general, the magnetic dipole moments in material interact with each other, known as dipole-dipole interaction. Because of this dipolar interaction, a field generated inside the materials opposite the magnetization is called demagnetization or dipolar field. The energy corresponding to the dipole-dipole interaction between two dipoles of strength $\vec{m_1}$ and $\vec{m_2}$, apart at a distance $\vec{r}$ can be expressed as

$$E_{dd} = \mu_0[\vec{m_1}.\vec{m_2} - (\vec{m_1}.\vec{r})(\vec{m_2}.\vec{r})/r^2]/4\pi r^3 \tag{1.5}$$

It can be seen from the expression that the strength of the dipole-dipole interaction depends on the magnitude of each magnetic moment, their mutual orientation, and the distance between the two magnetic moments. The strength of dipolar energy is in general very weak in comparison with other magnetic interactions. This dipolar energy is minimum when the $\vec{m_1}$ and $\vec{m_2}$ both lie in the same plane.

1.2.5 Zeeman Interaction

When the magnetic field is applied to magnetic material, the magnetic moments interact with the magnetic field. This interaction is known as Zeeman interaction and the corresponding energy can be written as

$$E_{Zeeman} = -\int_v \vec{M}.\vec{B}\ dv \tag{1.6}$$

where $\vec{M}$ stands for the magnetization of the system and $\vec{B}$ is the magnetic field applied to the sample.

The energy term is minimum when the direction of magnetization is parallel to the applied magnetic field and the strength of this energy depends on the magnitude of the magnetization.

1.3 Topological aspects of magnetic spin configuration

1.3.1 Brief discussion about Topology

Topology is an elementary and crucial concept in mathematics. The concept originated to describe the topological invariant (under continuous deformation) fundamental properties of topological spaces. When one topological space is continuously deformed into another by any kind of perturbation, then we can call that the topology of the two spaces are the same, in other words they are topologically equivalent spaces. In mathematical point of view, let's take u and v as two topological spaces, then a function $f : u \to v$ can be named as homeomorphism (an example of topological equivalence) if this transformation is continuous, bijective type, and there exists a inverse transformation function $f^{-1} : v \to u$. Therefore, these space u and v are called homeomorphic or topological equivalent spaces. For example, a glass geometry is topological equivalent to the egg shaped geometry as shown in Fig. 1.1(a)

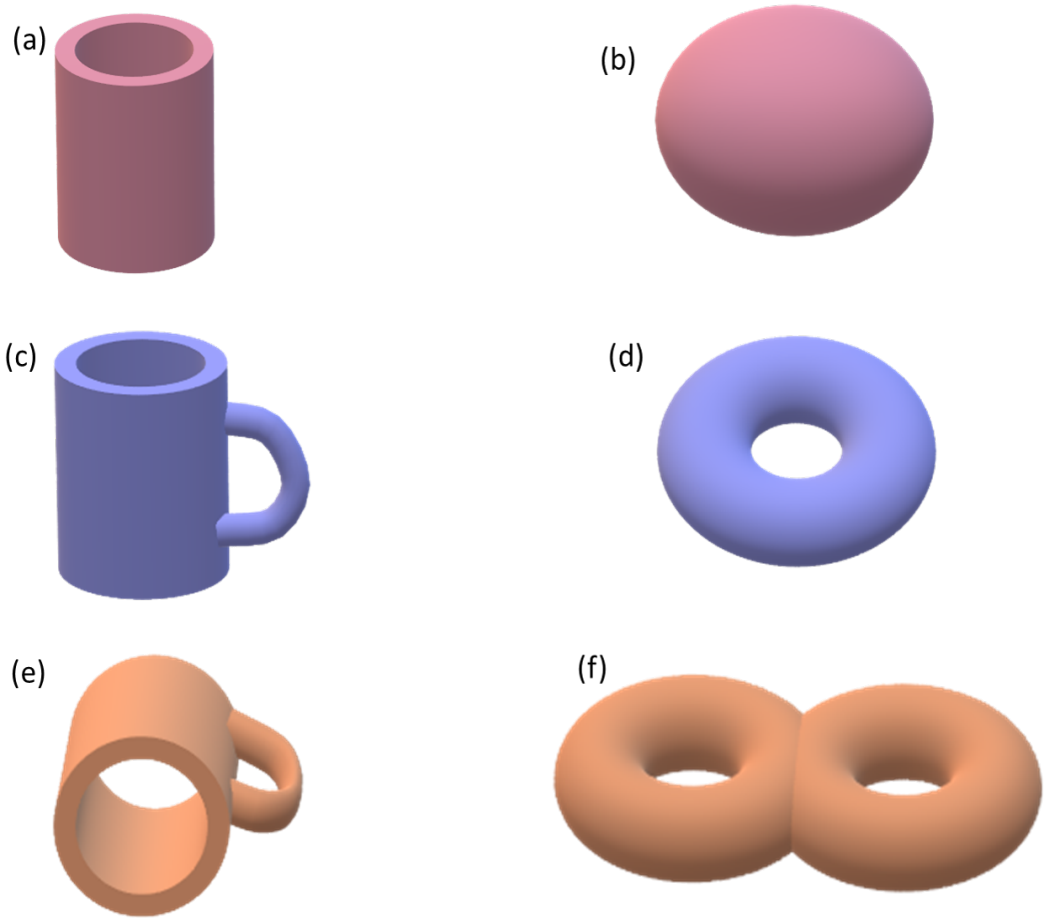

Figure 1.1: Examples of topologically equivalent geometry

and (b). This means the geometry of the glass can be transformed into the egg shaped object by point-to-point continuous mapping from the cylindrical shaped glass to the elliptical egg shaped object. This is also true for inverse continuous transformation of egg to glass geometry. Let's take another example as depicted in Fig. 1.1(c) and (d), a coffee mug with handle can be continuously converted or mapped into a doughnut shaped geometry by compressing and shrinking the cylindrical geometry of the mug. Hence, the geometry of coffee mug and doughnut are topologically equivalent to each other. In similar manner, the object in Fig. 1.1(e) can be transformed topologically into the object in Fig. 1.1(f) . It can be seen that the geometrical shape of the objects in Fig. 1.1(a), (c), and (e) [left panel] looks very similar to the eyes, however, they are not identical from the topological point

of view. Exactly the same remark can also be made for the geometrical shape of the objects in Fig. 1.1(b), (d), and (f). It is worth mentioning here that when the transformation from one topological object to another happens by tearing or by cutting the object, signifying the deformation is not continuous, then these objects are topologically non-equivalent to each other. Another important aspect to consider is that the topological property of topologically equivalent spaces. More clearly, considering A, B and C are topologically equivalent spaces, then the topological property of A spaces will be the same as that of B and C spaces. Therefore, topological equivalence between different spaces have its importance in topology from the application point of view. Nowadays, apart from mathematical branch, the concept of topology earns a lots of attention in condensed matter physics due to its extensive use in describing the unconventional properties related to the topology.

1.3.2 Topological Numbers /Chern number

Topological objects are generally characterized by a Chern number or topological number or winding number. In simple words, the winding number of a closed curve in the plane around any arbitrary point is defined as the number of times travelling of the curve around that point. In general, it is an integer and the sign of this numbers depends upon the traveling direction around the point. Conventionally, the Chern number in two-dimensional space is called as winding number. An important property of topological numbers/winding number is that it is invariant under continuous deformation of a topological object to another topological object. Hence, two different topological objects with distinct topological numbers cannot deform continuously from one to other.

To realize the topological spin texture in magnetism, it is important to understand the winding number of different spin configuration. Let's consider a 2D spin texture, where uniform spin configuration (all spins are parallel to each other) is propagating along the periphery of a circle as shown in Fig 1.2A. To find out the winding number of this spin configuration, first it is necessary to project each spin

vector of the physical space on to order-parameters space (here magnetization as the order parameter). Obviously, the order parameter space of the 2D spin vector is a circle. Therefore, the winding number in 2D spin texture represents the number of times the closed curve of spin vector mapping encloses around a circle (order parameter space). Here the mapping of spin configuration in Fig 1.2A,B onto order parameters space is shown in Fig 1.2AB. In the order parameter space, the mapping of this uniform spin configuration would be a single point of the circle. As there is no closed curve of mapping around the circle, henceforth, as per the definition, the winding number of these uniform spin configuration (n_{2D}) is zero. Now take another example of 2D spin texture as shown in Fig 1.2C,D where spin rotates on the circle. In this case, it is clearly seen that the closed curve of the spin vector mapping in order space wraps the circle once, as shown in Fig 1.2CD. Therefore, winding number in these system (n_{2D}) is equal to 1. In similar procedure, the winding number of other 2D spin texture as depicted in Fig 1.2E to I can also be obtained by mapping of the spin vector on the circle as in Fig 1.2EF to II. It is important to notice here that the spin configurations in Fig 1.2B and Fig 1.2I look completely different in physical space, but they are equivalent from the topological point of view, as the winding number of these spin structure are same. Similar conclusion is also valid for the spin configuration in Fig 1.2C and D. Note that the sign of the winding number is determined by the wrapping direction of the spin vector mapping around the circle.

In case of 3D spin vector, the order parameter space is not a circle, instead it is the surface of the 3D sphere. Then, the number of times 3D spin vector mapping wrap around the sphere in a close path is the winding number of that configuration. In 3D space, it is known as topological number/charge or skyrmion number. In mathematically, the topological number or skyrmion number is defined as

$$N_{sk} = \frac{1}{4\pi}\int\int n_{sk} d^2\boldsymbol{r} = \frac{1}{4\pi}\int\int \boldsymbol{m}.(\frac{\partial \boldsymbol{m}}{\partial x} \times \frac{\partial \boldsymbol{m}}{\partial y})\, dxdy \tag{1.7}$$

where, $n_{sk} = \boldsymbol{m}.(\frac{\partial \boldsymbol{m}}{\partial x} \times \frac{\partial \boldsymbol{m}}{\partial y})$ is the skyrmion number density, $\boldsymbol{m}$ is the unit vector of

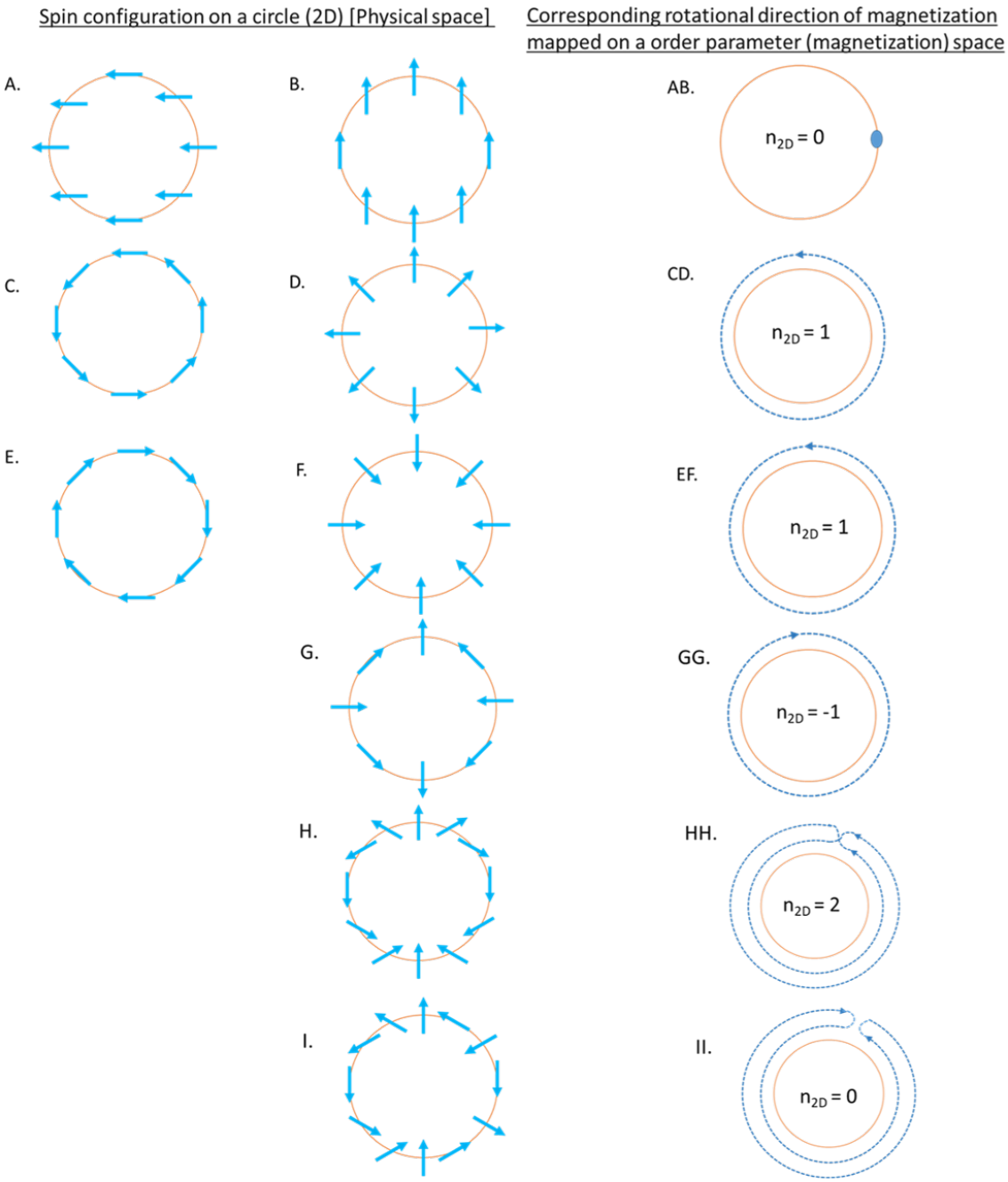

Figure 1.2: A-I: Different type of 2D spin vectors on a circle, and AB-II (right most panel): corresponding spin configuration mapping on order parameter space. Note that order parameter space in these case is a circle. n_{2D} represents the winding number of the respective spin texture

magnetization.

1.4 Non-collinear/Non-coplanar spin texture in magnetism

In recent times, non-collinear magnetic structures attract a lots of attention over the conventional well known collinear ones due to finding of enigmatic phenomena, such as different kind of Hall effects [45, 46, 47], spin-transfer torque in switching current [48], nanoscale electromagnetic inductor [49], etc. In general, the collinear ferro-, ferri-, antiferro-magnets exhibit either parallel or anti-parallel spin alignment dictated by the traditional Heisenberg exchange. However, competing Heisenberg exchange interactions and/or DM interaction can introduce non-collinearity into the system. In this context, it has been found that the Mn_2RhSn inverse tetragonal Heusler compound display a non-collinear magnetic structure [50]. The origin of this non-collinearity can be attributed to the competing exchange interactions, between the nearest neighbor Mn moments and the next nearest neighbor Mn spins [50]. In addition, Mn_2RhSn also support the DM interaction that favors perpendicular spin alignment. Moreover, magnetic systems with two or more competing interactions, e.g. dipole-dipole interaction, DM interaction, magneto-crystallographic anisotropy etc, are potential candidates to exhibit non-collinear or non-coplanar (if $\vec{S_i}.\vec{S_j} \times \vec{S_k} \neq 0$) magnetic state. Although different type of non-collinear/non-coplanar spin textures exists in magnetic materials depending on the competing interactions in the system, only few spin textures display the chirality. Here, 'chirality' term is used as a sense of rotational handedness of spin texture. A few examples of non-collinear or non-coplanar spin textures are described below.

1.4.1 Helical spin texture

Helical spin texture is an example of spin spiral state where the spins rotate in a plane perpendicular to the spin propagation direction. A schematic of the helical spin texture with spin modulation length λ is shown in Fig. 1.3. As it can be seen,

the helix propagates along the $+x$-direction, whereas, the spins rotate in the YZ plane. The helical spin structure is typically found in materials that can host DM interaction. Now, let's consider a magnetic system that can support DM interaction. The magnetic energy of the system can be written as $E = -J_{ij}\vec{S_i}.\vec{S_j} + \vec{D_{ij}}.\vec{S_i} \times \vec{S_j}$ or, $E = -J_{ij}S_iS_j\cos\theta + \vec{D_{ij}}.\vec{n}S_iS_j\sin\theta$, where $\vec{n}$ is unit vector of $\vec{S_i} \times \vec{S_j}$. The minimization of energy gives the twist angle between two adjacent spins in the helix chain. The twist angle between spins mainly depends on the ratio of DM constant (D) to exchange strength (J). The helical pitch or period of modulation, λ, is the minimum length required for 2π rotation of spins along the spin propagation direction and it is defined as $\lambda = 4\pi J/D$. The direction of propagation is mainly determined by the crystal symmetry and anisotropy of the system, whereas, the rotational sense of the helix is dictated by the direction of DM vector. This type of helical spin modulation has been observed in many non-centrosymmetric materials [2, 3, 4, 51, 52, 53].

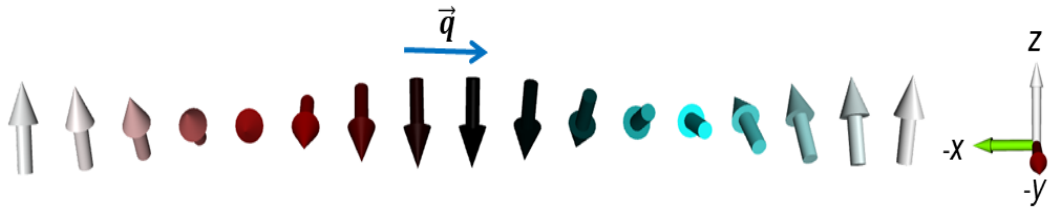

Figure 1.3: Spin textures of a helix propagating along the $+x$ direction.

1.4.2 Cycloid spin texture

In case of cycloid spin textures, the spins twist in such a manner that the plane of rotation lies along the propagation direction. A typical schematic spin configuration of the cycloid spin propagation is presented in Fig. 1.4. As it can be seen, the spins are rotating in the XZ plane and the spin cycloid propagate along the x-direction. Like the helical spin modulation, spin cycloid is also often generated by the competition between the DM interaction and the exchange interaction. In general, the cycloid spin modulation is mostly stabilized in layered thin films with interfacial DMI [54, 55, 56, 57]. In case of non-centrosymmetric bulk materials,

e.g. GaV_4S_8 [9] and Mn-Pt-Ga [12], the crystal symmetry is responsible for the observation of spin cycloid.

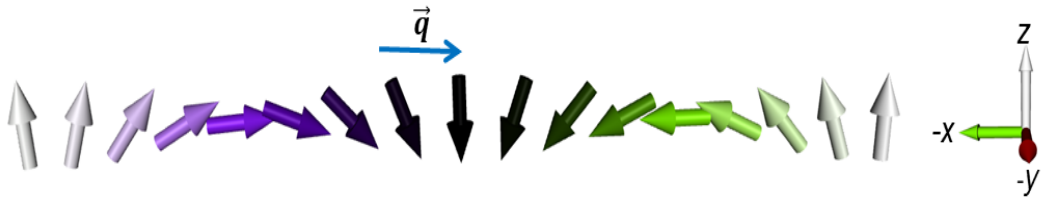

Figure 1.4: A schematic spin configuration of cycloid with wave vector ($\vec{q}$) along $+x$ direction.

1.4.3 Conical Spin texture

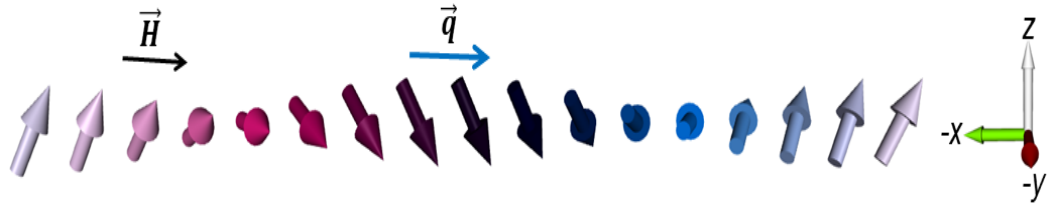

Figure 1.5: A schematic of conical spin configuration propagating along the $+x$ direction where the spins tilt with some angle along the magnetic field direction ($\vec{H}$).

Unlike the helical and cycloid spin textures, in general the conical spin modulation does not represent a ground state spin configuration, rather it appears as an excited state with the application of magnetic fields. The conical spins configuration very much resembles to that of spin helix. However, the spins tilt with some angle along the propagation direction under the application of magnetic field as depicted in Fig. 1.5. The angle of tilting depend on the strength of the applied magnetic field. At sufficiently high magnetic fields all the spins align along the magnetic field direction resulting in a field polarized magnetic state. The conical magnetic state have been realized over certain field ranges in many magnetic systems, e.g. MnSi [2], FeGe [4], FeCoSi [3], Cu_2OSeO_3 [8], β-Mn type Co-Zn-Mn materials [29], etc.

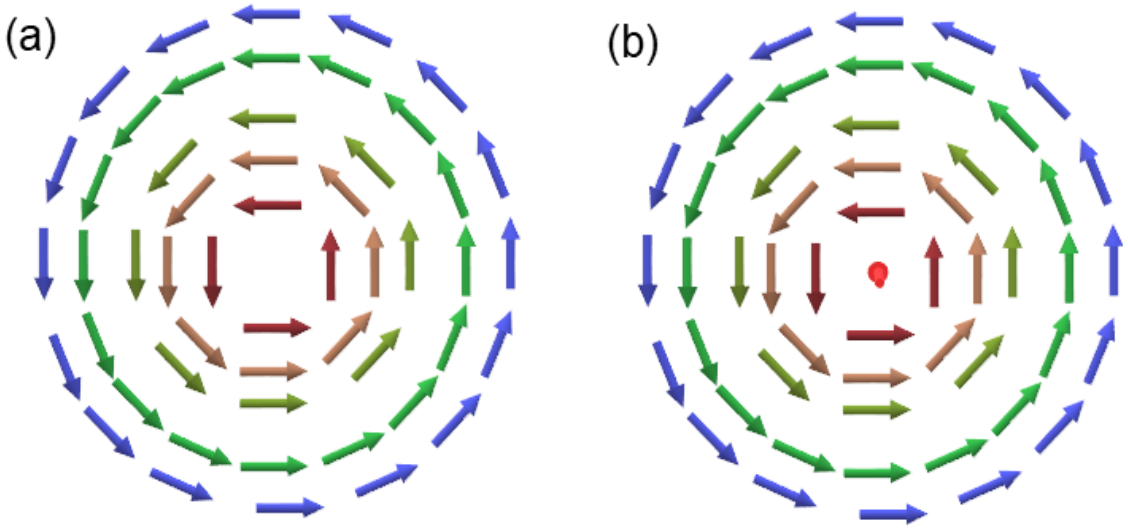

Figure 1.6: Schematic spin configuration of a magnetic vortex- (a) without core and (b) with core.

1.4.4 Magnetic Vortex

Vortex is a phenomenon having a strong existence in nature. Some of the familiar examples are the structure of a whirlpool (rotating water), winds flow configuration in cyclone storms, the shape of the stirred fluids, etc. In condensed matter, vortex exists in different forms, such as vortices in type-2 superconductor [58], magnetic vortex formation in permalloy [59], etc. In magnetism, vortex can be defined as a circular type spin configuration consisting of in-plane spin component as shown in Fig. 1.6. There exists two different types of magnetic vortices, namely, in-plane vortex and out-of-plane vortex depending upon the vortex core. In case of the in-plane vortex, spins rotates circularly within a plane and no out-of-plane magnetization component can be found at the center of the structure as depicted in Fig. 1.6(a). In case of the out-of-plane vortex, spins exhibit in-plane rotation along with out-of-plane alignment at the center, i.e. a vortex core exists at the center as shown in Fig. 1.6(b). In the vicinity of the vortex center, the angle between neighboring spins is large when the spins at the center remain within a plane. Therefore, in the case of out-of-plane vortex structure, the spins at the vortex core align parallel to the plane normal in order to minimize the exchange energy. In general, vortex is portrayed

by the chirality of the in-plane spins (clockwise or counter-clockwise rotation) and the polarization of the out-of-plane spin at center (up or down).

1.4.5 Magnetic Bubbles

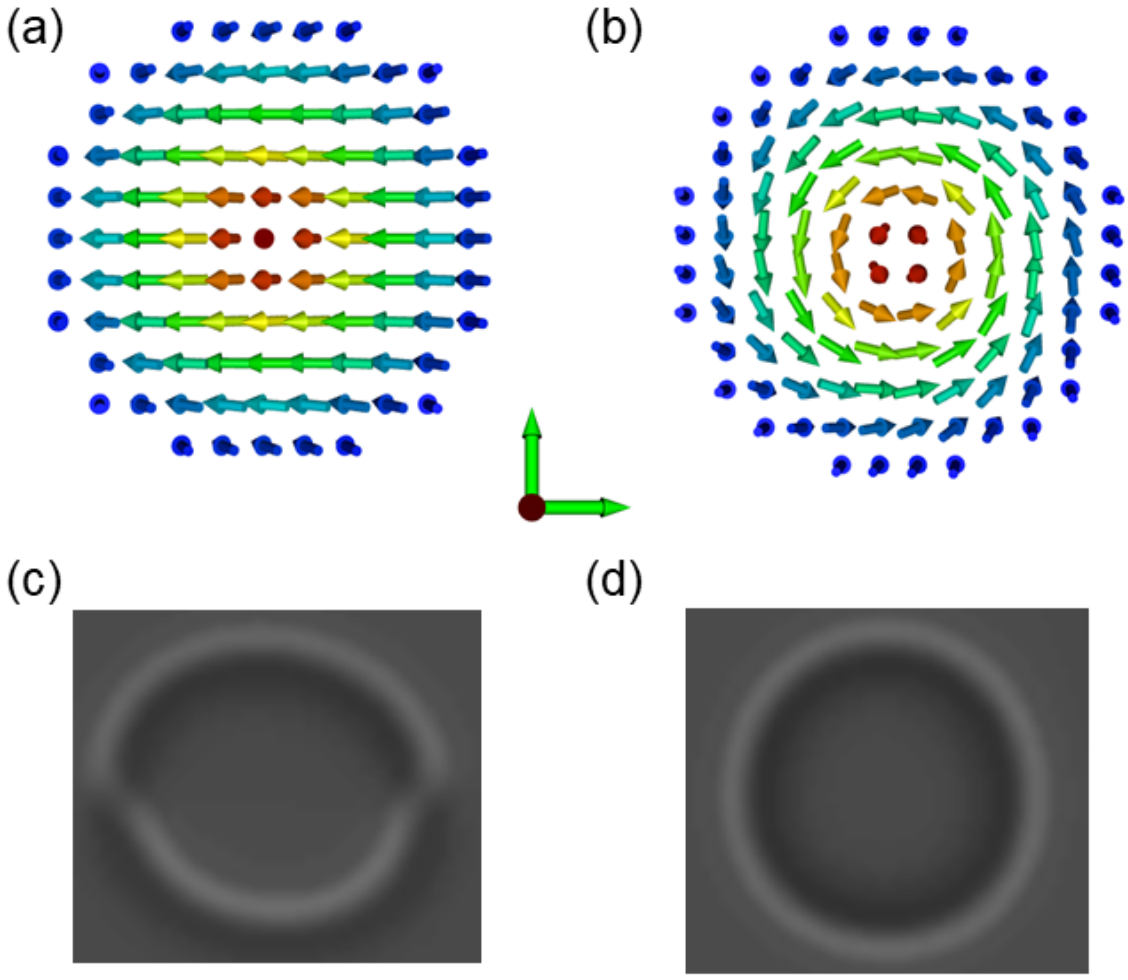

Figure 1.7: Spin textures of a trivial bubble (a), non-trivial bubble (b) and the corresponding simulated LTEM images (c) and (d)

Magnetic bubble is a vortex-type circular spin texture with slightly different core spin arrangement compared to that of a conventional vortex spin texture. In case of magnetic bubbles, the rotation of spins in the core region consists of both in-plane and out-of-plane components. This bubble type of spin texture is generally observed in thin film samples with high out-of-plane magnetic anisotropy. The competition between the dipolar interaction, which prefers in-plane spin alignment,

and the uniaxial magnetocrystalline anisotropy, that helps the spins to align in out of plane direction, is the primary mechanism behind the emergence of magnetic bubbles. Depending on the topology of the spin textures, the bubbles are categorized into two types- the trivial bubbles with zero topological charge and the non-trivial bubbles having topological charge one. Schematics of the magnetic bubbles (trivial and non-trivial both) along with their simulated Lorentz TEM images are shown in Fig. 1.7. In case of the trivial magnetic bubble, the inner spins do not form a fully circular configuration, instead two cuts line (Bloch lines) appears on the circle as shown in Fig. 1.7 (a). In case of non-trivial bubbles as depicted in Fig. 1.7 (b), complete ring type of spin configuration around the center point is found. Hence, the topological charge of the trivial bubble is zero, whereas, non-trivial magnetic bubble shows a topological charge of one.

1.5 Introduction to Skyrmion and Antiskyrmion

Magnetic skyrmions are topologically protected solitons, first proposed by T. H. R. Skyrme as a model for nucleons [60]. In condensed matter, the existence of skyrmions was theoretically proposed by A. N. Bogdanov *et al.* in 1989 [22]. It was proposed that like the vortex structure in type-2 superconductor, skyrmions can exist in magnetically order systems that exhibit certain class of crystallographic symmetry, such as, C_{nv}, C_n, D_n, D_{2d}, S_4 where n = 3,4,5. Experimentally, skyrmions were first discovered in 2009 by S. Muhlbauer *et al.* using small angle neutron scattering study in MnSi [2]. Subsequently, real space visualization of skyrmions in FeCoSi thin plate was carried out one year later in 2010, with the help of the Lorentz transmission electron microscopy (LTEM) technique by X. Z. Yu *et al.* [3].

In magnetism, skyrmions are soliton like nano-sized circular spin configurations protected by their topology. This means the topology of skyrmions cannot be deformed continuously into other topological spin configurations without altering the topological index. Here, the term 'soliton like' is used in the sense that the shape

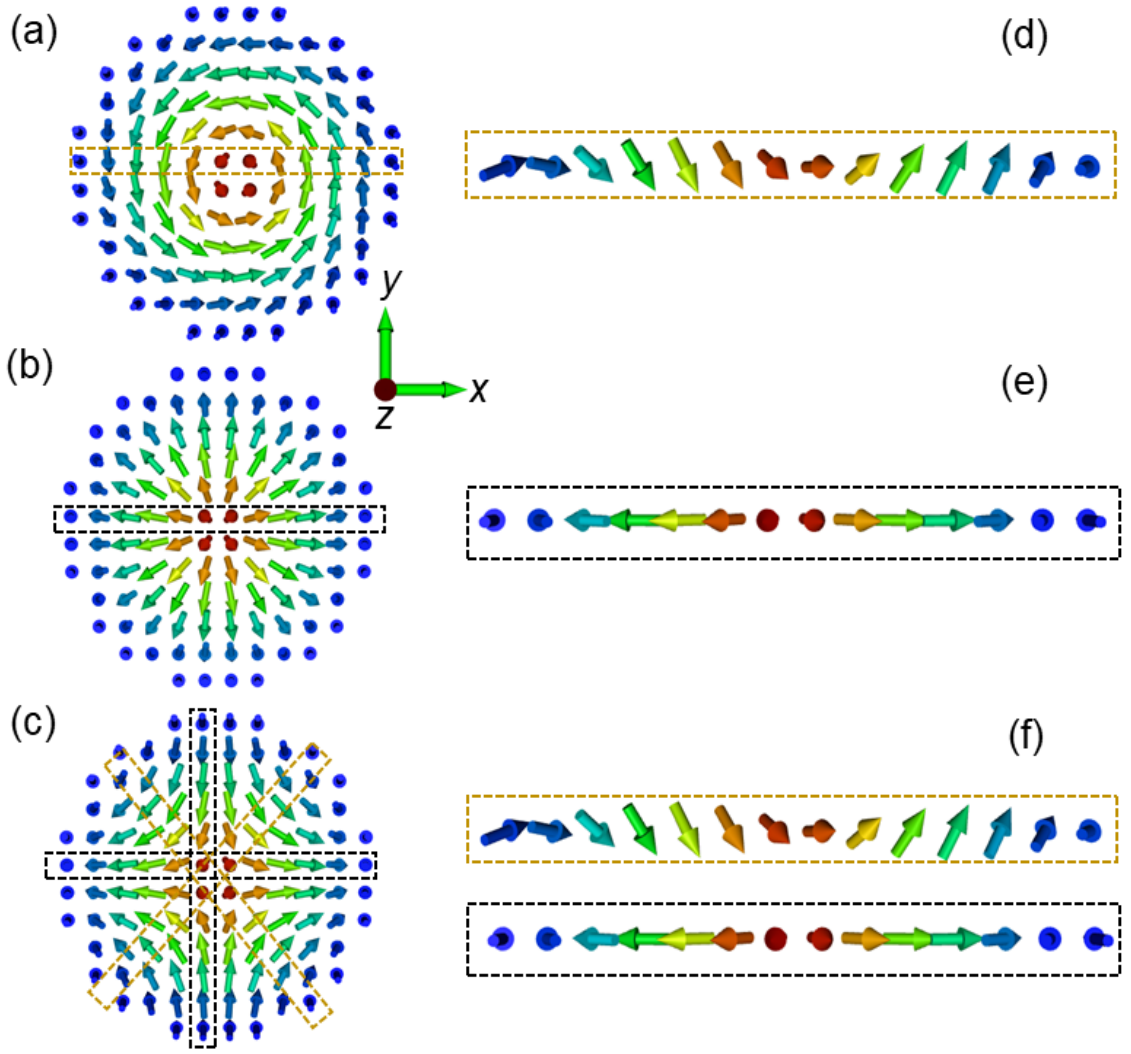

Figure 1.8: Spin texture for a Bloch skyrmion (a), Neel skyrmion (b) and antiskyrmion (c). The spin arrangement along the diameter for the respective spin textures are shown in (d)-(f).

and velocity cannot be modified during its motion through a nonlinear dispersive medium. Let us consider a typical two-dimensional picture of skyrmion given in Fig. 1.8. The spins are arranged in such a manner that the spin orientation changes from up to down as one move from the center to the periphery through a helical type of spin rotation in between. On the basis of spin modulation in the inner region, there exists mainly three class of skyrmions- (a) Bloch skyrmion, (b) Neel skyrmion, (c) Antiskyrmion. In Bloch and Neel skyrmions, the spin arrangement along the radial direction follow the helical and cycloid spin modulation, respectively, as seen in Fig.

1.8(a) and (b). In case of antiskyrmion, both helical and cycloid spin modulation can be seen together as shown in Fig. 1.8(c).

Now, it is important to understand the skyrmion from the topological point of view. From the earlier discussion of topology, it is clear that the topological properties of an object is firmly determined by its topological number or topological charge, as quantified mathematically in Eq. (1). The Eq. (1) can be rewritten as,

$$Q[N_{sk}] = \frac{1}{4\pi}\int_a n_{sk}\, dxdy = \frac{1}{4\pi}\int_a \boldsymbol{m}.(\frac{\partial \boldsymbol{m}}{\partial x} \times \frac{\partial \boldsymbol{m}}{\partial y})\, dxdy \tag{1.8}$$

where, $n_{sk} = \boldsymbol{m}.(\frac{\partial \boldsymbol{m}}{\partial x} \times \frac{\partial \boldsymbol{m}}{\partial y})$ is the skyrmion number density, $\boldsymbol{m}$ is the unit vector of the magnetization. For 2D spin textures, the circular disk is taken as the integration area and the corresponding coordinate in polar (r, ϕ) or Cartesian coordinate (x, y) systems. In three dimension, the integration can be done over the surface of a sphere, with the polar coordinate (r, θ, ϕ) and the Cartesian coordinate (x, y, z). Now consider a two dimensional picture of skyrmion. For the axis-symmetric spin texture skyrmion with radius R, the magnetization in spherical coordinate can be expressed as $\boldsymbol{m}$ (r)= m ($\sin\Theta$ (r) $\cos\Phi$ (r), $\sin\Theta(r)\sin\Phi(r)$, $\cos\Theta(r)$). As it is a 2D spin texture, the position vector can be expressed as $\boldsymbol{r}$=r ($\cos\phi$,$\sin\phi$). By replacing m (r) in Eq. (2), we get,

$$Q[N_{sk}] = -\frac{1}{4\pi}[\cos\Theta(r)]_{r=0}^{r=R}[\Phi(\phi)]_{\phi=0}^{\phi=2\pi} \tag{1.9}$$

Let's define the polarity $p = \cos\Theta(r)]_{r=0}^{r=R}$. Here, $\Theta(r=0) = \pi$ or 0, according to the orientation of the spin magnetic moment, i.e antiparallel or parallel to the direction of magnetic field (H). Now consider the skyrmion structure at core (r=0) where spin moment is anti-parallel to H giving $\Theta(r=0) = \pi$. Similarly, due to parallel arrangement of the spin moments to the magnetic field, $\Theta(r=R) = \pi$ at the periphery (r=R). In case of skyrmions $p = 1$. Now from Eq. (1.9) we get,

$$Q[N_{sk}] = p\omega = -\omega \tag{1.10}$$

where, $\omega = \frac{1}{2\pi}[\Phi(\phi)]_{\phi=0}^{\phi=2\pi}$ is called as the vorticity of the spin configuration. Therefore, the vorticity can be defined as the number of azimuthal rotation of m (r) around a closed loop of the center point. It can be mentioned here that the rotational nature of inner spin region is generally quantified by two parameters- helicity and vorticity. When the azimuthal angle Φ of the spin moment alters continuously with the azimuthal direction of the the position vector $\boldsymbol{r}$, then the helicity (γ) is related with vorticity (ω) as

$$\Phi = \omega\phi + \gamma \tag{1.11}$$

Hence, different kind of topological spin textures are represented by (Q, ω, γ), for instance, (+1, +1, -π/2) represents the Bloch skyrmion, whereas (+1, +1, 0) represents the Neel skyrmion.

1.5.1 Role of DM interaction in the stabilization of different kind of skyrmions

As discussed earlier, any non-coplanar spin texture can be stabilized by two or more competitive interactions. In case of skyrmion formation in non-centrosymmetric materials, the competition between the DM interaction and the Heisenberg exchange plays the vital role. In most of the cases, the competing Heisenberg and DM interactions stabilizes a helical/cycloid spin modulations as the ground state. Application of magnetic field perpendicular to spin-spiral propagation direction stabilizes the skyrmionic spin texture by breaking the helical/cycloid spin modulation. Therefore, the DM interaction plays a crucial role in the stabilization of skyrmions in non-centrosymmetric material. Depending on the nature of the DM interaction which is dictated by the crystal symmetry of the system, different kind of skyrmions, such as Bloch skyrmion, Neel skyrmion, and antiskyrmion can be stabilized. In the following, stabilization mechanisms for different types of skyrmion are discussed.

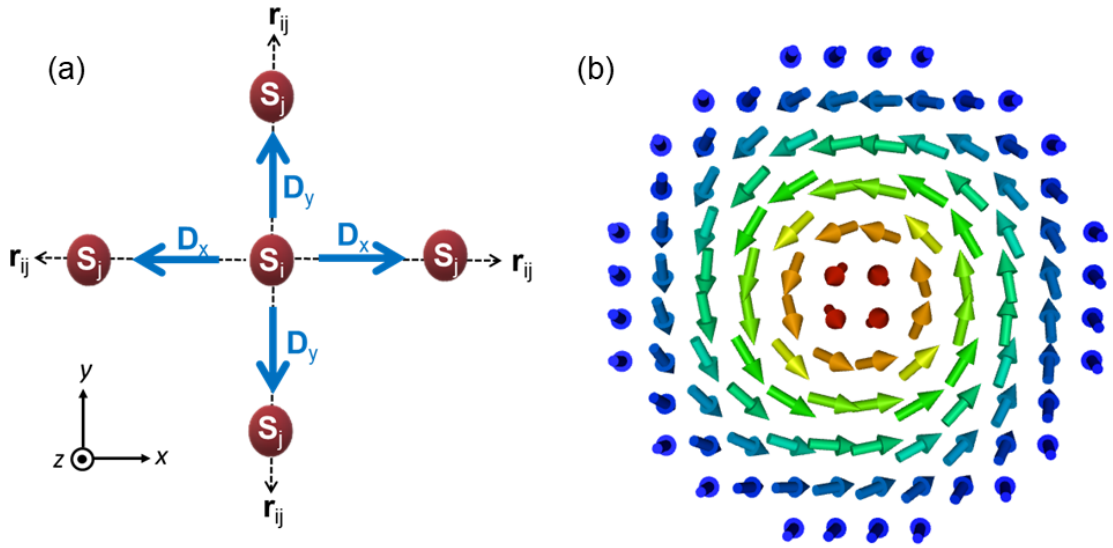

Figure 1.9: (a) A schematic representation of the direction of DM vectors acting between two neighboring spins that support Bloch skyrmions, (b) The spin configuration of a Bloch skyrmion.

1.5.1.1 Stabilization of Bloch skyrmion by DM interaction

The DM interaction energy between two spins $\vec{S_i}$ and $\vec{S_j}$ at i-th and j-th neighboring sites is given by $E_{DMI} = -\vec{D_{ij}}.(\vec{S_i} \times \vec{S_j})$, where $\vec{D_{ij}}$ is the DM vector. The energy of DM interaction is minimum when $\vec{D_{ij}}$ is parallel to $(\vec{S_i} \times \vec{S_j})$. In case of Bloch skyrmions, $(\vec{S_i} \times \vec{S_j}) \parallel \vec{r_{ij}}$ ($\text{-}\vec{r_{ij}}$), where $\vec{r_{ij}}$ is the distance vector between two neighboring spins, $\vec{S_i}$ and $\vec{S_j}$. Therefore, to stabilize the Bloch skyrmions, the direction of DM vector ($\vec{D_{ij}}$) must be parallel to the $\vec{r_{ij}}$. A schematic diagram showing direction of DM vectors and the corresponding spin configuration for Bloch skyrmion is depicted in Fig. 1.9. Here, $\vec{D_x}$ ($\vec{D_y}$) is the DM vector between the central spin, $\vec{S_i}$, and the neighboring spin, $\vec{S_j}$, located at x-direction (y-direction). When the DM vectors in all possible direction are parallel/antiparallel with the respective distance vectors ($\vec{r_{ij}}$) with $|\vec{D_x}| = |\vec{D_y}|$ (isotropic DM vectors), as shown schematically in Fig. 1.9(a), the Bloch skyrmion can be stabilized with homogeneous chirality as depicted in Fig. 1.9(b).

This type of DM vector configuration is generally found in B20 type compounds [2, 3, 4, 5, 7, 8, 61] and the corresponding DM interaction energy for B20 compounds

in the continuum limit can be written as

$$E_{DMI}^{B20} = -\int D[M_y\frac{\partial M_x}{\partial z} - M_x\frac{\partial M_y}{\partial z} + M_x\frac{\partial M_z}{\partial y} - M_z\frac{\partial M_x}{\partial y} + M_z\frac{\partial M_y}{\partial x} - M_z\frac{\partial M_y}{\partial x}]\, dV \tag{1.12}$$

The above discussed DM interaction supports the spin configuration with vorticity $(\omega) = 1$ and helicity $(\gamma) = \pi/2$ i.e., Bloch skyrmion.

1.5.1.2 Stabilization of Neel Skyrmions by DM interaction

In case of Neel skyrmions, $(\vec{S_i} \times \vec{S_j})$ is perpendicular to the distance vector, $\vec{r_{ij}}$. Therefore, the DM interaction energy is minimum when the DM vectors, $\vec{D_{ij}}$, between two neighboring spins, $\vec{S_i}$ and $\vec{S_j}$, is perpendicular to $\vec{r_{ij}}$. A schematic diagram of the direction of DM vectors between the neighboring spins and the corresponding Neel skyrmion are presented in Fig. 1.10(a) and (b), respectively. It is noticeable that $\vec{D_x}$ as well as $\vec{D_y}$ are placed $+\pi/2$ angle anticlockwise with the distance vector $\vec{r_{ij}}$ in all directions ($+x$, $+y$, $-x$, $-y$-directions) with $|\vec{D_x}| = |\vec{D_y}|$. This type of isotropic DM interaction stabilizes Neel skyrmion with homogeneous chirality, as shown in Fig. 1.10(b). The DM interaction with same configuration is observed in

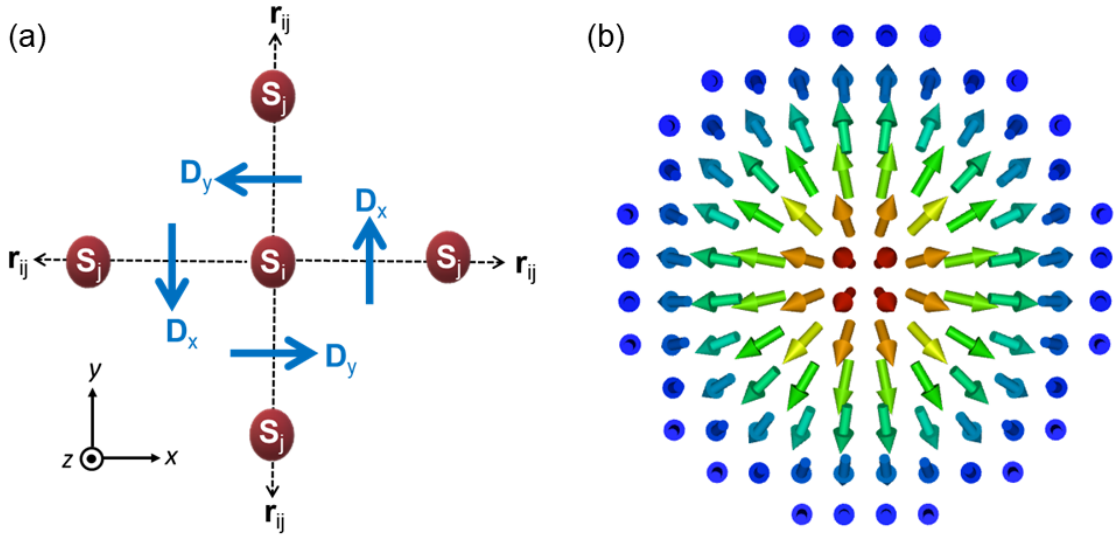

Figure 1.10: (a) A schematic representation of the direction of DM vectors acting between two neighboring spins that support Neel skyrmion, (b) The spin configuration of a Neel skyrmion.

the materials with C_{nv} point symmetry [9, 10, 11, 12]. The DM interaction energy in continuum limit for C_{nv} compounds can be expressed as

$$E_{DMI}^{C_{nv}} = -\int D[M_x\frac{\partial M_z}{\partial x} - M_z\frac{\partial M_x}{\partial x} + M_y\frac{\partial M_z}{\partial y} - M_z\frac{\partial M_y}{\partial y}]\, dV \tag{1.13}$$

The DM energy related to C_{nv} class of symmetry favors the spin configuration with ω =1 and $\gamma = 0$ i.e., Neel type of skyrmion.

1.5.1.3 Stabilization of Antiskyrmions by DM interaction

The pictorial representation of an antiskyrmion and the corresponding schematic of DM vector configurations are illustrated in Fig. 1.11. Here, $\vec{D_x}$ makes $\pi/2$ angle anticlockwise with the $\vec{r_{ij}}$ in x-direction, whereas, in contrast to the Neel skyrmion, $\vec{D_y}$ subtends $\pi/2$ angle clockwise with respect to the $\vec{r_{ij}}$ in y-direction with $|\vec{D_x}| = |\vec{D_y}|$. This inhomogeneous type DM vectors give opposite spin chirality in y-direction with respect to that in the x-direction, as depicted in Fig. 1.11(b). This kind of

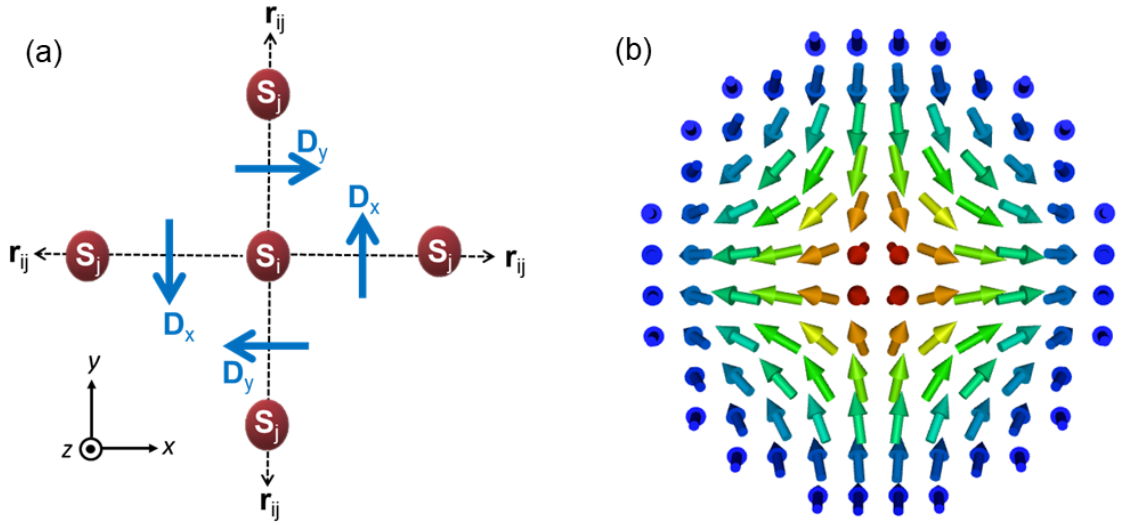

Figure 1.11: (a) A schematic representation of the direction of DM vectors acting between two neighboring spins that support antiskyrmion, (b) The spin configuration of an antiskyrmion.

inhomogeneous DM vectors configuration are generally observed in D_{2d} symmetric materials [14, 62] and the corresponding DM interaction energy for D_{2d} compounds

can be written as

$$E_{DMI}^{D_{2d}} = -\int D[M_x\frac{\partial M_z}{\partial y} - M_z\frac{\partial M_x}{\partial y} + M_y\frac{\partial M_z}{\partial x} - M_z\frac{\partial M_y}{\partial x}]\ dV \tag{1.14}$$

This category of DM interaction supports the spin texture with ω =-1 and $\gamma = \pm$ $\pi/2$ and 0, π i.e., antiskyrmion spin configuration.

1.6 A review on skyrmion/antiskyrmion hosting materials

1.6.1 Skyrmion in non-centrosymetric magnetic material

1.6.1.1 B20 and other non-centrosymetric skyrmion hosting magnetic materials

After the theoretical predication in different classes of magnetic materials by A. N. Bogdanov *et al.* [22], skyrmion was experimentally uncovered in a cubic non-centrosymmetric B20 type material- MnSi by S. Muhlbauer *et al.* in 2009 [2]. The skyrmion phase was found near the magnetic ordering temperature (T_C) of MnSi along with the well-known helimagnetic ground state (wave vector $\vec{Q} \perp$ to H) and field-induced conical state ($\vec{Q} \parallel \vec{H}$) using reciprocal space mapping technique- small angle neutron scattering (SANS) [2]. In a narrow magnetic field and temperature region near the T_C, six magnetic Bragg spots were observed in the SANS experiment. This arrangement of Bragg spots confirms the presence of skyrmion in the form of hexagonal skyrmion lattice (SkL). The hexagonal skyrmion lattice can also be understood as a superposition of three single-Q helices propagating along their respective wave vectors ($\vec{Q_1}$, $\vec{Q_2}$, and $\vec{Q_3}$) with an angle 120° apart from each other in a plane perpendicular to external magnetic field. Therefore, SkL forms 3Q type of spin modulation state, which is quite different from the single-Q conical or helical spin modulation states. later in 2010, the real-space visualization of the skyrmion spin

configuration was done in another B20 family compound- FeCoSi through Lorentz transmission electron microscopy (LTEM) technique [3]. In this report, the nature of skyrmion was found to be Bloch type. Afterwards, the Bloch skyrmions have also been observed in many other bulk B20 structured materials, such as FeGe [4], $Mn_{1-x}Fe_xGe$ [5], MnGe [61], $MnSi_{1-x}Ge_x$ (x = 0.0-1.0) [7] including multiferoic Cu_2OSeO_3 [8]. In the case of the B20 compounds, the SkLs acquire a narrow pocket region of H-T phase space close to the T_C. Most importantly, among all the B20 materials skyrmion lattice in FeGe exists up to the ambient temperature [4]. In these materials, the competition between the exchange and the DM interactions is the main reason for giving rise to their helical spin texture as the ground state. By applying small magnetic fields, the helical spin state transforms to the conical one with $\vec{Q} \parallel \vec{H}$. Further increase in the magnetic fields, the conical state transforms into a field-polarized state far from the T_C. But in a narrow region around the T_C, the skyrmion lattice can be nucleated from the helical ground state via conical state with the application of magnetic fields. It has been proposed that apart from the DM interaction and exchange interaction, thermal and magnetic field fluctuations also play a vital role in stabilizing the SkL. As a result, the SkL in the B20 materials can be found near the magnetic ordering temperature at a certain span of magnetic fields. Here, the rotational handness (either left-handed or right-handed) of helical spin is governed by the sign of DM vectors present in that particular system, while the direction of helical spin propagation is dictated by the magnetic anisotropy of the material. It is known that the helical modulation pitch λ is proportional to the ratio of the exchange constant (J) to the DM vector strength (D), i.e., $\lambda \approx J/D$. The helical pitch in the case of B20 materials can be obtained by evaluating the J for the T_C and the magnitude of DM vector ($\vec{D}$) from the critical magnetic field relation $H_c = D^2 M_c/J$. Here, M_c is the magnetization corresponding to the critical magnetic field. Apart from the 2D SkL (two-dimensional SkL means the wave vectors of the corresponding all three helices lies in a plane), 3D hedgehog lattices have also been observed in few B20 type magnetic materials, such as MnGe [41] and $Mn_{1-x}Fe_xGe$ [5]. Like the conventional SkL, the hedgehog lattice is also composed

of three helices, which lie separately in the three different planes instead of a single plane. It is important to mention here that the transformation of 3Q-hedgehog lattice to 3Q-skyrmion lattice via 4Q-modulated spin states has been recently observed by replacing Si with Ge in $MnSi_{1-x}Ge_x$ [7].

Beside these B20 cubic materials, skyrmions have also been observed in other noncentrosymmetric materials like β-Mn cubic structured- Co-Zn-Mn [6] and polar magnetic materials - rhombohedral structured GaV_4S_8 [9], GaV_4Se_8 [10], tetragonal $VOSe_2O_5$ [11], and hexagonal Mn-Pt-Ga [12]. For a large compositional range of Co-Zn-Mn alloys, mostly Bloch skyrmions in the form of triangular lattice is found in a small pocket of *H-T* phase diagrams near the magnetic ordering temperature, including room temperature. In these alloys, the existence of skyrmions in the form of square lattice instead of triangular SkL have also been found far from the magnetic ordering temperature after imposing a special kind of the field cooling (FC) process [63]. Most importantly, the size of the skyrmions in these Co-Zn-Mn alloys can be easily tuned from 115 nm to 187 nm by slightly changing the Co-Zn-Mn stoichiometric [6]. In general, Bloch-type skyrmion spin configurations are mostly formed in these bulk magnets due to their crystal symmetry (point group symmetry). Neel type of skyrmion lattice have been observed in case of polar magnetic materials- GaV_4S_8 [9], GaV_4Se_8 [10], $VOSe_2O_5$ [11], and Mn-Pt-Ga [12] as the DM interaction dictated by the crystal symmetry [C_{nv}] of these systems supports the Neel type skyrmion.

1.6.1.2 Heusler non-centrosymmetry tetragonal magnetic materials

In the early days of skyrmion research as discussed above, mostly Bloch skyrmions [2, 3, 4, 5, 6, 8, 41] and Neel skyrmions lattices [9, 10, 11, 12] have been reported in a tiny pocket of *H-T* phase diagram near the magnetic ordering temperature, T_C, depending on the crystal symmetry of these magnets. It has been proposed theoretically that different kind of topological spin configurations other than the Bloch- and Neel skyrmions can be stabilized is certain materials with particular crystal symmetries [22]. In this context, recently, a new kind of topological object with a

topological charge opposite to skyrmion, named antiskyrmion, has been discovered experimentally in inverse Heusler tetragonal system Mn-Pt-Pd-Sn with D_{2d} point group symmetry [14]. It can be mentioned here that inverse Heusler compound $Mn_{1.4}Pt_{0.9}Pd_{0.1}Sn$ crystallizes in a non-centrosymmetric tetragonal structure with space group I-42m. It has been shown in the LTEM studies that $Mn_{1.4}Pt_{0.9}Pd_{0.1}Sn$ exhibits ground state helical pattern with modulation period $\lambda = 135$ nm propagating in the tetragonal basal plane [14]. By applying magnetic field of about 0.1 T along the (001) direction, these helical stripes transform to two bright and two dark spots in the (010) and (100) directions, respectively. This confirms the emergence of antiskyrmion lattice from the helical magnetic state in the system [14]. Further application of sufficient magnetic field, these bright and dark spots disappear, and no magnetic contrast is found when the system reaches the ferromagnetic state. In this material, the hexagonal magnetic antiskyrmion lattice have been found in a broader temperature range from $T = 100$ K to $T = 390$ K. With increasing temperature, the stability of the antiskyrmion pockets becomes narrower and finally disappears around 400 K in the H-T phase diagrams. Most importantly, the antiskyrmions acquire ample space in the H-T phase diagrams instead of a small pocket in the case of B20 materials. It was found that the size of antiskyrmion is nearly the same at different temperatures. Interestingly, the antiskyrmion state appears at a zero magnetic field upon field-cooling the sample. The increase of anti-site disorder in $Mn_{1.4}Pt_{0.9}Pd_{0.1}Sn$ by replacing the Pd site with Pt atoms can give the metastable antiskyrmions upon the field-cooling process at a zero magnetic field. The controlled tunability of Heusler alloys, the discovery of the new topological spin texture, stability of the spin texture at a large temperature range, make the inverse Heusler tetragonal family more attractive towards skyrmion research.

Even though the materials with D_{2d} symmetry favor the antiskyrmions, the coexistence of skyrmions and antiskyrmions has also been realized recently in this system [15, 16]. By introducing in-plane magnetic fields to the sample (in-plane magnetic field applied by just tilting the sample) along with the out-of-plane field, the antiskyrmions can be converted into skyrmions via topological trivial magnetic

bubble states. The reason behind this conversion of topological phase transformation with the help of in-plane magnetic fields could be the following. These topological spin textures show almost identical degenerate energy states. The in-plane magnetic field helps the antiskyrmions (or skyrmion) to cross the little energy barrier between them. It has also been observed that the helicity of skyrmions (antiskyrmions) can also be modified from clockwise (CW) to counter-clockwise spins rotation (CCW) depending upon the in-plane magnetic field direction. Like the Mn-Pt-Pd-Sn compound, the antiskyrmions are very recently realized in another Heusler inverse tetragonal compound Mn-Rh-Ir-Sn with the same D_{2d} class of symmetry [62].

.

1.7 Emergent phenomenon related to the skyrmions

1.7.1 Topological Hall Effect

When a normal conductor is placed in a magnetic field perpendicular to the direction of current flow, a transverse electric field is generated perpendicular to both the current and magnetic field due to the Lorentz force acting on the charge carriers, known as Hall effect after its discovery by E.H. Hall in 1879 [64]. Two types of forces act on the charge carriers – one is Lorentz force and the second one is the electrostatic force. In equilibrium condition these two forces balance each other. Therefore, the traverse electric field (E_H) can be written as,

$$E_H = Rj_xB_Z \tag{1.15}$$

where R is the normal Hall coefficient, j_x represents the current density in x-direction, and B_z is the magnetic field along the z-direction. This magnetic field dependent Hall effect in conductor is known as normal Hall effect. After one year

from the discovery of normal Hall effect, E. H. Hall showed that ferromagnetic conductors exhibit many times larger Hall voltage in comparison to that of normal Hall effect, known as anomalous Hall effect (AHE). It was found that this anomalous Hall voltage in ferromagnetic materials does not linearly vary with the magnetic field. In 1932, Pugh and Lippert [64] proposed that the anomalous Hall effect scales with the magnetization of the sample and suggest an empirical relation between the Hall resistivity and magnetization [64]

$$\rho_{yx} = R_0\mu_0 H + R_s M \tag{1.16}$$

where R_s is the anomalous Hall coefficient. For many years it was considered that AHE is an extrinsic contribution arising from the scattering of the electrons from the magnetic moments. In 1954, Karplus and Luttinger (KL) presented the scattering independent theory of anomalous Hall conductivity that depends only on the band structure of the particular material [64]. Smit and Burger separately proposed the extrinsic mechanisms to AHE - skew (asymmetric) scattering and side jump mechanism [64]. In case of skew scattering (asymmetric mechanism), there is a change in the trajectory of the scattered electrons from the impurity ions due to the spin-orbit interaction, whereas, there is a sudden shift in the wave packet of the electrons after scattering from spin-orbit coupled impurities in case of side jump. Afterwards, the discovery of quantum Hall effect in 1980s brings a new horizon to the condensed matter research due to the topological nature of the electron wave function [64]. This discovery brings about the concept of Berry phase for the explanation of intrinsic mechanism of AHE.

In addition to the normal and anomalous Hall effect, topologically non trivial spin structures with specially varying non-coplanar order parameters (i.e. spins) generates an additional component in the Hall effect, known as topological Hall effect (THE). The exact origin of the THE can be inferred to the appearance of a fictitious magnetic field caused by the real space Berry curvature. This Berry curvature is proportional to the scalar spin chirality (SSC) $\chi = \sum S_i.(S_k \times S_j)$, defined as the

scalar product of three spins that corresponds to the solid angle subtended on a unit sphere. In other words, when electrons pass through the non-coplanar spin textures with finite SSC, they gain a quantum-mechanical Berry phase, which acts as a fictitious magnetic field similar to the classical Aharonov–Bohm effect. The corresponding emergent fictitious magnetic field in continuum limit can be written as

$$B_i = \frac{h}{2e}\frac{1}{2\pi}\psi_i = \frac{h}{2e}\frac{1}{2\pi}n(r).\partial_i n(r) \times \partial_j n(r) \tag{1.17}$$

Here ψ_i represents the Berry curvature = $n(r).\partial_i n(r) \times \partial_j n(r)$ where $n(r)$ is the unit vector of the local magnetization. The total emergent magnetic flux generated in the surface S enclosing the topological spin textures,

$$\phi_i = \int_s B_i \; dS = \frac{h}{2e}\frac{1}{2\pi}\int_s \psi_i \; dS = \frac{h}{2e}\frac{1}{\pi}\Psi_i \tag{1.18}$$

where $\Psi_i = \frac{1}{2}\int_s \psi_i \; dS$ is the Berry phase that corresponds to half of the solid angle formed by the spins, $\Omega/2$. This value is simply determined by the total SSC- $\sum S_i.(S_k \times S_j)$, where S_i, S_j, and S_k are three neighboring spins or the integral of $n(r).\partial_i n(r) \times \partial_j n(r)$ around the closed loop in continuum limit. Therefore, the total emergent magnetic flux can be written as

$$\phi_i = \int_s B_i \; dS = \frac{h}{2e}\frac{1}{2\pi}\Omega \tag{1.19}$$

In case of skyrmion (antiskyrmion), the solid angle formed by the constituent spins is Ω, = -4π (4π). Therefore, the total magnetic flux generated from one single skyrmion (antiskyrmion) is,

$$\phi_i = \int_s B_i \; dS = -(+)\frac{h}{e} = -(+)\phi_0 \tag{1.20}$$

where, ϕ_0 is the flux quanta. Hence, each skyrmion (antiskyrmion) can generate a quanta of magnetic flux, - (+) ϕ_0. The emergent magnetic field corresponding to a single skyrmion (antiskyrmion) can be expressed as $B_i \approx -(+)\phi_0/a_{sk}^2$, where a_{sk}

represents the size of the skyrmion (antiskyrmion). It can be easily seen that the strength of the emergent magnetic field inversely varies with the square of skyrmion (antiskyrmion) size.

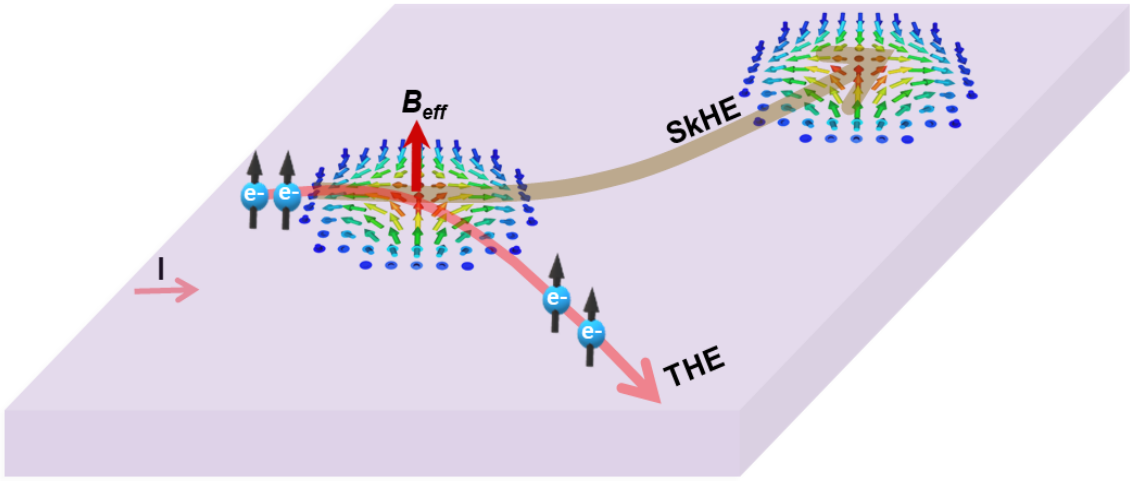

Figure 1.12: A schematic diagram related to Topological Hall effect (THE) and Skyrmion Hall effect (SkHE) when electron (current) passes through skyrmion.

This emergent magnetic field pushes the conduction electrons from their straight line path due to the Lorentz force, giving rise to the observed THE. A schematic diagram of THE arising from the skyrmion is presented in Fig. 1.12. As it can be seen, the path of the conduction electrons bends (shown by orange curve line) from the current direction by the emergent magnetic field B_i that exerts a Lorentz force on the electrons. Hence, the total Hall resistivity in a magnetic system with THE can be written as ,

$$\rho_{yx} = \rho_{NH} + \rho_{AH} + \rho_{TH} = R_0\mu_0 H + R_s M + PR_0 B_i. \tag{1.21}$$

Here, the normal Hall resistivity, $\rho_{NH} = R_0\mu_0 H$, $\rho_{AH} = R_s M$ is the anomalous Hall resistivity and the topological Hall resistivity is given by $\rho^T = PR_0 B_i$, where P is the spin polarization of the electrons at the Fermi surface. Therefore, the topological Hall resistivity depends on three factors; the spin polarization of the conduction electrons (P), normal Hall coefficient (R_0) and the magnitude of the emergent magnetic fields (B_i). The THE arising from the skyrmions has been found

in many bulk B20 compounds MnSi [23], MnGe [24], $Fe_{1-x}Co_xSi$ [25], Gd_2PdSi_3 [13] and in many thin films of Ir/Co/Pt multilayer [65]. In these systems, depending on the size of the skyrmions, the value of topological Hall resistivity changes drastically. For example, in MnSi [24] where the skyrmion size is about 18 nm, the ρ^T is found to be around 4 nΩ-cm, whereas, Gd_2PdSi_3 [13] shows a large ρ^T of about 2.6 $\mu\Omega$-cm with skyrmion size of 2.5 nm. The THE signal in Hall measurements can be extensively used as a tool to detect skyrmion like non-coplanar spin texture in many magnetic system.

When a large density of conduction electrons pass through the skyrmion spin texture, they try to move along the current direction due to spin-transfer torque phenomenon. As a counterpart of THE, the skyrmions also move in an opposite direction to the deflection of conduction electrons. This traverse motion of skyrmions is known as skyrmion Hall effect (SkHE), which is schematically presented by thick dark yellow line in Fig. 1.12. Like the induced emergent magnetic field, B_i, the skyrmion can also produce an emergent electric field, E_i, when it moves under the current according to Maxwell's equation, $\frac{\partial B_i}{\partial t} = -\nabla \times E_i$ (Faraday's law). This emergent electric field can be written as $E_i = V_s \times B_i$ where V_s is the drift velocity of the skyrmions.

1.8 Heusler Materials

The journey of Heusler materials start with the discovery of most interesting compound Cu_2MnAl in 1903 by F. Heusler where all the constituent elements Cu, Mn, and Al are non-magnetic, but the compound orders ferromagnetically [66]. At present, there have been reports of more than thousands of Heusler compounds exhibiting diverse properties. The most important point about these materials is that several important properties of these materials can be achieved as per the wish. Heusler compounds can be written as XYZ or X_2YZ where X and Y are transition metals and Z is a main group element. Based on the stoichiometric ratio, they are divided into two categories of Heusler compounds - Half Heusler and Full Heusler

with stoichiometric ratio 1:1:1 and 2:1:1, respectively. The structural and some of the important physical properties of these compounds are discussed in the following.

1.8.0.1 Structure and properties

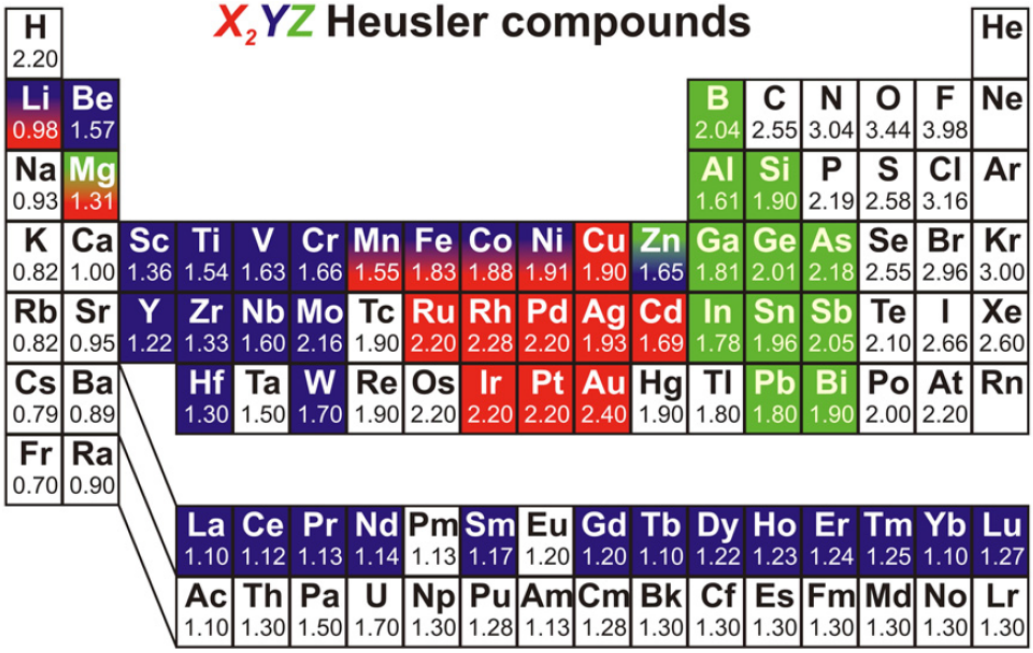

Figure 1.13: Periodic table of the elements showing the specific constituents of element that forms Heusler compounds indicated by different color shading [67].

The Half-Heusler compounds, typically represented with XYZ formula, consist of both covalent and ionic parts as X and Y atoms exhibit cationic behavior, whereas Z element gives the anionic counterpart. The most electropositive element X and Y, generally written at the starting of the formula, are the transition metals and/or rare-earth elements [as marked by red and blue color shadings in Fig. 1.13]. While Z, the most electro-negative element, is the main group elements [as indicated by the green color shading in Fig. 1.13]. The Half-Heusler compounds crystallize in non-centrosymmetric cubic structure with space group no. 216 (F-43m), where X, Y and Z atoms occupy the 4a (0, 0, 0), 4b (1/2, 1/2, 1/2), and 4c (1/4, 1/4, 1/4) position, respectively. The crystal structure of the half Heusler compounds can be described as a combination of ZnS type structure with Zn, and S atoms sitting at

4a (0, 0, 0), 4c (1/4, 1/4, 1/4) wycoff positions and the void octahedral site 4b (1/2, 1/2, 1/2) can be filled by another atom as in Fig. 1.14. As the bonding nature of ZnS is covalent type, the interaction between X and Z can be covalent one. On the other hand, the position 4a (0, 0, 0), 4b (1/2, 1/2, 1/2) occupied by X and Y form the NaCl-type structure where the interaction is ionic nature. It is important to mention here that X,Y and Z positions are not fixed at the above mentioned wycoff sites and often possible that X,Y, and Z can occupy any wycoff positions depending on the size of the atom and the type of inter-atomic interaction.

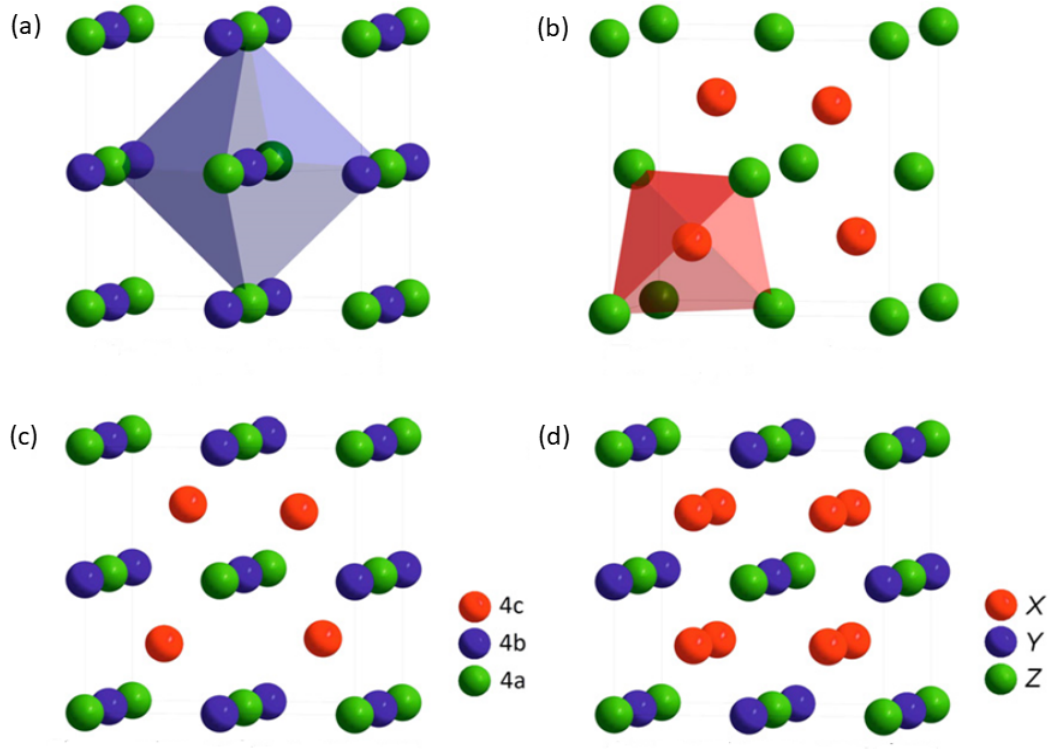

Figure 1.14: (a) Rock salt structure, (b) zinc blende structure and their relations to the (c) half-Heusler structure, and (d) full Heusler structure [67].

The Heusler compounds with stoichiometric ratio 2:1:1, represented by X_2YZ formula, are known as full-Heuslers. The X and Y atoms belong to the transition metals and Z is a main group element. The full Heusler alloys generally crystallize in centrosymmetric cubic structure with space group no. 225 (Fm-3m), in which the X atoms are located at 8c (1/4, 1/4, 1/4), whereas the Y and the Z atoms occupy the 4a (0, 0, 0) and 4b (1/2, 1/2, 1/2) positions, respectively. In full Heusler compounds the

most electro-positive element Y and the most electronegative element Z form rock-salt type (NaCl) structure due to their ionic character, hence, occupy the octahedral sites of the crystal structure. The four tetrahedral voids are occupied by the X atoms as shown in Fig. 1.14. The full Heusler structure can be understood easily as follows- the ZnS type of structure is formed by the X and Z atoms. The remaining tetrahedral positions and the octahedral voids are filled by the second X atom and Y atom, respectively, as given in Fig. 1.14.

Apart from the conventional Half-Heusler and full-Heusler structures, a special kind of full-Heusler structure known as inverse full Heusler can be found if the atomic number of Y is larger than that of X. As the electro-positivity of X is greater than that of Y [because of Z(Y)>Z(X)], the X atoms instead of Y form the NaCl type structure along with the Z atom. Therefore, the octrahedrally coordinated X and Z atoms show the ionic characteristics. The second X atom along with the Y atom occupy all the eight tetrahedral positions as illustrated in Fig 1.15. The inverse full Heusler compounds crystallize in noncentrosymmetric cubic structure with space group no. 216 (F-43m), in which the X atoms occupy two different Wyckoff positions-4a (0, 0, 0) and 4d (3/4, 3/4, 3/4), whereas, the Y and the Z atoms are placed on the Wyckoff positions 4b (1/2, 1/2, 1/2) and 4c (1/4, 1/4, 1/4), respectively. The inverse Heusler structure is generally seen in case of the Mn_2-based materials with Z(Y)>Z(X).

1.8.1 Some important aspects of full Heusler compounds

1.8.1.1 Tetragonally distorted Heusler compounds

The typically Heusler compounds crystallize in cubic form. Sometimes this conventional Heusler cubic structure can be distorted into another structure, for instance, the transformation from the cubic to a tetragonal structure. This type of distortion has been often observed in Mn_2YZ based inverse Heusler systems, where Mn atoms occupy the tetrahedral and octahedral positions lying in two different sub-lattices, namely Mn-Y and Mn-Z planes. It is found that the octahedrally coordinated Mn

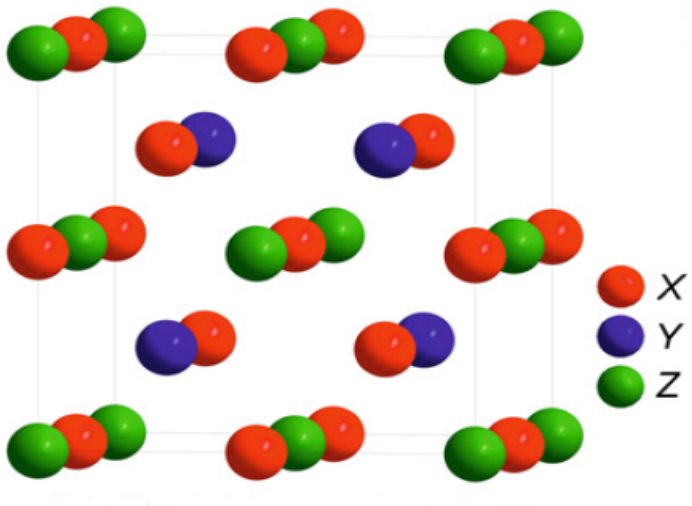

Figure 1.15: The inverse Heusler structure $CuHg_2Ti$ [67].

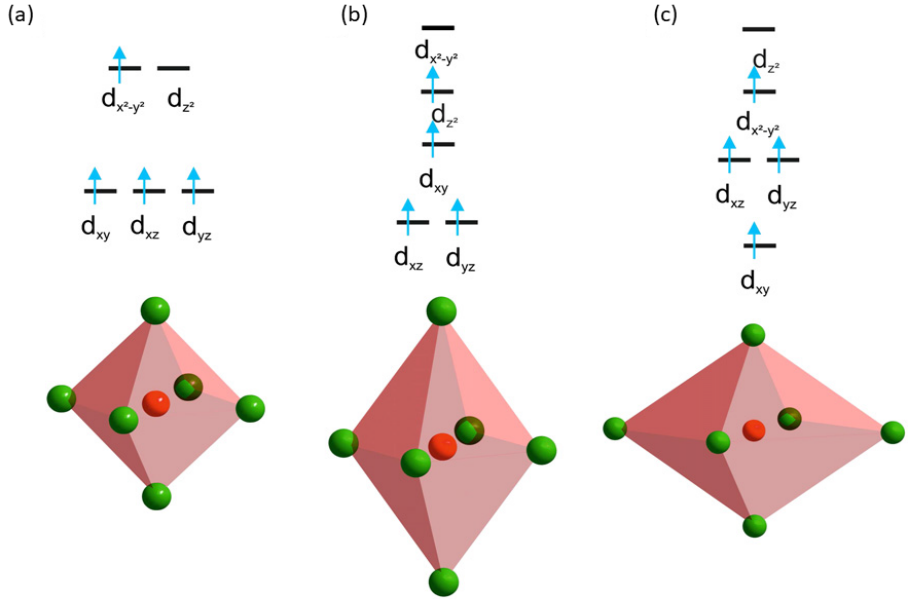

Figure 1.16: The d-orbital splitting due to crystal field for a d^4 ion in an octahedral coordination - (a) non distorted octahedron, (b) elongated octahedron, (c) compressed octahedron [67].

atoms exhibit two oxidation states, Mn^{3+} and Mn^{4+} [68]. The Mn atoms shown by red ball is surrounded octrahedrally by main group elements (green balls). The corresponding electronic state are shown in Fig. 1.16. In case of the non-distorted octahedral environment shown in Fig. 1.16 (a), the Mn d level splits into three degenerate sub-levels denoted by t_{2g} (d_{xy}, d_{xy}, d_{yz}), and two degenerate sub-level

e_g ($d_{x^2-y^2}$, d_z). As Mn^{3+} possesses four d-shell electrons, the electrons initially fill up the lower electronic state, t_{2g} level, and then occupy the upper electronic state, e_g, as shown in Fig. 1.16 (a). This configuration of electronic structure for the non-distorted octahedron is not a energetically stable one, as a consequence, it prefers to distort the octahedron by compressing or elongating it to minimize the overall energy of the system. The minimization of energy can be done by the following process- the energy required to distort the octahedron is balanced by lowering the electronic energy due to the splitting of t_{2g} and e_g level, thus, the mechanical energy is converted to the electronic energy and vice-versa. This type distortion is also known as Jahn-Teller distortion. An example of tetragonal distortion in Mn_2YZ is shown in Fig. 1.17, where the inverse cubic structure Mn_2NiGa is modified into inverse tetragonal structure by Jahn-Teller distortion.

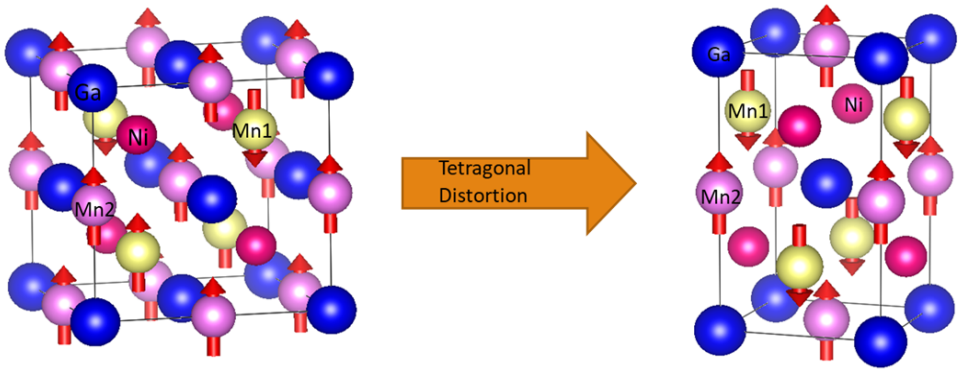

Figure 1.17: Tetragonal distortion of Mn_2NiGa (a prototype of Mn_2YZ) from cubic structure (left) to tetragonal structure (right).

1.8.1.2 Review on Shape Memory Heusler Alloys (SMAs)

Shape Memory alloys (SMAs) are the distinct category of materials, which can regain their original shape when the external force that cause the change is removed. The SMAs are always associated with a structural transformation between two structural phases [69]. In particular, some of the shape memory alloys undergo a structural phase transition from a low symmetry tetragonal to high symmetry cubic phase. This structural phase transition is named as martensite transition, whereas,

the reverse structural phase transformation is called as austenite transition. Due to the first order nature of the martensite/austenite phase transition, a large thermal hysteresis is always found in the transition region consisting of both phases. During the cooling process, the starting and finishing temperatures of phase transition are named as martensitic start (M_s) and martensitic finish (M_f) temperatures, respectively. Similarly, on the heating cycle A_s and A_f correspond to austenitic start and austenitic finish temperatures, respectively. Due to the lower symmetry of the tetragonal phase (martensite phase) in comparison to that of cubic phase (austenite phase), certain number of micro-structures, energetically equivalent to each other but crystallographically different orientation, called variants are formed in martensite phase. To minimize the elastic energy, these martensitic variants are self-accommodated to form twin like structures, named as twin variants.

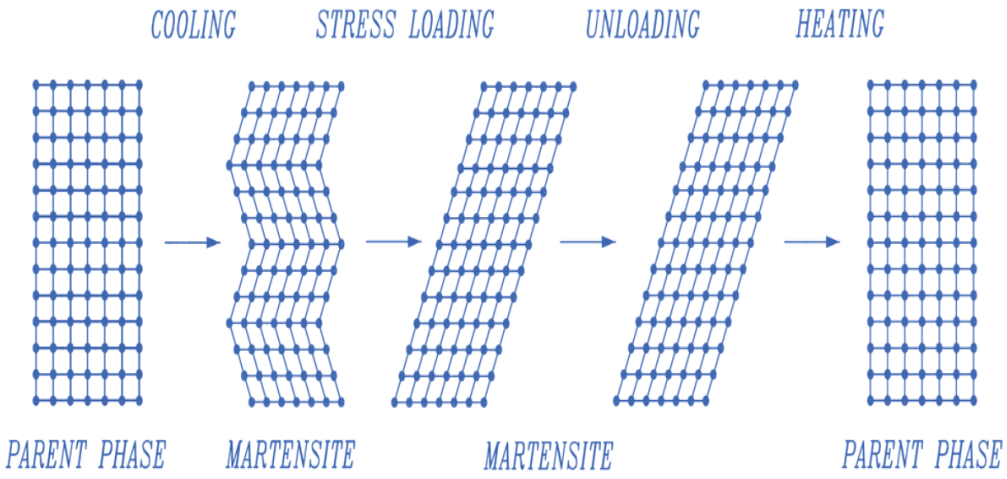

Figure 1.18: Schamatic diagram of stress induced shape memory effect [70].

A simple example of the shape memory effect is illustrated in Fig. 1.18, where the high temperature parent phase transforms into multi-variants low temperature martensite phases upon cooling the sample below M_s. The two variants of the martensite phase are shown in these Fig. 1.18. After applying stress in the martensitic state, some of the martensitic variants, which are favorable to stress direction, grow at the cost of the remaining variants due to twin boundaries motions. Finally, the martensite plates consist of only one type of twin variant (see Fig. 1.18). As a re-

sult, the shape of the material changes. After removal of stress and then heating the alloy above austenite starting temperature, A_s, the alloy regains its original shape, as seen in Fig. 1.18. This whole process is known as temperature-stress-induced-shape memory effects.

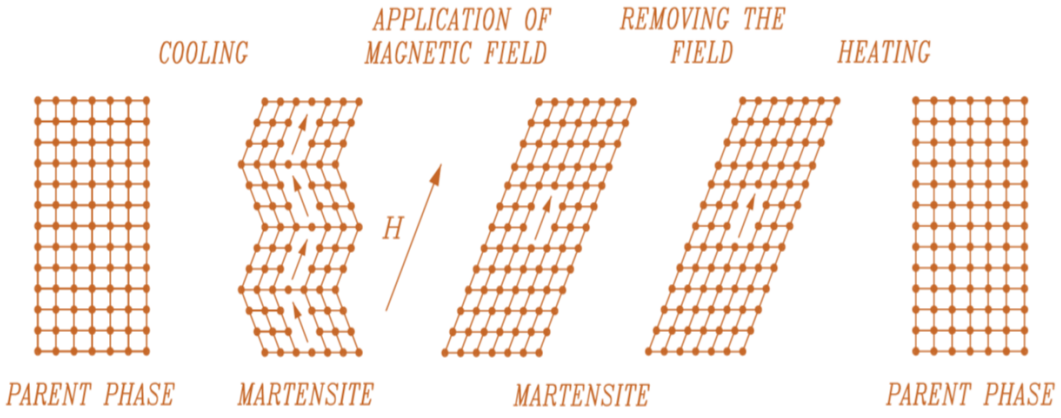

Figure 1.19: Schematic diagram of magnetic shape memory effect [70].

Another class of shape memory materials, known as magnetic shape memory alloys, exhibit change in the shape by application of magnetic field instead of stress. The schematic diagrams of the mechanism behind the magnetic shape memory effect are depicted as in Fig. 1.19. As discussed earlier, the parent phase transforms into a multi-variant martenstic structure (two variants are given in Fig. 1.19) upon cooling. When a magnetic field is applied to the crystalline ferromagnetic materials, the magnetization follows the direction of the magnetic field. When the anisotropy energy of the material is high, a large magnetic field is required to rotate the magnetization vector from the easy axis direction. At the same time, if the energy required for the twin boundaries motion is also sufficiently low enough, the magnetization can turn the unit cells of the twin variants. In such a case, magnetization vectors remain along the original easy axis direction of the changed unit cell of the twin variants. Consequently, the martensitic variants, which are favorable to the external magnetic field, grow at the cost of the remaining variants, resulting in twin boundary motions. Finally, the martensite plates consist of only one type of twin variant, and the change of the shape of the material can be achieved

(see Fig. 1.19). After removing the field and heating up the sample above the ending temperature of austenite, A_f, the deformed materials regains its original shape, as seen in Fig. 1.19. As this shape memory effect is achieved by the magnetic field instead of stress loading in the case of conventional shape memory effect, this type of shape memory alloy is known as magnetic shape memory effects.

Magnetic shape memory Heusler alloys (SMAs), which in general exhibit structural phase transformation from the high symmetric austenite (cubic) phase to a low symmetric martensite (tetragonal) phase, possess a great potential to host antiskyrmions [69, 71, 72, 73, 74]. When the nature of the tetragonal phase is noncentrosymmetric, it falls under the D_{2d} crystal symmetry category. Among the magnetic Heusler SMAs, Mn-Ni-Ga based materials have attracted a lots of attention due to their special structural, magnetic and other anomalous physical properties [69, 70, 71, 72, 73, 74, 75, 76, 77, 78]. The Mn-rich Ni-Mn-Ga materials are potential candidates for skyrmion study as the extra Mn breaks the inversion symmetry in the system [69, 71, 72, 73, 74]. The presence of tetragonal structure in the martensite phase combined with the non-centrosymmetric crystal structure sets up a favorable condition for the inhomogeneous type of Dzyaloshinskii–Moriya (DM) interaction required to stabilize antiskyrmions in the system. As the magnetic and structural property of Heusler alloys can be tuned easily in controlled way by chemical engineering, therefore, it can probably help to fill all the earlier mentioned potholes for the skyrmion based racetrack memory application.

Chapter 2

Experimental Section

The current chapter focuses on a detailed discussion about the experimental techniques along with the instrumental facilities used in the present thesis.

2.1 Sample preparation

2.1.1 Arc-melting Furnace

Arc-melting furnace have been used extensively to prepare intermetallic alloys/ compounds at very high temperature. In the arc-melting furnace, the arc is generated through electrical discharge due to ionization of the argon gas in high electric field produced between the tungsten electrode and the copper hearth. The typical arc-melting furnace and its important components are shown in Fig. 2.1.

A series of polycrystalline ingots of $Mn_{2+x}NiGa_{1-x}$, $Mn_{2+x}Ni_{1-x}Ga$, and $Mn_{1.4}Pt_{0.9}Pd_{0.1}Sn$ were prepared by melting the stoichiometric amount of high pure constituent elements using the arc-melting furnace under high-pure argon atmosphere. The arc-melting chamber is initially evacuated to a pressure around 10^{-3} mbar to develop the atmospheric-free environment before melting of samples. Then, high-pure argon gas is being used to purge the chamber several times to achieve oxygen free condition inside the chamber. To avoid heating problem arising from the

melting of the sample at very high temperature, the copper-hearth plate as well as the tungsten tip are cooled through regular flow of cold water. After finishing the evacuation process of the chamber, titanium is melted first to remove any oxygen present in the furnace. Then the samples are melted multiple times by flipping up side down to ensure a homogeneous mixture of the constituent elements. The as-prepared vacuum sealed-ingots are annealed in a box furnace at 1123 K for 7 days in case of $Mn_{2+x}NiGa_{1-x}$ and 1073 K for 7 days in cases of $Mn_{2+x}Ni_{1-x}Ga$, and $Mn_{1.4}Pt_{0.9}Pd_{0.1}Sn$ to get better homogeneity and good structural order of the samples.

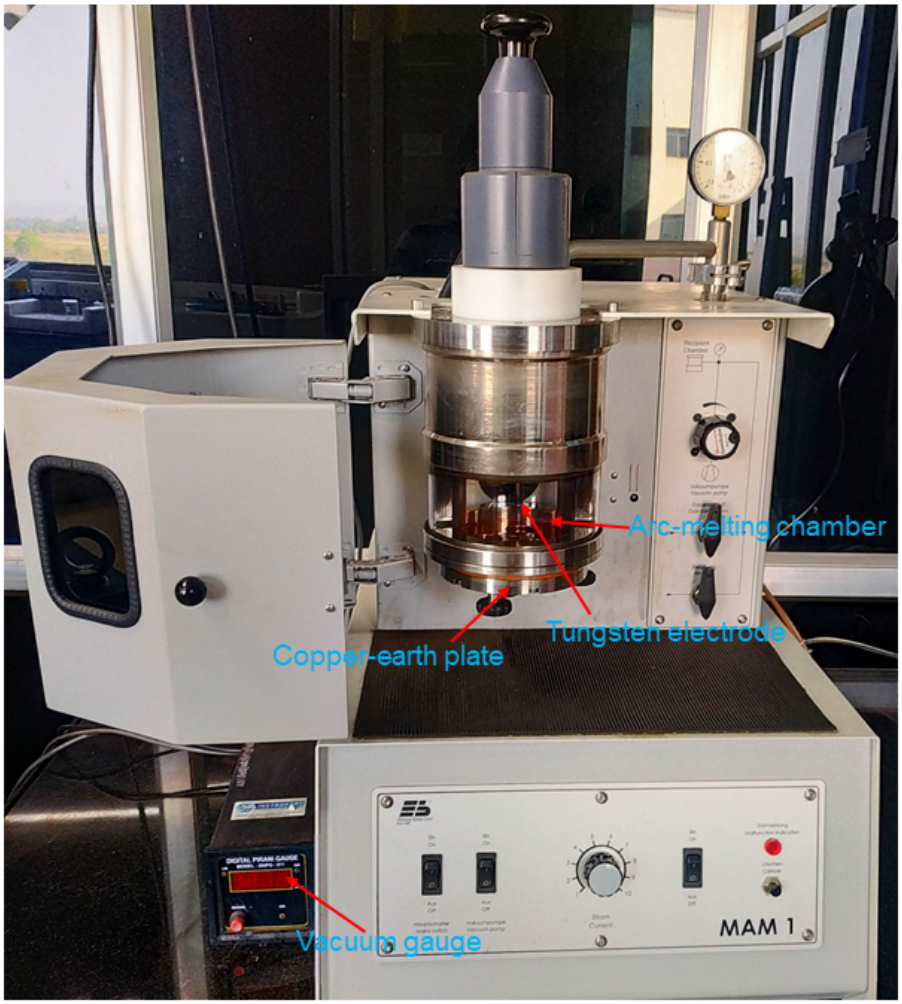

Figure 2.1: Arc-melting furnace used to prepare the samples.

2.2 Sample Characterization Technique

2.2.1 X-ray Diffraction

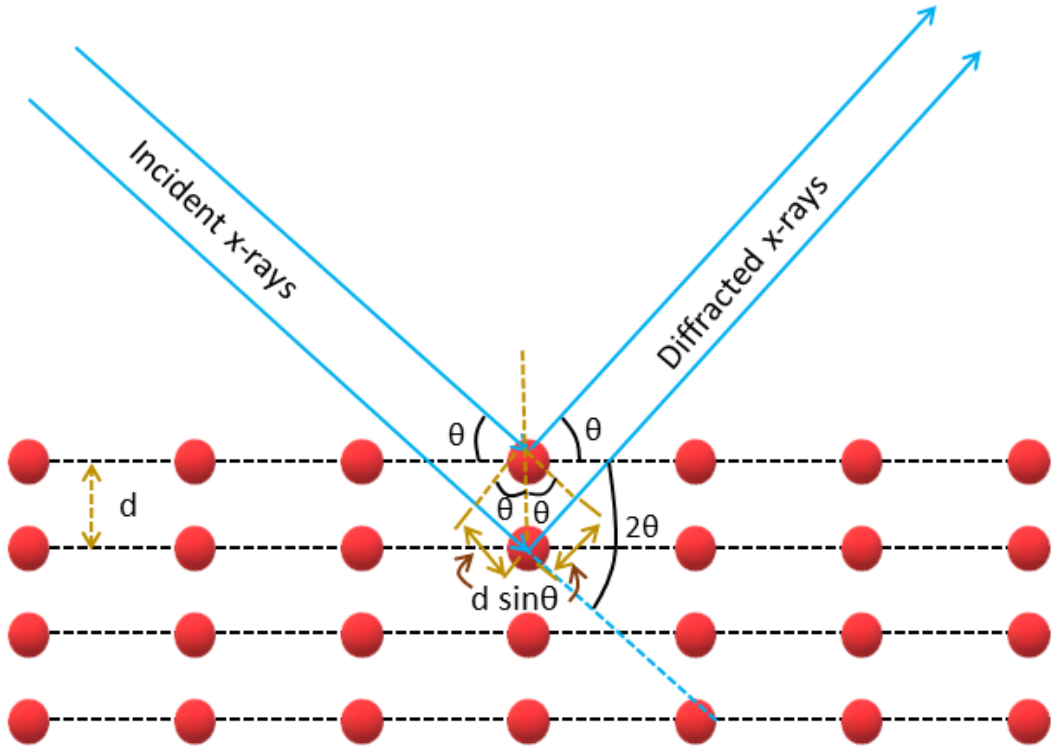

Figure 2.2: The schematic representation of Bragg's reflection from a set of lattice planes with spacing d. Red balls represent the atoms.

X-ray diffraction technique is used to examine the phase purity as well as to investigate the structural properties of the samples. The basic principle of x-ray diffraction experiments are described as follows. The theory of x-ray diffraction for the crystalline materials was first time introduced by W. H. Bragg and W.L. Bragg in 1913. When a parallel x-ray beam with a wavelength comparable to the lattice spacing of the crystalline material is bombarded on the crystalline sample, the incident x-ray diffracts from the crystal planes. The diffracted beams from two adjacent parallel planes with the path difference equal to the multiple integers of the incident x-ray wavelength give rise to constructive interference. The schematic representation of the Bragg's reflection is shown in Fig. 2.2. The Bragg's law can

be described as,

$$2d \sin\theta = n\lambda \tag{2.1}$$

where d is the lattice spacing between two adjacent atomic planes, θ is the angle of incident with respect to the lattice plane (also known as Bragg's angle), n is the integer number and λ represents the wavelength of the incident x-ray beam. For each crystal structure, a few sets of parallel atomic planes give rise to a non-vanishing x-ray intensity peak according to the earlier mentioned Bragg's law. By knowing Bragg's angle of the respective set of planes, the crystal structure of materials can be determined.

Figure 2.3: Rigaku SmartLab x-ray diffractometer used for the present thesis.

The room temperature x-ray diffraction (XRD) measurements are performed on each sample by using a Rigaku SmartLab x-ray diffractometer (as shown in Fig. 2.3)

operated at 40 kV and 30 mA current. Here, the XRD patterns are recorded using the Cu-K_α x-ray radiation of wavelength $\lambda = 1.54182$ A° in the θ-2θ scanning mode from the $2\theta = 10°$ to 90°. The temperature dependent x-ray patterns for specific composition of alloys are done by a PANalytical diffractometer from $T = 15$ K to $T = 650$ K. The x-ray patterns for each samples are analyzed using the Powdercell software package by comparing the model powder diffraction pattern.

2.2.2 Field Emission Scanning Electron Microscopy (FE-SEM)

In order to investigate the compositional homogeneity and composition of the samples used for the present thesis, high-resolution Field Emission Scanning Electron Microscopy (FESEM) imaging and Energy-Dispersive X-ray Spectroscopy (EDS) techniques are used as illustrated in Fig. 2.4. The basic working principle of FE-SEM is discussed thoroughly in the following paragraph.

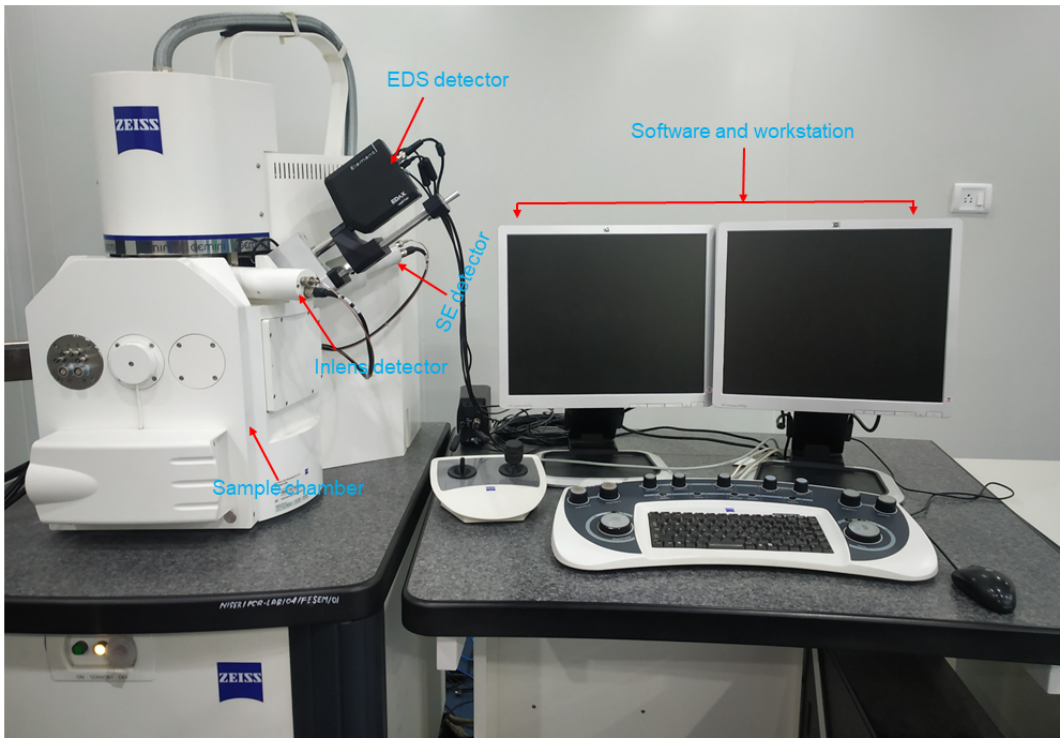

Figure 2.4: The field emission scanning electron microscope instrument, added with a EDS detector.

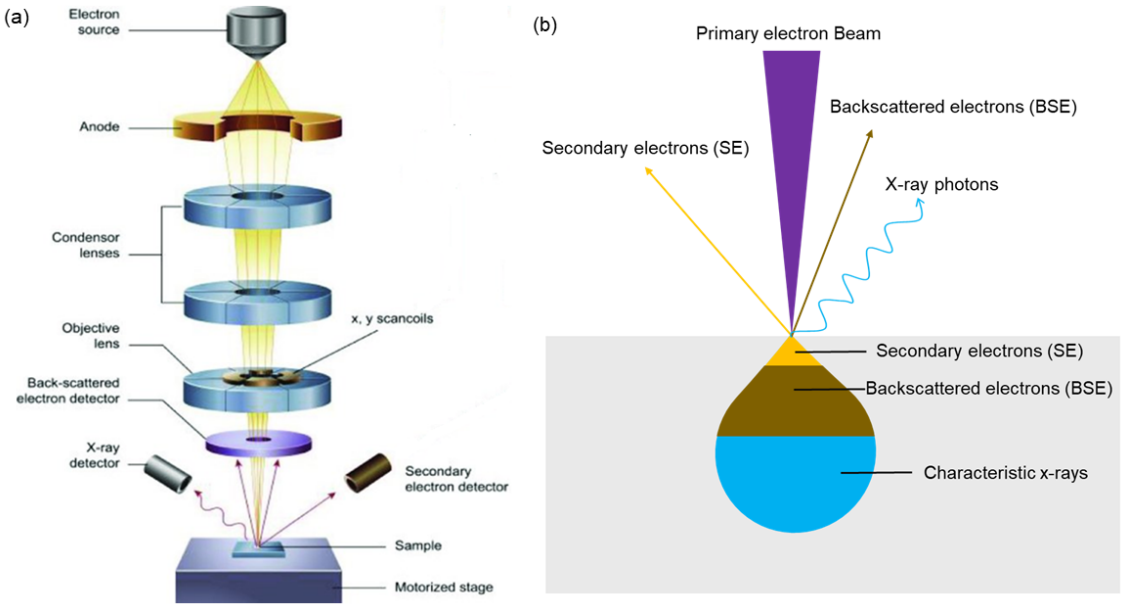

Figure 2.5: The schematic diagram of (a) different stages of FESEM instrument: the path of electron beam is controlled by several electromagnetic lenses and the electron and x-ray photon detectors [79]. (b) Schematic representation of interaction of the electron beam with the sample.

Field emission scanning electron microscopy is a high-resolution electron microscopy technique that is generally used to visualize the surface topography in micron or even nanometer scale in different branches of science. Different components of the FESEM system are shown in Fig. 2.5(a). The most important component of the FESEM instrument is the electron gun from which electrons are emitted by the conventional field emission process. In very high vacuum condition, these emitted electrons are accelerated by a gradient electric field and monitored by several electromagnetic lenses, such as condenser lenses and objective lens. The condenser lenses basically control the electron beam spot size (either narrower or wider), whereas, the objective lens is utilized to focus the electron beam on the objects under study. In between the condenser lens and objective lens, the scan coils are used to deflect the electron beam on the surface of the object. The incident electrons interact with the atoms of the object. In this process, several phenomenons related to these interactions emerges, as showing in Fig. 2.5(b). This can provide insight into the properties of the sample under study. In this process, the secondary electrons are

generated as a result of the inelastic scattering of the primary incident electrons with the atoms in the samples. Only the secondary electrons produced from the interaction between the primary incident electrons and the loosely bounded electrons of the surface the samples contribute to the mapping of the surface topography. The high-energy incident electrons that undergo elastic scattering by the atoms of the objects/samples with scattering angle greater than 180 degree are known as the primary backscattered electrons (BSE). As the backscattered electrons return back from relatively higher depth of the sample, the image constructed from them gives the information about the compositional homogeneity of the sample (either single phase or multiphase). It is to be noted here that the resolution of the image formed by the secondary electrons is better than the image constructed from the backscattered electrons. When the high energy incident electrons knock out the core shell electrons (K, L, M shells, etc.) of the samples, these voids are filled by the electrons of a higher energy shell, and consequently x-ray photons are generated. Every element in the periodic table emits a characteristic x-ray wavelength. According to the Moseley's law, this characteristic wavelength of the element inversely varies with the square root of the atomic number (Z) of that element. This is the fundamental principle of the Energy-Dispersive x-ray Spectroscopy (EDS) technique that is being used to determine the composition of the samples.

2.3 Magnetic Measurements

Magnetic measurements are performed using a Quantum Design-make Superconducting Quantum Interference Device Vibrating Sample Magnetometer (SQUID-VSM) (as shown in Fig. 2.7) and the VSM attached to Physical Properties Measurement System (PPMS) (as shown in Fig. 2.6).

Magnetization (M) as a function of temperature (T) are measured from 2 K to 400 K in the presence of a fixed magnetic field in three conventional modes. (1) In zero field cooled (ZFC) mode, the sample was initially cooled down to the lowest measuring temperature without any magnetic field, then the measurement

was carried out in the warming process under magnetic field (H= 0.1 T). (2) In the field cooled (FC) mode, the data was taken during the cooling process in the presence of magnetic field. (3) When the measurement was performed at the time of warming by applying field after the field-cooling process, then the mode is called as field heating (FH). High temperature $M(T)$ measurements are also performed on the samples in the temperature range 300 K – 800 K under applied magnetic fields. The isothermal magnetization vs. magnetic field (H) measurements are carried out over a maximum field range of -9.0 T $\leq$H$\leq$ +9.0 T, at different temperatures ranging from 2 K to 385 K.

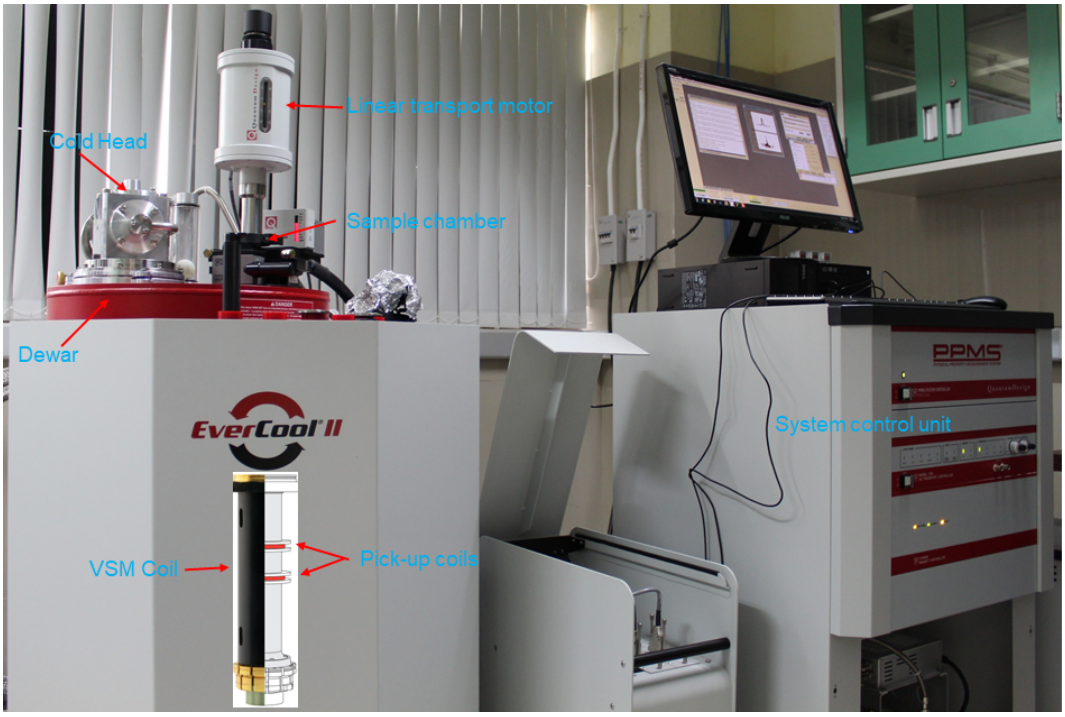

Figure 2.6: Physical properties measurement system (PPMS, Quantum Design) used to measure the magnetic, electrical, and thermal properties of the samples.

2.3.1 Vibrating Sample Magnetometer (VSM)

The VSM option in the PPMS is an effective and sensitive tool to measure the dc magnetization of the sample. The VSM option includes a linear VSM motor transport (head), a set of the pickup coil, and electronics for signal detection system (see Fig. 2.6). The basic principle of VSM measurement is related to the emf induced

in the pickup coil due to the change in flux, based on Faraday's law. Application of magnetic field using the superconducting solenoid magnet magnetize the sample. When the magnetized sample vibrates inside the pickup coil (vibrating amplitude 1-3 mm peak, frequency 40 Hz), a voltage is induced in the pickup coil. The induced voltage in the pickup coil can be explained as,

$$V_{coil} = d\phi/dt = \frac{d\phi}{dz}\frac{dz}{dt} \tag{2.2}$$

where, ϕ is the magnetic flux enclosed by the pickup coil, z is the vertical position of the sample with respect to the coil and t is time. For a sinusoidally oscillating sample position, the induced voltage in the pick cup coil is governed by the following equation-

$$V_{coil} = 2CmA\sqrt{f}\sin(2\sqrt{f}t) \tag{2.3}$$

where, C is a coupling constant, m is the DC magnetic moment of the sample, A is the amplitude of oscillation, and f is the frequency of oscillation. The sample is attached to the sample rod which vibrate sinusoidally. The sinusoidal vibration of the sample rod is controlled by the VSM linear motor transport. The center of oscillation is in the center of the gradiometer pickup coil. The VSM system uses the touch down process to define the sample centering. The system can measure the change of magnetic moment less than 10^{-6} emu.

The PPMS-VSM (Quantum Design) can be operated in the temperature range from 1.8 K to 400 K with a maximum magnetic field of 9 T. Here the magnetic field is produced by a superconducting solenoid coil. Liquid He is used to cool down the sample chamber. A flow control valve and heaters are used in the annulus region, a space between the sample chamber and dewar (storage of liquid He), to control the temperature in the sample chamber. In order to achieve the fixed temperature in the sample chamber, the liquid helium initially enters from the dewar to the annulus region through an impedance valve, and then the heater is switched on to boil up the liquid helium of the annulus region. Then by controlling the He gas pressure on the top of the liquid-He column through the flow control valve, the boiling point of

liquid He either increases or decreases. By doing so, the temperature of the chamber is controlled in disciplined manner.

The oven option attached with the VSM helps to measure the magnetic properties in the temperature range from 300 K to 1000 K. Here the magnetic moment is also detected in similar procedure as used in case of standard VSM option. But here a specific sample holder is used, in which the sample is heated by applying current to platinum heating element attached to the sample holder. To measure the temperature, a thermocouple is attached to the backside of the holder. An alumina based cement is used to glue the sample with the sample holder to get maximize the thermal contact. All the functionalities of the PPMS are controlled by the MultiVu software.

2.3.2 Superconducting Quantum Interference Device based magneto-meter (SQUID)

Superconducting Quantum Interference Device (SQUID), the most frequently used magneto-meter, possesses a great impact on condensed matter physics research owing to the ability to detect magnetic flux in very high precession. The basic principle of SQUID is solely based on the concept of Josephson junction in superconducting loop. Usually the Josephson junction is made of a superconducting loop interrupted by one or more missing links. Typically, normal metal or insulator, are used as the missing links. In 1962, Josephson predicated that super-current can also pass through this junction / weak link from one end to the other end of the superconductor via quantum-mechanical tunneling of cooper-pairs across it.

A SQUID consists of two Josephson junctions with a dc current used through it. The commercial SQUID can measure the magnetic moment very accurately of the order of 10^{-8} emu.

The magnetic property measurement system (MPMS-Quantum Design/SQUID magnetometer) is used to measure high precession magnetization at temperatures from $T = 1.8$ K to 400 K with the magnetic field up to 7 T. A typical picture of the

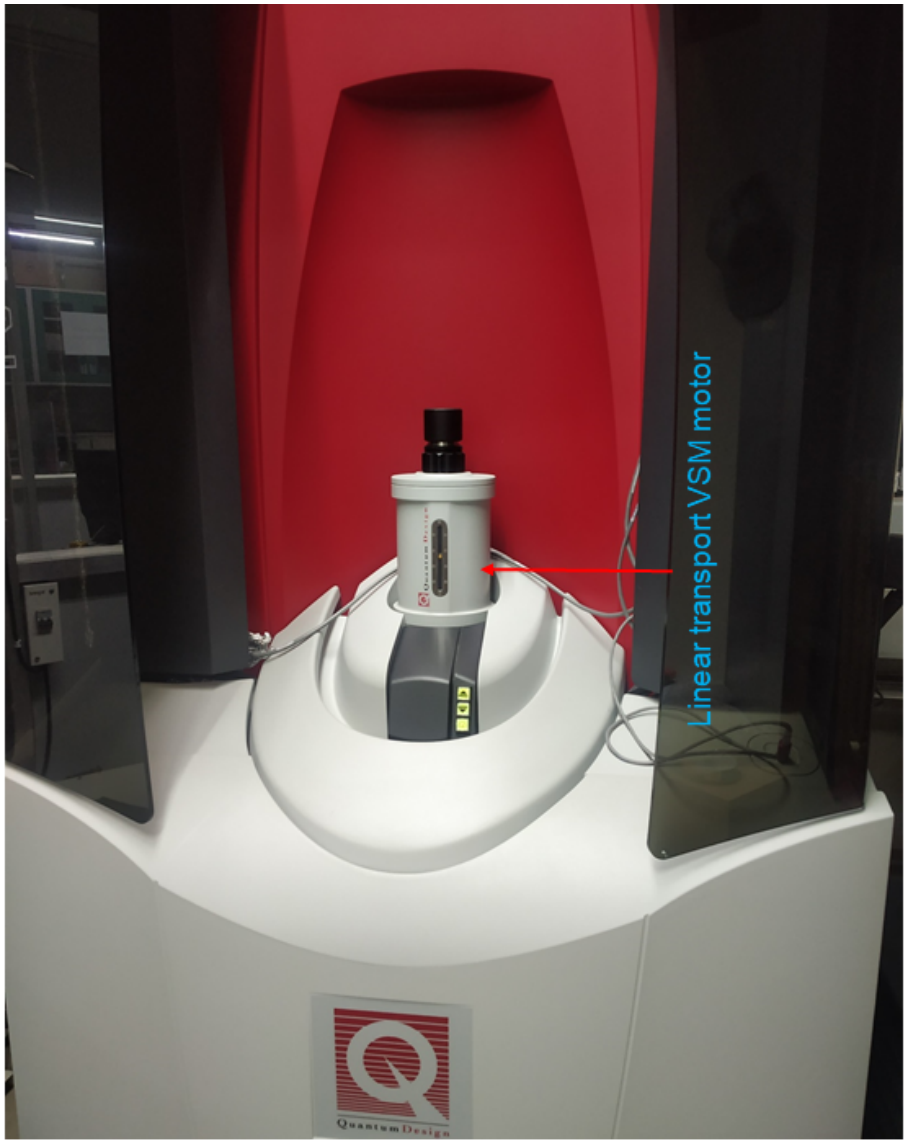

Figure 2.7: The VSM attached with superconducting quantum interference device (SQUID-VSM) made by Quantum Design.

MPMS-Quantum Design is given in Fig. 2.7. To perform high sensitive magnetic measurements, superconducting pick-up coils and SQUID sensors are used. In the SQUID-VSM mode, when the sample vibrates inside the pick up coil, an emf is induced according to the Faraday's law. Consequently, current is generated in the pick-up coil. The superconducting pick-up coils are inductively coupled to a direct current (DC) based SQUID sensors via input transformer as shown in Fig. 2.8. By this process, the change of magnetic flux can be measured through the SQUID sensors. Superconducting detection coils are arranged as a second order gradiometer,

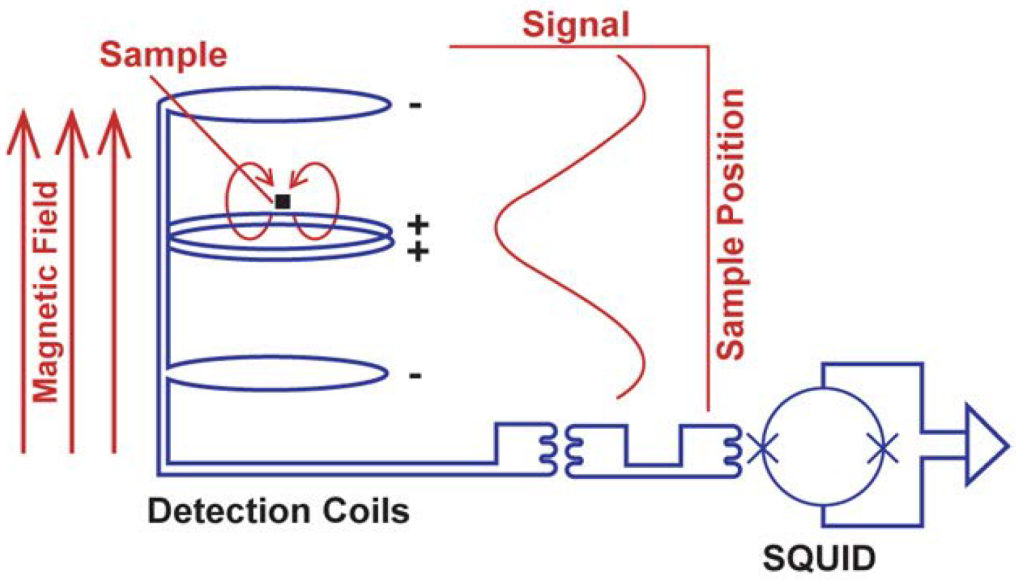

Figure 2.8: The schematic diagram of a VSM coils attached with SQUID sensor [taken from MPMS-3 (Quantum Design) user's manual].

where one of the detection coil wounds opposite to other as shown in Fig. 2.8. The DC-SQUID flux sensor is protected inside the superconducting shield chamber to counter the effect of any kind of magnetic flux from outside the MPMS-chamber. A maximum moment of about 3 emu can be detected by the MPMS. To measure the magnetic moment of the sample accurately, the sample must be located at the center of coils. The functionality of MPMS-SQUID is controlled externally by MultiVu software. In general, the temperature and the magnetic field dependence of magnetization can be measured with high accuracy using the MPMS.

2.3.3 AC susceptibility Measurements

Ac susceptibility measurement is generally extensively used as a probe to identify several dynamical phenomena associated with magnetic materials. For the present study, the ac susceptibility response of the samples is measured with the help of the ACMS option in the PPMS. To probe the dynamical properties of magnetic material, a small amount of ac magnetic field is applied along with the static/dc field when required. When the ac magnetic field is applied to a magnetic system,

the magnetic moments of the sample tries to follow the ac field. Therefore, the magnetic moments of the sample oscillate in time by the ac field. The oscillating magnetic moments induce a time dependent magnetic flux and thereby generate a time dependent electromotive force in pickup coils. This electromotive force induces an ac current in the coil. By measuring the ac current, the information about the amplitude and frequency of the ac magnetic response are detected by the pick-up coil/detection coil.

When an ac magnetic field is applied along with the dc magnetic field to the sample i.e. $H(t) = H_{dc} + h_{ac}\cos\omega t$, then the magnetization of the sample can not follow the ac magnetic field. As a consequence, the magnetization lags with the ac magnetic field, and the expression of time dependent magnetization $[M(t)]$ can be written as

$$M(t) = M_{dc} + m_{ac}\cos(\omega t - \phi) \tag{2.4}$$

$$M(t) = M_{dc} + m_{ac}\cos\omega t\cos\phi + m_{ac}\sin\omega t\sin\phi \tag{2.5}$$

where, M_{dc} is the dc magnetization, m_{ac} is the amplitude of the ac magnetization and ϕ represents the phase shift of ac magnetization with respect to the ac magnetic field. Now, analog to dc susceptibility $\chi_{dc} = M_{dc}/H_{dc}$, then the above time dependent magnetization can be written in terms of ac susceptibility as

$$M(t) = \chi_{dc}H_{dc} + \chi'_{ac}\cos\omega t + \chi''_{ac}\sin\omega t \tag{2.6}$$

where, $\chi' = m_{ac}\cos\phi/h_{ac}$ and $\chi'' = m_{ac}\sin\phi/h_{ac}$ are the real and imaginary part of ac susceptibility, respectively. It can be seen from the Eq. 2.6 that the real part of ac susceptibility is in-phase with ac magnetic field whereas the imaginary part of ac susceptibility is out of phase with ac magnetic field. Therefore, the real part and imaginary part of ac susceptibility are also known as in-phase and out-phase component of the ac susceptibility.

In complex notation, if the magnetic field $H(t) = H_{dc} + h_{ac}e^{i\omega t}$, then

$$M(t) = \chi_{dc}H_{dc} + \chi_{ac}h_{ac}e^{i\omega t} \tag{2.7}$$

Here, the complex susceptibility is given by

$$\chi_{ac} = \chi'_{ac} + i\chi''_{ac} = \chi_{ac}e^{i\phi} \tag{2.8}$$

where, mod $\chi_{ac} = \sqrt{\chi'^2_{ac} + \chi''^2_{ac}}$ and the phase shift $\phi = \arctan(\chi''_{ac}/\chi'_{ac})$

The χ'_{ac} is associated with the reversible magnetization process and generally very sensitivity to the change in magnetization with respect to the magnetic field. Whereas χ''_{ac} is related to the dissipation of energy due to irreversible magnetization process, such as the irreversible movement of domain walls, magnetic phase transition, spin reorientation, spin-spin relaxation and spin-lattice relaxation process.

To investigate the dynamical properties of a magnetic system, different parts of the $M(H)$ loop are probed by applying a small amplitude of ac magnetic field with different ac frequencies in addition to the dc magnetic field. As discussed above, the susceptibility of the system is a complex entity with phase factor (ϕ) and the amplitude χ_{ac}. By measuring the magnitude and the phase shift by the magnetometer circuit, the real and the imaginary part of ac susceptibility are obtained. Generally, χ_{ac} vs temperature, χ_{ac} vs dc magnetic field, χ_{ac} vs frequency, and χ_{ac} vs amplitude of ac field measurements are performed to study the dynamical properties, magnetic phase transition, etc. In this thesis, χ'_{ac}/χ''_{ac} vs dc magnetic field and χ'_{ac}/χ''_{ac} vs ac frequency measurements are performed to investigate the magnetic phase transition and dynamical properties of different samples using the ACMS option in PPMS with fixed ac amplitude $H_{ac} = 10$ Oe and the ac frequency f ranging from 111 Hz to 9999 Hz.

2.4 Electrical Transport Measurements

This section focuses on the magneto-transport measurements with the help of the ac transport (ACT) option in PPMS (Quantum Design). With the help of ACT option, one can measure the field and temperature dependence of longitudinal resistivity as well as the Hall resistivity. In ACT option, longitudinal resistivity is measured by the conventional four probe method, whereas, the five probe method is adopted to measure the Hall voltage of the sample.

In four probe method, two separate terminals (I_+ and I_-) are used to pass the alternative current through the sample and the longitudinal voltage drop across the sample is measured by two separate terminals (V_+ and V_-), as schematically represented in Fig. 2.9(a). The longitudinal resistivity is calculated by the Ohm's law. Due to separate terminals of voltage and current, the contribution of lead resistance and contact resistance to sample resistivity are canceled out. Therefore, a high precession of voltage drop across the sample can be measured by the four probe method. The resistivity of the sample can be calculated by the following formula-

$$\rho_{xx} = VA/lI \tag{2.9}$$

where, A and l is the cross sectional area of the sample and the lead separation between two voltage contact terminals, respectively. I is the current passing through the sample and the voltage drop across sample is denoted by V.

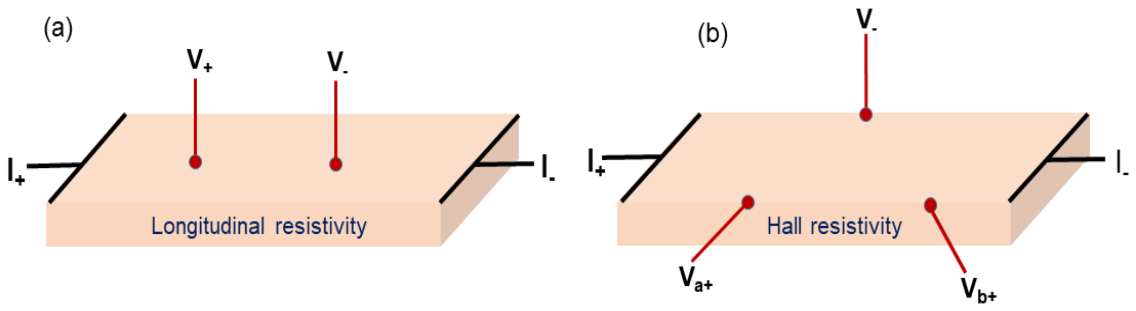

Figure 2.9: A schematic diagram of (a) four probe method for measuring the longitudinal resistivity, and (b) five probe method for measuring the Hall resistivity of a rectangular shaped sample.

It is to be noted here that the voltage leads must be parallel to the current flow direction to obtain the correct value of longitudinal resistivity.

To measure the Hall resistivity of our sample, five probe method is utilized as shown Fig. 2.9(b). The Hall voltage of the sample can also be measured by using the four probe method when the two voltage terminals are connected to the transverse direction of the current flow. To measure the actual voltage due to the Hall effect, the voltage must be measured perfectly perpendicular to the current direction. If the two voltage terminals are misaligned, i.e., the transverse voltage is not measured ideally perpendicular to the current direction, the measured transverse voltage can also contain additional component of the longitudinal voltage. To solve this problem, five probe method is used to nullify the longitudinal voltage contribution to the Hall voltage. For this purpose, a potentiometer is generally connected between the V_{a+} and V_{b+} leads. The potentiometer is tuned in such a way that V_{a+} - $V_{b+} = 0$. By doing so, the contribution due to the longitudinal resistance during the transverse voltage measurement is eliminated. It is to be noted here that the contribution due to the longitudinal resistance in Hall measurements may still present even after balancing the potentiometer when the Hall voltage is very small in comparison with the longitudinal Hall resistivity. Therefore, the Hall voltage is measured in both positive and negative field sweep, thereby, the actual Hall resistivity can be obtained by subtracting the contribution of symmetric field dependent resistivity part (longitudinal resistivity) from the measured transverse resistivity. In this thesis, the isothermal field dependent longitudinal as well as Hall voltage of the samples are measured using ac current of amplitude 50 mA and frequency 331 Hz at different temperatures from $T = 3$ K to 380 K. Temperature dependence of longitudinal voltage are also measured from $T = 3$ K to 300 K at a zero magnetic field.

Chapter 3

Antiskyrmions in D_{2d} symmetric $Mn_{2+x}NiGa_{1-x}$ Heusler Shape Memory Alloys

As discussed in the motivation section in Chapter 1, Mn_2NiGa exhibits all the essential properties to host the antiskyrmion phase. Hence, the current chapter mainly focuses on the realization of antiskyrmion phase in the tetragonal Heusler shape memory compound Mn_2NiGa that exhibits D_{2d} crystal symmetry. In this prospect, a series of $Mn_{2+x}NiGa_{1-x}$ (x = 0.0, 0.05, 0.10) samples are prepared by using arc melting furnace as discussed in Chapter-2. The structural property of the samples are characterized by means of X-ray diffraction (XRD) and Field Emission Scanning Electron Microscopy (FESEM) measurements. The magnetic properties of the samples are illustrated by using low temperature as well as high temperature magnetization measurements. The ac susceptibility measurements of these sample are also presented in this chapter. A detailed study on the magneto-transport properties, such as longitudinal and Hall resistivity of the samples are discussed at the end.

3.1 Sample characterization

In this section, the structural properties as well as the compositional homogeneity of the $Mn_{2+x}NiGa_{1-x}$ ($x = 0.0, 0.05, 0.10$) samples are discussed by using XRD and FESEM measurements.

3.1.1 XRD studies on $Mn_{2+x}NiGa_{1-x}$ ($x = 0.0, 0.05, 0.10$)

As shown in Fig. 3.1, room temperature XRD patterns are recorded on the $Mn_{2+x}NiGa_{1-x}$ ($x = 0.0, 0.05, 0.10$) samples to reveal the crystal structure. It is to be noted here that because of the ductile nature of the Mn-Ni-Ga alloys, the XRD studies are performed using highly polished disc-shaped samples of thickness of about 1 mm. The XRD patterns of all these samples are inspected through powder-cell software by comparing with the standard model of powder diffraction. It is found that Mn_2NiGa crystallizes mostly in a tetragonal crystal phase with space group I-4m2. In addition, a small amount of cubic phase with space group F-43m also exists at room temperature. The XRD analysis reveals the lattice parameters of a = b = 3.917 A° and c = 6.745 A° in the tetragonal phase, whereas, the cubic phase exhibits lattice parameter a = b = c= 5.90 A°. In the Mn_2NiGa tetragonal phase, the Ga and Ni atoms occupy the 2a (0.0, 0.0, 0.0) and 2d (0.0, 0.50, 0.75) positions, respectively, whereas, the Mn atoms sits in two different Wycoff positions at 2b (0.0, 0.0, 0.50) and 2c (0.0, 0.50, 0.25). In the cubic phase Ga atoms sit at 4a (0.0, 0.0, 0.0), Ni at 4d (0.75, 0.75, 0.75) and Mn atoms occupy 4b (0.5, 0.5, 0.5) and 4c (0.25, 0.25, 0.25) positions. The room temperature XRD patterns for $Mn_{2.05}NiGa_{0.95}$, and $Mn_{2.1}NiGa_{0.9}$ samples display a pure tetragonal phase with space group I-4m2 [Fig. 3.1 (b), and (c)]. The lattice parameters for $Mn_{2.05}NiGa_{0.95}$ sample are a = b = 3.900 A° and c = 6.744 A°, whereas, $Mn_{2.1}NiGa_{0.9}$ shows a = b = 3.840 A° and c = 6.740 A°.

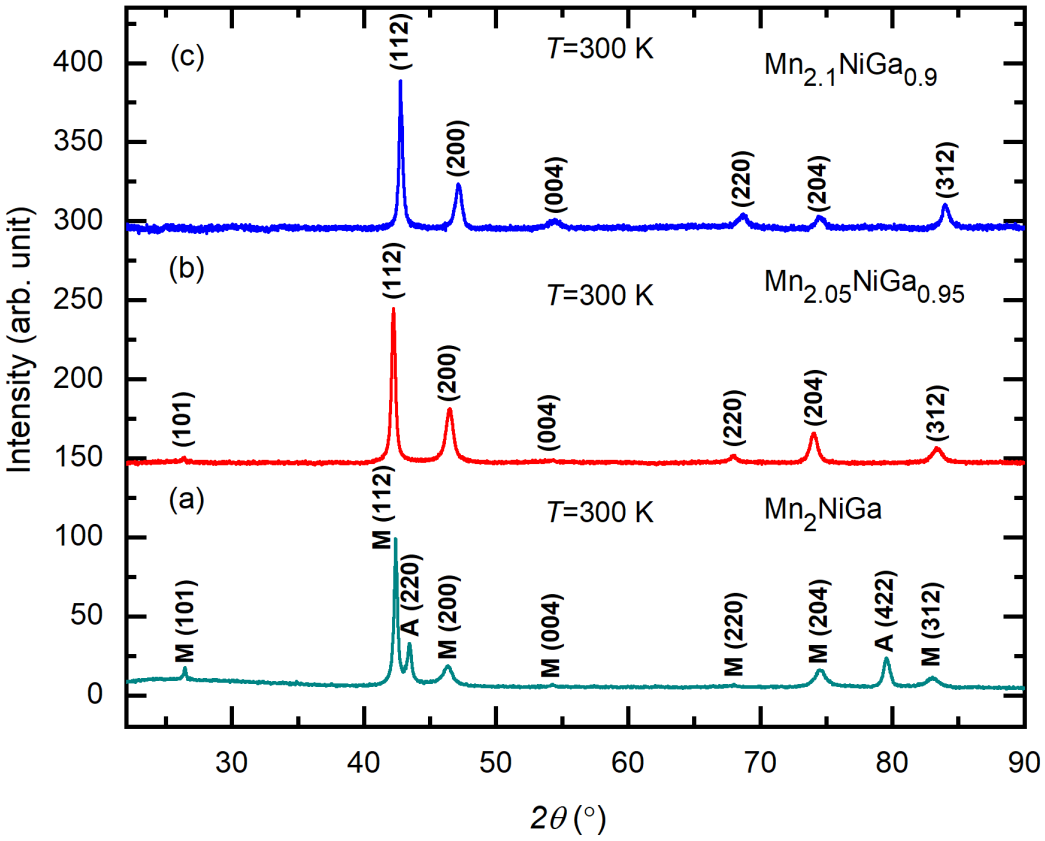

Figure 3.1: (Color online) The Room temperature XRD patterns for (a) Mn_2NiGa, (b) $Mn_{2.05}NiGa_{0.95}$, and (c) $Mn_{2.1}NiGa_{0.9}$. Here, the symbols 'M' and 'A' stand for the martensite and austenite, respectively.

3.1.2 Temperature dependent XRD studies on $Mn_{2+x}NiGa_{1-x}$ (x = 0.0, 0.10)

As discussed above, the room temperature XRD pattern for the shape memory alloy Mn_2NiGa exhibits structural coexistence of tetragonal and cubic phases. To further study the nature of this phase coexistence, temperature dependent XRD measurements are carried out from T = 15 K to T = 600 K as plotted in Fig. 3.2. As it can be seen, the intensity of the peaks corresponding to the cubic structure (austenite phase) A (220) and A (422) decreases gradually with decreasing temperatures. For $T < 150$ K, both the cubic peaks completely disappear, indicating the presence of a single tetragonal phase. At T = 15 K, the XRD pattern shows the peaks corresponding to the pure tetragonal phase. At $T > 300$ K, intensity of the peaks

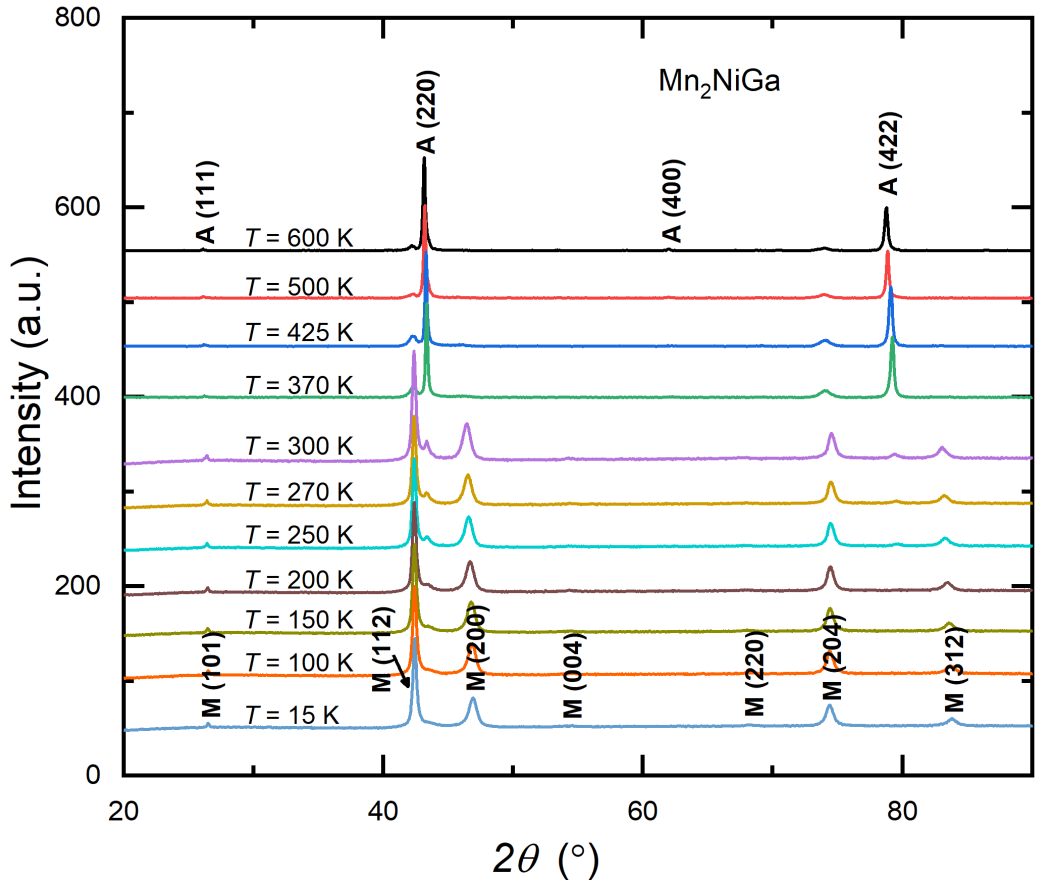

Figure 3.2: (Color online) The temperature dependent XRD patterns of Mn_2NiGa. The symbols 'M' and 'A' stand for martensite and austenite, respectively.

related to the tetragonal phase decreases with increasing temperatures, whereas, the intensity of the cubic peaks increases with temperature. From these temperature dependent XRD patterns, it can be concluded that the tetragonal phase is dominant in the sample over the cubic phase for temperatures below the room temperature, whereas, cubic phase is predominant at high temperatures.

Like Mn_2NiGa, the XRD measurements at various temperatures ranging from $T = 15$ K to $T = 550$ K are performed for the $Mn_{2.1}NiGa_{0.9}$ sample which shows a pure tetragonal structure at room temperature. These XRD patterns are plotted in Fig. 3.3. It can be seen that $Mn_{2.1}NiGa_{0.9}$ displays a pure tetragonal structure in the whole temperature range from $T = 15$ K to $T = 550$ K. This indicates that $Mn_{2.1}NiGa_{0.9}$ does not undergo any structural phase transition in the measured temperature range.

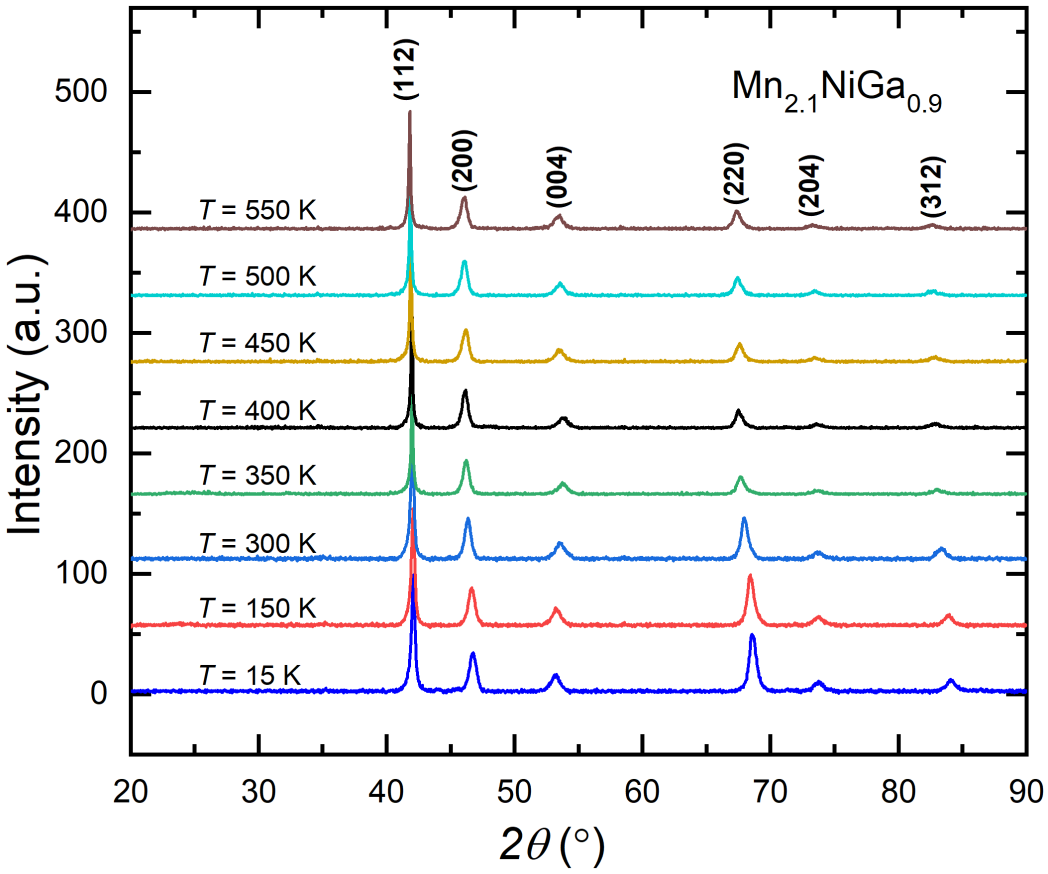

Figure 3.3: (Color online) The XRD patterns at various temperatures for $Mn_{2.1}NiGa_{0.9}$.

3.1.2.1 Field Emission Scanning Electron Microscopy (FESEM) and Energy Dispersive X-ray Spectroscopy (EDS) studies

Field Emission Scanning Electron Microscopy (FESEM) technique is used to examine the compositional homogeneity of the samples with the help of surface imaging and Energy Dispersive X-ray Spectroscopy (EDS) studies. The EDS measurements are performed to verify the stoichiometry of the samples. The FESEM images for x = 0.0, 0.05, 0.10 show homogeneous contrast as depicted in Fig. 3.4. The composition obtained from the EDS study is summarized in Table 3.1. The homogeneous contrast in FESEM images and the compositional study by EDS measurements, confirm that all the samples exhibit a single compositional phase.

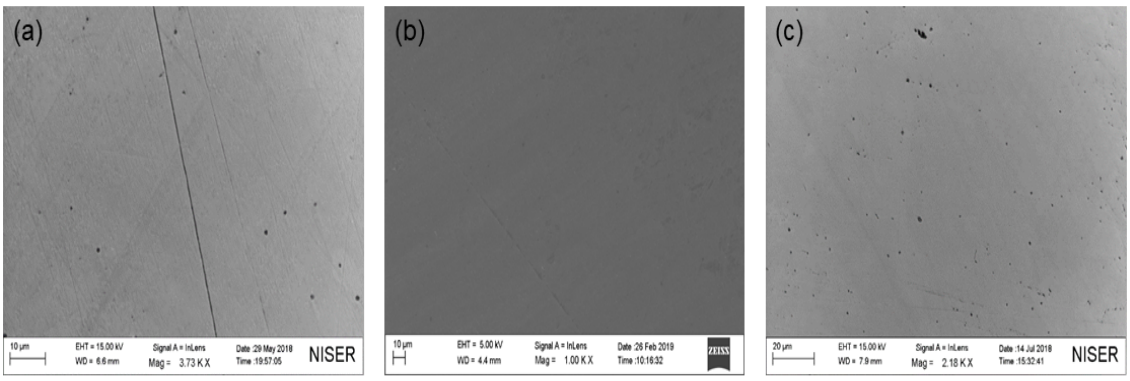

Figure 3.4: (Color online) The FESEM images for (a) Mn_2NiGa, (b) $Mn_{2.05}NiGa_{0.95}$, (c) $Mn_{2.1}NiGa_{0.9}$

Table 3.1: The EDS results for $Mn_{2+x}NiGa_{1-x}$ samples.

Initial composition	EDS composition
Mn_2NiGa	$Mn_{1.95}Ni_{0.96}Ga_{1.09}$
$Mn_{2.05}NiGa_{0.95}$	$Mn_{2.05}Ni_{0.99}Ga_{0.96}$
$Mn_{2.1}NiGa_{0.9}$	$Mn_{2.08}Ni_{0.96}Ga_{0.96}$

3.2 Magnetization Measurements for $Mn_{2+x}NiGa_{1-x}$

3.2.1 Magnetization Measurements for Mn_2NiGa

The temperature dependence of magnetization, $M(T)$, measured in field-cooling (FC) and field-heating (FH) modes at a fixed dc magnetic field (H) of 0.1 T for the Mn_2NiGa sample is depicted in Fig. 3.5(a). A sharp transition around $T = 300$ K appears both in the FC and FH $M(T)$ curves. As it can be seen, the magnetization curves do not follow the same path around the transition temperatures and thereby gives rise to a large thermal hysteresis between the FC and FH curves around $T = 300$ K. This hysteretic behavior is generally found due to the presence of first-order transition. As it is seen before in the temperature dependent XRD measurements of Mn_2NiGa, the hysteretic behavior in the $M(T)$ curves further exemplify the presence

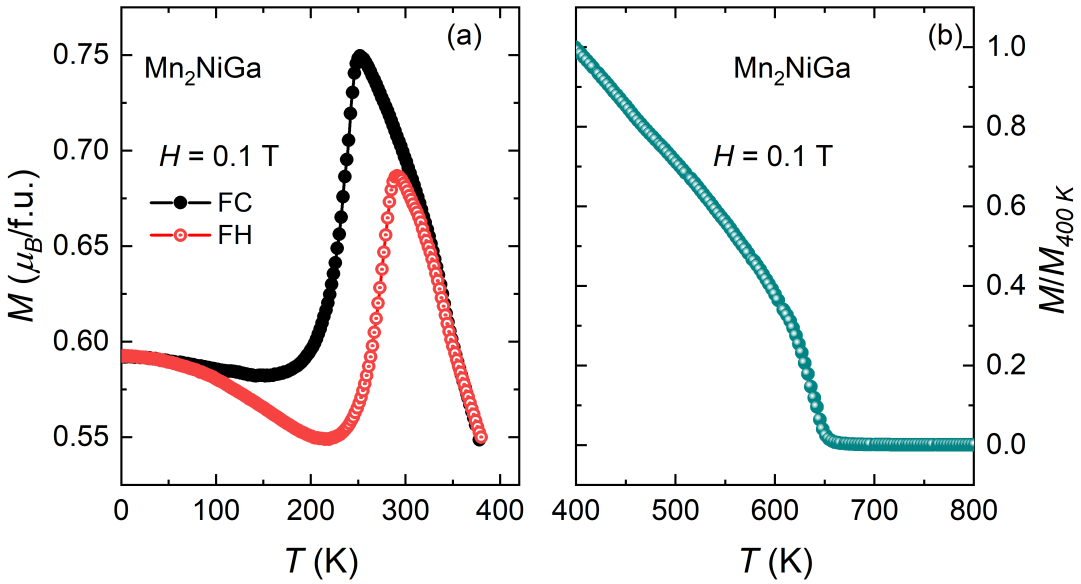

Figure 3.5: (Color online) The temperature dependence of magnetization, $M(T)$, curves at $H = 0.1$ T (a) from $T = 2$ K to 400 K and (b) from $T = 400$ K to 800 K for Mn_2NiGa. The FC and FH $M(T)$ curves are represented by the solid black and open red symbols, respectively.

of structural transformation from the high temperature cubic phase to the low temperature tetragonal phase. In order to find out the magnetic ordering temperature of Mn_2NiGa sample, the high temperature magnetization versus temperature data is recorded from $T = 400$ K to 800 K at $H = 0.1$ T. The high temperature magnetic measurement given in Fig. 3.5 (b) exhibits a magnetic ordering temperature (T_C) of about 650 K.

The magnetization measurement as a function of magnetic field, $M(H)$, is carried out to at several temperatures to map out the magnetic states in Mn_2NiGa. Fig. 3.6 (a) shows the $M(H)$ curve measured at $T = 2$ K, where a saturation magnetization of about 1.43 $\mu_B/f.u.$ is found. A dip kind of anomaly in the $M(H)$ curve, marked by blue arrows in Fig. 3.6 (a) can be observed around $H = 0.3$ T. The transition is clearly seen in the zoomed view of the $M(H)$ curve shown in Fig. 3.6 (b). To find out the possible existence of this anomaly in other temperatures, $M(H)$ measurements are carried out at different temperatures from $T = 2$ K to $T = 380$ K as plotted in Fig. 3.7. As it can be seen, the dip kind of anomaly in the $M(H)$ curves is visible for temperature up to $T = 300$ K. However, the anomaly is absent for the temperatures

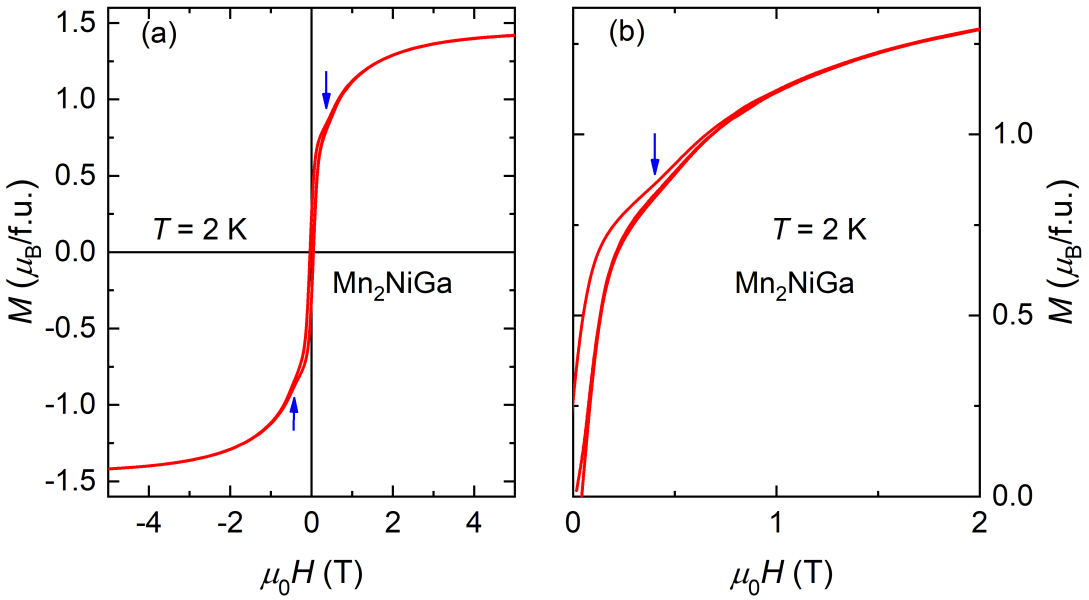

Figure 3.6: (Color online) (a) Isotherm magnetization as a function of magnetic field, $M(H)$, at $T = 2$ K for Mn_2NiGa. (b) The zoomed view of the anomaly region of the $M(H)$ curves. The anamolies in these curves are marked by blue arrows.

above 300 K as in Fig. 3.7 (h)-(i). This can be clearly seen from the field dependent magnetization curve at $T = 380$ K as shown in Fig. 3.8 (a) as well as in the zoomed view of the curve plotted in Fig. 3.8 (b). It is worth to point out here that the dip kind of anomaly in the $M(H)$ loops appears only in the tetragonal phase of the sample, whereas, no such anomalous behavior is found in the cubic dominated states of the sample. This kind of magnetic transition in the $M(H)$ loop has often been found in many skyrmion hosting materials [13, 14, 26, 27, 28, 80].

3.2.2 Magnetization Measurements for $Mn_{2.05}NiGa_{0.95}$

The temperature dependence of FC and FH magnetization curves for $Mn_{2.05}NiGa_{0.95}$ measured at $H = 0.1$ T are plotted in Fig. 3.9. Like the parent Mn_2NiGa alloys, $Mn_{2.05}NiGa_{0.95}$ also exhibits a difference between the FC and FH $M(T)$ curves. However, the thermal hysteresis behavior occurs in relatively high temperature region around $T = 380$ K in comparison to that of Mn_2NiGa. In other words, the temperature stability of the tetragonal phase is enhanced largely by slight change of the Mn/Ga ratio. The change in the total number of valance electrons due to the

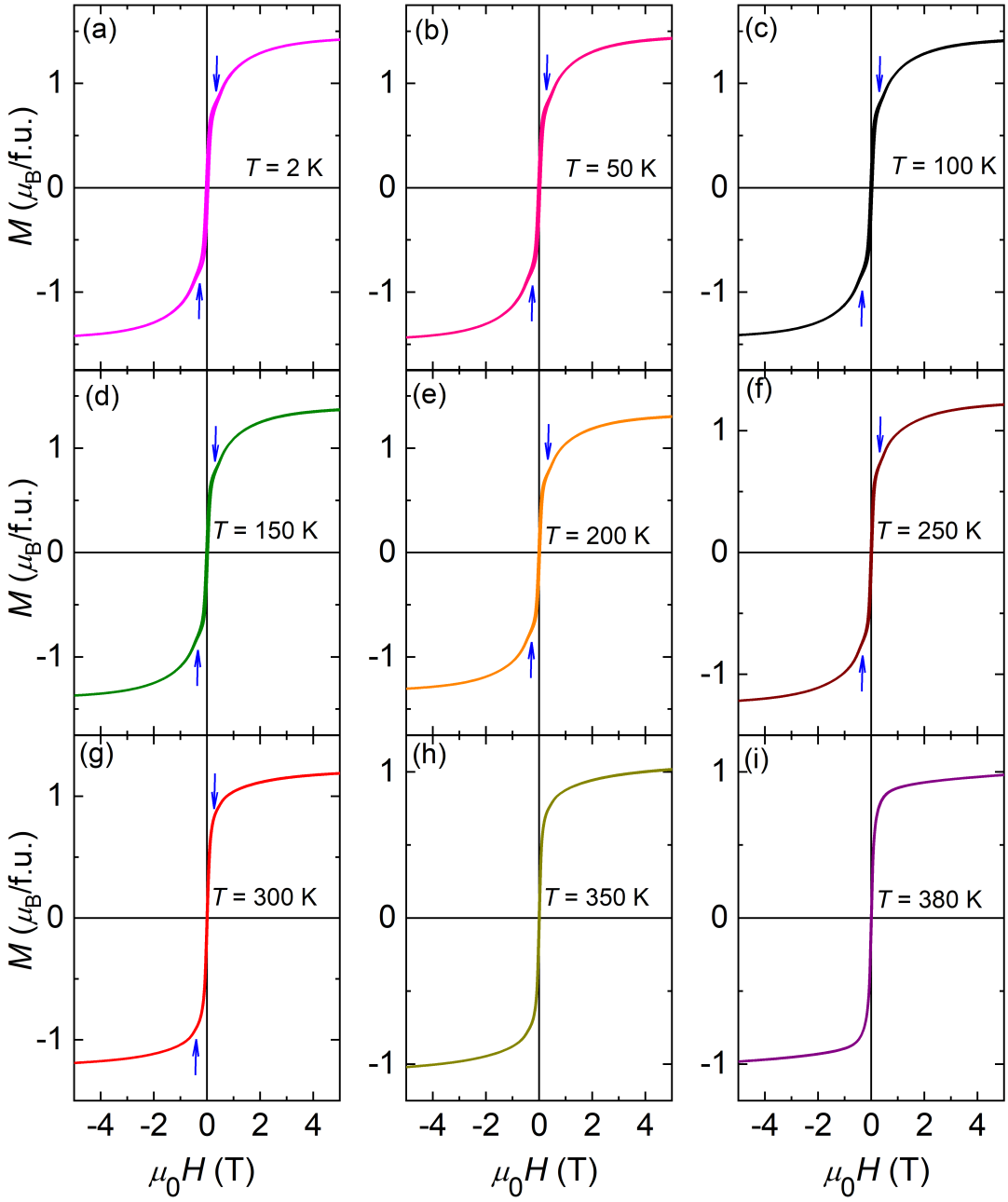

Figure 3.7: (Color online) The field dependence of magnetization curves at different temperatures from $T = 2$ K to $T = 380$ K for Mn_2NiGa. The anamolies in these curves are marked by blue arrows.

substitution of extra Mn atoms in place Ga might be responsible for this shift in the structural transformation in $Mn_{2.05}NiGa_{0.95}$. Fig. 3.10 shows the magnetic hysteresis loops measurements at different temperatures for $Mn_{2.05}NiGa_{0.95}$. Like Mn_2NiGa, a dip kind of anomaly (marked by black arows) is also found in the hysteresis curves

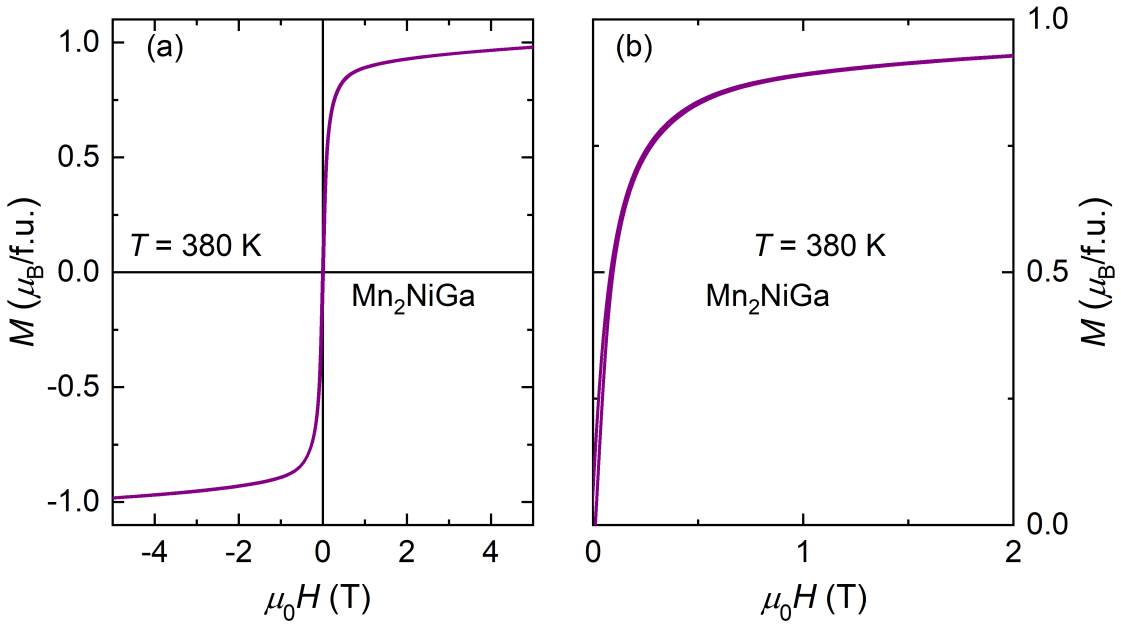

Figure 3.8: (Color online) (a) $M(H)$ loop measured at $T = 380$ K for Mn_2NiGa. (b) The zoomed view of the anamoly region of the $M(H)$ curve.

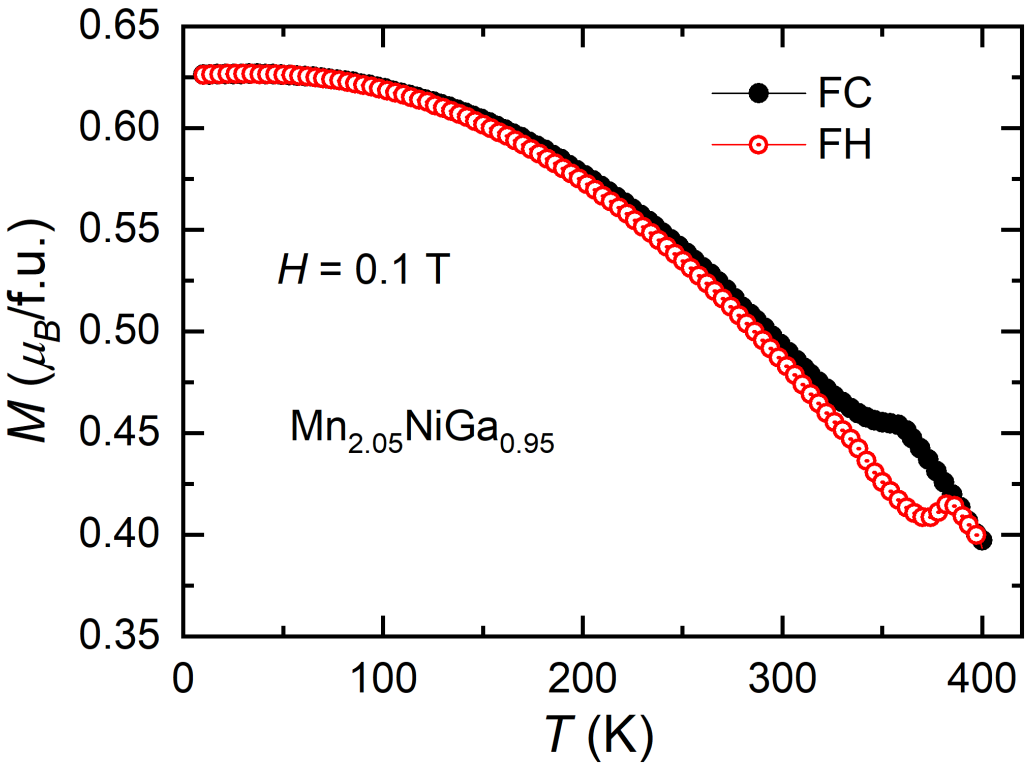

Figure 3.9: (Color online) The temperature dependence of magnetization curves for $Mn_{2.05}NiGa_{0.95}$ measured at $H = 0.1$ T.

of $Mn_{2.05}NiGa_{0.95}$. The existence of the dip kind of feature in the $M(H)$ curve is found up to the maximum possible measured temperature ($T = 380$ K) as can be seen in Fig. 3.10 (a)-(f). It is expected that this anomalous feature may disappear to $T > 380$ K as the structural transition falls at this temperature.

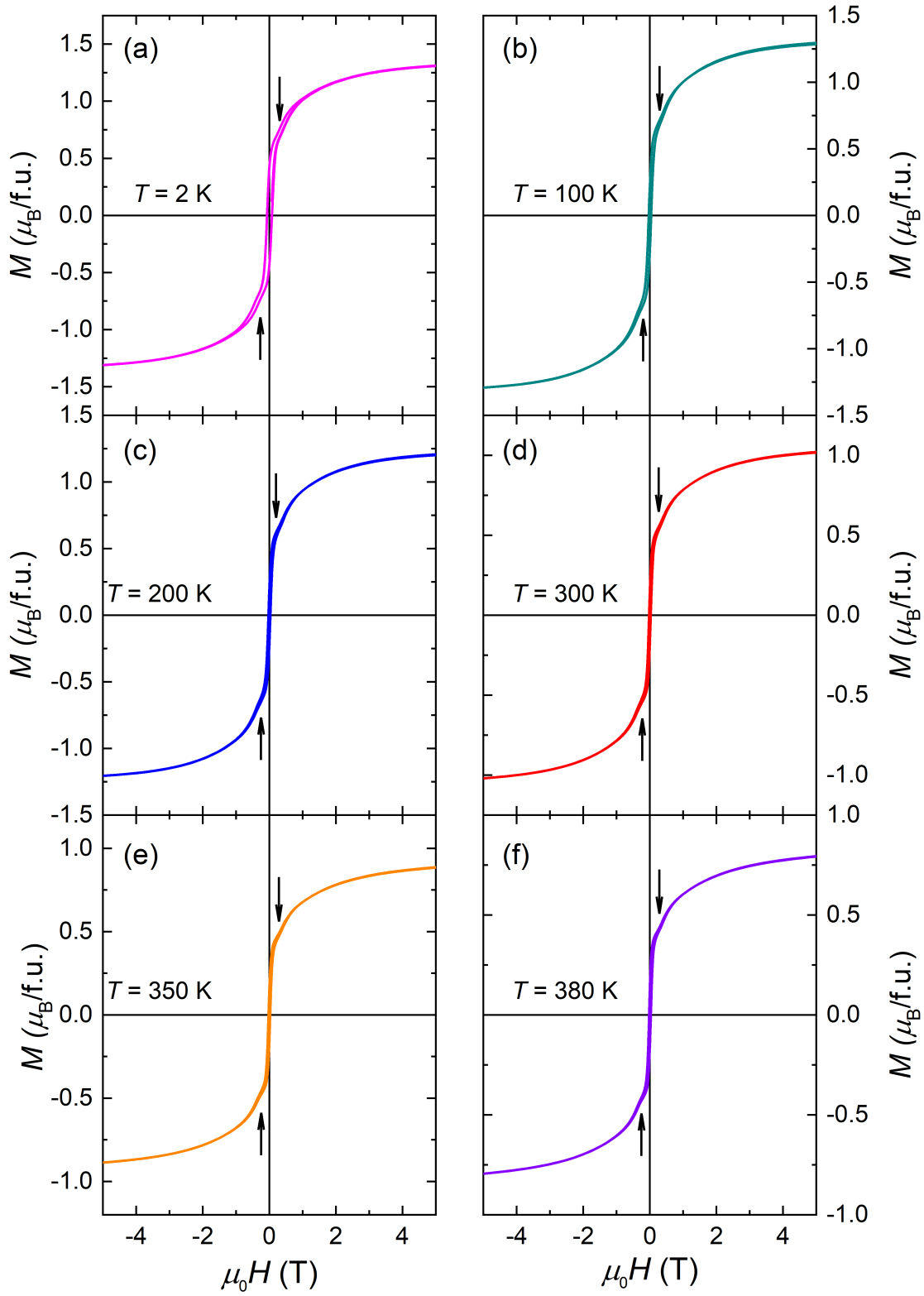

Figure 3.10: (Color online) The isothermal magnetization curves from $T = 2$ K to $T = 380$ K for $Mn_{2.05}NiGa_{0.95}$. The anomalies in these curves are marked by black arrows.

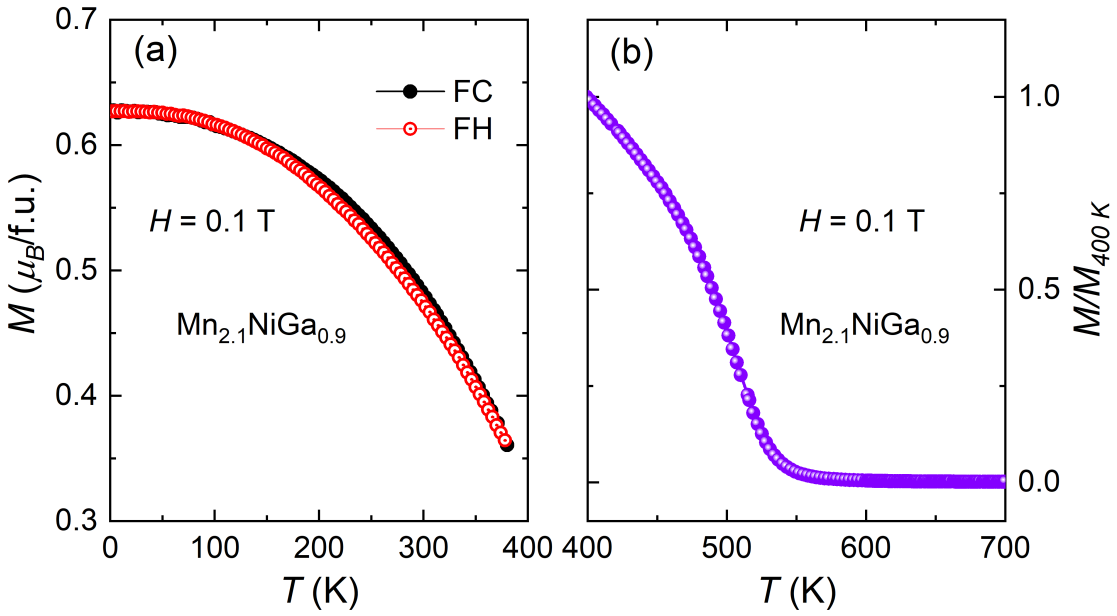

Figure 3.11: (Color online) The temperature dependence of magnetization, $M(T)$, curves at $H = 0.1$ T (a) from $T = 2$ K to 400 K and (b) from $T = 400$ K to 800 K for $Mn_{2.1}NiGa_{0.9}$. The FC and FH $M(T)$ curve are represented by the solid black and open red symbol, respectively.

3.2.3 Magnetization Measurements for $Mn_{2.1}NiGa_{0.9}$

The temperature dependent magnetization measurements performed at $H = 0.1$ T in usual FC and FH modes for the $Mn_{2.1}NiGa_{0.9}$ sample is given in Fig. 3.11(a). Unlike Mn_2NiGa and $Mn_{2.05}NiGa_{0.95}$, no thermal hysteresis between the FC and FH magnetization curves is observed below $T = 400$ K for $Mn_{2.1}NiGa_{0.9}$. Fig. 3.11(b) shows the $M(T)$ curve measured at high temperature from $T = 400$ K to 700 K. The Curie temperature of the sample is found to be about 550 K. Most importantly, no structural transition is observed up to the magnetic ordering temperature, as supported by the temperature dependent XRD measurements shown previously in Fig. 3.3. The isothermal magnetization measurements performed at several temperatures ranging from $T = 2$ K to 380 K are shown in Fig. 3.12 . The saturation magnetic moment at $T = 2$ K is found to be around 1.12 $\mu_B/f.u.$. The magnetic hysteresis loops for all the temperatures measured up to 380 K exhibit the dip kind of anomaly found before. It is expected that these anomalies could possibly exist up

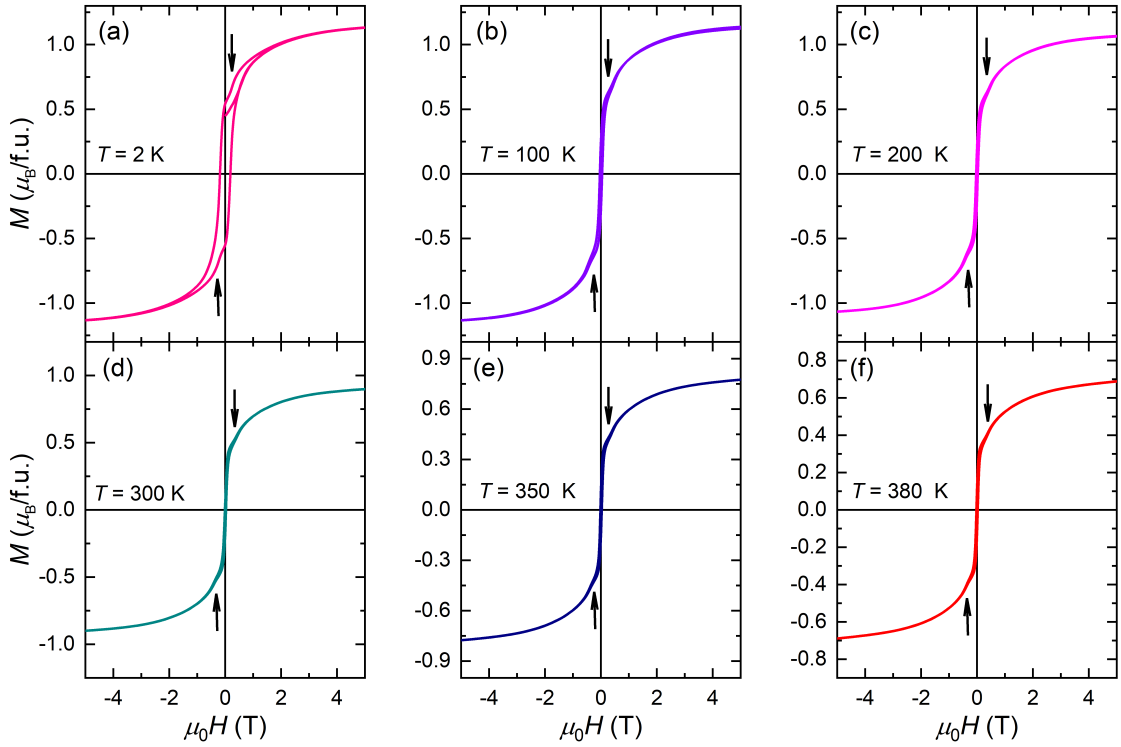

Figure 3.12: (Color online) The field dependent magnetization curves at fixed temperatures ranging from $T = 2$ K to $T = 380$ K for $Mn_{2.1}NiGa_{0.9}$. The anamolies in these curves are marked by black arrows.

to the magnetic ordering temperature of 550 K as no structural transition is found in this sample.

3.3 AC susceptibility measurements

The ac susceptibility measurement have been extensively used to identify various magnetic phase transitions present in magnetic materials. To study the nature of magnetic transition found in the in the $M(H)$ curves shown in the previous section, field dependent ac susceptibility measurement is carried out extensively in these samples. The real part of ac susceptibility data as a function of magnetic field $[\chi'(H)]$ measured at different temperatures for the Mn_2NiGa sample is depicted in Fig. 3.13. At $T = 2$ K, a hump-like feature, marked by the asterisk $(*)$ symbol as given in Fig. 3.13(a), is observed at $H = \pm 0.35$ T in both the positive as well as negative field

quadrants. This broad hump like feature in the $\chi'(H)$ data is also found for other temperatures as shown in Fig. 3.13(a)-(f). It is noticeable that the sharpness of this transition gradually enhances with temperatures up to $T = 200$ K before starting to diminish for the higher temperatures. This anomaly exists up to $T = 300$ K, as no peak/hump feature in the the $\chi'(H)$ curve is found for $T = 370$ K, as seen from Fig. 3.13(f). It is to be noted here that the peak behavior in the $\chi'(H)$ data is only found in the tetragonal phase of the sample and disappears when the sample enters into the cubic phase. This kind of field-induced transition in the ac susceptibility data has been previously observed in various skyrmion hosting materials [28, 29, 30, 31, 32, 33]. In these materials, the transition in the ac susceptibility data is found when the system undergoes from the helical to skyrmion and skyrmion to the field polarized states. Recently, similar kind of hump-like feature has also been found in the antiskyrmion hosting Mn-Pt-Pd-Sn system [81]. As the crystal symmetry of the Mn_2NiGa sample falls into the same category that of Mn-Pt-Pd-Sn sample (D_{2d}), the observed peak behavior in the $\chi'(H)$ curve in Mn_2NiGa sample can be attributed to the presence of magnetic first-order phase transition from the helical to antiskyrmion phase. As expected, the hump kind of features in the ac susceptibility measurements exist only in the tetragonal phase of the sample, whereas, a very smooth kind of ac susceptibility curve is found in the cubic phase.

To identify the antiskyrmion phase in other off-stoichiometric Mn-Ni-Ga samples, the field dependence of ac susceptibility measurements are also performed in the $Mn_{2.05}NiGa_{0.95}$ and $Mn_{2.1}NiGa_{0.9}$. The ac susceptibility data for the $Mn_{2.05}NiGa_{0.95}$ and $Mn_{2.1}NiGa_{0.9}$ are plotted in Fig. 3.14 and 3.15, respectively. Like the parent Mn_2NiGa sample, both $Mn_{2.05}NiGa_{0.95}$ and $Mn_{2.1}NiGa_{0.9}$ exhibit hump kind of behavior in the ac susceptibility data. The existence of this hump like features in the ac susceptibility curves are found up to $T = 380$ K (the maximum possible measured temperature) for both the samples. These anomalies in the ac susceptibility data indicate the presence of antiskyrmions phase in $Mn_{2.05}NiGa_{0.95}$ and $Mn_{2.1}NiGa_{0.9}$. Here, the transitions in the ac susceptibility measurements appear more prominently at the high temperatures in comparison to that of low temperatures.

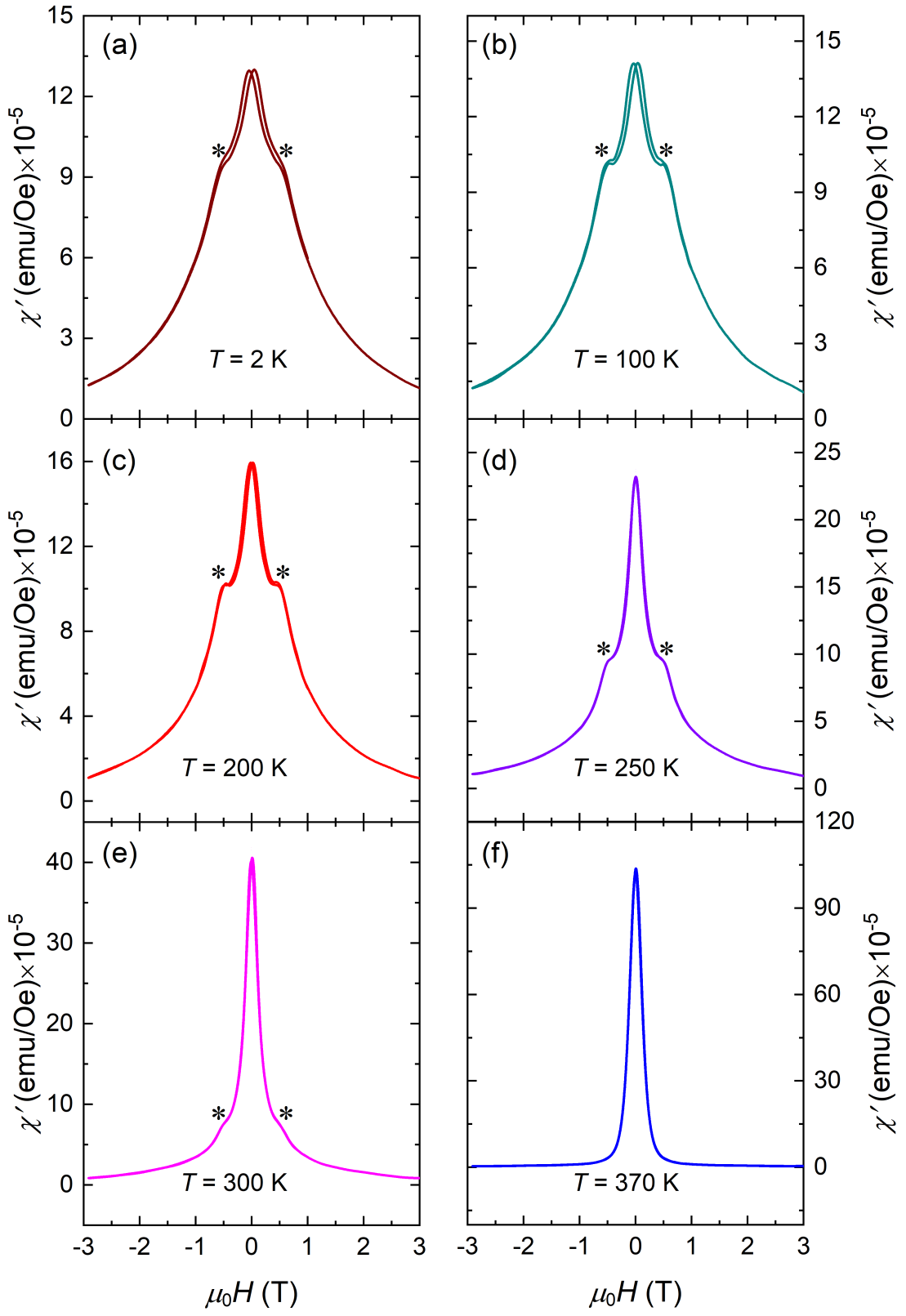

Figure 3.13: (Color online) The real part of ac susceptibility (χ') as a function of magnetic field (H) at various temperatures for Mn_2NiGa. The asterisk ($*$) symbols represent the anamolies in the $\chi'(H)$ curves.

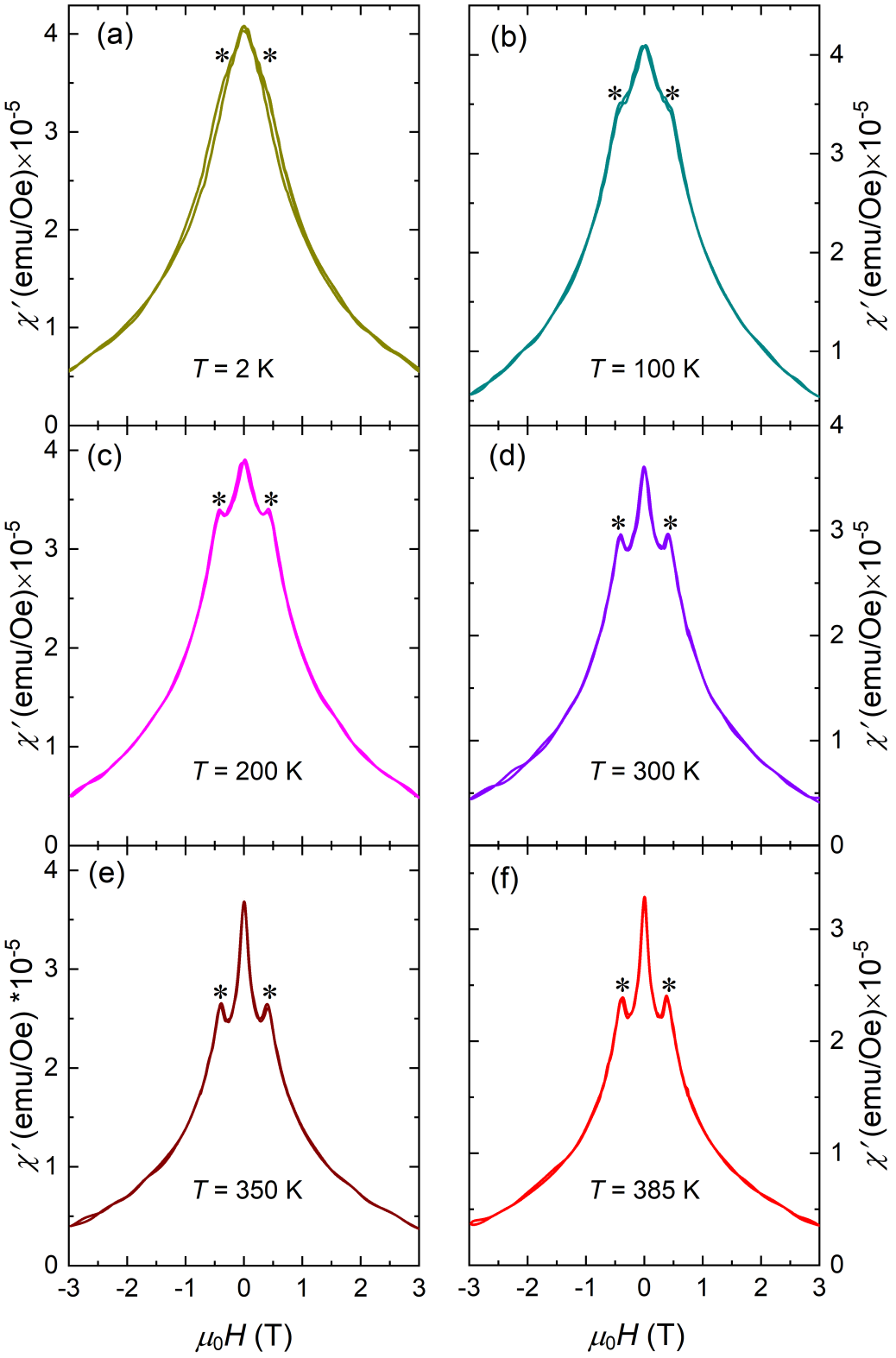

Figure 3.14: (Color online) Field dependent real part of ac susceptibility, $\chi'(H)$, at different temperatures for $Mn_{2.05}NiGa_{0.95}$. The asterisk ($*$) symbols show the anomalies in the $\chi'(H)$ curves.

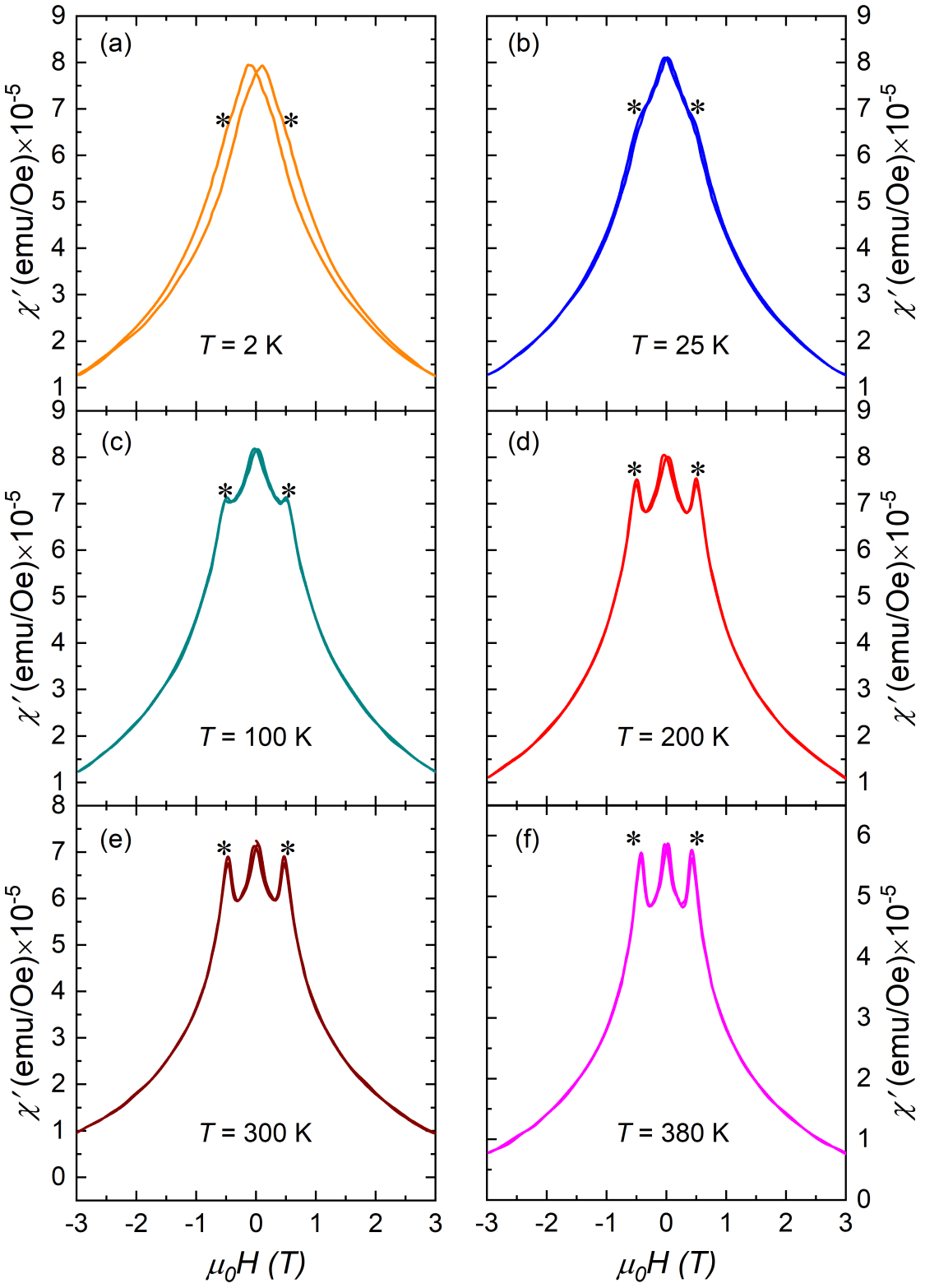

Figure 3.15: (Color online) Field dependent real part of ac susceptibility, $\chi'(H)$, at different temperatures for $Mn_{2.1}NiGa_{0.9}$. The asterisk ($*$) symbols indicate the anomalies in the $\chi'(H)$ curves.

3.4 Magneto-transport studies

As discussed previously in Chapter-1, when the conduction electrons pass through the skymions/antiskyrmions spin textures, an extra-component of Hall resistivity, named as topological Hall effect, arises in addition to the conventional normal and anomalous Hall resistivities in ferro-/ferri-magnetic samples. Therefore, any presence of topological objects like skyrmions/antiskyrmions in a magnetic system must be reflected in the Hall effect measurement. For the present Mn-Ni-Ga samples, the signature of antiskyrmion phase is already seen in the ac susceptibility measurements. Hence, the magneto-transport study is carried out on rectangular shape Hall bar (as discussed in Chapter-2) of the $Mn_{2+x}NiGa_{1-x}$ samples.

The temperature dependence of longitudinal resistivity for Mn_2NiGa shows a typical metallic behavior as the longitudinal resistivity increases with temperature, as depicted in Fig. 3.16 (a). The field dependence of Hall resistivity ($\rho_{xy}(H)$) measured at $T = 2$ K for the Mn_2NiGa sample is shown in Fig. 3.16 (b). It can be clearly seen that $\rho_{xy}(H)$ curve measured at $T = 2$ K exhibits a dip kind behavior in the second and fourth quadrants around $H = 0.35$ T, as marked by black arrows in Fig. 3.16 (b). This anomaly is in agreement with that is found in the $M(H)$ and ac susceptibility measurements. In addition, this dip kind of anomaly in the field dependence of Hall resistivity can be found for temperatures ranging from $T = 2$ K to $T = 300$ K, as shown in Fig. 3.17. Interestingly, it can be seen from Fig. 3.17 (f) that the dip anomaly disappear for $T = 385$ K that falls in the cubic region.

It is well understood that the total Hall resistivity in ferro-/ferri-magnetic materials generally consist of the normal and the anomalous Hall resistivities. An extra-component of Hall resistivity, ρ^T, arising due to the presence of any non-coplanar spin texture can also be included in the total Hall resistivity for any magnetic material. Therefore, the total Hall resistivity can be written as- $\rho_{xy}(H) = \rho^N + \rho^A + \rho^T$. Here, $\rho^N = R_0 H$ represents the normal Hall resistivity, R_0 is the normal Hall coefficient, $\rho^A = R_s M$ is the anomalous Hall resistivity, R_s is the anomalous Hall coefficient, and ρ^T stands for the topological Hall resistivity. Therefore, the expres-

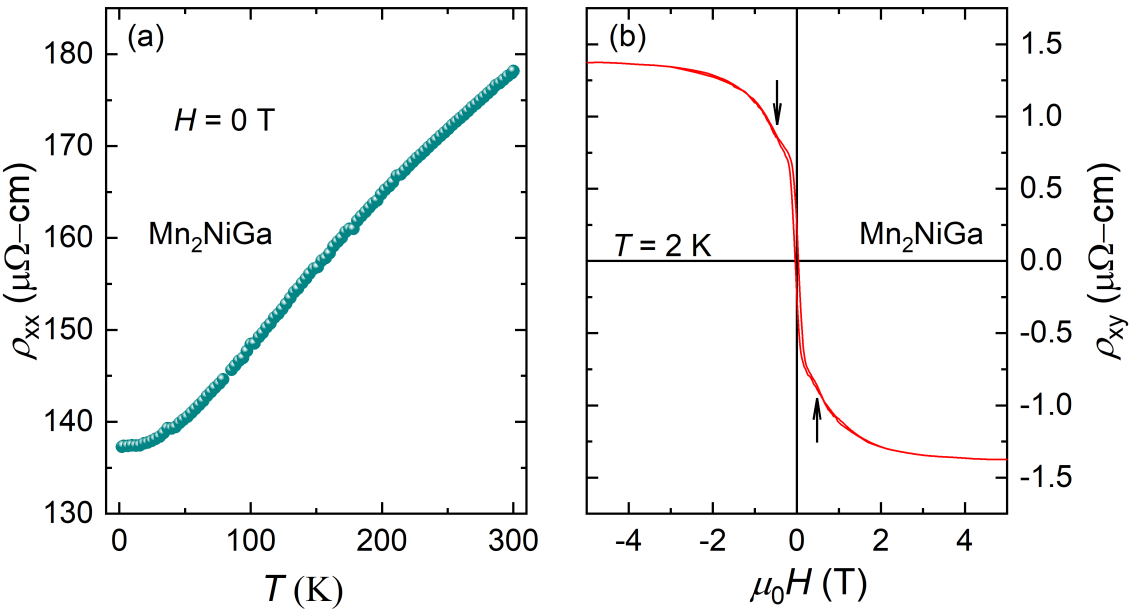

Figure 3.16: (Color online) (a) Temperature dependence of longitudinal resistivity $\rho_{xx}(T)$ for Mn_2NiGa. (b) The Hall resistivity as a function of magnetic field $\rho_{xy}(H)$ for Mn_2NiGa at 2 K. The anamolies in these curves are marked by black arrows.

sion for the total Hall resistivity can be rewritten as $\rho_{xy}(H) = R_0H + R_sM + \rho^T = R_0H + b\rho_{xx}^2M + \rho^T$. In this expression, the contribution due to the intrinsic mechanism of anomalous Hall resistivity, which is proportional to ρ_{xx}^2, is only considered. The contributions from the extrinsic mechanisms like skew scattering and side jumps to the anomalous Hall effect are neglected as the longitudinal conductivity of present samples (σ_{xx}=$1/\rho_{xx}$≈10^4 $\Omega^{-1}cm^{-1}$) falls under the category of moderate conductivity regime ($10^4 < \sigma_{xx}$ $(\Omega^{-1}cm^{-1}) < 10^6$). At very high fields the sample enters into the field polarized state, and hence the contribution of ρ^T to the total Hall resistivity can be ignored safely. Hence, the total Hall resistivity of the system at high fields can be expressed as $\rho_{xy}(H) = R_0H + b\rho_{xx}^2M$ or, $\rho_{xy}(H)/H = R_0 + b\rho_{xx}^2M/H$. The R_0 and b can be evaluated from the straight line fitting between the $\rho_{xy}(H)/H$ vs. ρ_{xx}^2M/H curve at high fields. Using the R_0 and b in the total Hall resistivity expression, the contributions due to the normal Hall resistivity and anomalous Hall resistivity are evaluated over all field regimes ($\mp$5 T≤H≤$\pm$5 T). Now onwards this contribution is refereed as calculated Hall resistivity. After deducing the calculated

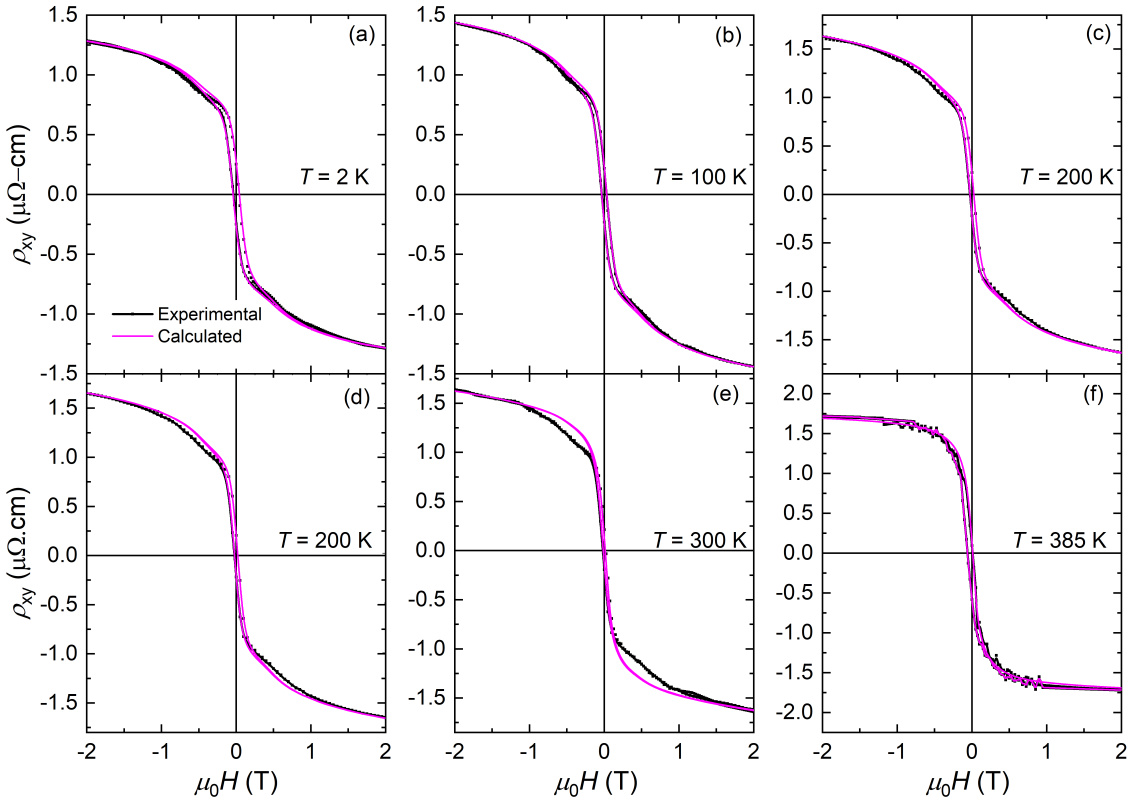

Figure 3.17: (Color online) (a)-(f) The experimental Hall resistivity, $\rho_{xy}(H)$, (black color symbol) fitted with calculated Hall resistivity as a function of magnetic field (magenta color line) for Mn_2NiGa from $T = 2$ K to $T = 380$ K.

Hall resistivity, the experimental Hall resistivity (black color symbol) is fitted with the calculated Hall resistivity curve (magenta color) as presented in Fig. 3.17 for Mn_2NiGa. It can be clearly seen from Fig. 3.17(a)-(e) that a substantial difference between the experimental and calculated Hall resistivity appears around a certain field region where the anomalies in magnetic and Hall transport data are present for $T = 2$ K to $T = 300$ K. At $T = 380$ K, no difference between the experimental and the calculated Hall resistivity curve is found. To obtain the extra-contribution of Hall resistivity, the contribution of calculated Hall resistivity is deducted from the experimental Hall resistivity. The plots for the extracted component of Hall resistivity, ρ^T, at different temperatures are presented in Fig. 3.18. The peak value of ρ^T for Mn_2NiGa continuously increases with increasing temperature and finally attains a maximum value of about 150 nΩ-cm at $T = 300$ K. Nearly zero value of ρ^T is obtained for $T > 300$ K. It is important to mention here that this kind of

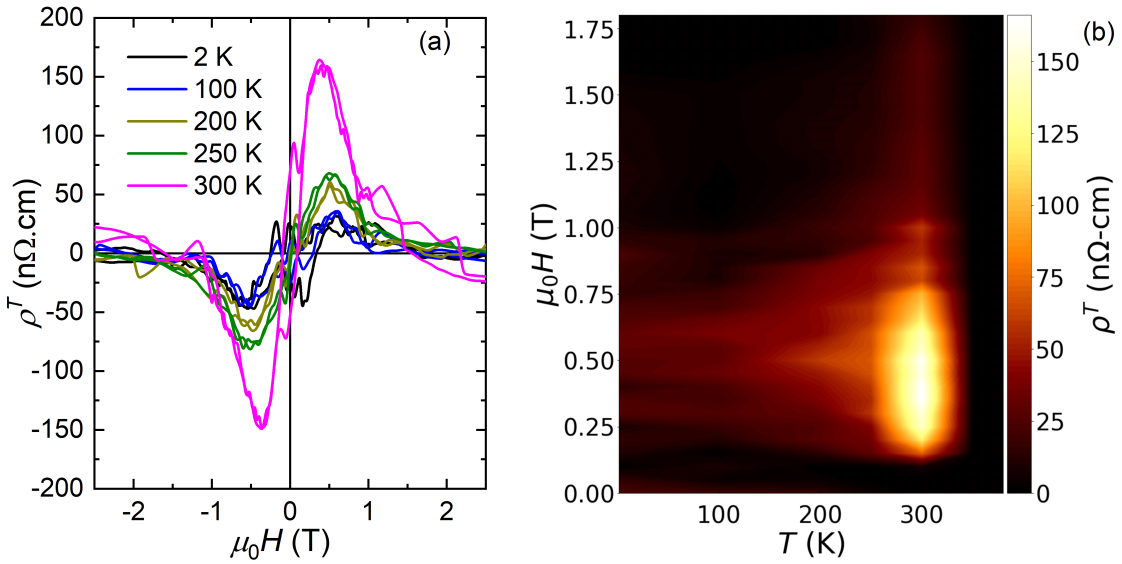

Figure 3.18: (Color online) (a) The topological Hall resistivity, ρ^T, at different temperatures for Mn_2NiGa, (b) The H-T phase diagram for Mn_2NiGa sample based on the topological Hall resistivity measurements showing the evolution of ρ^T with respect to the magnetic field (H) and temperature (T).

hump like signal in Hall resistivity, known as topological Hall resistivity, has been observed in the skyrmion phase of different suitable magnetic materials [13, 23, 24, 25, 26, 27]. Therefore, the finite value of ρ^T along with the anomaly in the magnetic measurements strongly suggest the presence of skyrmion like topological magnetic object in Mn_2NiGa system.

It is seen that a finite value of ρ^T is obtained when the tetragonal crystal phase is dominant in the system (T$\leq$300 K), on the other hand, the ρ^T value goes to zero when the system enters into the cubic dominated phase (T>300 K). Exactly same kind of trend is observed in the anomaly found in the dc hysteresis and ac susceptibility measurements. Hence, the magnetization, ac susceptibility and Hall transport data firmly support the presence of topological magnetic objects like skyrmions in the low temperature tetragonal phase of Mn_2NiGa system. However, the D_{2d} class of crystal symmetry of the low temperature tetragonal phase of Mn_2NiGa allows the formation of antiskyrmions rather than skyrmions in the system. The large value of ρ^T at relatively high temperature could be possibly referred to the enhancement of the nucleation probability of antiskyrmions due to the thermal fluctuation at high

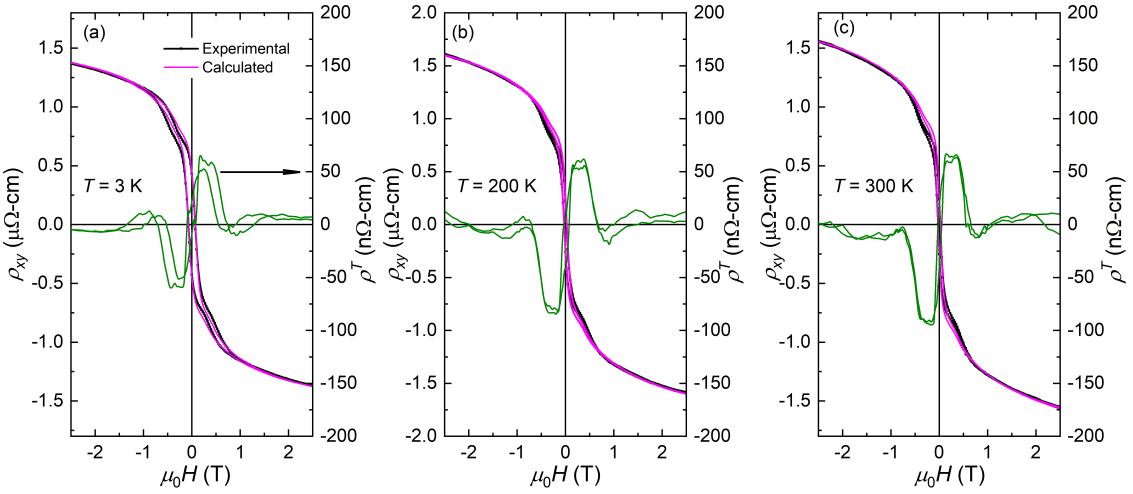

Figure 3.19: (Color online) (a) Field dependence of experimental Hall resistivity (black lines) along with the calculated Hall resistivity (magenta lines) at different temperatures for $Mn_{2.05}NiGa_{0.95}$. The calculated topological Hall resistivity is shown as olive lines.

temperatures.

The field dependence of experimental Hall resistivity curves $[\rho_{xy}(H)]$ for $Mn_{2.05}NiGa_{0.95}$ measured at different temperatures are presented as black lines in Fig. 3.19. As it can be seen, $Mn_{2.05}NiGa_{0.95}$ exhibits dip kind of anomaly in the $\rho_{xy}(H)$ curve for $H = 0.40$ T. The calculated Hall resistivity at each temperature estimated by the above discussed method are plotted as magenta lines in Fig. 3.19. Like the parent Mn_2NiGa sample, a difference between the experimental and calculated Hall resistivity curves is also found around the anomaly region of the $\rho_{xy}(H)$ curves. After the subtraction of the calculated Hall resistivity from the experimental data, the extracted topological Hall resistivity, ρ^T, curves are illustrated by olive lines (y-axis) in Fig. 3.19. The maximum value of ρ^T is found to be 70 nΩ-cm at $T = 300$ K.

Figure 3.20 shows the field dependent experimental Hall resistivity $[\rho_{xy}(H)]$ curves (black solid line) and the corresponding calculated Hall resistivity curves (presented by magenta line) at different temperatures for $Mn_{2.1}NiGa_{0.9}$. The experimental $\rho_{xy}(H)$ data also display dip kind of anomaly around $H = 0.60$ T. A clear-cut difference between the experimental and calculated Hall resistivity is also observed around for temperatures $T = 2$ K to $T = 380$ K. The corresponding ex-

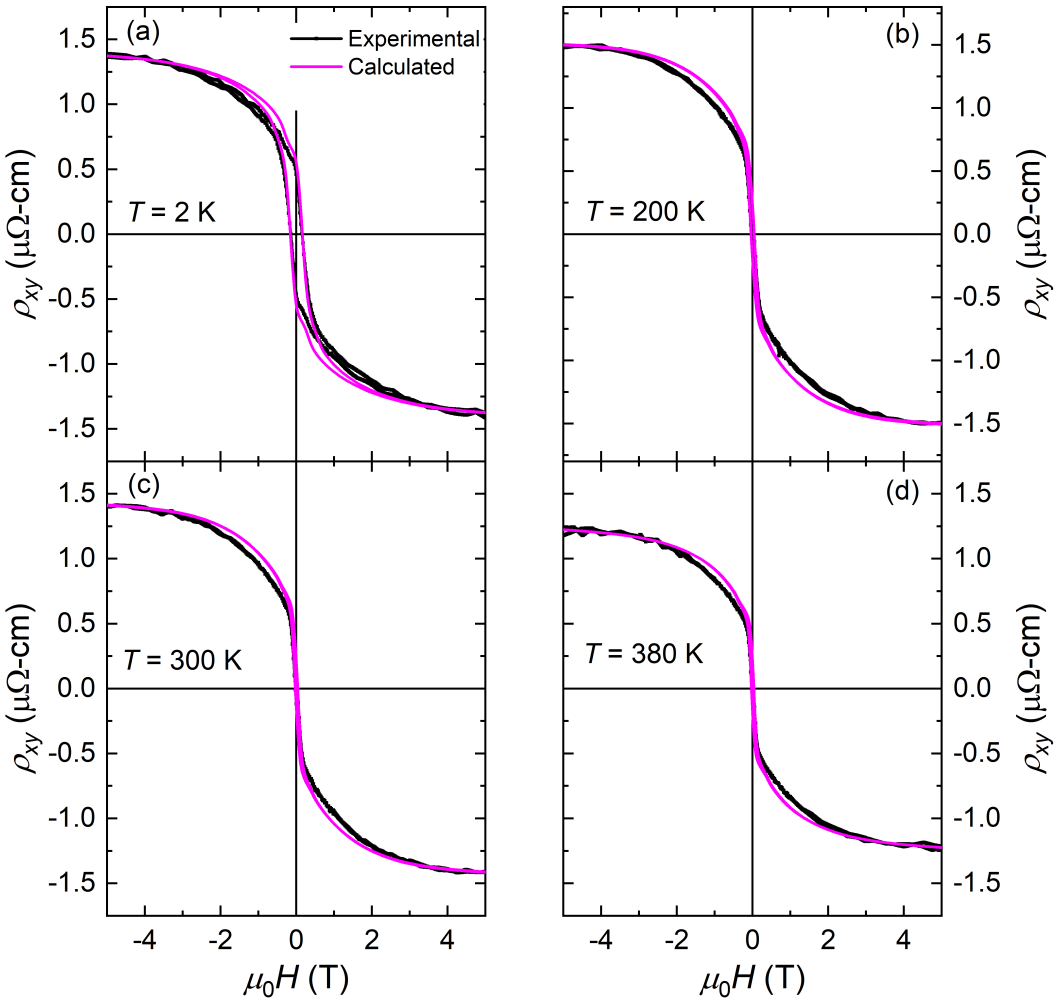

Figure 3.20: (Color online) (a) The experimental Hall resistivity, $\rho_{xy}(H)$, (black color symbol) fitted with calculated Hall resistivity as a function of magnetic field (magenta color line) for $Mn_{2.1}NiGa_{0.9}$ from $T = 2$ K to $T = 380$ K.

tracted topological Hall resistivity, ρ^T, curves are plotted for each temperature in Fig. 3.21 (a). The average maximum value of ρ^T is calculated to be about 100 nΩ-cm. The strong topological Hall effect signal along with the peak/dip kind of behavior in ac susceptibility and dc hysteresis measurements categorically suggest the presence of antiskyrmion phase in the $Mn_{2.1}NiGa_{0.9}$ sample. Figure 3.21 (b) shows the H vs. T phase diagram for $Mn_{2.1}NiGa_{0.9}$. It can be seen from this H-T phase diagram that the finite value of ρ^T exist up to $H \leq \pm$ 3 T at all measured temperatures from $T = 2$ K to $T = 380$ K. The present results indicate the presence of antiskyrmion phase at all measured temperature range up to high magnetic fields

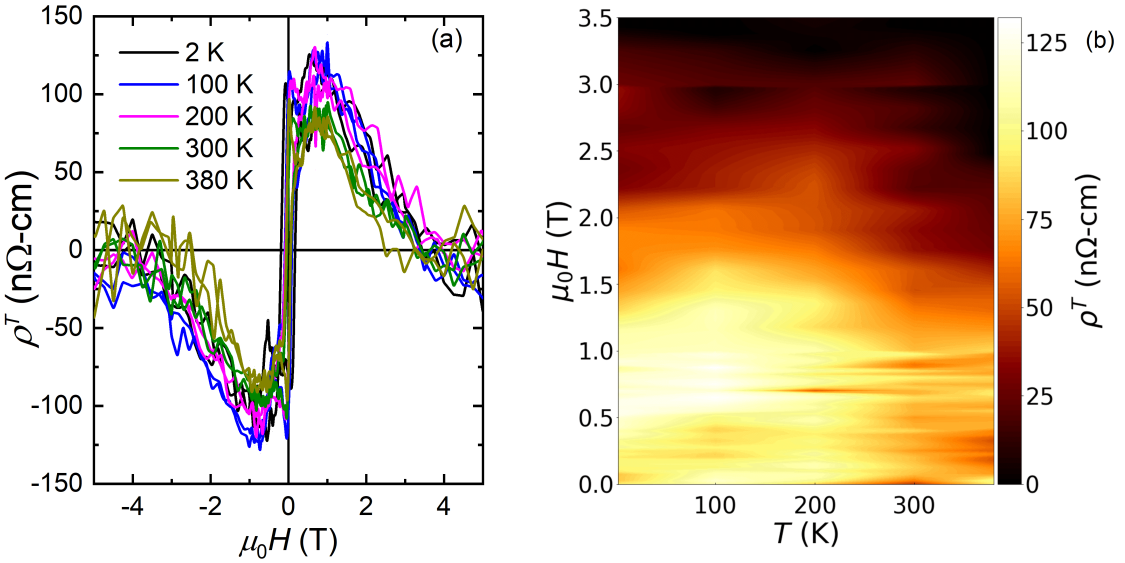

Figure 3.21: (Color online) (a) The topological Hall resistivity, ρ^T, curves at various temperature for $Mn_{2.1}NiGa_{0.9}$. (b) The H-T phase diagram for $Mn_{2.1}NiGa_{0.9}$ sample based on the topological Hall resistivity measurements showing the evolution of ρ^T with respect to the magnetic field (H) and temperature (T).

in $Mn_{2.1}NiGa_{0.9}$.

In conclusion, a large topological Hall effect is revealed in the tetragonal phase of $Mn_{2+x}NiGa_{1-x}$ samples. The emergence of large topological Hall effect is attributed to the existence of antiskyrmion phase in the D_{2d} symmetric $Mn_{2+x}NiGa_{1-x}$ materials. The hall resistivity data is also supported by the finding of anomalies in the dc hysteresis and ac susceptibility measurements. For Mn_2NiGa, the antiskyrmion phase sustains up to only room temperature, whereas, $Mn_{2.1}NiGa_{0.9}$ exhibits antiskyrmion phase over a wide temperature range up to the magnetic ordering temperature, $T = 550$ K. The existence of antiskyrmion phase above the room temperature makes the Mn-Ni-Ga alloys as a potential antiskyrmion hosting material for the future racetrack memory device application.

Chapter 4

Tunable antiskyrmion phase in $Mn_{2+x}Ni_{1-x}Ga$ tetragonal Heusler system

In the previous chapter, the existence of antiskyrmion phase is already demonstrated in Mn_2NiGa sample by means of magnetic and Hall transport measurements. For any future spintronics application, it is necessary to stabilize small size antiskyrmions in a wider temperature and magnetic field range. All these properties can be easily accomplished through suitable modification of the strength of different energy contributions, such as exchange interaction, DM interaction, and magneto-crystalline anisotropy. The exchange coupling strength of a system depends on the bond length and the electronic filling in band, whereas, the DM interaction and magneto-crystalline anisotropy rely upon the strength of the spin-orbit coupling (SOC). This kind of modification can be easily achieved by tuning the material parameters. In this prospect, a series of $Mn_{2+x}Ni_{1-x}Ga$ (x = 0.0, 0.10, 0.13, 0.16, 0.20, 0.25 and 0.28) samples are prepared using the arc-melting furnace as discussed in Chapter-1. The structural and compositional properties of these samples are analyzed through XRD, FESEM and EDS measurements. A detatied magnetic properties and Hall transport studies of theses samples are presented here. To better

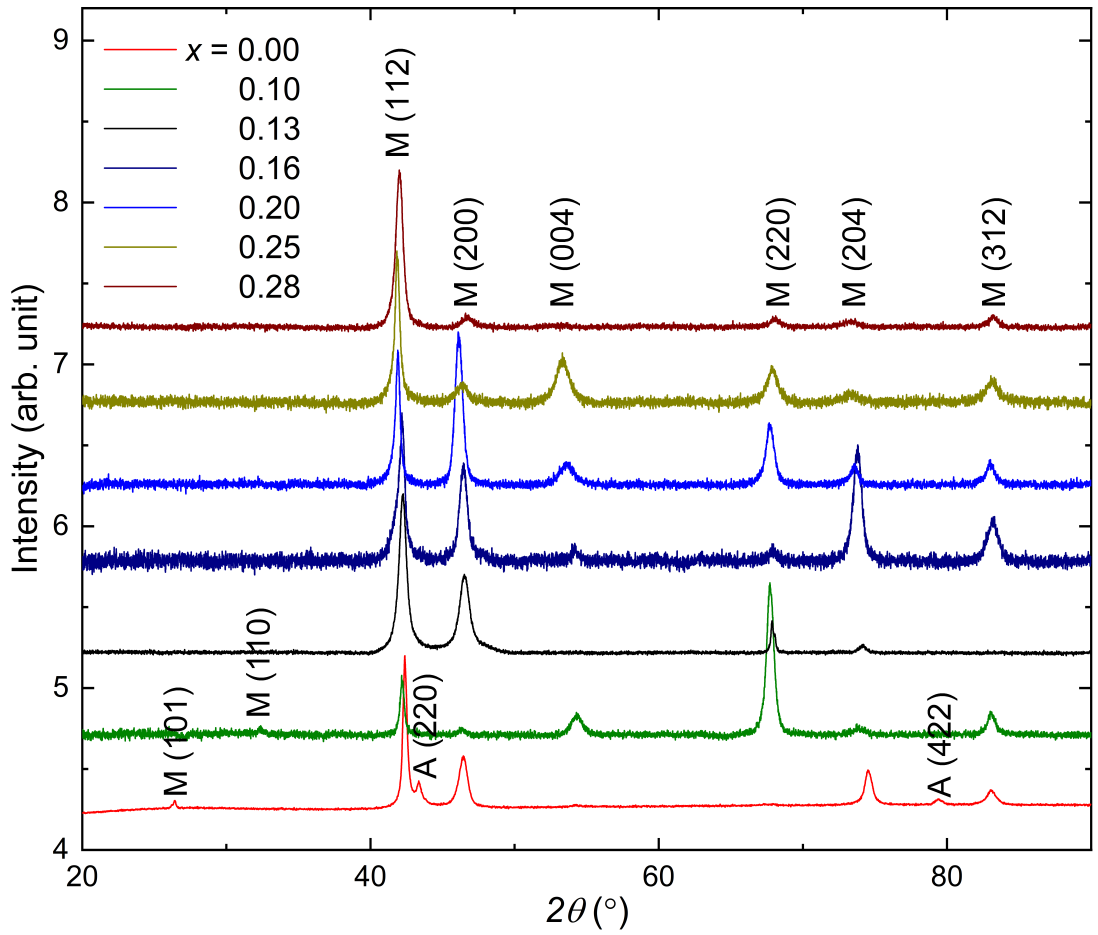

Figure 4.1: (Color online) The XRD patterns for the $Mn_{2+x}Ni_{1-x}Ga$ (x = 0.0, 0.10, 0.13, 0.16, 0.20, 0.25 and 0.28) samples at T = 300 K. Here, the symbols M and A stand for the peak corresponding to the martensite and austenite phase, respectively.

understand the experimental results, a detailed micro-magnetic simulation is also carried out.

4.1 Sample characterization

The structural property of the $Mn_{2+x}Ni_{1-x}Ga$ (x = 0.0, 0.10, 0.13, 0.16, 0.20, 0.25 and 0.28) samples is analyzed through XRD measurements. The compositional homogeneity is verified by FESEM and EDS measurements.

Table 4.1: The lattice parameters for $Mn_{2+x}Ni_{1-x}Ga$ samples.

Sample	a	b	c	c/a
$Mn_{2.1}Ni_{0.9}Ga$	3.905	3.905	6.750	1.7286
$Mn_{2.13}Ni_{0.87}Ga$	3.908	3.908	6.765	1.7310
$Mn_{2.16}Ni_{0.84}Ga$	3.9105	3.9105	6.780	1.7391
$Mn_{2.20}Ni_{0.80}Ga$	3.920	3.920	6.850	1.7475
$Mn_{2.25}Ni_{0.75}Ga$	3.915	3.915	6.865	1.75351
$Mn_{2.28}Ni_{0.72}Ga$	3.895	3.895	6.878	1.7659

4.1.1 XRD measurements of $Mn_{2+x}Ni_{1-x}Ga$

Room temperature XRD patterns for the $Mn_{2+x}Ni_{1-x}Ga$ (x = 0.0, 0.10, 0.13, 0.16, 0.20, 0.25 and 0.28) samples are plotted in Fig. 4.1. It is found that the XRD pattern for $x \geq 0.1$ transforms into pure tetragonal phase with space group I-4m2 from the mix-structural phase of tetragonal (space group: I-4m2) and cubic phase (space group: F-4m3) as found earlier for the Mn_2NiGa parent compound. For $x \geq 0.1$, the Ni atoms and Ga atoms occupy the 2d (0.0, 0.50, 0.75) and 2a (0.0, 0.0, 0.0) wycoff positions, respectively, whereas, the Mn atoms sit in the 2b (0.0, 0.0, 0.50) and 2c (0.0, 0.50, 0.25) wycoff positions. The lattice parameters for each sample are tabulated in Table 4.1. As it can be found, the lattice parameter c increases monotonically with increasing x in $Mn_{2+x}Ni_{1-x}Ga$, whereas, a does not show any significant change with x. Obviously, the tetragonality represented by c/a also increases with x.

4.1.2 FESEM and EDS measurements for $Mn_{2+x}Ni_{1-x}Ga$

To check the compositional homogeneity, the FESEM measurements are performed on the $Mn_{2+x}Ni_{1-x}Ga$ sample as shown in Figure 4.2. The homogeneous contrast of these images confirms the formation of single compositional phase for all the $Mn_{2+x}Ni_{1-x}Ga$ samples. The exact stoichiometry of the samples is studied with

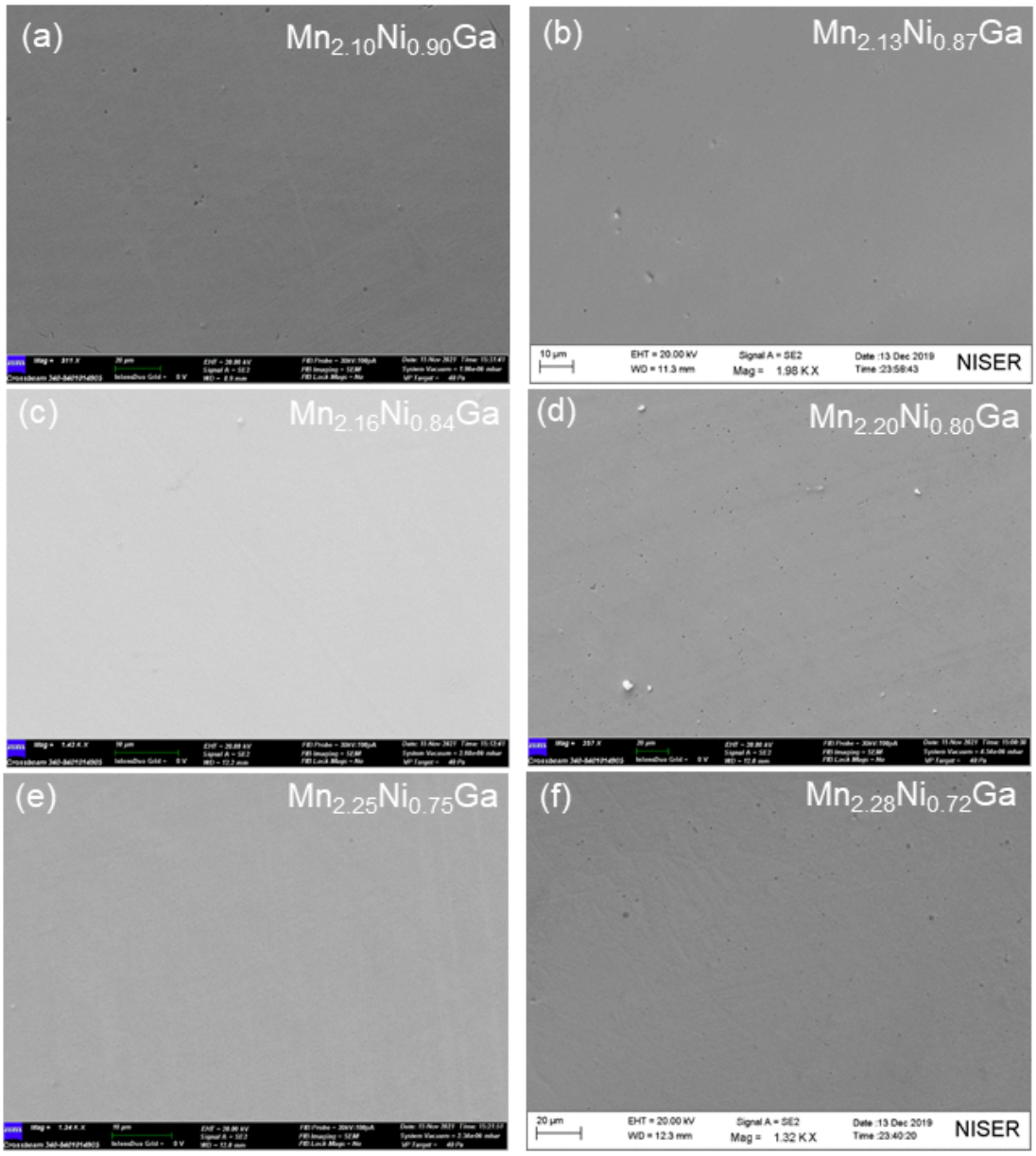

Figure 4.2: (Color online) The FESEM images for (a) $Mn_{2.1}Ni_{0.9}Ga$, (b)$Mn_{2.13}Ni_{0.87}Ga$, (c) $Mn_{2.16}Ni_{0.84}Ga$, (d) $Mn_{2.20}Ni_{0.80}Ga$, (e) $Mn_{2.25}Ni_{0.75}Ga$ and (f) $Mn_{2.28}Ni_{0.72}Ga$.

help of the EDS measurement. The EDS results given in Table 4.2 vindicate the homogeneous nature of these samples. As it can be seen, the actual composition of each sample approximately matches with the initial composition.

Table 4.2: The EDS results for $Mn_{2+x}Ni_{1-x}Ga$ samples.

Initial composition	EDS composition
$Mn_{2.1}Ni_{0.9}Ga$	$Mn_{2.103}Ni_{0.895}Ga_{1.004}$
$Mn_{2.13}Ni_{0.87}Ga$	$Mn_{2.128}Ni_{0.869}Ga_{1.003}$
$Mn_{2.16}Ni_{0.84}Ga$	$Mn_{2.172}Ni_{0.841}Ga_{0.987}$
$Mn_{2.20}Ni_{0.80}Ga$	$Mn_{2.193}Ni_{0.798}Ga_{1.009}$
$Mn_{2.25}Ni_{0.75}Ga$	$Mn_{2.268}Ni_{0.754}Ga_{0.978}$
$Mn_{2.28}Ni_{0.72}Ga$	$Mn_{2.274}Ni_{0.713}Ga_{1.023}$

4.2 Magnetic measurements for $Mn_{2+x}Ni_{1-x}Ga$

To investigate the magnetic properties of the present samples, temperature dependence of magnetization measurement is carried out on the $Mn_{2+x}Ni_{1-x}Ga$ samples from $T = 2$ K to $T = 400$ K at fixed magnetic field of 0.1 T in *field cooling* (FC) and *field heating* (FH) protocols [Figs. 4.3 (a)-(g)]. As discussed in Chapter-3, a thermal hysteresis between the FC and FH $M(T)$ curves is prominently seen for the Mn_2NiGa sample around $T = 300$ K [Fig. 4.3 (a)]. Similar kind of thermal hysteresis is also observed for $Mn_{2.10}Ni_{0.90}Ga$, but the transition temperature corresponding to the thermal hysteresis shifts to relatively high temperature of about 350 K, as shown in Fig. 4.3(b). The aforementioned transition associated with the thermal hysteresis is absent below 400 K for $x \geq 0.13$, as shown in Fig. 4.3(c)-(g). The high temperature $M(T)$ data for some specific compositions are also recorded from $T =$ 400 K to $T = 750$ K, as plotted in Fig. 4.3(h). The magnetic ordering temperature of all the samples lies between $T = 600$ K and $T = 650$ K. Moreover, any kind of structural transition is not found from the high temperature measurements.

The field dependence of magnetization, $M(H)$, measurements are performed at different temperatures ranging from $T = 3$ K to $T = 300$ K for $Mn_{2.1}Ni_{0.9}Ga$ as shown in Fig. 4.4. The saturation magnetic moment for the $Mn_{2.1}Ni_{0.9}Ga$ sample is found to be around 1.12 μ_B/f.u. at $T = 3$ K. The presence of a dip kind of features,

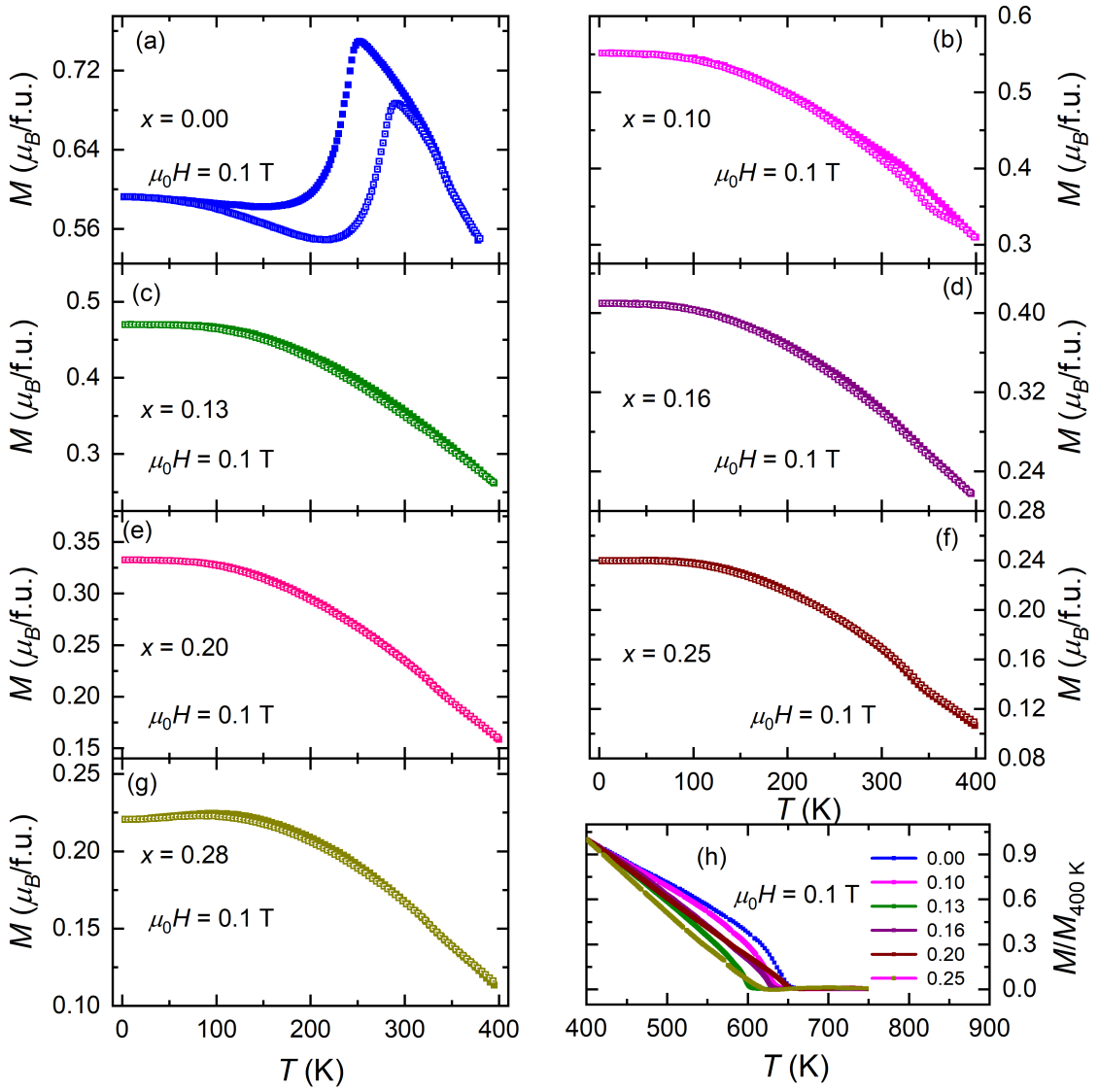

Figure 4.3: (Color online) The temperature dependent magnetization, $M(T)$, curves for the $Mn_{2+x}Ni_{1-x}Ga$ samples measured in $H = 0.1$ T for (a)-(f) $T = 2$ K to 400 K, and (h) $T = 400$ K to 750 K. The FC and FH $M(T)$ curves are represented by the solid and open symbols, respectively.

marked by arrows in Fig. 4.4(a)-(d), can be distinctly seen around $H = 0.6$ T for all measured temperatures. Figure 4.5 shows the $M(H)$ for $Mn_{2.13}Ni_{0.87}Ga$, which exhibits a saturation magnetic moment of about 0.90 μ_B/f.u. at $T = 3$ K. Most importantly, instead of a single peak/dip kind transition observed in other samples, the $M(H)$ data at 3 K for $Mn_{2.13}Ni_{0.87}Ga$ exhibits three field induced transitions at 0.3 T, 1 T, and 1.8 T, marked by ⋆, arrow, and ⧫, respectively [Fig. 4.5(a)]. These

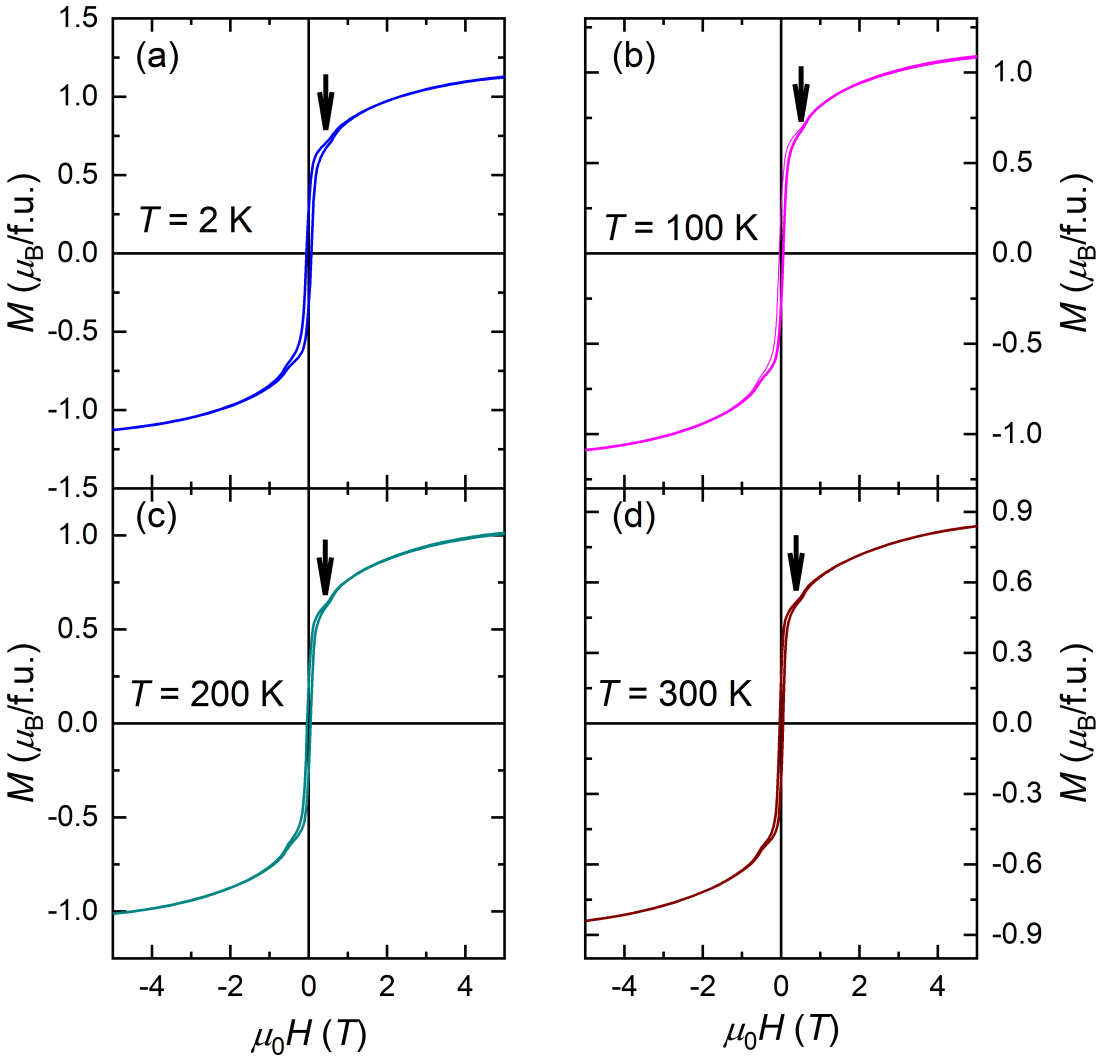

Figure 4.4: (Color online) Field dependent magnetization curves, $M(H)$, curves at different temperatures for $Mn_{2.1}Ni_{0.9}Ga$. The arrows indicate the presence of anomaly in these curves.

unusual transition features in the $M(H)$ loop are also present at other temperatures including at room temperature, as shown in Fig. 4.5 (b)-(f). The $M(H)$ loops measured at different temperatures for the $Mn_{2.16}Ni_{0.84}Ga$ sample are presented in Fig. 4.6. The saturation magnetic moment for the $Mn_{2.16}Ni_{0.84}Ga$ sample is found to be 0.82 μ_B/f.u. at $T = 3$ K. $Mn_{2.16}Ni_{0.84}Ga$ also exhibits multiple transitions in the $M(H)$ data as pointed by down and up arrows in Fig. 4.6. A further increase in the manganese concentration in $Mn_{2.20}Ni_{0.80}Ga$ results in a single kind of transition anomaly indicated by arrows in Fig. 4.7(a)-(b). The saturation magnetization

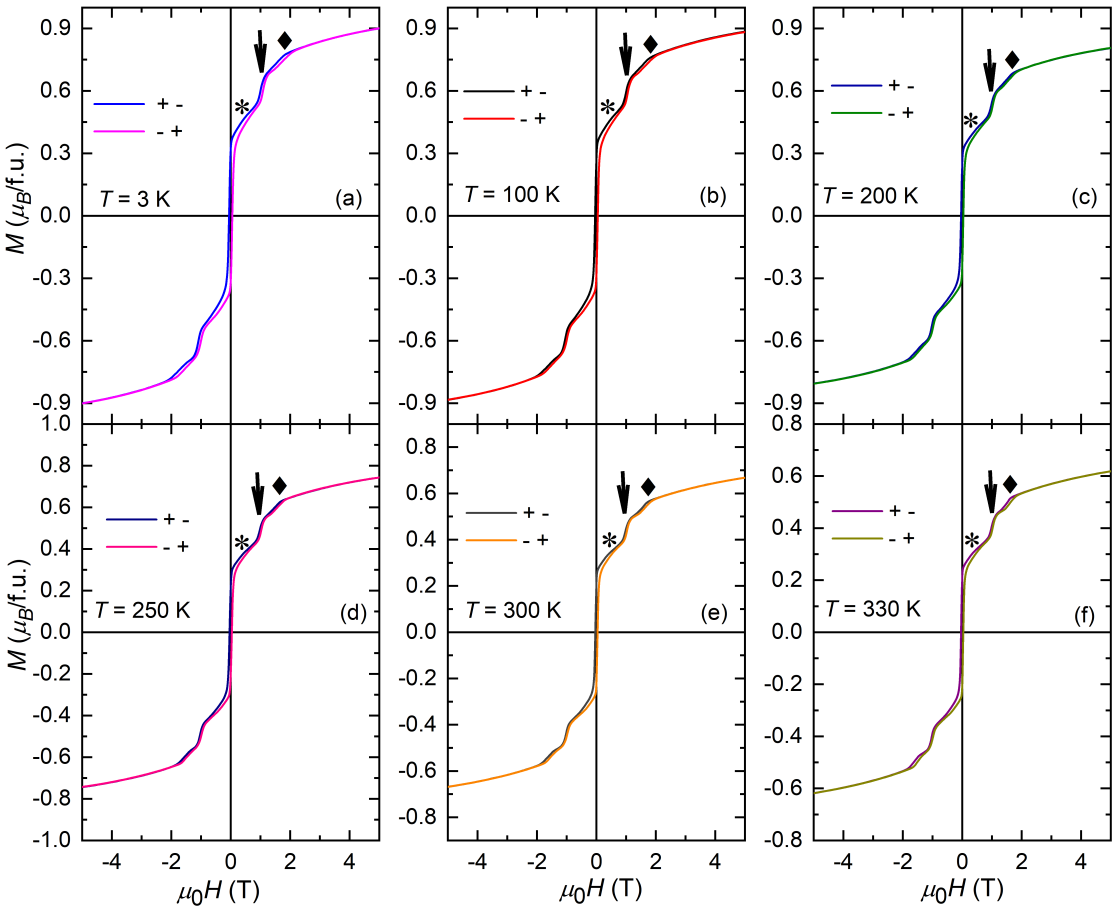

Figure 4.5: (Color online) $M(H)$ loops at different temperatures for $Mn_{2.13}Ni_{0.87}Ga$. Here, the anomalies in these curves are indicated by $*$, arrows, and ♦.

for $Mn_{2.20}Ni_{0.80}Ga$ further decreases to 0.64 μ_B/f.u. at 3 K. Figure 4.8(a)-(b) and Figure 4.8(c)-(d) show the $M(H)$ loops for $Mn_{2.25}Ni_{0.75}Ga$ and $Mn_{2.28}Ni_{0.72}Ga$, respectively. Interestingly, no peak/dip kind of transition anomaly is found in the $M(H)$ data for both the samples. Very small saturation magnetic moments of 0.50 μ_B/f.u. and 0.43 μ_B/f.u. are found for $Mn_{2.25}Ni_{0.75}Ga$ and $Mn_{2.28}Ni_{0.72}Ga$, respectively.

For the sake of comparison, the $M(H)$ curves at $T = 3$ K for all the $Mn_{2+x}Ni_{1-x}Ga$ samples are replotted in Fig. 4.9(a) and the corresponding variation of saturation magnetization with the composition is plotted in Fig. 4.9(b). It is seen that the saturation magnetization decreases continuously from 1.43 μ_B/f.u. for $x = 0.00$ to 0.43 μ_B/f.u. for $x = 0.28$ with the enhancement of the Mn concentration. The de-

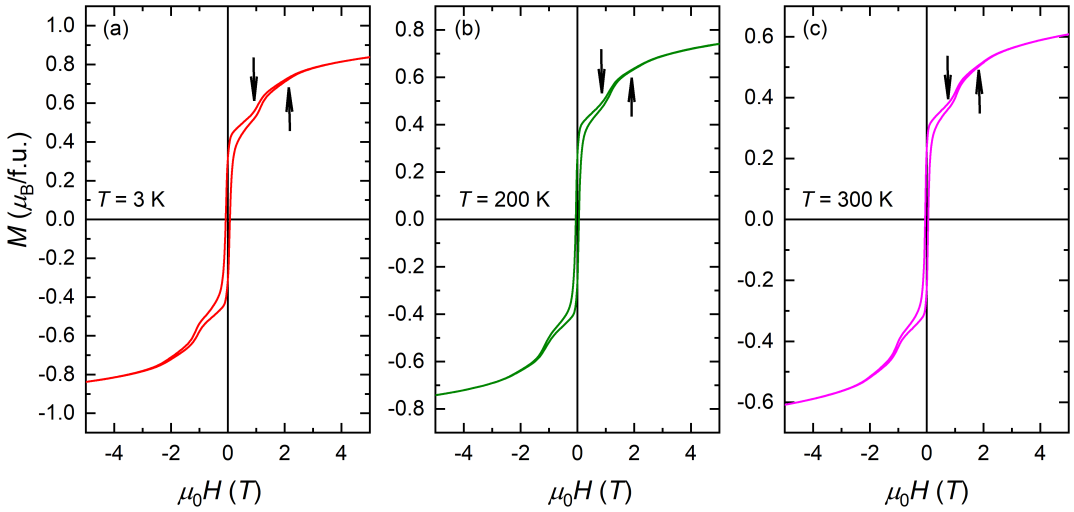

Figure 4.6: (Color online) $M(H)$ loops at different temperatures for $Mn_{2.16}Ni_{0.84}Ga$. Here, the anomalies in these curves are marked by down and up arrows.

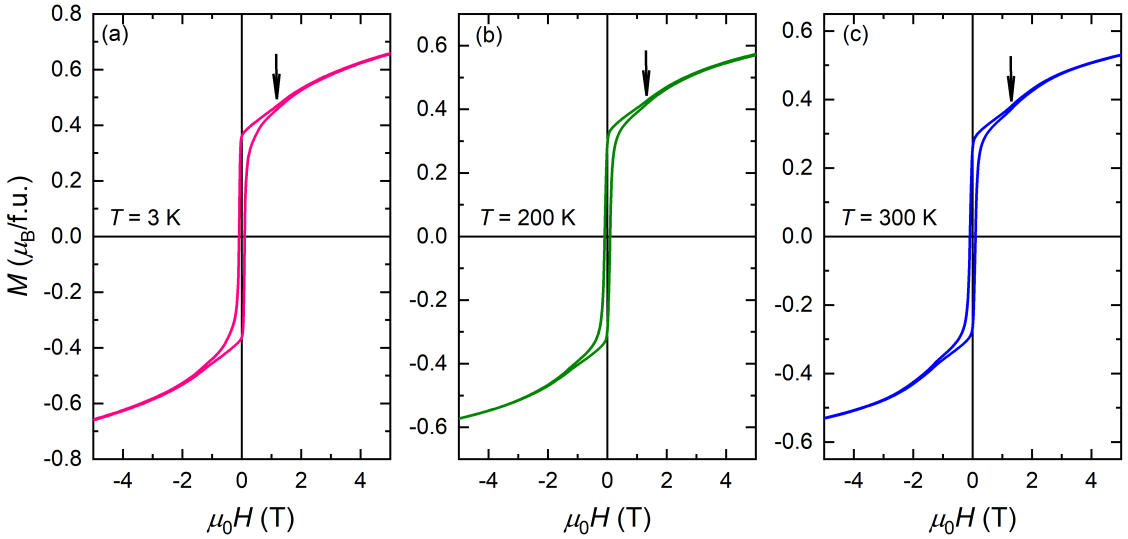

Figure 4.7: (Color online) $M(H)$ loops at different temperatures for $Mn_{2.20}Ni_{0.80}Ga$. The arrows represent the presence of anomaly in these curves.

creasing trend of magnetization with the composition can be understood as follows. It is well established that the Mn atoms are located at two separate lattice sites in case of Mn_2YZ system. The Mn atoms surrounded by octahedral environment at the Mn-Z planes exhibits a larger magnetic moment than that for the Mn atoms in the tetrahedral environment at the Mn-Y planes. The Mn atoms sitting in these two different sub-lattices are coupled antiferromagnetically. Since the extra Mn oc-

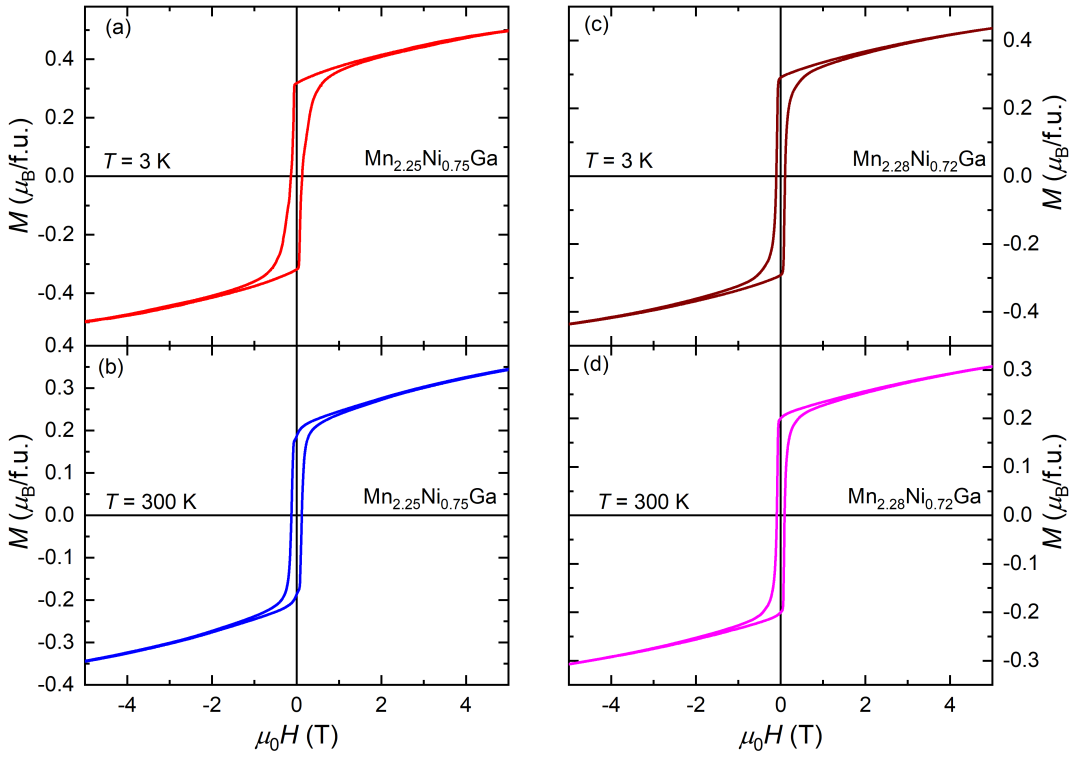

Figure 4.8: (Color online) Field dependence of magnetization, $M(H)$, at different temperatures for (a)-(b) $Mn_{2.25}Ni_{0.75}Ga$ and (c)-(d) $Mn_{2.28}Ni_{0.72}Ga$.

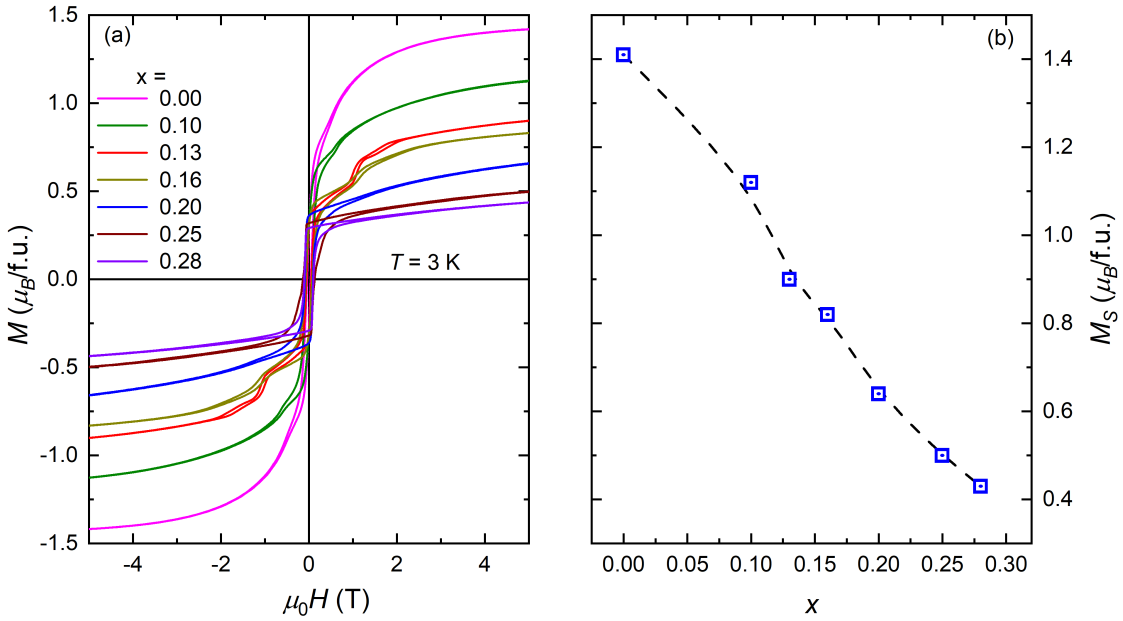

Figure 4.9: (Color online) (a) $M(H)$ loops measured at $T = 3$ K for $Mn_{2+x}Ni_{1-x}Ga$, (b) Variation of the saturation magnetization with the composition of the $Mn_{2+x}Ni_{1-x}Ga$ samples.

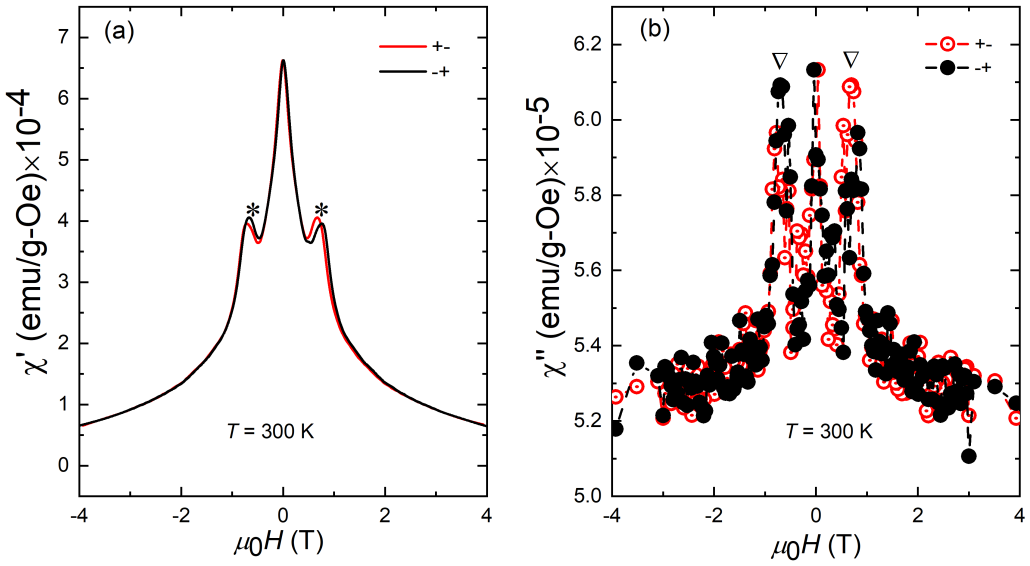

Figure 4.10: (Color online) Field dependence of (a) real part of ac susceptibility, $\chi'(H)$, (b) imaginary part of ac susceptibility $\chi''(H)$, measured at $T = 300$ K for $Mn_{2.1}Ni_{0.9}Ga$. The asterisk ($*$), $\bigtriangledown$ symbols indicate the presence of anomalies in these curve. The notations '+-' and '-+' represent the field sweeping from +5 T to -5 T and -5 T to +5 T, respectively.

cupy the Ni sites of the Mn-Ni basal planes, it gives a better compensation of the magnetic moments in the Mn-Ga planes, thereby, resulting in a net decrease in the magnetic moment of the system.

4.3 AC susceptibility measurements for $Mn_{2+x}Ni_{1-x}Ga$

To gain more information about the magnetic transition observed in the $M(H)$ measurements, ac susceptibility measurement is carried out on the $Mn_{2+x}Ni_{1-x}Ga$ samples. The field dependent real part of ac susceptibility, $\chi'(H)$, data measured at $T = 300$ K for $Mn_{2.1}Ni_{0.9}Ga$ is plotted in Fig. 4.10. As it can be seen, a peak/dip kind of transition around $H = \pm 0.6$ T (marked by $*$) appears with a significant hysteresis between the field increasing and decreasing curves.

Figure 4.11 shows the field dependence of $\chi'(H)$ data for $Mn_{2.13}Ni_{0.87}Ga$ at different temperatures. Most importantly, the $\chi'(H)$ data display peak/dip kind of anomalies for fields about 0.3 T (indicated by a down arrow), $H \approx 1$ T (marked by

$*$) and $H{\approx}2$ T (indicated by an up arrow). It is noticeable that all these transitions also exhibit a prominent hysteresis behavior in field increasing and decreasing curves. Like $Mn_{2.13}Ni_{0.87}Ga$, the $\chi'(H)$ data for $Mn_{2.16}Ni_{0.84}Ga$ also exhibit similar kind of anomalies in three different field regimes as marked an up arrow, $*$, and down arrow in Fig. 4.12. Increasing the Mn concentration results in the observation of weak transition anomalies in the $\chi'(H)$ curves except the low field transition at $H{\approx}0.3$ T for $Mn_{2.20}Ni_{0.82}Ga$, as shown in Fig. 4.13. Finally, theses anomalies completely disappear in the $\chi'(H)$ data for $Mn_{2.25}Ni_{0.75}Ga$ and $Mn_{2.28}Ni_{0.72}Ga$, as given in Fig. 4.14(a) and (c), respectively.

The presence of the transition anomaly around 1 T is also distinctly seen with the presence of hysteresis behavior between the field decreasing (open circle symbols) and increasing curves (solid circle symbols) in the imaginary part of the ac susceptibility, $\chi''(H)$, as indicated by $\bigtriangledown$ in Figs. 4.10, 4.11, 4.12, and 4.13 (right panels) for the $Mn_{2+x}Ni_{1-x}Ga$ samples (x = 0.10, 0.13, 0.16, and 0.20, respectively). It can be noted here that the lower field transitions could not be observed in the $\chi''(H)$ data as the magnitude of $\chi''(H)$ falls under the instrumental resolution limit. The presence of hysteresis around the anomaly regions in the $\chi'(H)$ as well as $\chi''(H)$ data suggests the first-order kind of transition.

As discussed previously, these transitions in the $\chi''(H)$, and $\chi''(H)$ measurements suggest the presence of skyrmion/antiskyrmion in the system. Therefore, the ac susceptibility measurements suggest a strong presence of antiskymion phase for $x{\leq}0.20$ samples. In contrast, no anomalies in the ac susceptibility data signify the absence of the antiskyrmion phase for x=0.25, and 0.28 samples.

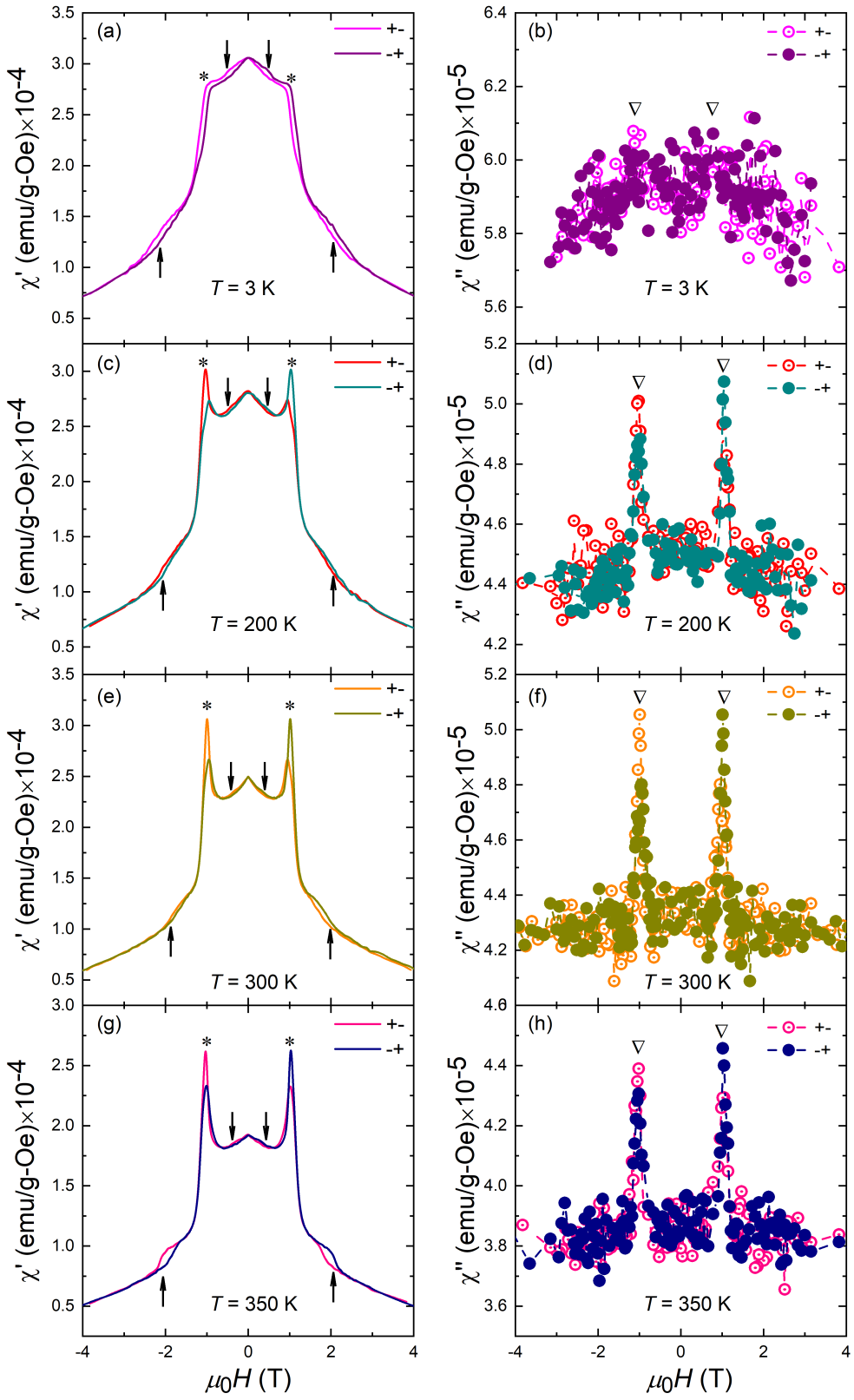

Figure 4.11: (Color online) Field dependent (a) real part of ac susceptibility χ' (H), (b) imaginary part of ac susceptibility χ'' (H), at different temperatures for $Mn_{2.13}Ni_{0.87}Ga$. The asterisk $(*)$ symbols, up arrows, down arrows, $\bigtriangledown$ symbols indicate the presence of anomalies in these curve. The notations '+-' and '-+' represent the field sweeping from +5 T to -5 T and -5 T to +5 T, respectively.

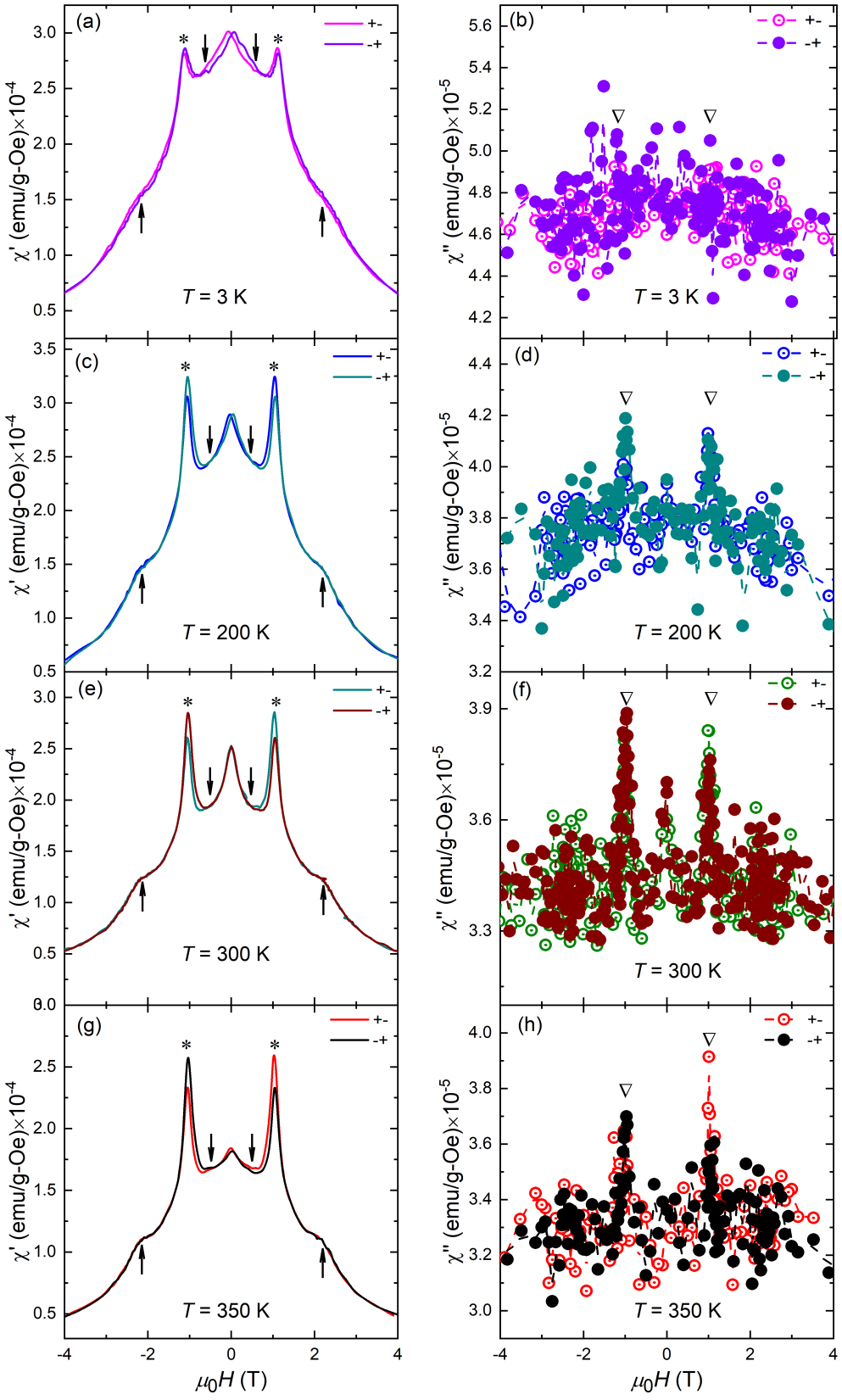

Figure 4.12: (Color online) Field dependence of (a) real part of ac susceptibility χ' (H), (b) imaginary part of ac susceptibility χ'' (H) at different temperatures for $Mn_{2.16}Ni_{0.84}Ga$. The asterisk $(*)$, up arrows, down arrows, $\bigtriangledown$ indicate the presence of anamolies in these curve. The notations '+-' and '-+' represent the field sweeping from +5 T to -5 T and -5 T to +5 T, respectively.

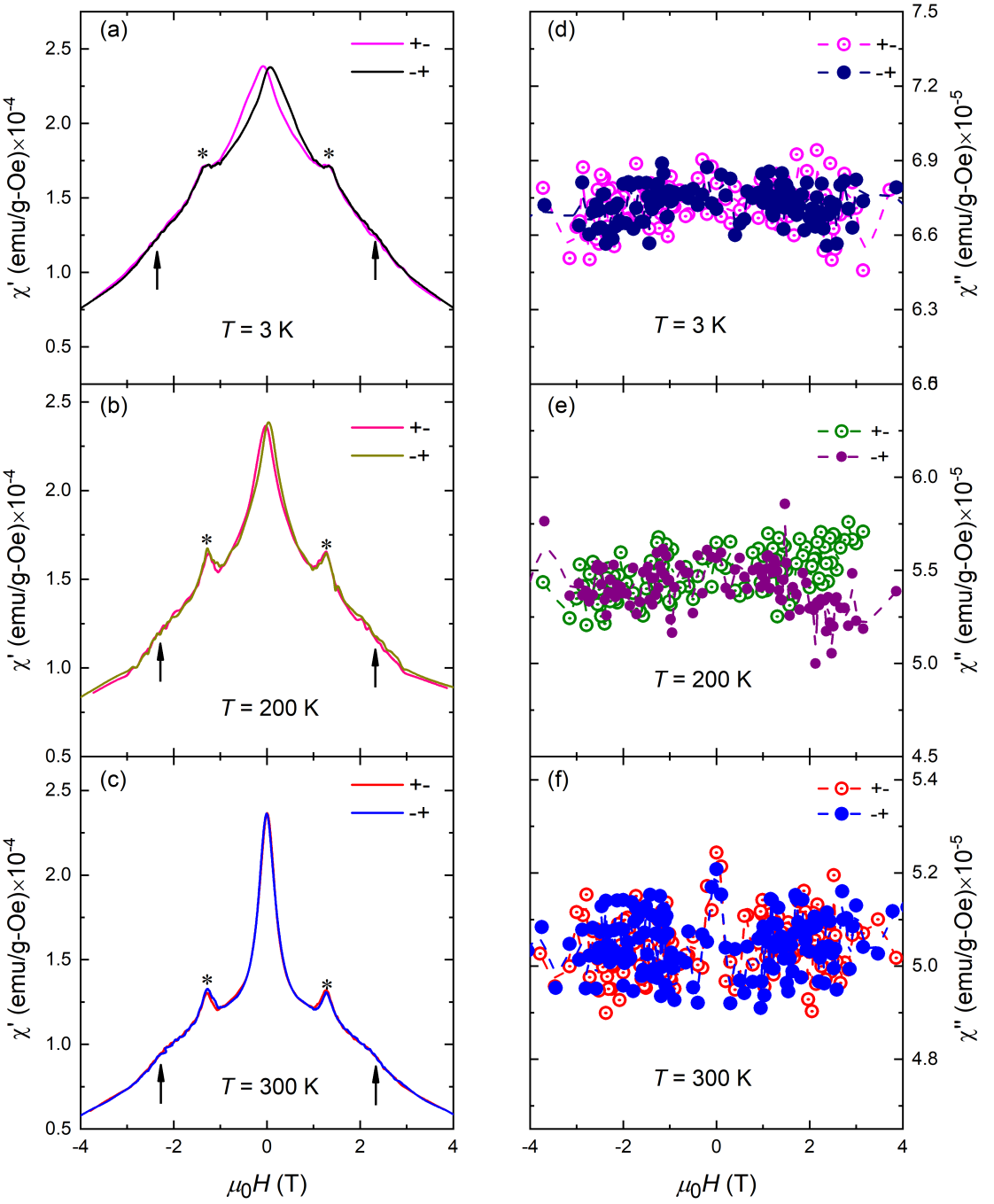

Figure 4.13: (Color online) Field dependent (a) real part of ac susceptibility χ' (H), (b) imaginary part of ac susceptibility χ'' (H), at different temperatures for $Mn_{2.20}Ni_{0.80}Ga$. The $*$ symbols, down arrows, $\bigtriangledown$ symbols indicate the presence of anomalies in these curves. The notations '+-' and '-+' represent the field sweeping from +5 T to -5 T and -5 T to +5 T, respectively.

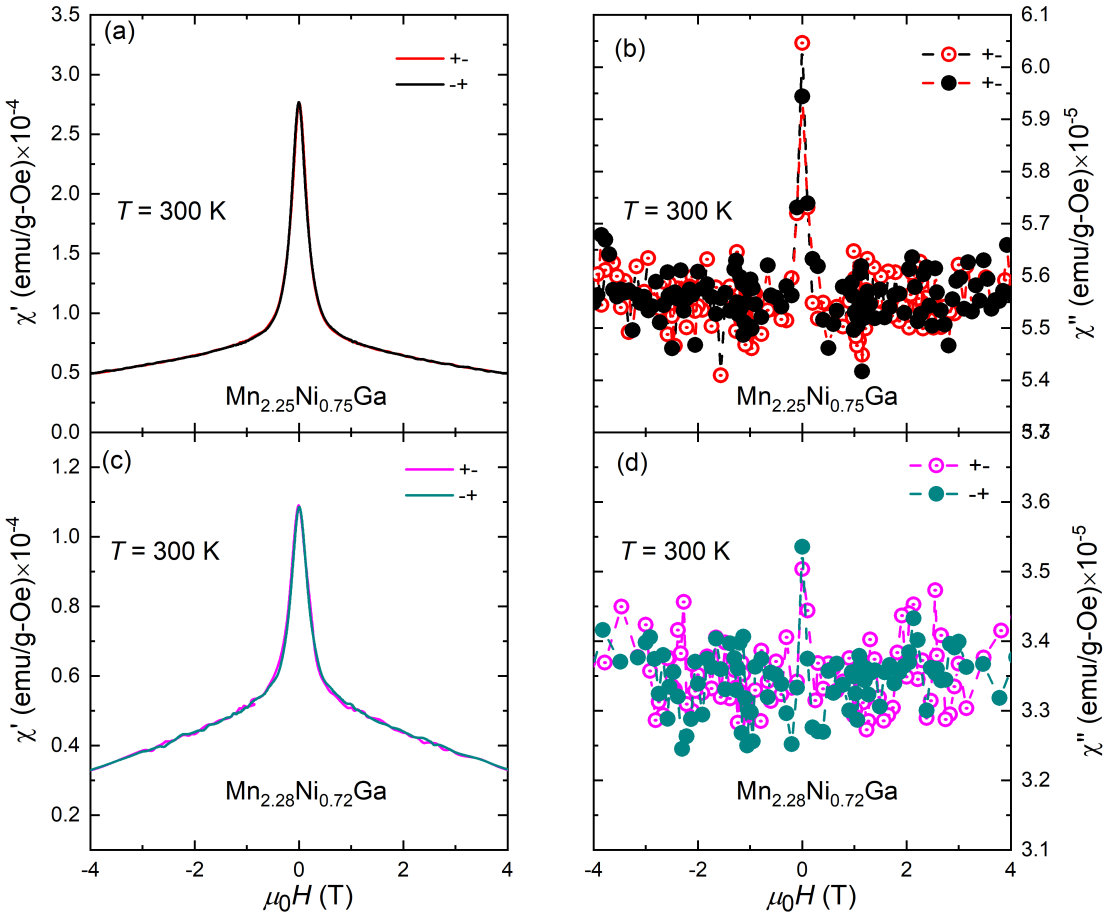

Figure 4.14: (Color online) Field dependent real part of ac susceptibility χ' (H) (a) $Mn_{2.25}Ni_{0.75}Ga$, and (b) $Mn_{2.28}Ni_{0.72}Ga$. Field dependent imaginary part of ac susceptibility χ'' (H), measured at $T = 300$ K for (c) $Mn_{2.25}Ni_{0.75}Ga$, and (d) $Mn_{2.28}Ni_{0.72}Ga$.

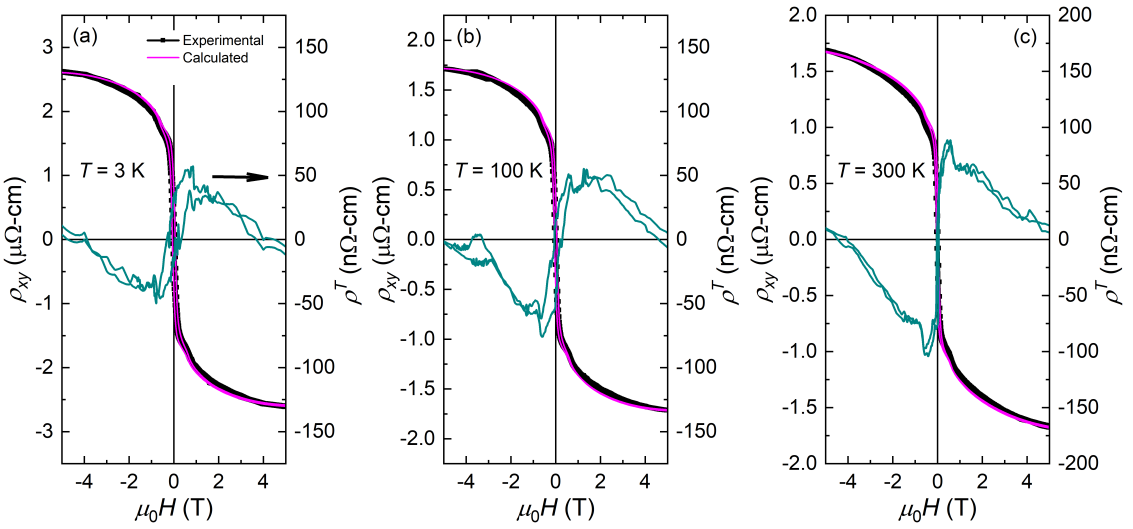

Figure 4.15: (Color online) Field dependence of experimental Hall resistivity (black lines) along with the calculated Hall resistivity (magenta lines) at different temperatures for $Mn_{2.10}Ni_{0.90}Ga$. The extracted topological Hall resistivity, ρ^T, is shown as dark cyan lines.

4.4 Electrical transport measurements for $Mn_{2+x}Ni_{1-x}Ga$

The existence of multiple field induced anomalies in the dc magnetization and ac susceptibility data inspire us to investigate the topological properties of the spin configuration present in the systems. For this purpose, the magneto-transport measurement is carried on the $Mn_{2+x}Ni_{1-x}Ga$ samples. The experimental Hall transport data for the $Mn_{2.10}Ni_{0.90}Ga$ sample is plotted by black solid line in Fig. 4.15 at T = 3 K, 100 K and 300 K. Like the Mn_2NiGa sample, an anomaly in the ρ_{xy} data is also seen around H = 0.6 T. To extract the topological Hall resistivity (ρ^T), the contribution due to normal and anomalous Hall effect (calculated Hall resistivity) is evaluated by adopting the similar method as discussed in the Chapter 3. The calculated Hall resistivity is plotted by magenta lines in Fig. 4.15. A clear difference between the two curves is also observed at all measured temperatures under certain range of magnetic fields. The extracted topological Hall resistivity, ρ^T, is obtained by subtracting the two curves, is illustrated by a dark cyan lines (right y-axis) in

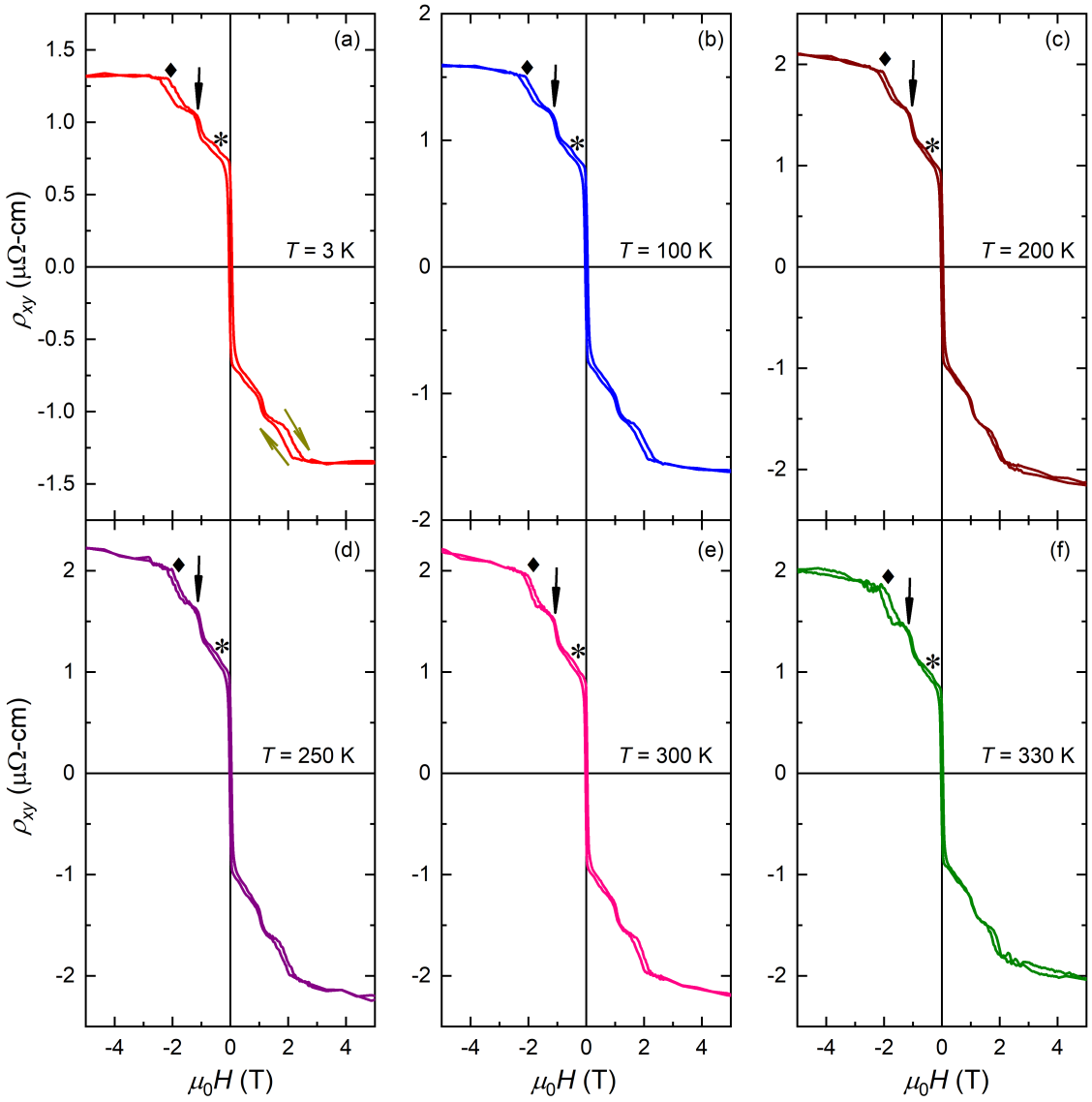

Figure 4.16: (Color online) Field dependent experimental Hall resistivity at different temperatures for $Mn_{2.13}Ni_{0.87}Ga$. The $*$ symbols, down arrows, and ♦ symbols indicate the presence of anamolies in these curve.

Fig. 4.15(a)-(c). It can be seen that the magnitude of ρ^T continuously increases with temperature as seen in the case of Mn_2NiGa. Finally, the ρ^T reaches 90 nΩ-cm at room temperature. It is interesting to mention here that unlike the single peak behavior for Mn_2NiGa, a soft double peak-like behavior appears in the ρ^T curve for $Mn_{2.10}Ni_{0.90}Ga$.

Figure 4.16 shows the field dependent Hall resistivity, $\rho_{xy}(H)$, plots for $Mn_{2.13}Ni_{0.87}Ga$ at different temperatures. Interestingly, three transition anomalies are found in the

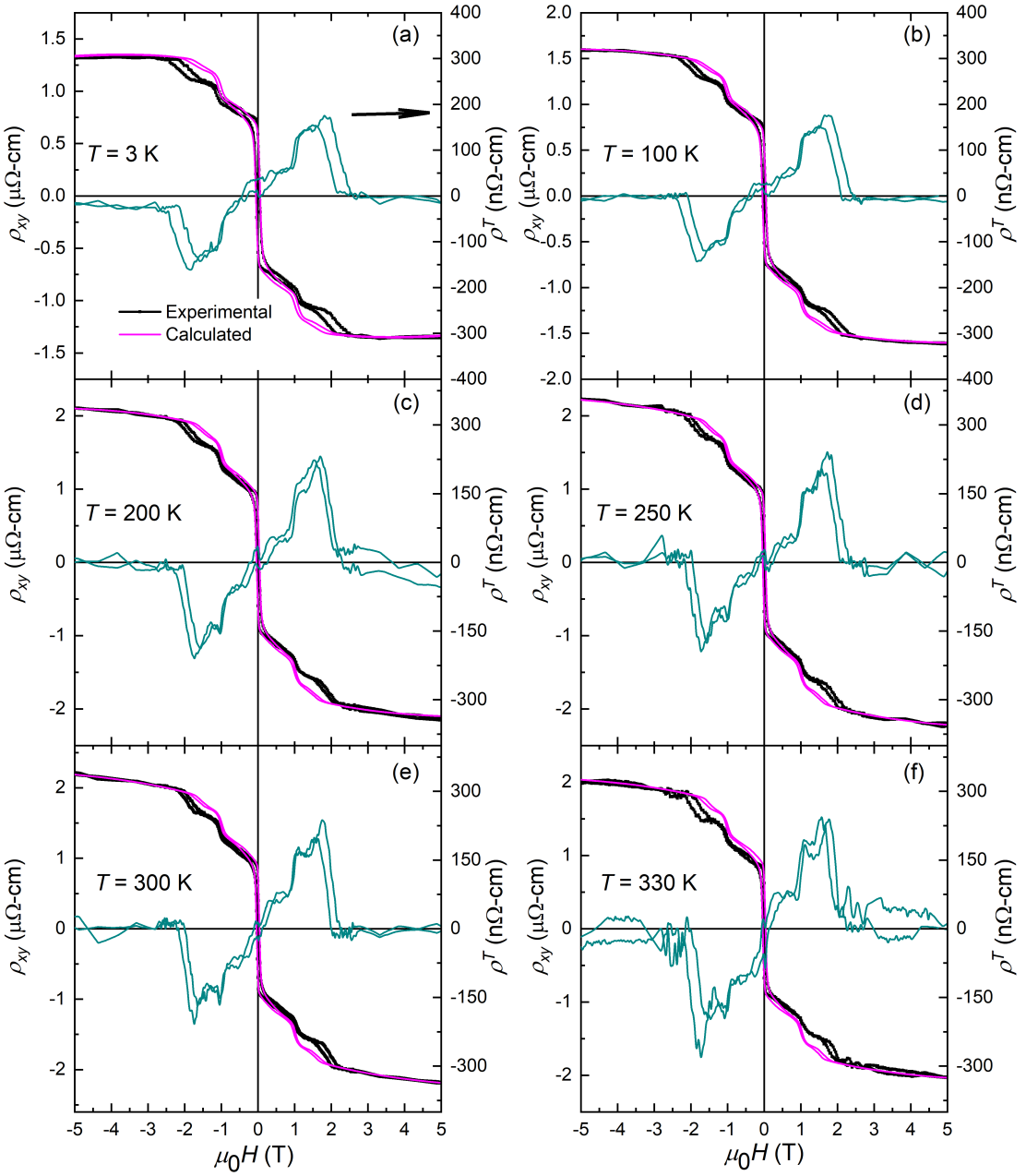

Figure 4.17: (Color online) Field dependence of experimental Hall resistivity (black lines) along with the calculated Hall resistivity (magenta lines) at different temperatures for $Mn_{2.13}Ni_{0.87}Ga$. The extracted topological Hall resistivity, ρ^T, is shown as dark cyan lines.

ρ_{xy} data around the magnetic fields of 0.3 T (marked by a $\star$ symbol), 1 T (indicated by an arrow) and 2 T (marked by a $\star$ symbol), as shown in Fig. 4.16. Similar kind of behavior in the ρ_{xy} data is seen at all measured temperatures, as given in Fig. 4.16(a)-(f). The calculated Hall resistivity curves for each temperature are plot-

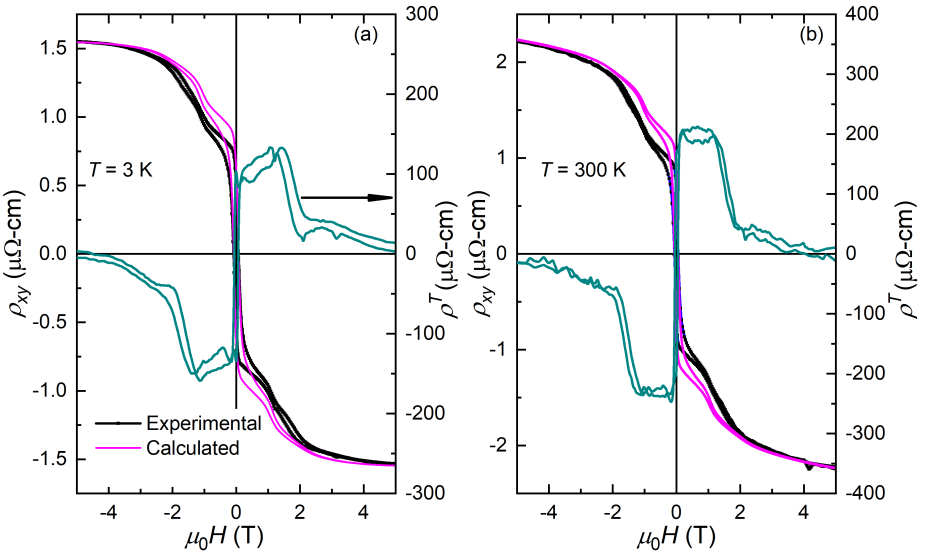

Figure 4.18: (Color online) Field dependent experimental Hall resistivity (black lines), the calculated Hall resistivity (magenta lines), and the extracted topological Hall resistivity (ρ^T) (dark cyan lines) at different temperatures for $Mn_{2.16}Ni_{0.84}Ga$.

ted by magenta lines as depicted in Fig. 4.17(a)-(f). A significant difference between the experimental and calculated curves is observed from $H \approx 0.3$ T to $H \approx 2$ T. The extracted ρ^T curves are plotted by dark cyan lines in Fig. 4.17(a)-(f). The ρ^T value increases with the temperature. The maximum value of the ρ^T is found to be about 232 nΩ-cm at $T = 300$ K. This value is much larger than the maximum ρ^T value observed in case of $x \leq 0.1$. Most importantly, a pronounced double peak kind feature is distinctly seen in the field-induced ρ^T curves at all measured temperatures.

Figure 4.18 and Figure 4.19 show the field dependence of Hall resistivity, $\rho_{xy}(H)$, curves for $Mn_{2.16}Ni_{0.84}Ga$ and $Mn_{2.20}Ni_{0.80}Ga$, respectively, measured at $T = 3$ K and 300 K. The calculated Hall resistivity curves (magneta line) for the respective samples are plotted on the top of the experimental curves in Fig. 4.18 and 4.19. A clear difference between the experimental and calculated Hall resistivity is observed around the anomaly regions of the $\rho_{xy}(H)$ data. The dark cyan color lines in the Fig. 4.18 and 4.19 represent the ρ^T curves for $Mn_{2.16}Ni_{0.84}Ga$ and $Mn_{2.20}Ni_{0.80}Ga$, respectively. In case of $Mn_{2.16}Ni_{0.84}Ga$, the maximum value of ρ^T is found to be around 200 nΩ-cm at $T = 300$ K. Whereas, the ρ^T value decreases to 50 nΩ-cm with a change of sign for $Mn_{2.20}Ni_{0.80}Ga$. The double peak kind feature in the ρ^T

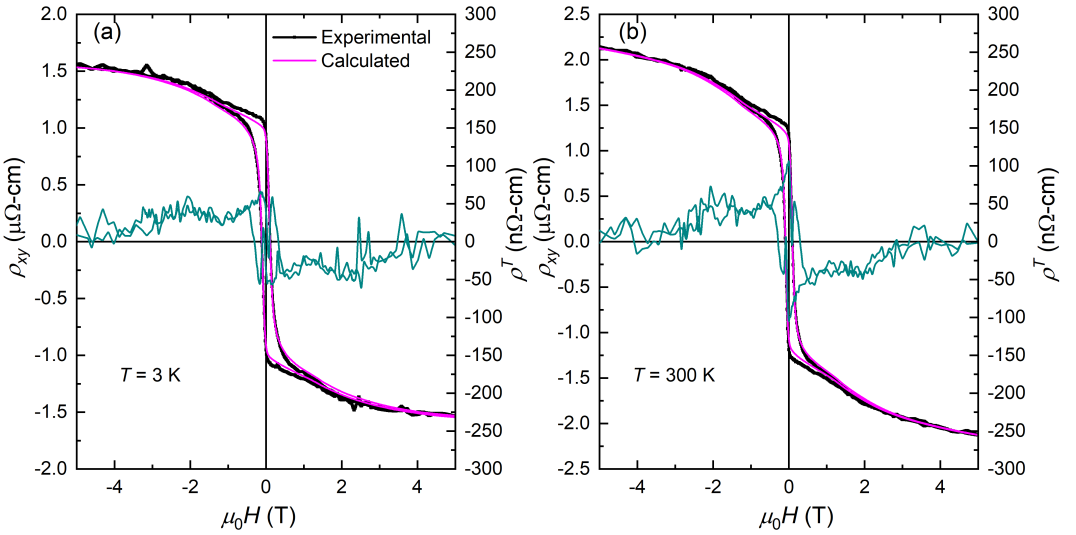

Figure 4.19: (Color online) Field dependence of the experimental Hall resistivity (black lines), the calculated Hall resistivity (magenta lines), and the extracted topological Hall resistivity (ρ^T) (dark cyan lines) at different temperatures for $Mn_{2.20}Ni_{0.80}Ga$.

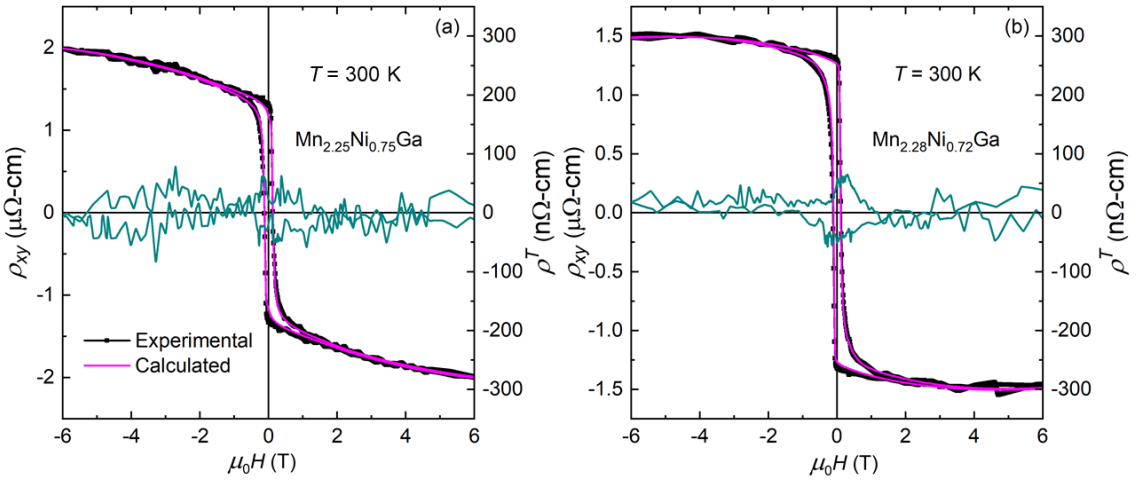

Figure 4.20: (Color online) Field dependent experimental Hall resistivity (black lines) along with the calculated Hall resistivity (magenta lines) at $T = 300$ K for (a) $Mn_{2.25}Ni_{0.75}Ga$, and (b) $Mn_{2.28}Ni_{0.72}Ga$. The extracted topological Hall resistivity, ρ^T, curves of these samples are shown as dark cyan lines.

curves is also seen for the $Mn_{2.16}Ni_{0.84}Ga$ sample. This anonymous feature almost dies out for $Mn_{2.20}Ni_{0.80}Ga$.

The experimental $\rho_{xy}(H)$ data (black solid line), calculated Hall resistivity (magenta solid line) and the topological Hall resistivity, ρ^T, curves (blue solid line) are plotted in Fig. 4.20(a) and (b) for $Mn_{2.25}Ni_{0.75}Ga$ and $Mn_{2.28}Ni_{0.72}Ga$, respectively at $T = 300$ K. Here, the calculated Hall resistivity curves perfectly match with the $\rho_{xy}(H)$ data at all the measured magnetic field regions, resulting in the vanishing ρ^T values for $Mn_{2.25}Ni_{0.75}Ga$ and $Mn_{2.28}Ni_{0.72}Ga$. The variation of ρ^T values with the composition of $Mn_{2+x}Ni_{1-x}Ga$ samples is illustrated in Fig. 4.21(a). It can be easily seen that the ρ^T value increases initially with the composition for $x \leq 0.16$ and reaches the maximum value for $x = 0.13$. Finally, ρ^T decreases to zero for $x > 0.20$. The finite value of the ρ^T, including the anomalies in the magnetic data, demonstrates the presence of the antiskyrmion phase for $x \leq 0.20$.The absence of such anomalous behavior implies the absence of antiskyrmion phase for $x \geq 0.20$.

4.5 Magnetic anisotropy calculation and their correlation to topological Hall effect for $Mn_{2+x}Ni_{1-x}Ga$

It is well known that the stability and size of skyrmions/antiskyrmions firmly depend on the different energy parameters, e.g., exchange constant (J), DM constant (D) and magnetocrystalline anisotropy (K) as discussed in Chapter-1. Therefore, for the better understanding of the evolution of antiskyrmion phase in the $Mn_{2+x}Ni_{1-x}Ga$ samples, it is necessity to look into the role of these different energy parameters. In this framework, it has been reported that the size of skyrmion (R) is related as $R = \pi D\sqrt{A/(16AK^2 + \pi^2 D^2 K)}$ [82]. As the magnetic ordering temperature for all the samples lies between 600 K and 650 K, it is expected that the exchange stiffness constant remains almost same for all the $Mn_{2+x}Ni_{1-x}Ga$ samples. Therefore, the magneto-crystalline anisotropy along with inhomogeneous DM interaction may possess crucial roles in the evolution of antiskyrmion phase. Hence, the law of approach

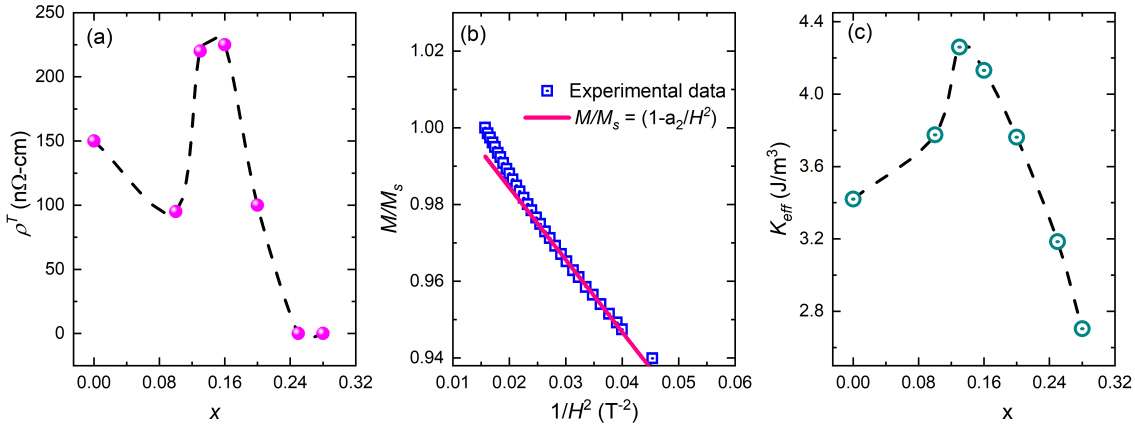

Figure 4.21: (Color online) (a) The variation of topological Hall resistivity (ρ^T) with the composition (x) of the $Mn_{2+x}Ni_{1-x}Ga$ samples, (b) the experimental M/M_s vs. $1/H^2$ plots (blue square open symbol) and the fitted curve (magenta solid line) based on the $M/M_s = 1 - a_2/H^2$ equation, (c) the change of effective anisotropy (K_{eff}) with the composition (x) of the $Mn_{2+x}Ni_{1-x}Ga$ samples.

to saturation method is adopted to evaluate the magnetocrystalline anisotropy of the system [83]. The magnetization (M) of the highly anisotropic sample in the region where $M \geq 0.95M$ can be expressed in accordance with the law of saturation method as,

$$M(H) = M_s(1 - a_2/H^2) \tag{4.1}$$

$$or, M/M_s = 1 - a_2/H^2 \tag{4.2}$$

where, M_S is the saturation magnetization of the sample and H stands for the magnetic fields. In case of uniaxial ferromagnetic sample, the constant a_2 is related as $a_2 = \frac{4K_{eff}^2}{15M_s^2}$, where K_{eff} is the effective uniaxial anisotropy of the sample.

The variation of the magnetocrystalline anisotropy (K_{eff}) with the composition (x) of the $Mn_{2+x}Ni_{1-x}Ga$ samples is illustrated in Fig. 4.21(c). The anisotropy value increases initially with the composition for $x \leq 0.13$ and then a decreasing trend is found for $x \geq 0.16$. It is interesting to note here that the topological Hall resistivity curves exhibit similar kind of trend with the composition for the $Mn_{2+x}Ni_{1-x}Ga$ samples. It is known that the topological Hall resistivity is inversely proportional to the square of the size of skyrmions/antiskyrmions. The anisotropy is related to the

size of antiskyrmion(R) as $R = \pi D\sqrt{A/(16AK^2 + \pi^2 D^2 K)}$. Therefore, the higher anisotropy value for $x = 0.13$ and 0.16 leads to a reduction in antiskyrmion size for the present system.

4.6 Micromagnetic simulation

To gain a better understanding of the multiple field-induced transitions in the topological Hall resistivity curves for $x = 0.13$, micromagnetic simulation studies are carried out with the assistance of public domain software package Object Oriented Micromagnetic Framework (OOMMF) [84], combined with the DMI extension module [85]. A thin film of dimension $1000 \times 1000 \times 5$ nm^3 is taken with a cell size of $5 \times 5 \times 5$ nm^3 to perform the simulation studies. The simulations are initially started from a random magnetization state with experimental parameters, such as the saturation magnetization $M_s = 1.65 \times 10^5$ A/m, the exchange stiffness constant $A = 3 \times 10^{-11}$ J/m, and the DM constant $D = 6.0$ mJ/m^2. Then the evolution of simulated states at a fixed magnetic field of 0.55 T are studied with different values of magnetic anisotropies, as given in Fig. 4.22. It can been seen that a mixed spin state of stripe domains, antiskyrmions with different helicities, and antiskyrmioniums are present for the anisotropy values varying from $K = 1 \times 10^5$ J/m^5 to $K = 4 \times 10^5$ J/m^5. Further increase in the anisotropy value to 5×10^5 J/m^5 nucleates a pure topological magnetic spin configurations of antiskyrmions, antiskyrmioniums (marked by a yellow box), and antiskyrmion bags (indicated by a black box). Finally, the pure antiskyrmions state is obtained for $K = 6 \times 10^5$ J/m^5.

To extract more information from the multiple field-induced transitions observed in the ρ^T curves for $x = 0.13$, field dependent micromagnetic simulation studies are performed with $A = 3 \times 10^{-11}$ J/m, $M_s = 1.65 \times 10^5$ A/m, $D = 6.0$ mJ/m^2 and $K = 5 \times 10^5$ J/m^5 taking the random magnetic state as initial state. A possible connection between the simulated magnetic states with the field evolution topological Hall resistivity is illustrated in Fig. 4.23. Different regimes of the field dependent ρ^T curves and the corresponding simulated magnetic states are designated by A,

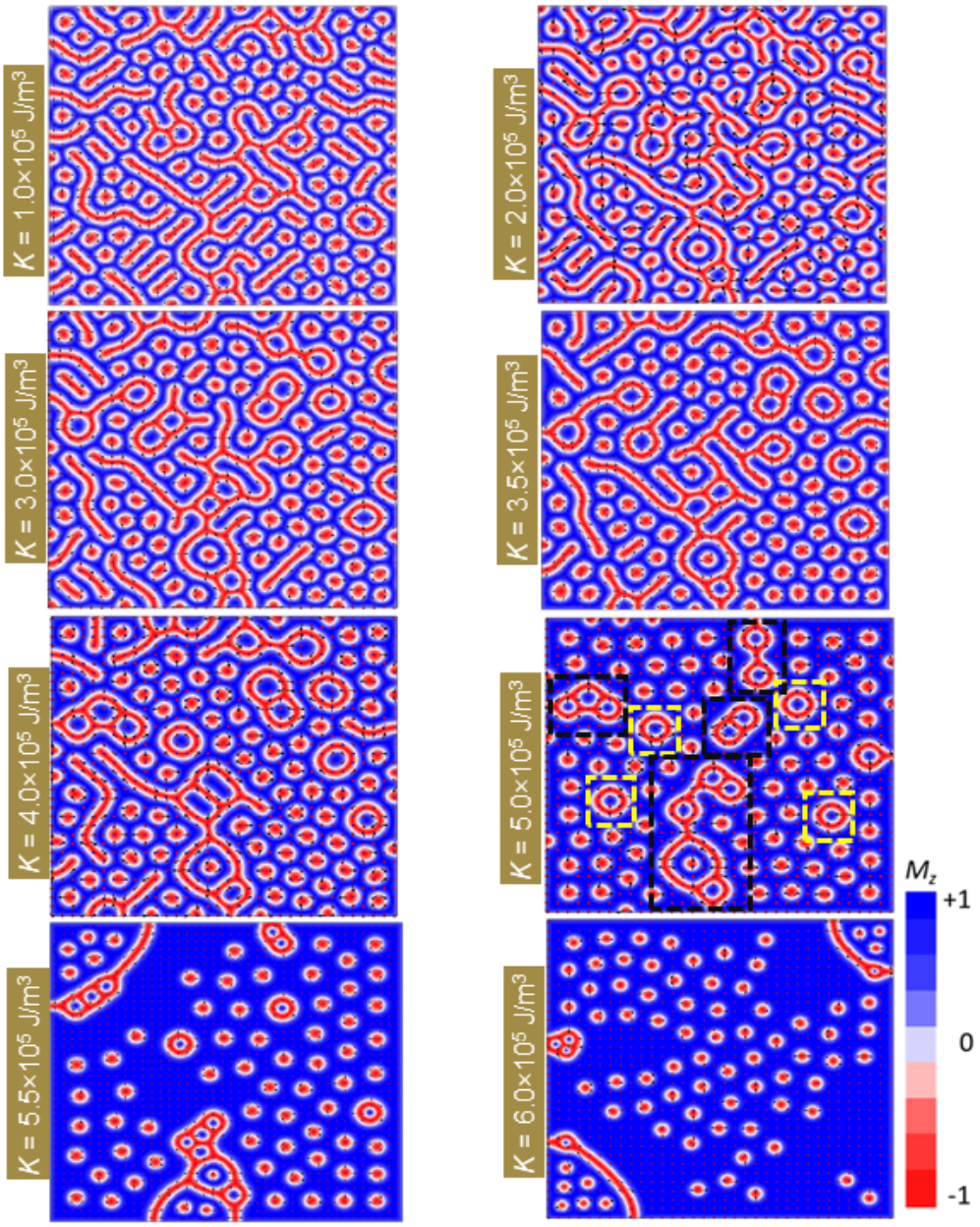

Figure 4.22: (Color online) The simulated magnetic states with different anisotropies is obtained using $A = 3 \times 10^{-11}$ J/m, $M_s = 1.65 \times 10^5$ A/m, and $D = 6.0$ mJ/m^2 at a fixed magnetic field of 0.55 T. The antiskyrmion pockets and the antiskyrminiums are marked by black boxes, and yellow boxes, respectively.

B, C, and D in Fig. 4.23. Following conclusions can be drawn from the correlation between the experimental and the simulated data. After applying a magnetic field of 0.30 T to the random magnetic states, a mixed states with the stripe domains, antiskyrmions (topological charge -1), antiskyrmion pockets (topological charge >

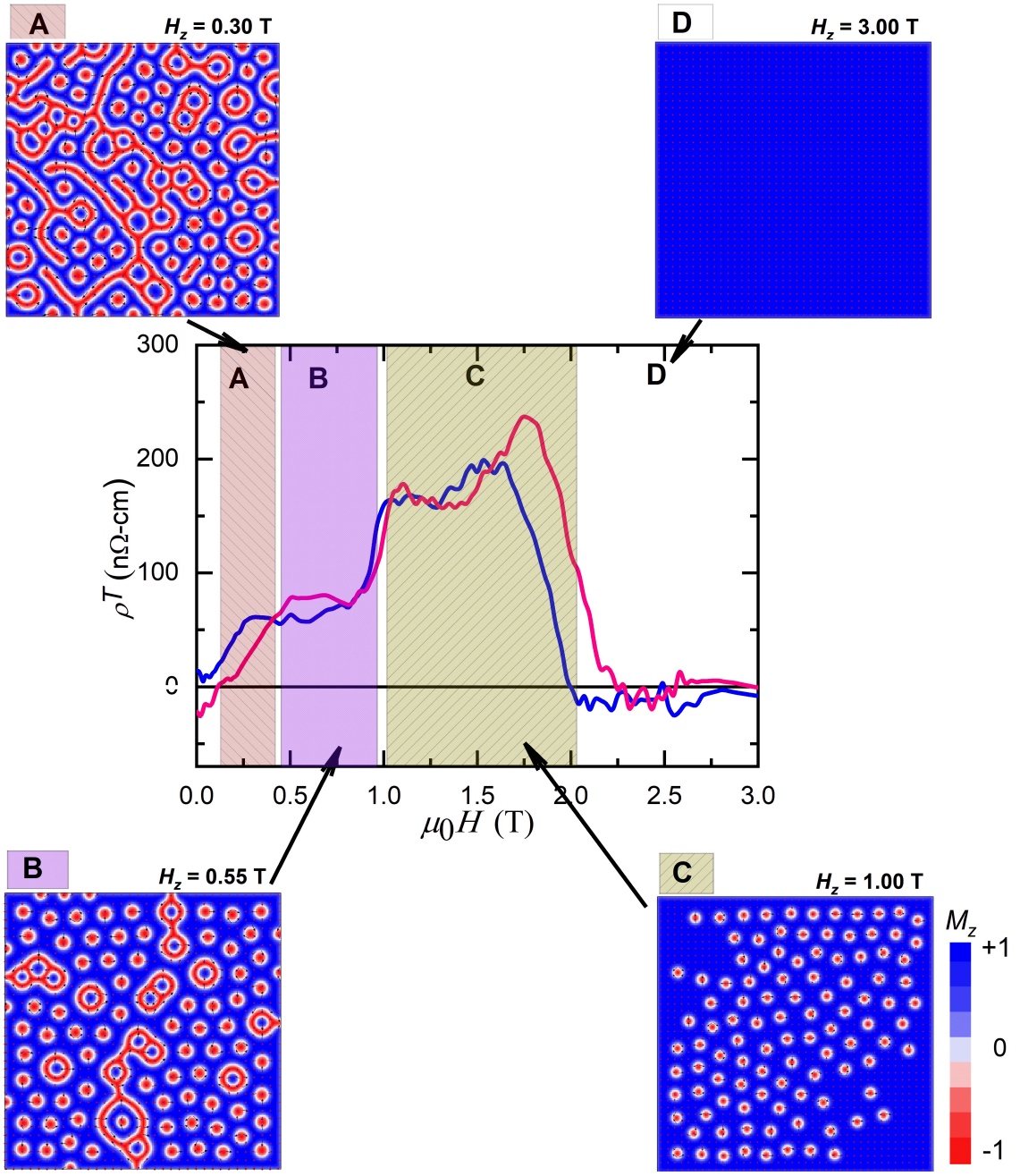

Figure 4.23: (Color online) Field evolution of topological Hall resistivity, ρ^T, curves for $Mn_{2.13}Ni_{0.87}Ga$. The simulation is performed with $A = 3 \times 10^{-11}$ J/m, $M_s = 1.65 \times 10^5$ A/m, $D = 6.0$ mJ/m^2, and $K = 5 \times 10^5$ J/m^5. Different regimes of field dependent of the ρ^T curves and the corresponding micromagnetic simulated states are denoted by A, B, C, and D.

+1) antiskyrmioniums with (zero topological charge) are obtained, as denoted by A. The finite value of ρ^T around A region is probably due to the dominate presence of antiskyrmion phase. Upon further increment of the magnetic field to 0.55 T,

the strip domain patterns vanish entirely, and mostly antiskyrmions, antiskyrmioniums, and antiskyrmion pockets are observed, as seen in the simulated magnetic state denoted by B. Therefore, a slight enhancement of the ρ^T value from the A region to B region could be the consequence of the nucleation of antiskyrmions in large numbers due to the breaking of the strip domains pattern. Most interestingly, an abrupt change in the ρ^T value is clearly identified when going from the B to C region. The simulated magnetic states at $H_z = 1.00$ T, marked by C, show the presence of pure antiskyrmions. Hence, the conversion of antiskyrmioniums with zero topological charge and antiskyrmion pockets with topological charge $> +1$ into the conventional antiskyrmions (topological charge -1) increases the total effective topological charge, thereby, resulting in the sudden increase of the ρ^T values for C region. At $H_z = 3.00$ T, all the antiskyrmions completely disappear and eventually a field polarized simulated state is obtained, as marked by D. Therefore, the zero value of the ρ^T is found for the D region.

In conclusion, the existence of various kinds of antiskyrmion phase in the $Mn_{2+x}Ni_{1-x}Ga$ samples is established by means of the magnetic and the Hall effect measurements. In contrast to the parent Mn_2NiGa compound, the antiskyrmions in the tetragonal phase of the present materials can probably exist upto 600 K. The large value of topological Hall resistivity (≈ 200 nΩ-cm) implies the presence of very small antiskyrmion (< 10 nm) at room temperature. It is noteworthy to mention here that there are very few materials that show skyrmions with size less than 10 nm at room temperature [13, 26, 27, 41, 56, 86]. The skyrmion phase is generally observed at very low temperatures in these materials and the narrow range of temperature stability is the primary limitation for future spintronic application. In contrast, the existence of small size antiskyrmions in the wider temperature stability including the room temperature are found for the present systems. The presence of different kinds of topological phases in certain range of composition is strongly evident from the magnetic and Hall effect measurements. Therefore, the coexistence of antiskyrmion and antiskyrminium can be utilized as '1' and '0' databits in racetrack memory devices. It is important to mention here that the amtiskyrmions

in the high magnetic moment samples are transformed into skyrmions via trivial bubbles by application of small in-plane magnetic fields. Hence, the benefit of antiskyrmion over skyrmion regarding the skyrmion Hall effect disappears upon this topological transformation. The low magnetic moment of these Mn-Ni-Ga samples can give robust protection of the antiskyrmions phase against the in-plane magnetic fields. Finally, the presence of small size antiskyrmions and the coexistence of various topological phases at extensive temperature ranges, including room temperature in the low magnetic Mn-Ni-Ga samples, make the present system attractive for future application in next-generation racetrack memory devices.

Chapter 5

Relaxation dynamics studies on antiskyrmion hosting materials

Dc magnetic measurements have been extensively employed to uncover different magnetic properties, such as magnetization, magnetic phase transitions, magnetic ordering, etc, in various magnetic materials. However, dc magnetic measurement is not a suitable technique to measure the dynamical properties unless the magnetic relaxation process is very slow (under the dc limit). When the dynamics are faster than the experimental timescale, ac magnetic measurements instead of dc magnetization measurements are extensively used to probe the dynamical properties of magnetic materials. In this regards, ac susceptibility measurements have been rigorously used to study the relaxation dynamics and to identify magnetic phase transition [87, 88, 89]. In recent times, the ac susceptibility measurement technique emerges as an important tool to characterize the skyrmion phase of various skyrmion hosting magnetic systems [28, 29, 30, 31, 32, 33]. Besides identifying the skyrmion phase, relaxation dynamics study on several skyrmion hosting materials have also been carried out through ac susceptibility measurements [30, 31, 32]. However, the relaxation dynamics of antiskyrmions remain unknown. Therefore, a detailed relaxation dynamics study using the ac susceptibility measurements on the antiskyrmion hosting materials Mn-Pt-Pd-Sn and Mn-Ni-Ga is presented in this chapter. Before

elaborating on the experimental results, the Cole-Cole relaxation model used for the present study is briefly discussed below.

5.1 Relaxation Dynamics and Cole-Cole relaxation model in magnetic system

When a magnetic material is applied with an oscillating magnetic field of frequency comparable to the characteristic frequency (equivalent timescale) of the magnetic relaxation process, then there is a phase lag between the magnetization and the applied ac magnetic field. In such scenario, the ac susceptibility is a complex quantity, as discussed in Chapter-2. The total ac susceptibility response can be written in terms of in-phase (χ') and out-phase (χ'') components as,

$$\chi = \chi' + i\chi'' \tag{5.1}$$

where χ' represents the change of magnetization with respect to the applied field, also known as reversible magnetization. χ'' corresponds to the dissipation of the absorbed energy from the high frequency ac field, known as the irreversible magnetization. This irreversibility occurs due to the involvement of relaxation processes of various origin, such as irreversible movement of domain walls, spin reorientation, hysteresis loss in ferromagnets, spin-lattice relaxation, spin-spin relaxation, magnetic phase transition, etc. Since different kind of spin textures exhibit unique relaxation process, study of the magnetic relaxation can give important insight into the magnetic structures, spin-spin and spin-lattice interactions in a system.

Analogous to the well-known Debye model of dielectric relaxation [90], Casimir and du Pré [91] derived the expression for complex susceptibility based on a thermodynamic model of relaxation for a magnetic system. This complex susceptibility

can be expressed as,

$$\chi(f) = \chi_S + (\chi_T - \chi_S)\frac{1}{1 + (i2\pi f\tau_0)} \tag{5.2}$$

where χ_T ($f \to 0$) is the isothermal / dc / static susceptibility in the limit of the lowest frequency and χ_S ($f \to \infty$) stands for the adiabatic susceptibility in the limit of the highest frequency. Here adiabatic means the characteristic frequency of the system is outside the experimental frequency range. f is the frequency, whereas, τ_0 is the average relaxation time. The Eq. (5.2) is known as the 'Debye relation' process.

As the ac susceptibility is a complex quantity, therefore, the real part $[\chi'(H)]$ and imaginary part of ac susceptibility $[\chi''(H)]$ can be written as follows.

$$\chi'\,(f) = \chi_S + (\chi_T - \chi_S)\frac{1}{1 + (2\pi f\tau_0)^2} \tag{5.3}$$

$$\chi''\,(f) = (\chi_T - \chi_S)\frac{2\pi f\tau_0}{1 + (2\pi f\tau_0)^2} \tag{5.4}$$

The frequency dependency of the χ' and χ'' is always associated with one or more relaxation processes. It is to be noted here that Eq. 5.3 is valid when the magnetization of the system relaxes slowly with a single time scale (single relaxation process). On the other hand, when the spins interact each other, then the dynamics of the system is no longer governed by the Eq. 5.3. In such cases, a distribution of relaxation time is obtained due to the clustering effect. To counter this problem in case of the interacting systems, a phenomenological parameter α is introduced in the Eq. 5.3. The above Eq. 5.3 can be written as,

$$\chi'(f) = \chi_\infty + (\chi_0 - \chi_\infty)\frac{1}{1 + (i2\pi f\tau_0)^{1-\alpha}}. \tag{5.5}$$

This is known as the generalized Debye relation/ Cole-Cole relation. Here α is the bandwidth of the relaxation times distribution, which varies in between 1 and 0. A zero value of α represents the single relaxation process, whereas, α=1 indicates

infinitely broad distribution of the relaxation time. The frequency dependence of the real and imaginary components of the Eq. 5.5 can be expressed as,

$$\chi'(f) = \chi_\infty + (\chi_0 - \chi_\infty)\frac{1 + (2\pi f\tau_0)^{1-\alpha}\sin(\frac{\pi\alpha}{2})}{1 + 2(2\pi f\tau_0)^{1-\alpha}\sin(\frac{\pi\alpha}{2}) + (2\pi f\tau_0)^{2(1-\alpha)}} \tag{5.6}$$

$$\chi''(f) = (\chi_0 - \chi_\infty)\frac{1 + (2\pi f\tau_0)^{1-\alpha}\cos(\frac{\pi\alpha}{2})}{1 + 2(2\pi f\tau_0)^{1-\alpha}\sin(\frac{\pi\alpha}{2}) + (2\pi f\tau_0)^{2(1-\alpha)}} \tag{5.7}$$

The relaxation dynamics of various systems having spin texture with considerable large correlated length or spin cluster are often inspected with the help of the Cole-Cole model of ac susceptibility. This model is utilized to analyze the ac susceptibility data of the present antiskyrmion hosting materials to uncover the relaxation phenomenon associated with the system.

5.2 Magnetic relaxation dynamics studies on antiskyrmion host Mn-Pt(Pd)-Sn

5.2.1 Magnetic measurements in Mn-Pt(Pd)-Sn

In order to inspect the magnetic properties of $Mn_{1.4}Pt_{0.9}Pd_{0.1}Sn$, the temperature dependence of the magnetization, $M(T)$, at a fixed magnetic field of 0.1 T is plotted in Fig. 5.1(a). As it can be seen, $Mn_{1.4}Pt_{0.9}Pd_{0.1}Sn$ exhibits a magnetic ordering temperature, T_C, of 400 K and a spin reorientation transition (T_{sr}) around 130 K. Due to this spin reorientation, a sudden change of magnetization in the $M(T)$ data is observed. This transition appears as a peak/dip kind of anomaly in the real part of ac susceptibility (χ') vs. temperature (T) measurement, as shown in Fig. 5.1(b). It is important to mention here that the existence of antiskyrmion phase in the $Mn_{1.4}Pt_{0.9}Pd_{0.1}Sn$ is found only above the T_{sr}. The change of magnetic structure below the T_{sr} prevents the formation of antiskyrmion phase in the system.

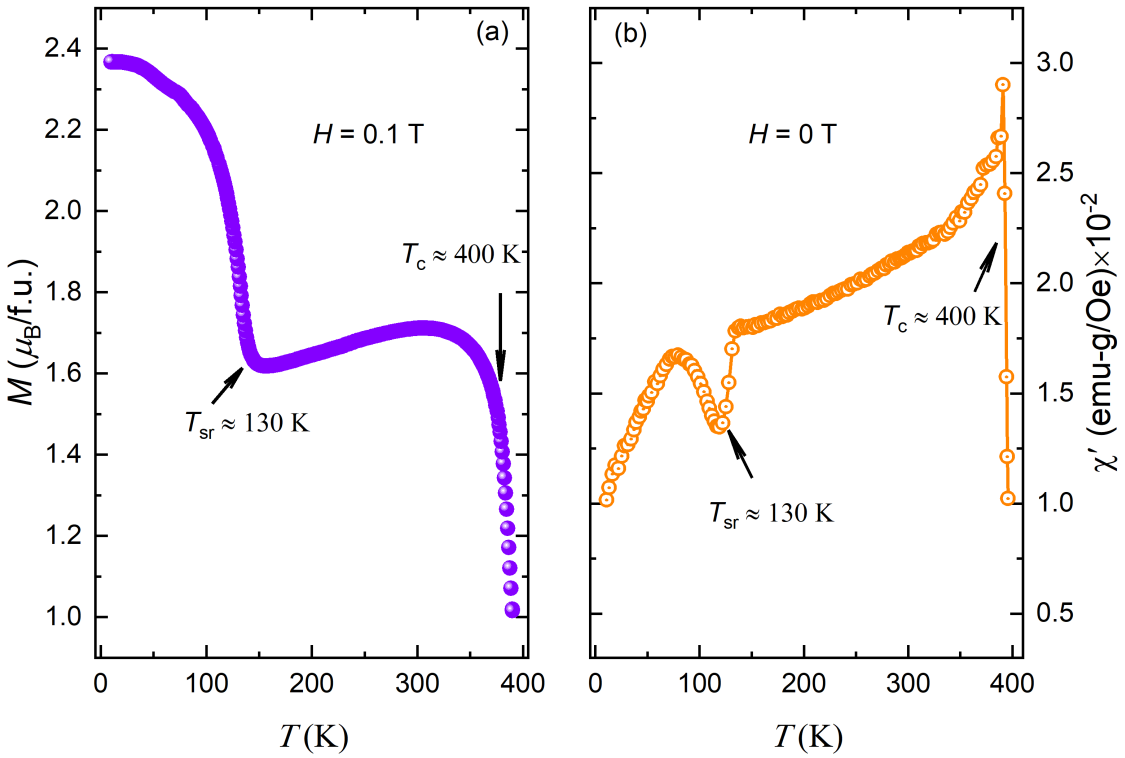

Figure 5.1: (Color online) (a) The temperature dependent magnetization, $M(T)$, curves measured at $H = 0.1$ T, (b) The real part of ac susceptibility data as a function of temperature, $\chi'(T)$, for $Mn_{1.4}Pt_{0.9}Pd_{0.1}Sn$.

5.2.2 Relaxation dynamics study using ac susceptibility measurements for Mn-Pt(Pd)-Sn

To verify the existence of antiskyrmion phase in the Mn-Pt(Pd)-Sn material, field-dependent ac susceptibility, $\chi(H)$, measurement is carried out with an ac magnetic field of 10 Oe and frequency $(f) = 9984$ Hz at different temperatures ranging from $T = 10$ K to $T = 350$ K, as plotted in Figs. 5.2. As can be seen in Figs. 5.2(c)-(f), the $\chi'(H)$ data exhibit pronounce peak/dip kind of features around the magnetic field range of 0.06-0.13 T (marked by down arrows), followed by another broad hump like transition around 0.6-0.2 T (marked by up arrows). As per the previously reported LTEM studies for $Mn_{1.4}Pt_{0.9}Pd_{0.1}Sn$, the peak/dip at the low magnetic field (H_L^{AskX}) in the $\chi'(H)$ data corresponds to the helical (H) to antiskyrmion (AskX) magnetic phase transition, and the broad hump-like feature at a relatively high

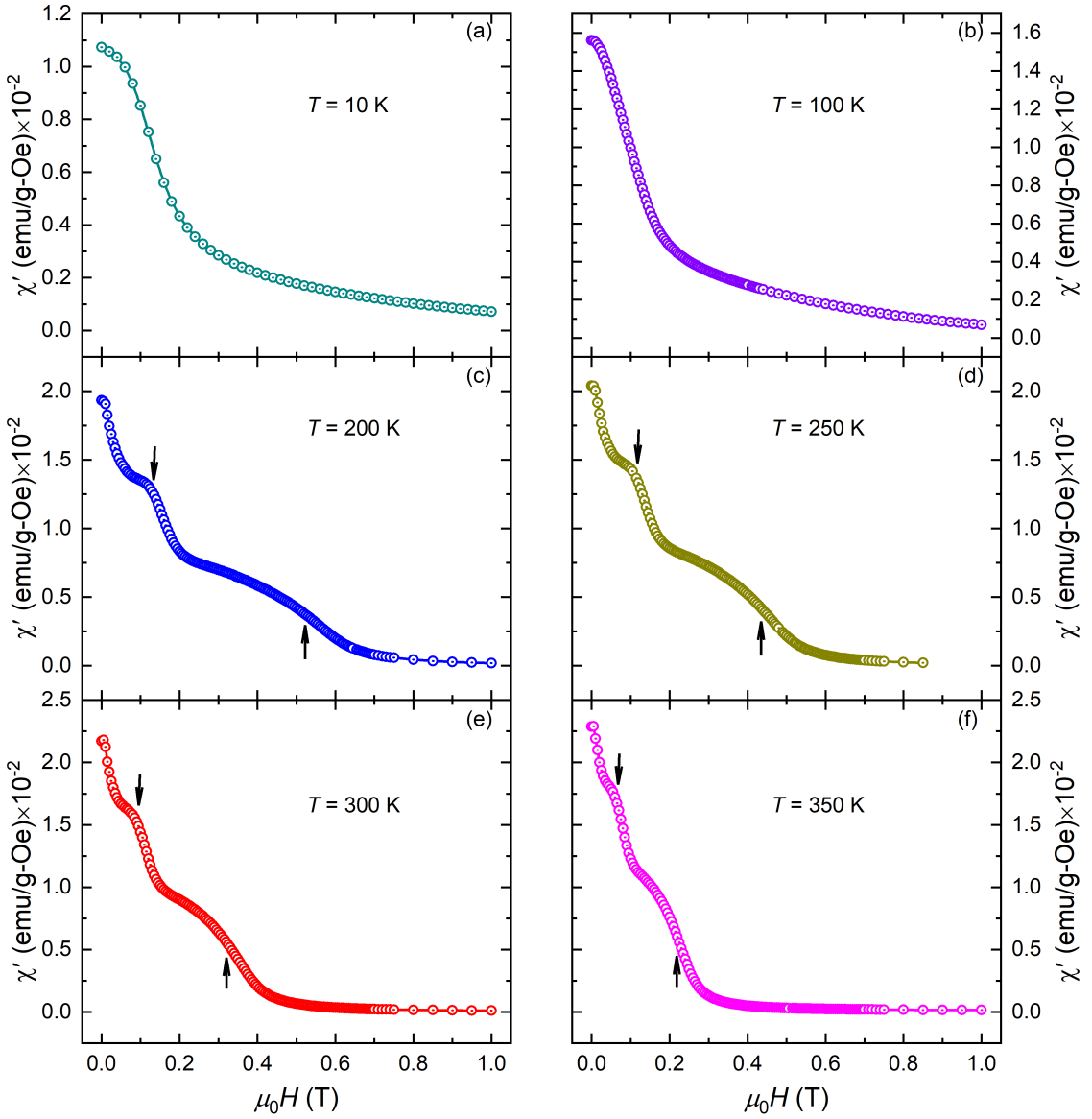

Figure 5.2: (Color online) Field dependent real part of ac susceptibility χ' (H) at different temperatures for $Mn_{1.4}Pt_{0.9}Pd_{0.1}Sn$. The anomalies in these curves are indicated by up and down arrows.

magnetic field (H_U^{AskX}) represent the magnetic phase transition from antiskyrmion (AskX) to field polarized state (FP). Therefore, the magnetic state at $H < H_L^{AskX}$ represents the helical spin modulation (H), whereas, the field polarized state is achieved in the magnetic field of $H > H_U^{AskX}$. In between these two field limits ($H_L^{AskX} < H < H_U^{AskX}$), the antiskyrmions phase appears. It is noticeable that the anomalies corresponding to the magnetic phase transition are present in all $\chi'(H)$ measurements of $T \geq 200$ K, whereas, no such unusual behavior is found at $T = 10$

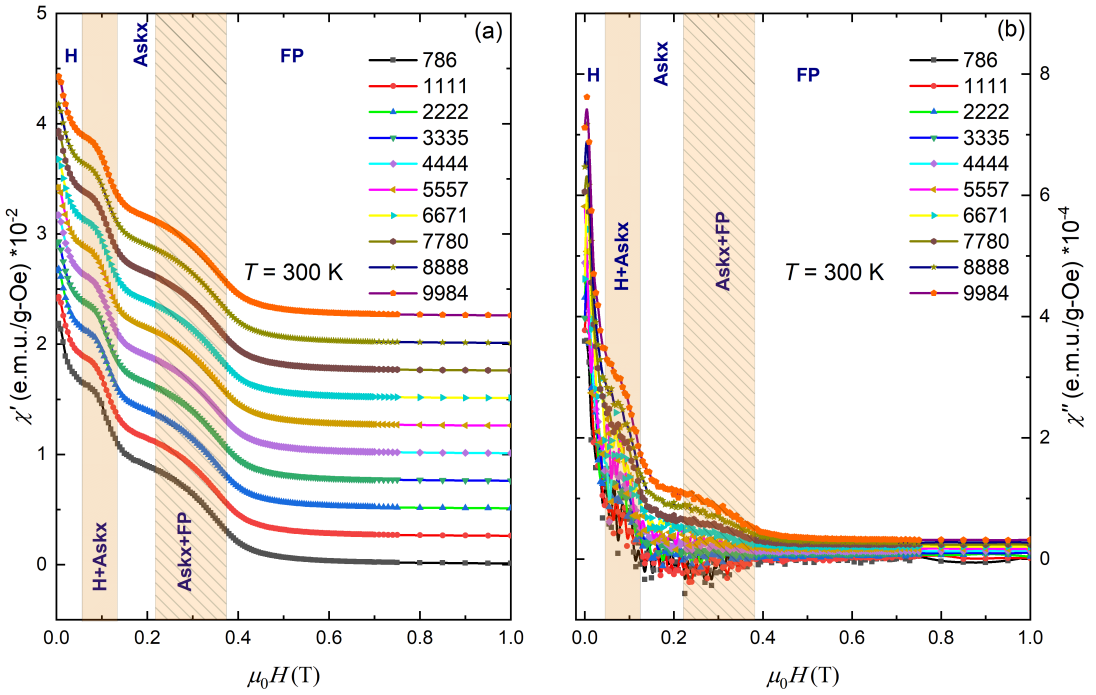

Figure 5.3: (Color online) Field dependence of (a) real part of ac susceptibility χ' (H), (b) imaginary part of ac susceptibility χ'' (H), at T = 300 K measured in different frequencies ranging from 786 Hz to 9984 Hz for $Mn_{1.4}Pt_{0.9}Pd_{0.1}Sn$. The magnetic phase crossover region are highlighted by the color shading. Note that for clarity purposes, the χ' (H) data for the successive frequencies are shifted upwards by constant factor starting from the data at f = 9984 Hz.

K and 100 K. These facts suggest the absence of antiskyrmion phase below the T_{sr}, i.e., $T \leq$ 130 K.

In order to study the magnetic relaxation phenomena, frequency dependent ac susceptibility measurements are performed on $Mn_{1.4}Pt_{0.9}Pd_{0.1}Sn$ at different temperatures ranging from T = 200 K to T = 350 K. The $\chi'(H)$ and $\chi''(H)$ at different frequencies for T = 300 K are presented in Fig. 5.3(a) and (b), respectively. The magnetic phase transitions appear as peaks or humps in the ac susceptibility curves, highlighted by color shading.

To better understand the frequency dependence of the χ' at different magnetic phase regimes, such as helical (H), mixed state of helical and antiskyrmion (H + AskX), pure antiskyrmion phase (AskX), phase coexistence of antiskyrmion and field-polarized state (AskX+ FP), and field polarized state (FP), the χ' data are

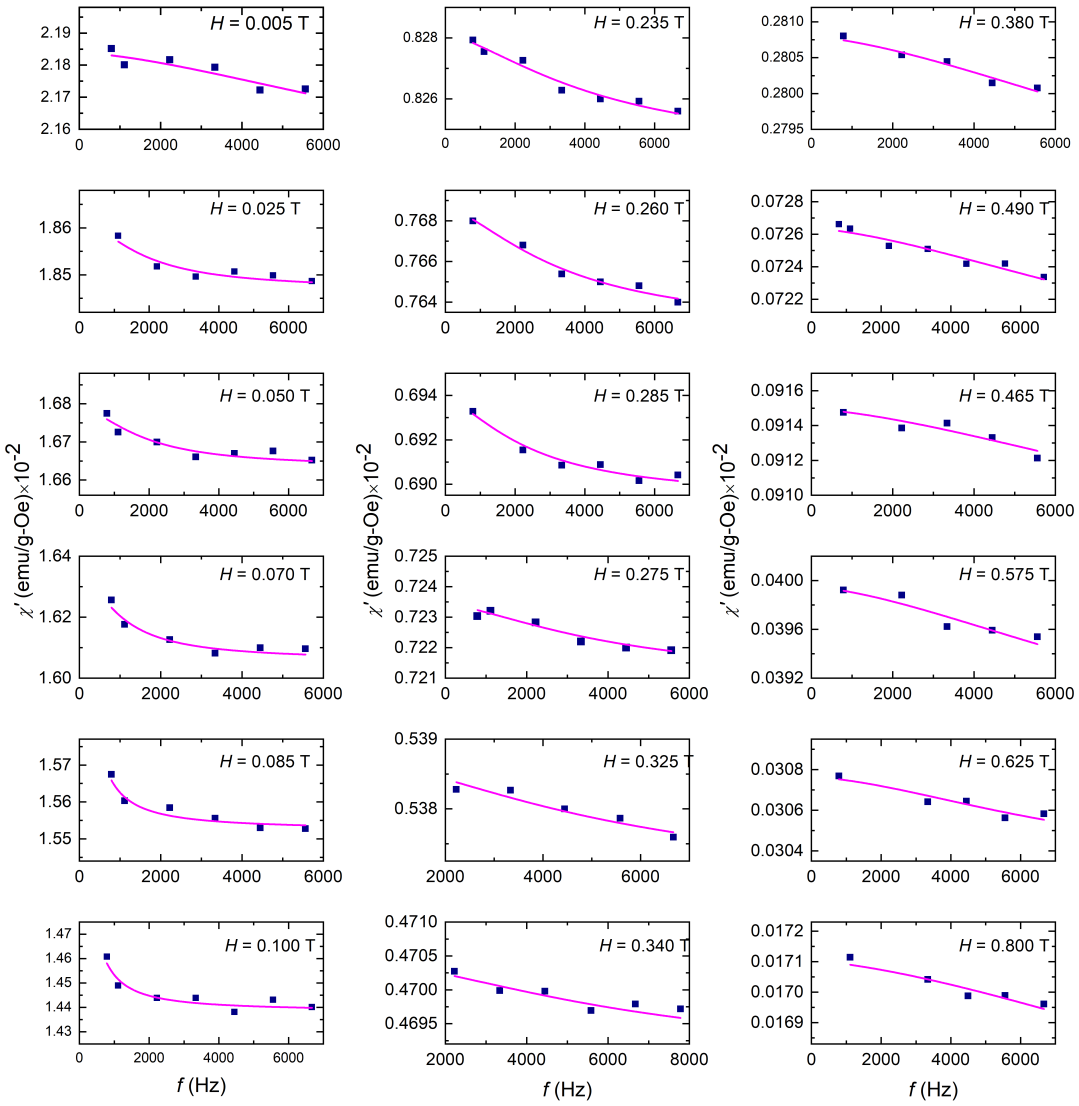

Figure 5.4: (Color online) The real part of ac susceptibility data as a function of frequency $\chi'(f)$ at different fixed dc magnetic fields at $T = 300$ K for $Mn_{1.4}Pt_{0.9}Pd_{0.1}Sn$. The experimental data and the corresponding fitted curve based on the Eq. 5.8 are plotted by blue square symbols and solid magenta line, respectively.

replotted as a function of frequency $[\chi'(f)]$ at fixed dc magnetic fields, as given in Fig. 5.4 (blue square symbols). It is noticeable that the nature of frequency dependence of $\chi'(f)$ at different dc magnetic fields differs from each other. This is evident from the shift of inflection point of the $\chi'(f)$ data to higher frequencies when going from lower to higher value of dc magnetic fields.

In order to gain knowledge about the magnetic relaxation phenomenon associ-

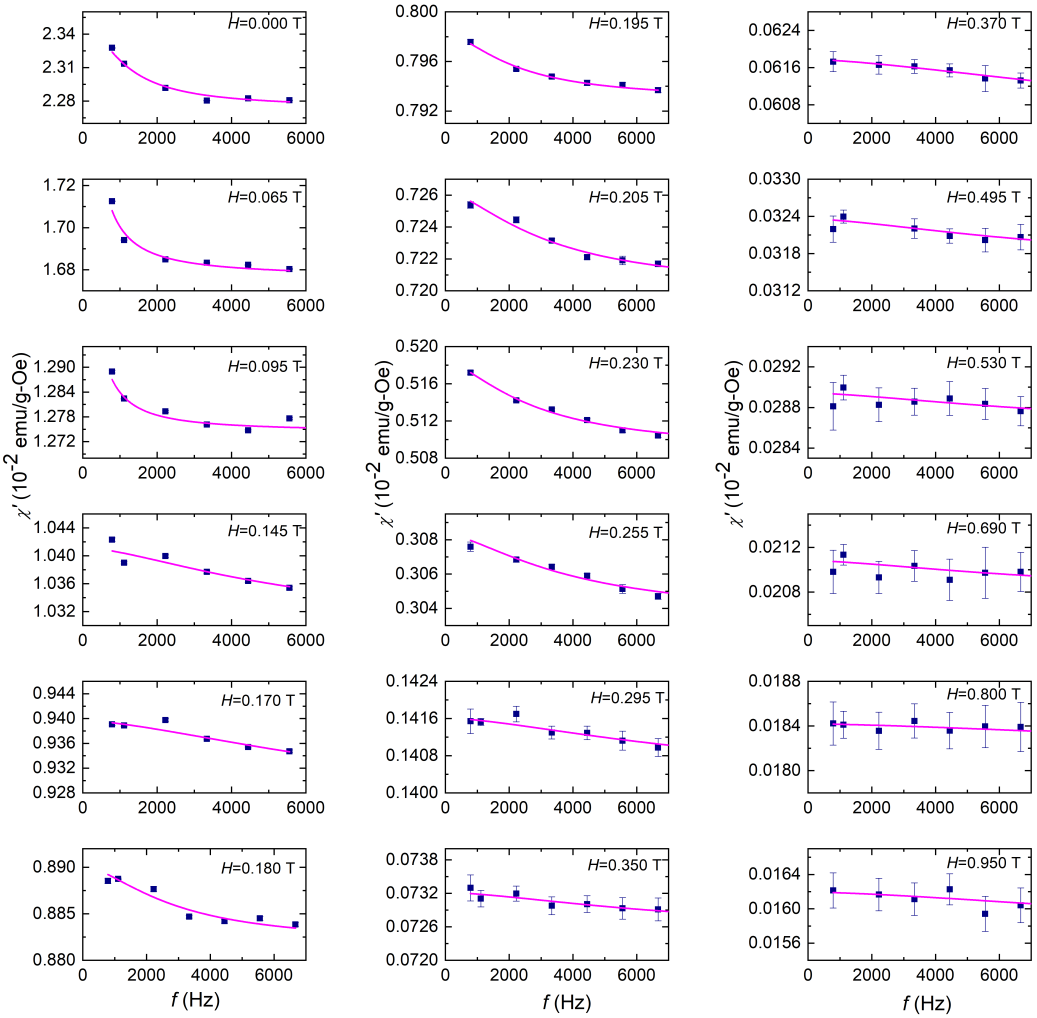

Figure 5.5: (Color online) The real part of ac susceptibility data as a function of frequency $\chi'(f)$ at different fixed dc magnetic field at $T = 350$ K for $Mn_{1.4}Pt_{0.9}Pd_{0.1}Sn$. The experimental data, and the corresponding fitted curve based on the Eq. 5.8 are plotted by blue square symbols and solid magenta line, respectively.

ated with the topological phase like antiskyrmion, here the Cole-Cole formalism is adopted to fit the $\chi'(f)$ data. As discussed earlier, the frequency dependency of the $\chi(f)$ can be written using the Cole-Cole relation as

$$\chi'(f) = B + A\frac{1 + (2\pi f\tau_0)^{1-\alpha}\sin(\frac{\pi\alpha}{2})}{1 + 2(2\pi f\tau_0)^{1-\alpha}\sin(\frac{\pi\alpha}{2}) + (2\pi f\tau_0)^{2(1-\alpha)}} \tag{5.8}$$

$$\chi''(f) = A\frac{1 + (2\pi f\tau_0)^{1-\alpha}\cos(\frac{\pi\alpha}{2})}{1 + 2(2\pi f\tau_0)^{1-\alpha}\sin(\frac{\pi\alpha}{2}) + (2\pi f\tau_0)^{2(1-\alpha)}} \tag{5.9}$$

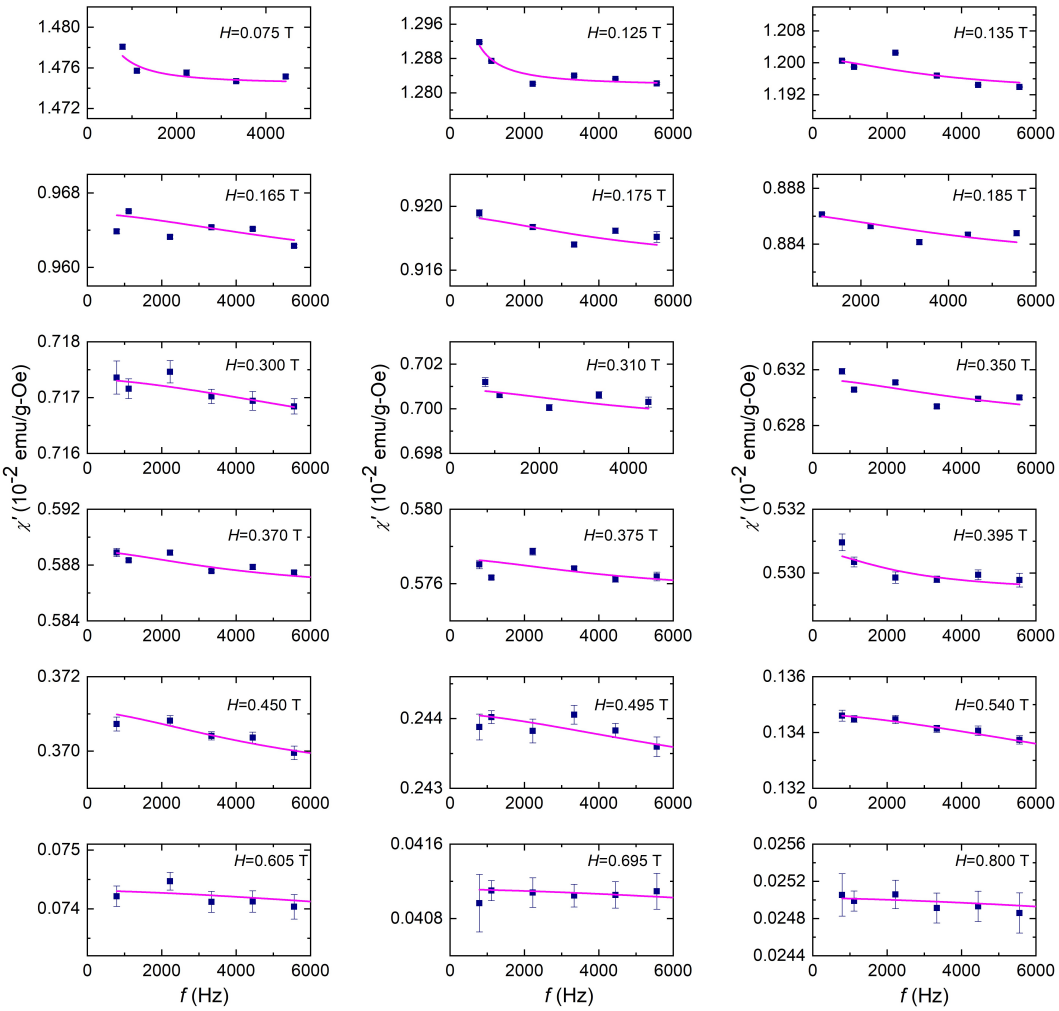

Figure 5.6: (Color online) The real part of ac susceptibility data as a function of frequency $\chi'(f)$ at different fixed dc magnetic field at $T = 250$ K for $Mn_{1.4}Pt_{0.9}Pd_{0.1}Sn$. The experimental data and the corresponding fitted curve based on the Eq. 5.8 are plotted by blue square symbols and solid magenta line, respectively.

where $B = \chi_\infty$, and $A = \chi_0 - \chi_\infty$.

Here the experimental $\chi'(f)$ curve is fitted using the above equation by considering the B, A, α, and τ_0 as free parameters. The best fitted curve for each experimental $\chi'(f)$ data is plotted by magenta lines in Fig. 5.4. Using similar method, the experimental $\chi'(f)$ data are fitted for $T = 200$ K, 250 K and 350 K, as illustrated in Fig. 5.7, 5.6, and 5.5, respectively. In this process, for a given temperature, a particular value of B, A, α, and τ_0 parameters are obtained at each dc magnetic field. The field evolution of all these parameters at different temperatures are depicted in

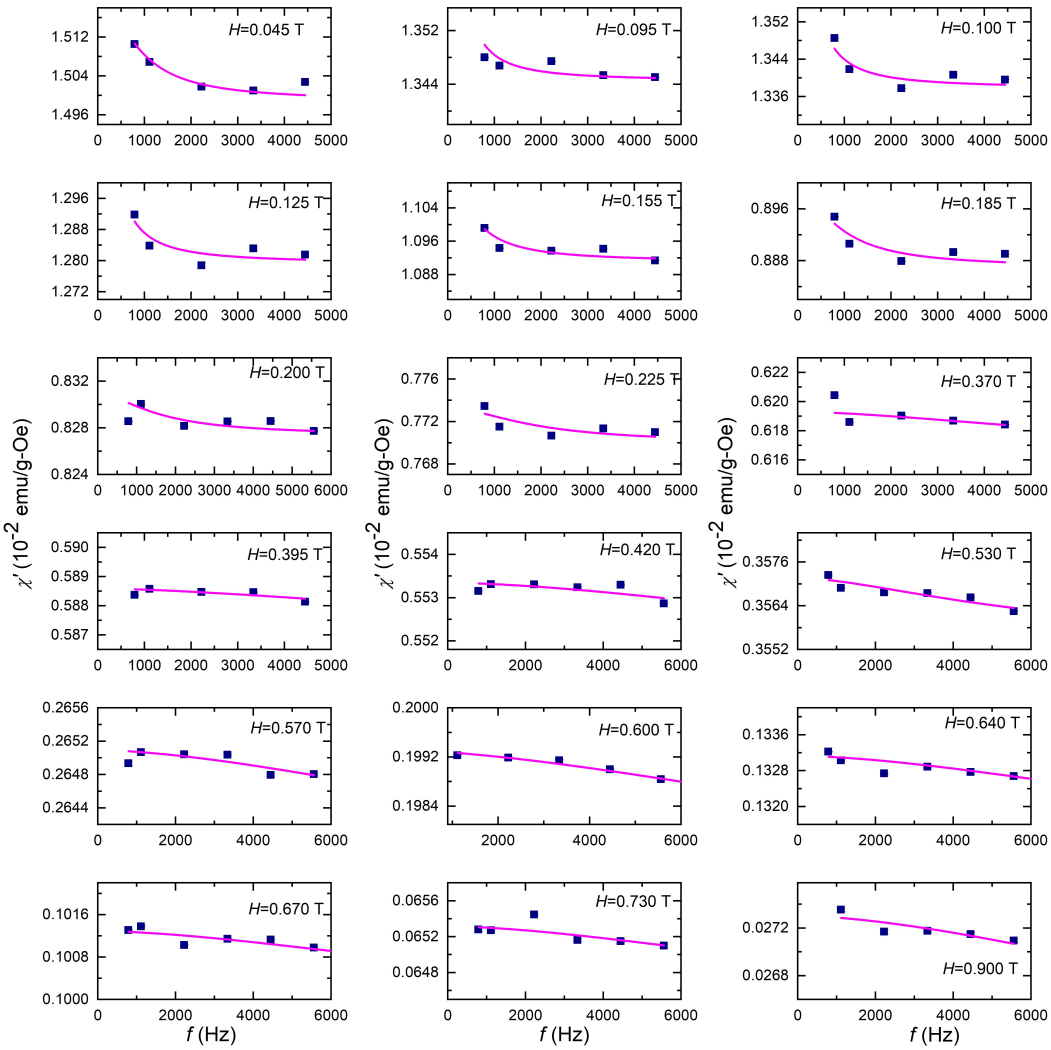

Figure 5.7: (Color online) The real part of ac susceptibility data as a function of frequency $\chi'(f)$ at different fixed dc magnetic field at $T = 200$ K for $Mn_{1.4}Pt_{0.9}Pd_{0.1}Sn$. The experimental data and the corresponding fitted curve based on the Eq. 5.8 are plotted by blue square symbols and solid magenta line, respectively.

Fig. 5.8. From the field variation of these parameters, the following assessments can be drawn. (1) The parameters B, A, α, and τ_0 vary non-monotonically with the magnetic fields. The field evolution of these parameters exhibit a peak like transition at $H = H_1 \approx H_L^{AskX}$, along with the broad hump like transition at $H = H_2 \approx H_U^{AskX}$. The magnitude of H_1 and H_2 also vary with the temperature. (2) The peak and broad hump-like features for the parameter A at $H = H_1$ and H_2 suggests that the frequency dependence of the χ' at each coexist phase (H+AskX, and AskX+FP) region are comparably larger than the pure magnetic phase regions (H, AskX, and

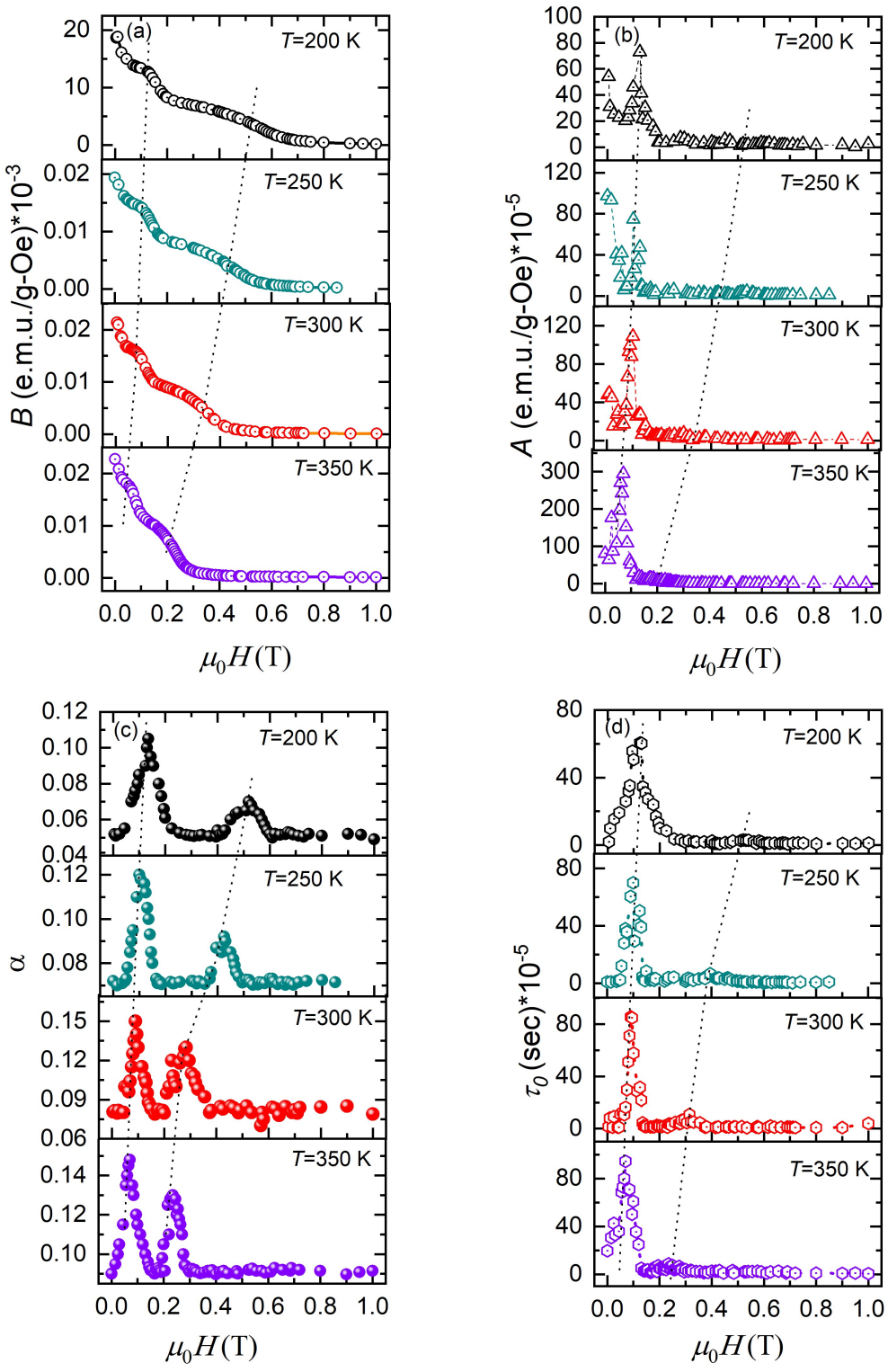

Figure 5.8: (Color online) Field evolution of the Cole-Cole fitting parameters (a) B, (b) A, (c) α, and (d) τ_0 for $Mn_{1.4}Pt_{0.9}Pd_{0.1}Sn$. The dashed lines are to guide eye.

FP). This fact strongly indicates the involvement of a slow magnetic relaxation process around the phase boundary regions. (3) It can be seen from Fig. 5.8(d) that the magnetic relaxation time $\tau_0(H)$ around each phase crossover regions ((H+AskX, and AskX+FP)) is higher than the pure magnetic phase. In other words, the relaxation process associated with the mix phase regions is much slower than that of pure phase. Similar kind of observation has also been made in the skyrmion hosting $Fe_{1-x}Co_xSi$ [32], Cu_2OSeO_3 [30], and GaV_4S_8 [31]. This slow relaxation process around the phase boundaries can be attributed to the irregularities of spin coordination in these regions arising as a result of the coexistence of multiple magnetic phases [31, 92]. (3) The value of the relaxation time distribution parameter α falls in between 0.05 to 0.15. The small value of α suggests that a nearly single relaxation process is involved in different phase regions except the phase boundaries. The higher value of the α around the phase crossover regions compared to that in the pure phase indicates the existence of more than one relaxation process around these regions due to the conjunction of multiple phases. (4) The smaller value of τ_0 around 10^{-5} sec compared to that for the skyrmion host Cu_2OSeO_3 [30] suggests the faster relaxation process for the present system. This might be due to the large spin orbit coupling strength arising from the presence of heavy element Pt in the present system.

Figure 5.9 shows the frequency dependence of imaginary part of ac susceptibility $\chi''(f)$ curves at different magnetic fields for $Mn_{1.4}Pt_{0.9}Pd_{0.1}Sn$ at $T = 300$ K. Interestingly, the $\chi''(f)$ data exhibit a shoulder kind of behavior near to the frequency (f_0) where an inflection point of the $\chi'(f)$ curve appears. The experimental $\chi''(f)$ data is fitted by the Eq. 5.9 using the same values of parameters as initial input values obtained from the $\chi'(f)$ analysis. Then all the parameters are relaxed to fit the $\chi''(f)$ curve. The fitted curves (magenta color solid lines) together with the experimental data (square blue symbols) are plotted in Figure 5.9. It is important to mention here that in general the $\chi''(f)$ curve in the Debye like relaxation model given by the Eq. 5.9 exhibit a peak at characteristics frequency $f_0 = 1/2\pi\tau_0$. It is seen from Fig. 5.9 that the fitted curve matches well with experimental data up to

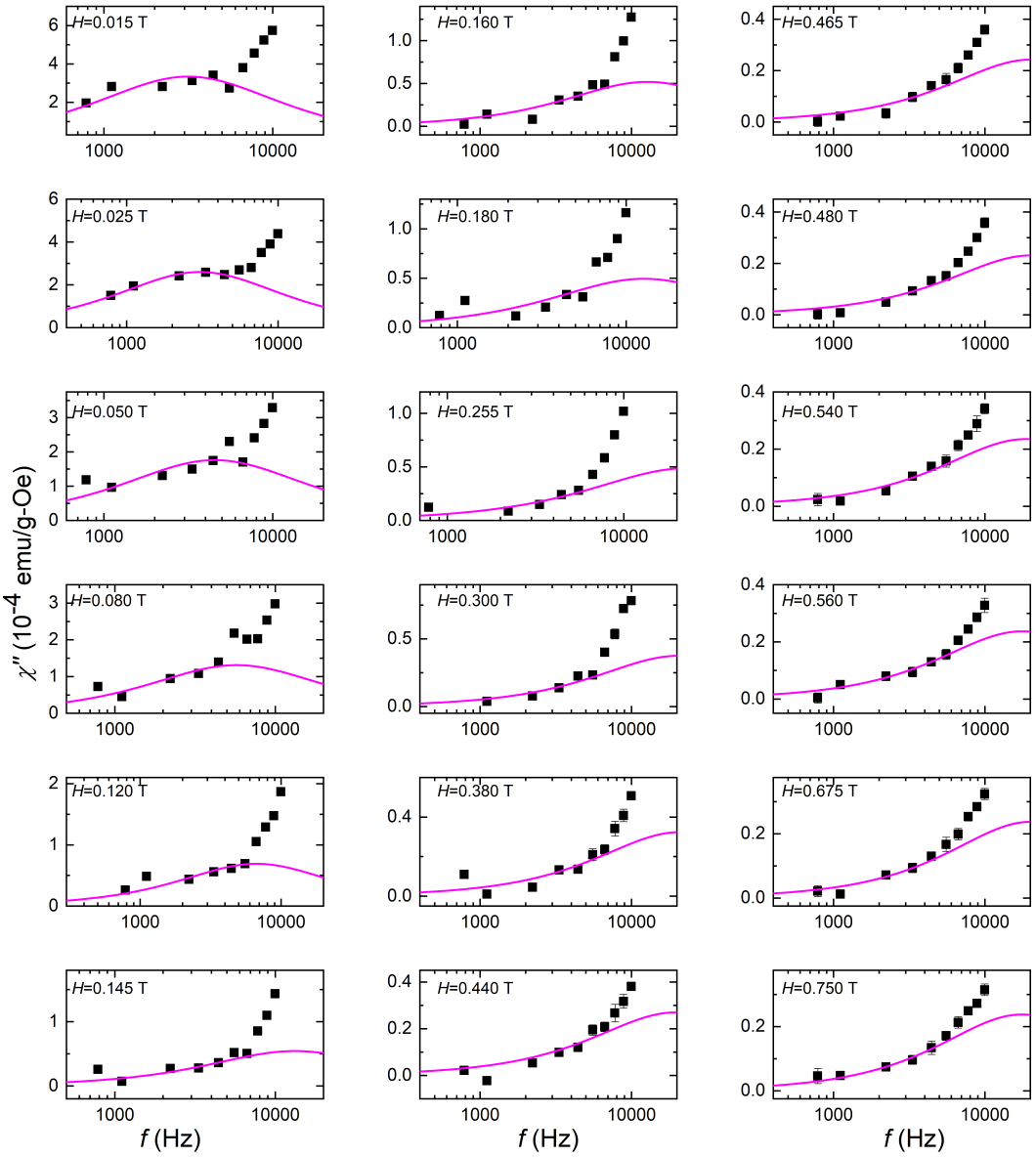

Figure 5.9: (Color online) The imaginary part of ac susceptibility data as a function of frequency χ'' (f) at different dc magnetic fields at T = 300 K for $Mn_{1.4}Pt_{0.9}Pd_{0.1}Sn$. The experimental data and the corresponding fitted curve based on the Eq. 5.9 are plotted by blue square symbols and solid magenta line, respectively.

a certain frequency where a shoulder kind of behavior in the $\chi''(f)$ data appears. For higher frequencies, the fitted curve largely deviates from the experimental data. This deviation may be due to the eddy current loss, which badly affect the ac susceptibility signal in the range of higher frequencies. When the ac susceptibility signals

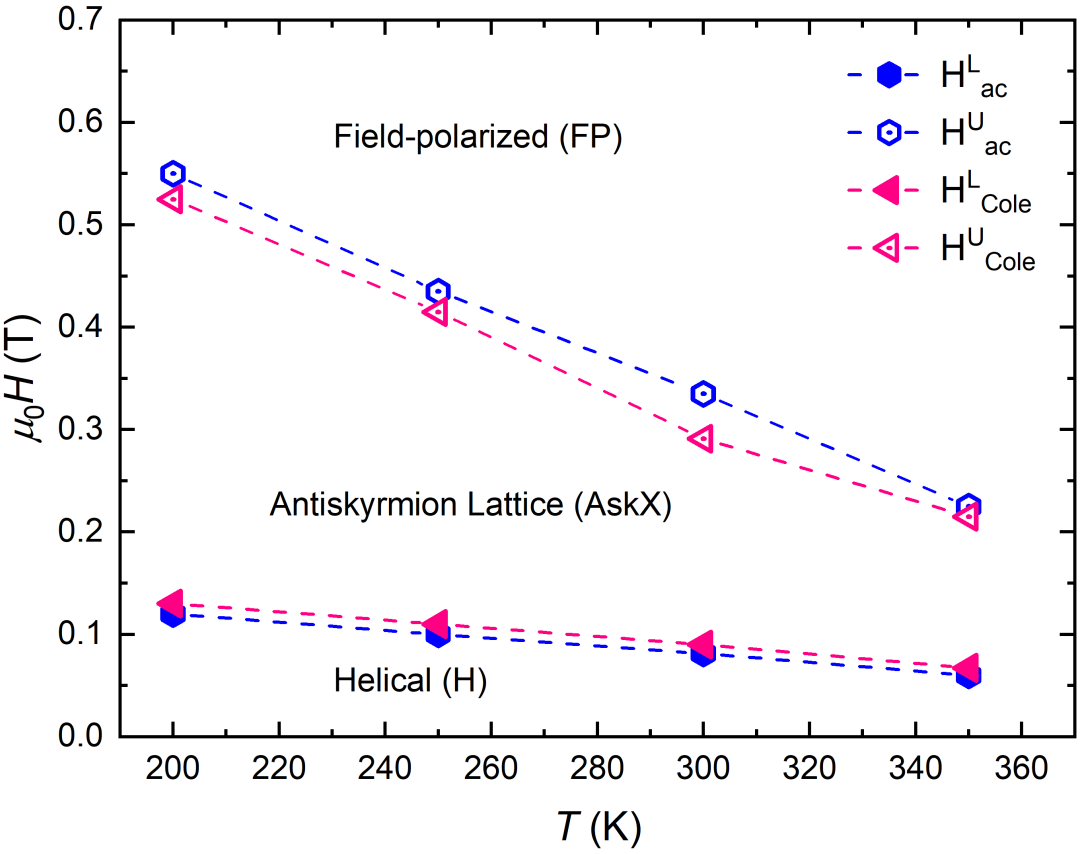

Figure 5.10: (Color online) The H-T phase diagram is drawn based on the peak anomalies in the field evolution of ac susceptibility data and the Cole-Cole fitting parameters. The upper and lower boundaries of antiskyrmion phase are represented by the open and close symbols. H_L^{ac} (H_U^{ac}) are the lower (upper) boundaries of the antiskyrmion phase according to ac susceptibility data. The lower (upper) boundaries of the antiskyrmion phase inferred from the Cole-Cole analysis are denoted by H_L^{Cole} (H_U^{Cole}).

are low, the eddy current effect may be seen in the ac susceptibility data [93]. As the signal of the $\chi''(f)$ data (10^{-5}-10^{-6} emu/Oe) falls under the lower resolution limit of the instrument, therefore, a predominant behavior of eddy current effects is seen in the $\chi''(f)$ data. However, the fitting parameters inferred from the $\chi''(f)$ analysis are nearly the same order as that obtained from the $\chi'(f)$ analysis.

A H-T phase diagram is also drawn on the basis of the $\chi'(H)$ data and the calculated field dependent Cole-Cole parameters for the present system, as illustrated in Fig. 5.10. In this case, H_{ac}^L (H_{Cole}^L) and H_{ac}^U (H_{Cole}^U) represent the lower (H + AskX) and upper (AskX + FP) critical boundaries of antiskyrmion phase. It is important

to mention here that the phase boundaries extracted from the Cole-Cole analysis approximately matches with that obtained from the LTEM [14] and magneto-entropy [81] studies of this material. A slight difference of the phase boundaries, especially the upper one, between the present study and previously reported studies may arise due to the nonidentical orientation of grain in the polycrystalline materials as the angle between the applied magnetic field direction and the <001> orientated grain of the tetragonal materials defines the required field to stabilize the antiskyrmion phase. Moreover, all these observations suggest that the present method can be used to characterize the skyrmion/antiskyrmion phase in any suitable magnetic materials.

In conclusion, a detailed relaxation dynamics study on the D_{2d} symmetric antiskyrmion hosting Mn-Pt-Pd-Sn tetragonal material is demonstrated utilizing the frequency-dependent ac susceptibility measurements. The magnetic relaxation of the Mn-Pt-Pd-Sn system obeys the Debye type relation with a negligible distribution of relaxation time. The isothermal susceptibility, adiabatic susceptibility, and the relaxation time change nonmonotonically at the phase crossover regions (H+AskX, and AskX+FP). The larger value of relaxation time at the phase boundary regions compared to that of the pure magnetic phase suggests a slower relaxation process at the phase coexistence area. The finding of higher relaxation time in the present system compared to superparamagnets and single molecular magnets implies a lower damping process in the antiskyrmion host Mn-Pt-Pd-Sn system.

5.3 Magnetic relaxation dynamics studies on antiskyrmion host Mn-Ni-Ga

As discussed in Chapter-1, the tetragonal phase of the Mn-rich Mn-Ni-Ga alloys can exhibit magnetic antiskyrmions due to its D_{2d} type of crystal symmetry. In Chapter-3, and 4, the existence of antiskyrmion phase in these alloys is well established through the dc magnetization, ac susceptibility, and Hall measurements. Most importantly, the estimated antiskyrmion size in case of Mn-Ni-Ga alloys is

found to be very small in comparison to that for the Mn-Pt-Pd-Sn system. In the previous section, a through study of the relaxation dynamics is demonstrated on the known antiskyrmion host Mn-Pt-Pd-Sn using the Cole-Cole relaxation model. To find out the difference in the magnetic relaxation phenomenon as a result of small size antiskyrmions, a detailed frequency dependent ac susceptibility measurements is performed on the Mn-rich Mn-Ni-Ga alloys.

5.3.1 Frequency dependent ac susceptibility studies on Mn_2NiGa

In Chapter-3, the presence of antiskyrmion phase is demonstrated in Mn_2NiGa through dc magnetization, ac susceptibility, and Hall measurements. In the field driven ac susceptibility measurements, the presence of peak/dip kind of anomalies in particular field region establish the antiskyrmion phase in Mn_2NiGa. Motivated by this anomalous behavior, field-dependent ac susceptibility measurement, $\chi'(H)$, at a frequency window of 1111 Hz to 8111 Hz is carried out to study the relaxation phenomena associated with the topological objects present in the Mn-Ni-Ga system. Figure 5.11 shows the $\chi'(H)$, and $\chi''(H)$ data at different frequencies for $T = 200$ K. Here the peak kind of transition in these curves are highlighted by the color shading.

To observe the frequency dependence of the χ' data in different magnetic phase regimes in the present system, $\chi'(f)$ plots are constructed at each magnetic field from the $\chi'(H)$ data, as depicted in Fig. 5.12 (black symbol). It is seen that the inflection point of the $\chi'(f)$ curve appears at relatively high magnetic field in comparison with that at low magnetic field.

In order to investigate the magnetic relaxation phenomenon associated with the present Mn_2NiGa sample, the experimental $\chi'(f)$ data is fitted using the Eq. 5.8 by taking B, A, α, and τ_0 as free parameters. The fitted curve (magneta solid line) along with experimental data (black solid ball symbols) at each magnetic field is plotted in Fig. 5.12 at $T = 200$ K. Similiar kind of operations are also done for $T =$ 100 K, and $T = 250$ K. The obtained field depedent B, A, α, and τ_0 data from the

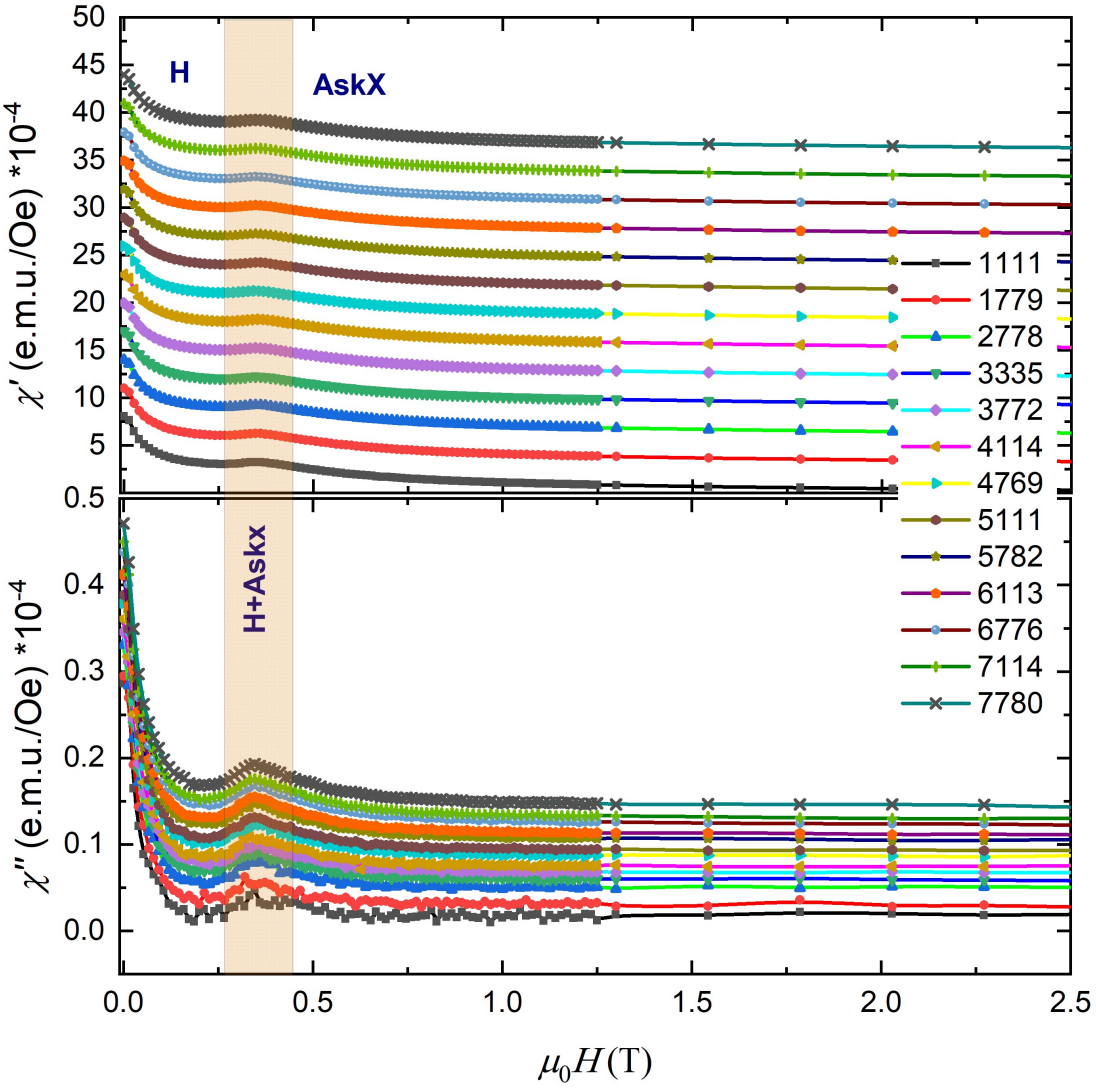

Figure 5.11: (Color online) Field dependence of (a) real part of ac susceptibility χ' (H), (b) imaginary part of ac susceptibility χ'' (H), at $T = 300$ K measured in different frequencies ranging from 1111 Hz to 7780 Hz for Mn_2NiGa. The region corresponding to the anomaly is highlighted by the color shading. Note that for clarity purposes, the χ' (H) data for the successive frequencies are shifted upwards by constant factor starting from the data at $f = 7780$ Hz.

Cole-Cole analysis of the χ' data at different temperature are illustrated in Fig. 5.13. It is seen that the all the fitting parameters shows the peak/dip kind of behavior around $H = 0.40$ T. The peak kind of behavior in the field dependent A (as given in Fig. 5.13(b)) indicates that frequency dependence of the χ' data is larger around this field region. Similar kind of observation is also found for the Mn-Pt-Pd-Sn due to the coexistence of mix magnetic phase like helical+ antiskyrmion/ antiskyrmion+field

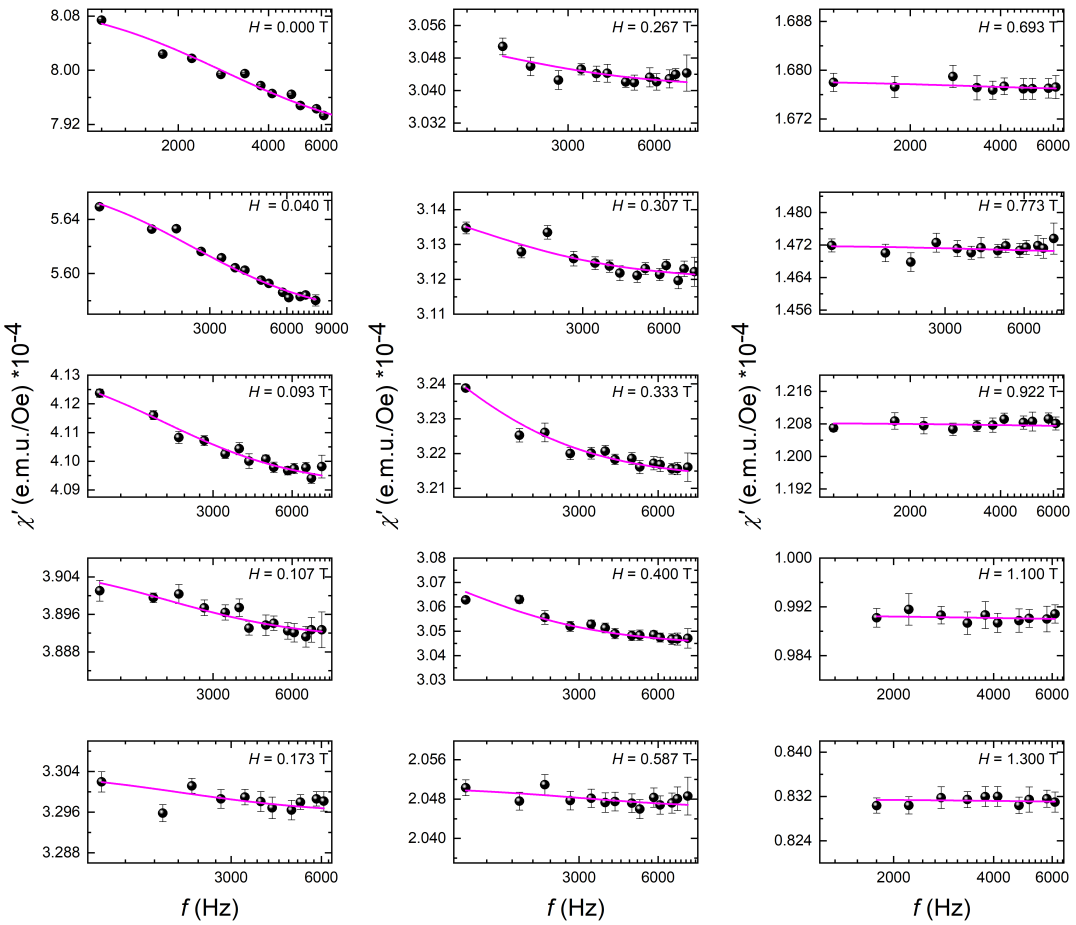

Figure 5.12: (Color online) The real part of ac susceptibility data as a function of frequency χ' (f) at different fixed dc magnetic field at $T = 200$ K for Mn_2NiGa. The experimental data, and the corresponding fitted curve based on the Eq. 5.8 are plotted by black solid ball, and solid magenta line, respectively.

polarized state. As it can be seen in Fig. 5.13(d), the $\tau_0(H)$ value also shoots out around the similar field region ($H = 0.40$ T). The high value of the relaxation time suggests that the system exhibit sluggish type relaxation process around this region compared to other field regions. This fact also suggests the presence of mix magnetic phase around the field region where peak behavior in the χ' data is detected. The distribution of the relaxation time, represented by α, falls between 0.04-0.15 [Fig. 5.13(c)]. The overall low value of α represents the single relaxation process for the present system. But, relatively higher value of α around $H = 0.40$ T compared to the other magnetic field regions [Fig. 5.13(c)] suggests the involvement of the multiple relaxation process. These multiple relaxation processes may probably

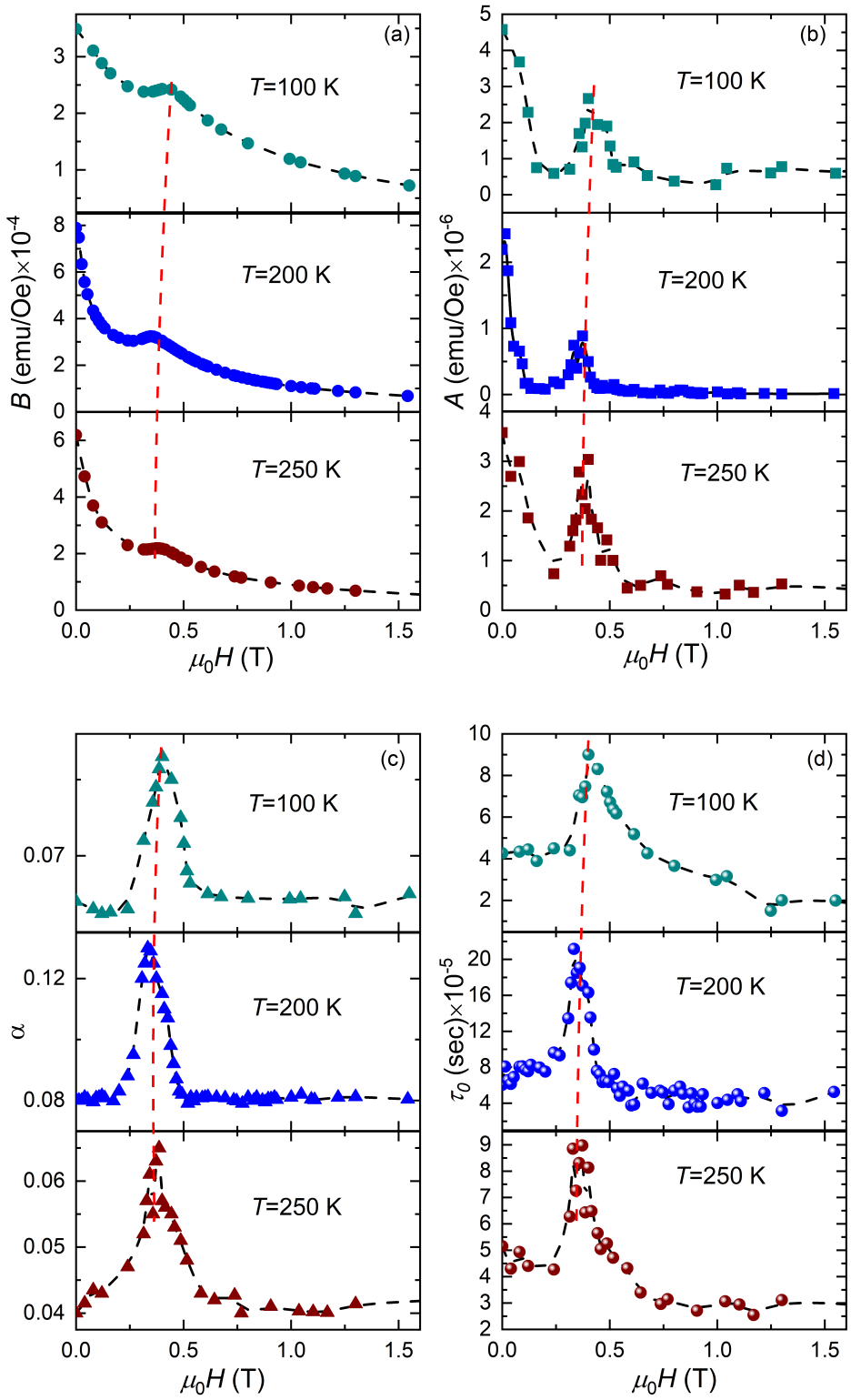

Figure 5.13: (Color online) Field dependence of the Cole-Cole fitting parameters (a) B, (b) A, (c) α, and (d) τ_0 for Mn_2NiGa at different temperature.

happen due to the coexistence of different magnetic spin configurations.

To better understand the peak kind of behavior present in the the $\chi'(H)$ data, it is necessary to compare the relaxation dynamics phenomenon of Mn_2NiGa with that of Mn-Pt-Pd-Sn material. From these comparison, the following assessments can be made. In comparison with relaxation dynamics behavior of Mn-Pt-Pd-Sn, the sluggish behavior of relaxation process around $H = 0.40$ T can be attributed to the irregularities of spin coordination as a result of the presence of topological defects, helical domain, and antiskyrmion lattice. Therefore, at zero magnetic field, the helical spin texture is stabilized as a magnetic ground state by the competing exchange and DM interactions. At $H > 0.4$ T, the helical (H) state transforms into the antiskyrmion lattice (AskX). Around $H = 0.4$ T, the helical and antiskyrmion phases coexist.

5.3.2 Frequency dependent ac susceptibility studies for $Mn_{2.13}Ni_{0.87}Ga$

In Chapter-4, the presence of antiskyrmion phase in $Mn_{2.13}Ni_{0.87}Ga$ is established by means of the magnetic and Hall effect measurements. It is demonstrated through the topological Hall effect measurements that the size of antiskymions in this sample is extremely small (< 10 nm). An indication of the presence of the various magnetic phases is also evident from the multiple transition found in the field dependent ac susceptibility measurements. To understand the effect of small size of the antiskyrmions on the relaxation phenomena associated to it, a detailed frequency dependent study for this sample is presented in this section. Figure 5.14 displays the $\chi'(H)$, and $\chi''(H)$ data at different frequencies at $T = 300$ K. In the $\chi'(H)$ data, a sharp kind transition around the magnetic field of 1 T accompanied with a broad hump-like anomaly around 2 T is also observed, as discussed in Chapter-4. These anomalies in the ac susceptibility curves are highlighted by different color shading.

To analyze the frequency dependence of different magnetic phase regimes by the Cole-Cole model, χ' data are replotted as a function of frequency at a particular dc

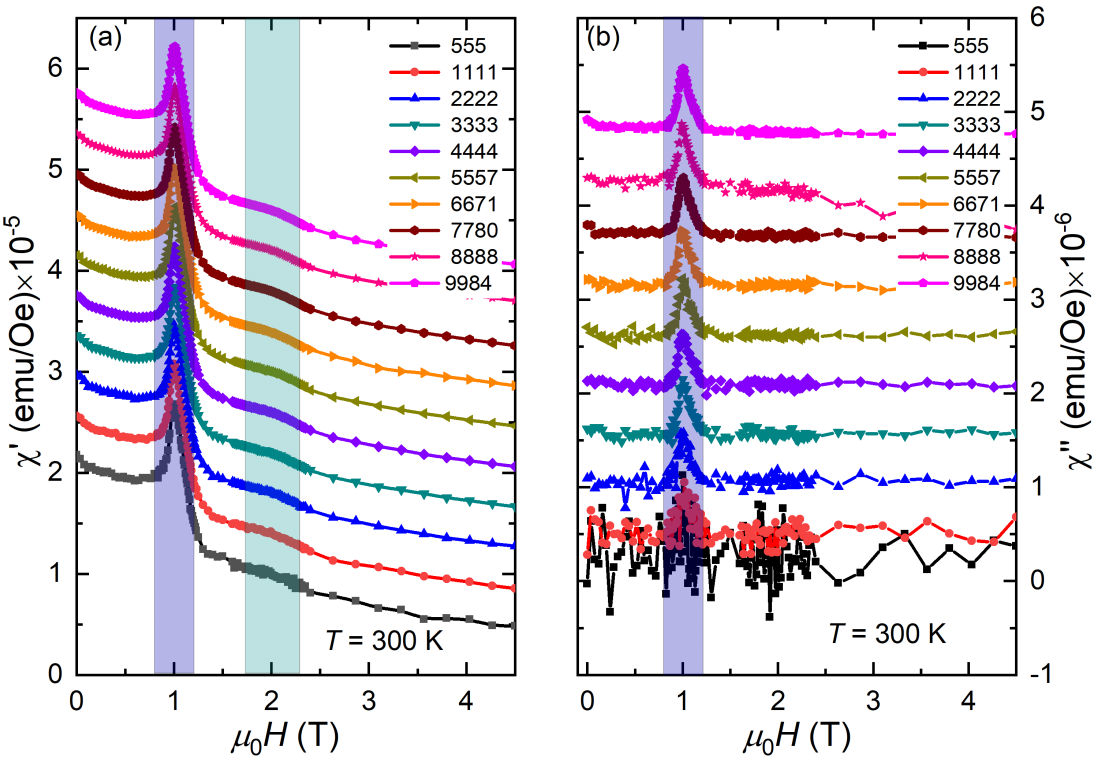

Figure 5.14: (Color online) Field dependence of (a) real part of ac susceptibility $\chi'(H)$, (b) imaginary part of ac susceptibility $\chi''(H)$ at $T = 300$ K measured in different frequencies ranging from 555 Hz to 9984 Hz for $Mn_{2.13}Ni_{0.87}Ga$. The region corresponding to the anomalies are highlighted by the color shading. Note that for clarity purposes, the $\chi'(H)$ data for the successive frequencies are shifted upwards by constant factor starting from the data at $f = 9984$ Hz.

magnetic field, as illustrated in Fig. 5.15. As it can be seen, the inflection point of the $\chi'(f)$ curve shift to lower frequency compared to that in other field regions.

To inspect the magnetic relaxation phenomena associated with the different magnetic phases present in the system, the experimental $\chi'(f)$ data is fitted with the Cole-Cole relation provided by Eq. 5.8. The fitted curve (magenta solid line) together with the experimental data (black solid ball symbols) are presented for $T = 300$ K in Fig. 5.15. Similar kind of analysis is also performed from $T = 200$ K and 300 K. The variation of Cole-Cole fitting parameters with respect to the magnetic field at different temperatures is illustrated in Fig. 5.16. Unlike the Mn_2NiGa sample, all the fitting parameters exhibit peak/dip kind behavior around two different magnetic field regimes for the $Mn_{2.13}Ni_{0.87}Ga$ sample. As seen previously, the fre-

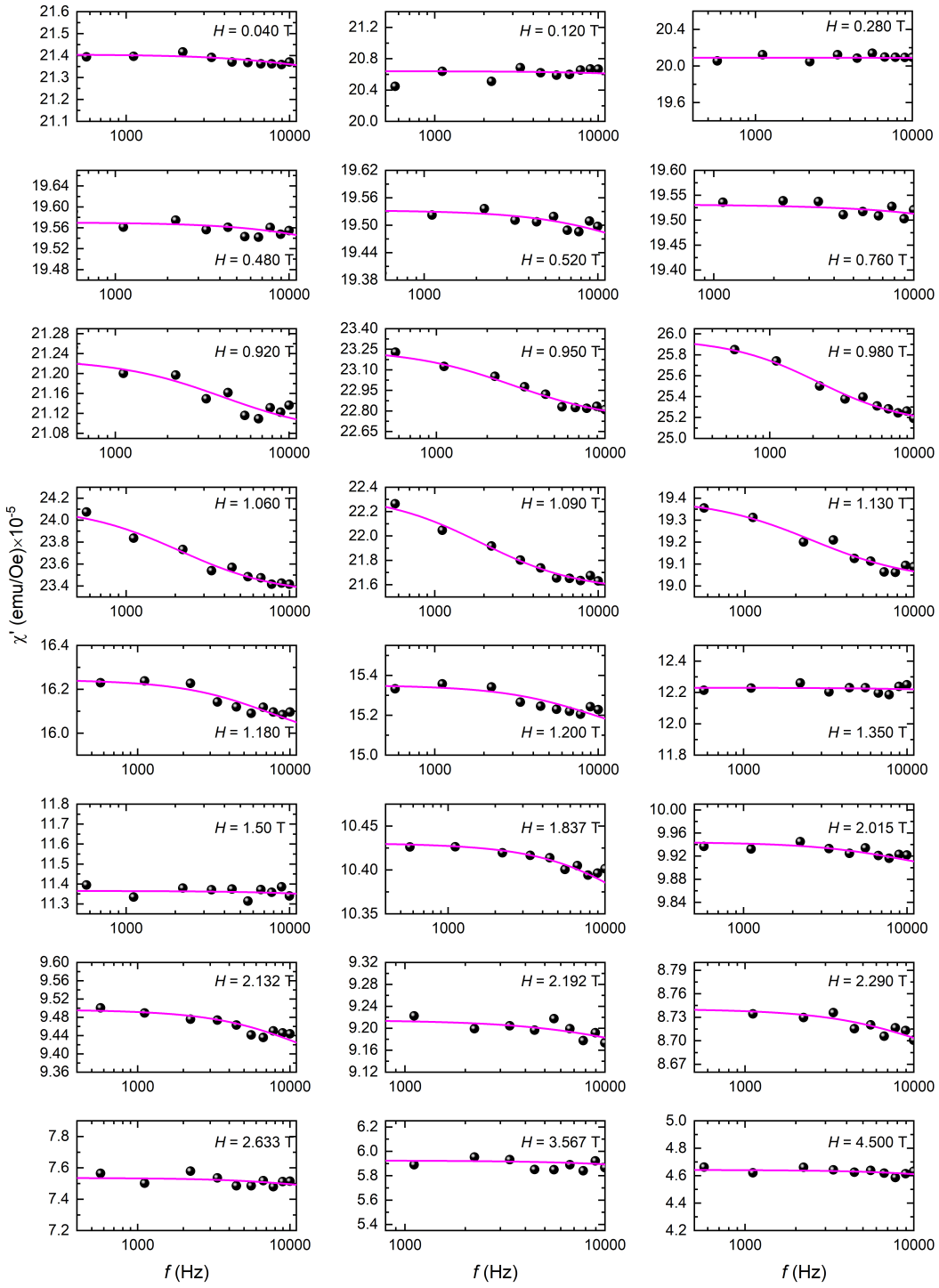

Figure 5.15: (Color online) The real part of ac susceptibility data as a function of frequency $\chi'(f)$ at different fixed dc magnetic field at $T = 300$ K for $Mn_{2.13}Ni_{0.87}Ga$. The experimental data and the corresponding fitted curve based on the Eq. 5.8 are plotted by black solid ball and solid magenta line, respectively.

quency depedency of the $\chi' data$ is provided by the A parameter. This behavior also suggests the presence of mix magnetic phase in the system. Therefore, a significant frequency-dependency around 1 T and 2 T field indicates the presence of a slow relaxation process due to the presence of mixed magnetic phases. It can be seen from the Fig. 5.16(d) that $\tau_0(H)$ is larger around the magnetic fields of 1 T and 2 T in comparison to that in the other field regions. As discussed in the context of other samples, this behavior srises due to the irregularities in the spin coordination at magnetic phase boundaries where more than one magnetic phase coexist. The relaxation time distribution parameter α lies between 0.12-0.18 (Fig. 5.16(c)). The higher α value around 1 T and 2 T indicates the involvement of multiple relaxtion process. This might be due to the coexistence of the magnetic phases, as different magnetic structures relax in a non-coherent maner. In case of the $Mn_{2.13}Ni_{0.87}Ga$ sample, the value of τ_0 is found to be in the order of 10^{-4}-10^{-6} sec.

In conclusion, a detailed relaxation dynamics study of the antiskyrmion hosting D_{2d} symmetric materials are demonstrated through the Cole-Cole analysis of the frequency dependence of ac susceptibility measurements. In case of the antiskyrmion hosting Mn-Pt-Pd-Sn material, the Cole-Cole fitting parameters show a non-monotonic behavior at the phase boundaries (helical + antiskyrmion phase, and antiskyrmion + field-polarized state). The higher value of τ_0 at phase boundaries indicates a slower relaxation process than the pure magnetic phase, like the helical, antiskyrmion, and field polarized state. Similar behavior of all the Cole-Cole fitting parameters are also observed in the case of Mn-Ni-Ga system. Therefore, the relaxation process involved in the Mn-Ni-Ga system can be easily understood in light of similar behavior of the Cole-Cole fitting parameters for Mn-Pt-Pd-Sn. Hence, the slow relaxation process around the field regions where peaks appear in the ac susceptibility data can be described as follows. The helical state may occur at zero magnetic field in the D_{2d} symmetric Mn-Ni-Ga systems due to the competing exchange and DM interactions. When the magnetic field is around 1 T, the antiskyrmions start appearing by breaking the helical spin chains. Thereby, a mixed magnetic state of helical and antiskyrmion appears at this field region. As a result,

the relaxation process in this region slows down in comparison to the pure helical phase. Above 1 T magnetic field, pure antiskyrmion state is obtained. Further increase of the magnetic field above 2 T annihilates the antiskyrmion state to stabilize the field polarized state. Therefore, the coexistence of antiskyrmion and field polarized state results in the sluggish behavior of relaxation around 2 T. The relaxation time is found to be around 10^{-3}-10^{-5} sec for the Mn-Pt-Pd-Sn system, whereas, it falls in the range of 10^{-4}-10^{-6} sec in case of Mn-Ni-Ga alloys. The smaller relaxation time indicates that the relaxation process involved in Mn-Ni-Ga is faster than that for the Mn-Pt-Pd-Sn system. This might be due to the presence of small antiskyrmion in the Mn-Ni-Ga materials.

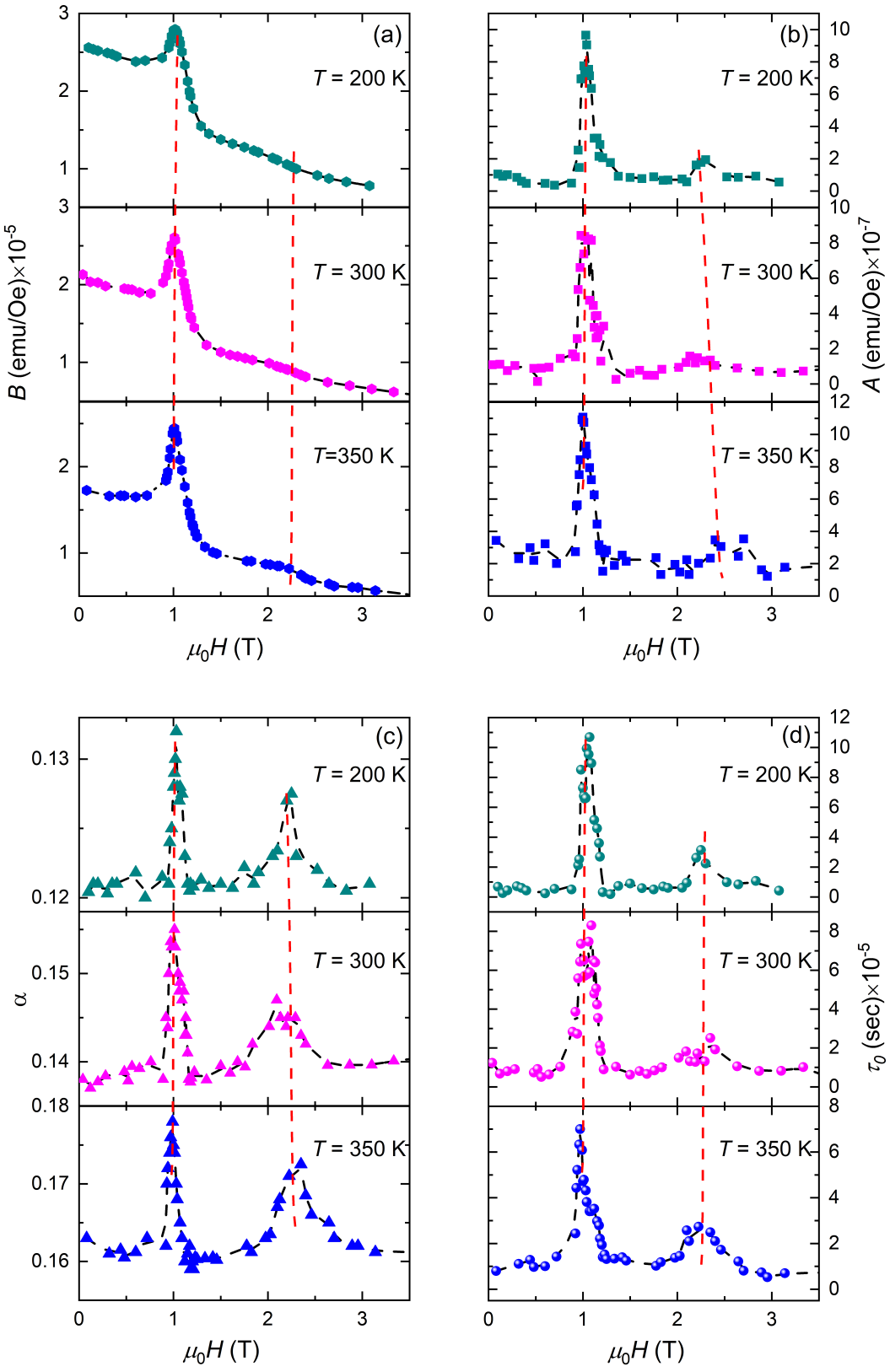

Figure 5.16: (Color online) Field dependence of the Cole-Cole fitting parameters (a) B, (b) A, (c) α and (d) τ_0 for $Mn_{2.13}Ni_{0.87}Ga$ at different temperature.

Chapter 6

Summary, conclusion, future aspects of the thesis

The present chapter summarizes all the results that are presented in this thesis. The present thesis mainly deals with the finding of noble topological magnetic states in the D_{2d} symmetry based tetragonal Heusler materials. In addition, advantages of these topological magnetic objects to counter different kinds of problems arising as a result of skyrmion motion in the racetrack devices are also discussed. It has been discussed in Chapter-1 that the antiskyrmions possess a first-hand advantage over the skyrmions. In this framework, the Mn-rich Mn-Ni-Ga shape memory alloys meet all the criterias to host the antiskyrmion phase. Therefore, the finding of antiskyrmion phase in the D_{2d} symmetric Mn-rich Mn-Ni-Ga system is the primary focus of this thesis. Various aspects of the antiskyrmions and their application perspectives are discussed thoroughly. The crucial results presented in this thesis are discussed briefly in the following.

The Mn-rich Mn-Ni-Ga bulk polycrystalline materials are prepared using the arc-melting furnace. The structural properties of all the samples are analyzed through XRD measurements. In order to check the compositional homogeneity of the samples, the FESEM and EDS measurements are performed on the highly polished sample surface. The homogeneous contrast of the FESEM images of all the sam-

ples vindicates the presence of single compositional phase in these samples. From the XRD pattern for the parent Mn_2NiGa compound, the presence of dominant tetragonal phase with space group I-4m2 and a small amount of cubic phase with space group F-43m are detected at ambient temperature. To further examine the structure below and above the room temperature, the temperature-dependent XRD measurements are also performed on this sample at temperature ranging from $T =$ 15 K and $T = 650$ K. It is found from the temperature-dependent XRD patterns that the crystal structure of the Mn_2NiGa sample below 150 K is pure tetragonal, whereas, above 350 K, the sample crystallizes in a pure cubic structure.

In order to inspect the magnetic properties of the samples, the temperature dependence of magnetization, $M(T)$, measurements and isothermal dc hysteresis measurements are carried out from $T = 2$ K to 400 K using SQUID-VSM. The high temperature $M(T)$ measurements from $T = 400$ K to 750 K are performed using PPMS-VSM. For Mn_2NiGa, a thermal hysteresis between the FC and FH $M(T)$ curves is seen around 300 K due to the presence of structural transition, as confirmed by the temperature-dependent XRD measurements. From the high temperature $M(T)$ data, the magnetic ordering tempearture, T_C, for the Mn_2NiGa sample is found to be about 650 K. The saturation magnetic moment for the Mn_2NiGa sample is found to be 1.41 $\mu_B/f.u.$ at $T = 2$ K. Most interestingly, peak/dip kind of anomalies are distinctly seen at certain magnetic fields in the isothermal $M(H)$ loops. The existence of this anomalous behavior is found at all temperatures up to 300 K, whereas, it is absent above the room temperature. It is important to note that the anomaly in the $M(H)$ loops sustains only in the tetragonal phase of the sample, and disappears in cubic dominated temperature region. Similar kind of anomalies in the dc hystresis curve have also been found due to the presence of (anti-)skyrmion like object [13, 14, 26, 27, 28, 80].

In order to find out the existence of antiskyrmions in the present system, field-dependent Hall transport measurements are carried out at different temperatures. The field-dependent Hall data exhibit similar peak/dip-like anomalies in the tetragonal-dominated temperature range as seen in the dc hysteresis measurements. To detect

the topological Hall-like signal, often emerged in the presence of (anti-)skyrmions [13, 23, 24, 25, 26, 27], the contributions due to the normal and anomalous Hall effect are subtracted from the total measured Hall signal. It is observed that Mn_2NiGa shows a non-zero topological Hall resistivity only in the temperature range where the tetragonal phase exists dominantly. No such topological Hall like signal is found for the cubic dominated phase of the sample. The finite value of the topological Hall effect in the D_{2d} symmetric Mn_2NiGa suggests the presence of antiskyrmion phase up to room temperature. To further prove the existence of the antiskyrmion phase, the ac susceptibility measurements, which are generally used to detect the skyrmion phase [28, 29, 30, 31, 32, 33], are also performed at several temperatures. From the ac susceptibility measurements, a sharp kind of transition can be found in the field range where a finite value of topological Hall resistivity exists. Similar to the dc hystresis measurements and topological Hall effect studies, this unconventional feature in the ac susceptibility measurements sustains only in the tetragonal phase of the sample, whereas, it vanishes in the cubic phase. Therefore, the anomalies in all the magnetic measurements and topological Hall resistivity proves the presence of antiskyrmion phase upto room temperature. The antiskyrmion size estimated from the topological Hall resistivity is found to be about 20 nm. The smaller size of antiskyrmions and the lower saturation magnetization compared with the antiskyrmion host Mn-Pt-Pd-Sn makes the Mn_2NiGa alloy better suitable candidate for the future application of antiskyrmion based racetrack memory.

A part of the present thesis is fully concentrated on manipulation of the antiskyrmion phase in the Mn_2NiGa alloy. Although the antiskyrmions in the Mn_2NiGa alloy possess several advantages over skyrmion, the stability of antiskyrmions against temperature is the major shortcoming for the future application as the antiskyrmion phase does not survive above the room temperature in Mn_2NiGa. Again the reduction of the antiskyrmion size is an important step in order to achieve high density data storage. Even though the saturation magnetic moment in the Mn_2NiGa alloy is smaller than other existing antiskyrmion host materials, further lowering of the magnetic moment is crucial to reduce the antiskyrmion Hall effect by protecting the

antiskyrmion against the in-plane magnetic fields perturbation. In order to achieve all the above mentioned essential properties, a series of $Mn_{2+x}Ni_{1-x}Ga$ ($x = 0.1$-0.28) samples are prepared by using the arc-melting furnace. All these samples are properly characterized through the XRD, FESEM, and EDS measurements. The room temperature XRD patterns confirm that all the sample crystallize in the pure tetragonal phase in contrast to the mix-structural phase found in the parent Mn_2NiGa alloy. The temperature-dependent magnetization measurements for these alloys reveal the absence of structural transition up to the magnetic ordering temperature of 650 K, except for $x = 0.1$. From the dc hysteresis measurements of these samples, it is found that the saturation magnetic moment decreases monotonically from 1.43 $\mu_B/f.u.$ for $x = 0.00$ to 0.43 $\mu_B/f.u.$ for $x = 0.28$. Most importantly, a peak kind of anomaly, as observed in Mn_2NiGa, is also detected for $x \leq 0.20$, whereas, no such kind of abnormality is found for $x = 0.25$ and 0.28. Interestingly, a new type of transition with pronounced hysteresis appears in the $M(H)$ loops at relatively high magnetic fields for $x = 0.13$ and 0.16. In order to explore the presence of topological magnetic objects, Hall transport measurements are performed in these alloys. The topological Hall resistivity extracted from the Hall effect measurements increases initially with composition and reaches the maximum value of around 232 nΩ-cm for $x = 0.13$. A decreasing trend in the topological Hall resistivity is found for $x \geq 0.16$ and finally no THE is observed for $x = 0.25$, and 0.28. Interestingly, in a specific composition range ($0.10 < x < 0.20$), a pronounced double peak kind of behavior is observed instead of the single peak-like behavior of the parent compound seen in the field-induced topological Hall resistivity. In order to study more details about the unusual topological Hall resistivity behavior, ac susceptibility measurements are also performed. In the field induced real part of ac susceptibility measurements, a small kind of transition is found for the composition $x \leq 0.1$, whereas, more than two transitions are seen for the compositions $x = 0.13$ and 0.16. A faint behavior of these anomalies is observed for $x = 0.20$. Therefore, all the anomalies in the dc hysteresis and ac susceptibility measurements, in addition to that finite value of topological Hall resistivity, demonstrate the presence of the antiskyrmion phase

in these materials. In contrast, no peak/hump kind behavior in ac susceptibility and zero topological value suggests the disappearance of antiskyrmion phase for x = 0.25 and 0.28. It is also found that the anisotropy of the system dictates the size of the antiskyrmion that results in the variation of the topological Hall resistivity with the composition. Largest value of topological Hall resistivity and the maximum value of anisotropy for $x = 0.13$ and 0.16 suggest the reduction of antiskyrmion size for this sample. The presence of multiple transitions in the ac susceptibility data and double peak kind of behavior in the field driven topological Hall data indicate the coexistence of various topological phases for $0.10 < x < 0.20$. According to the micromagnetic simulation studies, these topological phases are antiskyrmion, antiskyrminionums, and antiskyrmion pockets. The small size antiskyrmions and the coexistence of various topological phases in a large temperature range in the low magnetic Mn-Ni-Ga samples possess an important prospect for the realization of room temperature high density storage devices based on antiskyrmions.

Final part of the thesis is fully devoted to the relaxation dynamics study of antiskyrmion hosting materials by the means of ac susceptibility measurements. To study the relaxation dynamics, frequency dependent ac susceptibility study for the known antiskyrmion hosting Mn-Pt-Pd-Sn system is carried out in the context of Cole-Cole model. It is found from this analysis that the relaxation process at magnetic phase boundaries between the helical and antiskyrmion phase, antiskyrmion and field polarized state, is slower than that of in the pure magnetic phases. The slower relaxation process at the phase boundaries may occur due to the irregularities in the spin coordination between different spin configurations as a result of the coexistence of magnetic phases. It is also found that the relaxation process in the pure magnetic phase obeys the Debye type relation with negligible distribution of the relaxation time. In contrast, a slight deviation from this behavior is found at the phase crossover regions due to the presence of multiple relaxation processes resulting from the conjunction of two or more magnetic phases. The relaxation time for the Mn-Pt-Pd-Sn materials is found to be about 10^{-3}-10^{-5} sec. Similar relaxation dynamics study is performed on the Mn-Ni-Ga systems where the presence of smaller

antiskyrmion size compared to Mn-Pt-Pd-Sn materials is demonstrated through various measurement techniques. In this case, almost similar sluggish type of relaxation process appears around the magnetic field regions where peak-like transitions are found in the ac susceptibility data. A shorter relaxation time of approximately 10^{-4}-10^{-6} sec indicates the faster relaxation process in the Mn-Ni-Ga alloys compared to that of Mn-Pt-Pd-Sn system. This might be due to the small size of antiskyrmions present in the Mn-Ni-Ga system.

In conclusion, a detailed study of the antiskyrmion phase in the Heusler inverse tetragonal alloys is illustrated in the present thesis. In most part of the thesis, ac susceptibility study and the Hall transport measurements are performed to explore the presence of antiskyrmion in the Mn-Ni-Ga alloys. It is demonstrated that the temperature stability range and size of antiskyrmions, in addition to the magnetization, can be easily tuned via a systematic engineering of the chemical composition. The existence of multiple topological magnetic phases is established through the field dependent topological Hall effect measurements, ac susceptibility measurements and the micromagnetic simulation studies. To investigate the relaxation dynamics, frequency dependence of ac susceptility measurements are performed on the known antiskyrmion hosting Mn-Pt-Pd-Sn system. The magnetic relaxation process in this material is governed by the Debye type relation. The higher relaxation time at the phase boundaries is attributed to the slower relaxation process than the pure magnetic phase. In order to study the relaxation dynamics process for Mn-Ni-Ga alloys, similar type of relaxation study to that of Mn-Pt-Pd-Sn system is performed. Higher relaxation time at the phase boundaries indicates the presence of mixed-phase comprising helical and antiskyrmion phase and/or coexistence of antiskyrmion and field polarized state. It is found that the relaxation process in the Mn-Ni-Ga alloys is relatively faster than that of Mn-Pt-Pd-Sn system.

6.1 Future aspects of the thesis

The finding of smaller antiskyrmion size and the coexistence of different topological phases at a wide temperature range, along with small magnetic moment in Mn-Ni-Ga alloys possess a great importance for the realization of storage devices based on antiskyrmions. However, the small size of these magnetic spin configurations with size less than 10 nm prevents their real-space visualization. Therefore, other high-resolution imaging techniques, e.g., small-angle neutron scattering and resonant soft x-ray scattering needs to be performed in the future for the direct visualization of these spin configurations. It has been found that antiskyrmions in high magnetic moment based materials can be easily converted to skyrmion via trivial bubble by applying small amount of in-plane magnetic fields [15, 62]. Therefore, it would be interesting to investigate the stability of the antiskyrmion phase against in-plane magnetic fields in the low magnetic Mn-Ni-Ga samples. Besides the static properties, the current-driven motion of these small size antiskyrmions in the low magnetic Mn-Ni-Ga samples needs to be studied in the near future. It has been found theoretically that skyrmions/antiskyrmions in the antiferromagnet or compensated ferrimagnetic materials probably move in a straight-line path irrespective of the current direction [94]. Although the magnetic moment of the Mn-Ni-Ga alloys is successfully tuned to a reasonable lower value, further reduction of moment to zero value will be very helpful for the realization of antiskyrmion motion in compensated ferrimagnetic materials. A detailed study on the antiskyrmion phase in the Mn-Ni-Ga thin films will be an essential prospect for the future nanoscale spintronic applications. As the emergent electromagnetic induction is inversely proportional to the skyrmion size [49], the Mn-Ni-Ga alloys with antiskyrmion size less than 10 nm can be a promising candidate for achieving room-temperature nanoscale electromagnetic inductors with the same efficiency as the bulky conventional inductors.

References

[1] Albert Fert, Vincent Cros, and João Sampaio, *Nature Nanotechnology*, **8**, 152–156 (2013).

[2] S. Mühlbauer et al., *Science*, **323**, 915–919 (2009).

[3] X. Z. Yu et al., *Nature*, **465**, 901–904 (2010).

[4] X. Z. Yu et al., *Nature Materials*, **10**, 106–109 (2011).

[5] K. Shibata et al., *Nature Nanotechnology*, **8**, 723–728 (2013).

[6] Y. Tokunaga et al., *Nature Communications*, **6**, 7638 (2015).

[7] Y. Fujishiro et al., *Nature Communications*, **10**, 1059 (2019).

[8] S. Seki et al., *Science*, **336**, 198–201 (2012).

[9] I. Kézsmárki et al., *Nature Materials*, **14**, 1116–1122 (2015).

[10] S. Bordács et al., *Scientific Reports*, **7**, 7584 (2017).

[11] Takashi Kurumaji et al., *Phys. Rev. Lett.*, **119**, 237201 (2017).

[12] Abhay K. Srivastava et al., *Advanced Materials*, **32**, 1904327 (2020).

[13] Takashi Kurumaji et al., *Science*, **365**, 914–918 (2019).

[14] Ajaya K. Nayak et al., *Nature*, **548**, 561–566 (2017).

[15] Licong Peng et al., *Nature Nanotechnology*, **15**, 181–186 (2020).

[16] Jagannath Jena et al., *Nature Communications*, **11**, 1115 (2020).

[17] F. Jonietz et al., *Science*, **330**, 1648–1651 (2010).

[18] X. Z. Yu et al., *Nature Communications*, **3**, 988 (2012).

[19] T. Schulz et al., *Nature Physics*, **8**, 301–304 (2012).

[20] Wanjun Jiang et al., *Nature Physics*, **13**, 162–169 (2017).

[21] Siying Huang et al., *Phys. Rev. B*, **96**, 144412 (2017).

[22] AN Bogdanov and DA Yablonskii, *Zh. Eksp. Teor. Fiz*, **95**, 182 (1989).

[23] A. Neubauer et al., *Phys. Rev. Lett.*, **102**, 186602 (2009).

[24] N. Kanazawa et al., *Phys. Rev. Lett.*, **106**, 156603 (2011).

[25] C. Franz et al., *Phys. Rev. Lett.*, **112**, 186601 (2014).

[26] Max Hirschberger et al., *Nature Communications*, **10**, 5831 (2019).

[27] Nguyen Duy Khanh et al., *Nature Nanotechnology*, **15**, 444–449 (2020).

[28] A. Bauer and C. Pfleiderer, *Phys. Rev. B*, **85**, 214418 (2012).

[29] Y. Tokunaga et al., *Nature Communications*, **6**, 7638 (2015).

[30] F. Qian et al., *Phys. Rev. B*, **94**, 064418 (2016).

[31] Ádám Butykai et al., *Phys. Rev. B*, **96**, 104430 (2017).

[32] L. J. Bannenberg et al., *Phys. Rev. B*, **98**, 184430 (2018).

[33] Kosuke Karube et al., *Science Advances*, **4**, eaar7043 (2018).

[34] M. N. Baibich et al., *Phys. Rev. Lett.*, **61**, 2472–2475 (1988).

[35] G. Binasch et al., *Phys. Rev. B*, **39**, 4828–4830 (1989).

[36] M. Julliere, *Physics Letters A*, **54**, 225–226 (1975).

[37] Stuart S. P. Parkin, Masamitsu Hayashi, and Luc Thomas, *Science*, **320**, 190–194 (2008).

[38] M. Yamanouchi et al., *Nature*, **428**, 539–542 (2004).

[39] Yoshihiko Togawa et al., *Japanese Journal of Applied Physics*, **45**, L683–L685 (2006).

[40] Luc Thomas et al., *Science*, **330**, 1810–1813 (2010).

[41] Toshiaki Tanigaki et al., *Nano Letters*, **15**, 5438–5442 (2015).

[42] B. D. Cullity and C. D. Graham. *Introduction to Magnetic Materials*. 2nd ed. Wiley-IEEE Press, 2008. ISBN: 0471477419.

[43] I. Dzyaloshinsky, *Journal of Physics and Chemistry of Solids*, **4**, 241–255 (1958).

[44] Tôru Moriya, *Phys. Rev.*, **120**, 91–98 (1960).

[45] Satoru Nakatsuji, Naoki Kiyohara, and Tomoya Higo, *Nature*, **527**, 212–215 (2015).

[46] Ajaya K. Nayak et al., *Science Advances*, **2**, e1501870 (2016).

[47] Pradeep K. Rout et al., *Phys. Rev. B*, **99**, 094430 (2019).

[48] N. L. Chung et al., *Journal of Applied Physics*, **104**, 084502 (2008).

[49] Tomoyuki Yokouchi et al., *Nature*, **586**, 232–236 (2020).

[50] O. Meshcheriakova et al., *Phys. Rev. Lett.*, **113**, 087203 (2014).

[51] M L Plumer and M B Walker, *Journal of Physics C: Solid State Physics*, **14**, 4689–4699 (1981).

[52] Masayoshi Ishida et al., *Journal of the Physical Society of Japan*, **54**, 2975–2982 (1985).

[53] B Lebech, J Bernhard, and T Freltoft, *Journal of Physics: Condensed Matter*, **1**, 6105–6122 (1989).

[54] P. Ferriani et al., *Phys. Rev. Lett.*, **101**, 027201 (2008).

[55] S. Meckler et al., *Phys. Rev. Lett.*, **103**, 157201 (2009).

[56] Niklas Romming et al., *Science*, **341**, 636–639 (2013).

[57] Seonghoon Woo et al., *Nature Materials*, **15**, 501–506 (2016).

[58] Charles Kittel. *Introduction to Solid State Physics*. 8th ed. Wiley, 2004. ISBN: 9780471415268.

[59] T. Okuno et al., *Journal of Magnetism and Magnetic Materials*, **240**, 1–6 (2002).

[60] T. H. R. Skyrme and Basil Ferdinand Jamieson Schonland, *Proceedings of the Royal Society of London. Series A. Mathematical and Physical Sciences*, **260**, 127–138 (1961).

[61] Toshiaki Tanigaki et al., *Nano Letters*, **15**, 5438–5442 (2015).

[62] Jagannath Jena et al., *Nano Letters*, **20**, 59–65 (2020).

[63] K. Karube et al., *Nature Materials*, **15**, 1237–1242 (2016).

[64] Naoto Nagaosa et al., *Rev. Mod. Phys.*, **82**, 1539–1592 (2010).

[65] M. Raju et al., *Nature Communications*, **10**, 696 (2019).

[66] E. Haupt F Heusler W Starck, *Verh DPG*, **5**, 220–222 (1903).

[67] Tanja Graf, Claudia Felser, and Stuart S.P. Parkin, *Progress in Solid State Chemistry*, **39**, 1–50 (2011).

[68] J. Kübler, A. R. William, and C. B. Sommers, *Phys. Rev. B*, **28**, 1745–1755 (1983).

[69] G. D. Liu et al., *Applied Physics Letters*, **87**, 262504 (2005).

[70] Antoni Planes, Lluís Mañosa, and Mehmet Acet, *Journal of Physics: Condensed Matter*, **21**, 233201 (2009).

[71] G. D. Liu et al., *Phys. Rev. B*, **74**, 054435 (2006).

[72] J. Zhang et al., *Scripta Materialia*, **58**, 798–801 (2008).

[73] Christian G. F. Blum et al., *Applied Physics Letters*, **98**, 252501 (2011).

[74] Sanjay Singh et al., *Applied Physics Letters*, **104**, 051905 (2014).

[75] P. J. Webster et al., *Philosophical Magazine B*, **49**, 295–310 (1984).

[76] PJ Brown et al., *Journal of Physics: Condensed Matter*, **14**, 10159 (2002).

[77] Jordi Marcos et al., *Phys. Rev. B*, **68**, 094401 (2003).

[78] Sanjay Singh et al., *Journal of Physics: Condensed Matter*, **25**, 212203 (2013).

[79] Ali Salman Ali. "Application of Nanomaterials in Environmental Improvement". In: *Nanotechnology and the Environment*. Ed. by Mousumi Sen. Rijeka: IntechOpen, 2020. Chap. 2.

[80] E. Ruff et al., *Scientific Reports*, **5**, 15025 (2015).

[81] Sk Jamaluddin et al., *Advanced Functional Materials*, **29**, 1901776 (2019).

[82] X. S. Wang, H. Y. Yuan, and X. R. Wang, *Communications Physics*, **1**, 31 (2018).

[83] SV Andreev et al., *Journal of alloys and compounds*, **260**, 196–200 (1997).

[84] Michael Donahue. *OOMMF User's Guide, Version 1.0*. en. 1999.

[85] S. Rohart and A. *Thiaville DMExchange6Ngbr, http://math.nist.gov/oommf/contrib/oxsext.* 2012.

[86] Stefan Heinze et al., *Nature Physics*, **7**, 713–718 (2011).

[87] A. H. Morrish, *New York*, **3**, 87–101 (1965).

[88] M Bałanda, *Acta Phys. Pol. A.*, **124**, 964–976 (2013).

[89] C V Topping and S J Blundell, *J. Phys. Condens. Matter*, **31**, 013001 (2019).

[90] P. Debye. *in Polar Molecules*. (The Chemical Catalog Company, New York, 1929.

[91] H.B.G. Casimir and F.K. du Pré, *Physica*, **5**, 507–511 (1938).

[92] Jayaraman Rajeswari et al., *Proceedings of the National Academy of Sciences*, **112**, 14212–14217 (2015).

[93] Yaakov Kraftmakher, *American Journal of Physics*, **68**, 375–379 (2000).

[94] Xichao Zhang, Yan Zhou, and Motohiko Ezawa, *Scientific Reports*, **6**, 24795 (2016).